**UNIVERSITY OF LEEDS**

# Magnetic and electric properties of bismuth ferrite lead titanate ceramics

Timothy James Stevenson

Submitted in accordance with the requirements for the degree of
Doctor of Philosophy
The University of Leeds
Institute for Materials Research
School of Process, Environmental and Materials Engineering

September 2010

The candidate confirms that the work submitted is his own, except where work which has formed part of jointly-authored publications has been included. The contribution of the candidate and the other authors to this work has been explicitly indicated below. The candidate confirms that appropriate credit has been given within the thesis where reference has been made to the work of others.

All neutron experiments were completed with Dr. Tim Comyn as the principal investigator, and have resulted in the jointly-authored publications listed, where the article has been written by the principal investigator based on the work completed by the author. The work herein is the authors own analysis of the data, except where explicitly highlighted in the text. This is summarised below.

(i)   Chapter 4.5. Pressure Induced Phase Transformation. Structure refinement included in this chapter has been completed by Dr. Comyn.

1. Stevenson, T., T. P. Comyn, A. D-Aladine and A. J. Bell. (2010) "Change in incommensurate magnetic order towards commensurate order in bismuth ferrite lead titanate." Journal of Magnetism and Magnetic Materials. **322**, 22. pp.64-67. DOI: 10.1016/j.jmmm.2010.07.043

2. Comyn, T. P., T. Stevenson, M. Al-Jawad, S. Turner, R. I. Smith, A. J. Bell and R. Cywinski (2009) "High temperature neutron diffraction studies of $0.9BiFeO_3$-$0.1PbTiO_3$." Journal of Applied Physics. **105**. 9, 094108. DOI: 10.1063/1.3116735

3. Comyn, T. P., T. Stevenson, M. Al-Jawad, S. L. Turner, R. I. Smith, W. G. Marshall, A. J. Bell and R. Cywinski (2008) "Phase-specific magnetic ordering in $BiFeO_3$ – $PbTiO_3$." Applied Physics Letters. **93**, 23, 232901. DOI: 10.1063/1.3042209

4. Stevenson, T., T. P. Comyn, A. J. Bell and R. Cywinski (2007) "Multiferroic (ferroelectro-magnetic) properties of bismuth ferrite lead titanate." 16th IEEE International Symposium on Applications of Ferroelectrics. Nara, Japan. pp. 421-423.

5. Comyn, T. P., T. Stevenson and A. J. Bell (2005) "Piezoelectric properties of $BiFeO_3$ – $PbTiO_3$ ceramics." Journal de Physique IV. **128**, 128. pp. 13-17. DOI: 10.1051/jp4:2005128003.

# Acknowledgments

# ABSTRACT

Solid solutions of multiferroic $BiFeO_3$ doped with ferroelectric $PbTiO_3$ (BFPT) can be prepared by conventional mixed oxide processing to produce a range of polycrystalline ceramics ranging throughout the $xBiFeO_3$ - $(1-x)PbTiO_3$ series.

Sintered ceramics are shown to exhibit mixed tetragonal (P4mm) and rhombohedral (R3c) phase perovskite distortions from 0.4 ≤ x < 0.75, where at x ~ 0.75 a morphotropic phase boundary exists and compositions x > 0.75 are entirely rhombohedral.

From extensive use of neutron diffraction experiments, the phase coexistence is attributed to compensation for the internal strain induced upon cooling through the ferroelectric Curie point from cubic, to the distorted tetragonal perovskite phase ($c/a$ = 1.17). This drives a further partial transformation to the (~4 %) lower volume rhombohedral phase as a relief mechanism.

Increasing the sinter temperature and fast cooling (> 900 °C/hr) sees the monolithic samples x ≤ 0.7 disintegrate to various levels of particulate size, when a critical grain size is exceeded (7 μm), which in turn is inversely proportional to the grain boundary fracture energy. The magnetic properties studied using high resolution powder diffractometry of these two states present G-type antiferromagnetism (AFM) in both the rhombohedral and tetragonal phases; but with $T_N$ above ambient temperature for R3c, and below for P4mm for all compositions except x = 0.3. Compositions below this $PbTiO_3$ rich solution are never observed to support antiferromagnetic order, as the dilution of magnetic iron ions exceeds the percolation threshold via substitution with titanium ions.

The rhombohedral phase is shown to exhibit an incommensurate, modulated magnetic order, with a propagation vector perpendicular to the magnetization vector, which decreases in periodicity with increasing bismuth ferrite, from 840 Å for x = 0.75. At room temperature, transforming the paramagnetic tetragonally distorted powder to a G-type AFM rhombohedral phase, is observed with the application of hydrostatic pressure. Evident from neutron experiments, using the Pearl instrument at ISIS, full transformation can be achieved with moderate pressures of 0.77 GPa, effectively 'switching' on the magnetic order.

The monolithic samples were used at 250 K to observe the changes in simultaneous structural and *G*-type antiferromagnetic properties as a function of applied electric field (0 to 10 MVm$^{-1}$) for the most piezoelectrically active samples, around the MPB composition (x = 0.7), using neutron diffraction at the Berlin neutron scattering centre; instrument E2.

An observed increase in rhombohedral phase occurs with the application of electric field from peak analysis, which relates to a proportional increase in observed antiferromagnetic intensity (5 %).

These two behaviours are proposed to be linked by the internal strain developed within the system, from increased polarisation forcing a partial phase transformation from the tetragonal to the rhombohedral phase which can support the antiferromagnetic order at room temperature.

# CONTENTS

# LIST OF FIGURES

# LIST OF TABLES

## ABBREVIATIONS

AFE – Antiferroelectric

AFM – Antiferromagnetic

BENSC – Berlin Neutron Scattering Centre

BFO – Bismuth ferrite

BFPT – Bismuth ferrite lead titanate system

CCD - Charge Coupled Device

CDS – Chemical Database Service

CW – Constant Wavelength

emf – Electro-motive Force

ESRF – European Synchrotron Radiation Facility

FE – Ferroelectric

FEG – Field Emission Gun

FM – Ferromagnetism

FWHM – Full Width Half Maximum

HFR – High Flux Reactor

HRPD – High Resolution Powder Diffractometer

IC – Incommensurate

ICSD – Inorganic Crystal Structure Database

ILL – Institute Laue-Langevin

IRF – Instrument Resolution File

ISS – International Short Symbol for space group identifying

LLB – Laboratoire Leon Brillouin

ME – Magnetoelectric Effect

MPB – Morphotropic Phase Boundary

MPR – Mixed Phase Region

PASS – Programmable Antiscatter Slits

PDS – Programmable Divergence Slits

PE – Paris-Edinburgh

PSD – Position Sensitive Detectors

PTO – Lead titanate

PZT – Lead zirconate titanate $Pb(ZrTi)O_3$

SE – Superexchange

SEM – Scanning Electron Microscopy

SQUID – Superconducting Quantum Interference Device

TOF – Time Of Flight

VSM – Vibrating Sample Magnetometry

XRD – X-ray Diffraction

# SYMBOLS

$(B_0)D$ = Demagnetization Field

$B_j(y)$ = Brillouin Function

$E_C$ = Coercive Field

$H_C$ = Magnetic Coercive Field

$M_r$ = Remnant Magnetization

$M_s$ = Saturated Magnetization

$P_r$ = Remnant Polarization

$P_s$ = Saturation Polarization

$T_0$ = Ferroelectric Curie Temperature

$T_C$ = Curie Point

$T_N$ = Néel Temperature

$V_m$ = Molar Volume

$d_{ij}$ = Piezoelectric Charge Coefficient

$k_{eff}$ = Piezoelectric Coupling Coefficient

$m_e$ = Mass of an electron = 9.1091 x10$^{-31}$ kg

$\mu_0$= Permeability of Free Space = $4\pi$ x10$^{-7}$ Hm$^{-1}$

$\mu_B$ = Bohr Magneton = 9.2732 x10-24 J T$^{-1}$

$\mu_N$= Nuclear magneton = 5.051 x10-27 J T$^{-1}$

$\mu_n$ = Neutron magnetic dipole moment = -1.913 µN

$\mu_r$ = Relative Magnetic Permeability

$\chi_V$ = Magnetic Susceptibility per volume

$\chi_m$ = Magnetic Susceptibility per mole

g = Landau 'g' factor

$h$ = Planck's constant = 6.6256 x10-34 J s

ε$_r$ = Relative Permittivity

$A$ = Area

$B$ = Magnetic Induced Field

$C$ = Capacitance

$C$ = Curie Constant

$E$ = Electric Field Strength

$F$ = Force (Newtons) (or dynes (dyn) where 1 dyn = 1 µN)

$H$ = Magnetic Field Strength

$I$ = Electric Current

$J$ = Total Angular Momentum

$L$ = Orbital Angular Momentum

$M$ = Magnetization (magnetic moment per unit volume)

$N$ = Number of atoms per mole (Avagadro's no.) = 6.0225 x1023 mole$^{-1}$

$P$ = Electric Polarization

$Q$ – Dielectric quality factor

$Q$ = Piezomagnetic Coefficient

$Q$ = Piezomagnetic Coefficient

$Q$ = Quality Factor

$S$ = Spin Angular Momentum

$T$ = Temperature

$V$ = Volume

$X$ = Lorentzian Isotropic Strain

$X$ = Mechanical Stress

$Z$ = Atomic Number

$b$ = Neutron scattering length

$e$ = Charge of an electron = $1.6021 \times 10^{-19}$ coulomb

$g$ = Free Energy Density

$k$ = Boltzmann's Constant = $1.3805 \times 10\text{-}23 \text{ JK}^{-1}$

$k$ = Piezoelectric Coupling Factor

$k$ = wavevector

$s$ = Elastic Compliance

$x$ = Engineering Strain

$\Phi$ = Neutron Flux

$\alpha$ = Magnetoelectric coefficient

$\gamma$ = Molecular Field Coefficient

$\varepsilon$ = Electric Permittivity

$\theta$ = Magnetic Curie Temperature

$\lambda$ = Wavelength

$\mu$ = Magnetic Permeability

$\rho$ = Density

$\sigma$ = Engineering Stress

$\upsilon$ = Velocity

$\varphi$ = Magnetic Flux

$\chi$ = Magnetic Susceptibility per unit mass

# INTRODUCTION

## *Background*

Electroceramics are an advanced class of modern engineering materials. These materials have been successful mainly due to their remarkable electronic properties which are readily exploitable in many different applications. The electrical properties are dependent on a number of factors including microstructure, chemical composition and porosity to name but a few. Ferroelectric materials are an essential component of modern electronic devices. Their use spans from capacitors, to sensors. For over 50 years $Pb(Zr,Ti)O_3$ (PZT) has remained at the forefront of piezoelectric, ferroelectric materials. PZT generally displays a high piezoelectric constant, remnant polarization and low coercive field.

More recently the characterisation of magnetic properties in ferroelectrics has been researched increasingly intently, with the aim to produce magnetoelectric materials for application where an electric or magnetic field can affect the magnetic or electric response respectively.

Magnetoelectric ferroics, however, are intrinsically rare as the partial filling of the transition metal *d* electron shells, which is required for magnetism to be exhibited, reduces the likelihood of an off-centred ion structure; the basis of the ferroelectric effect. Some do exist though, with the most promising material in the literature expressed as bismuth ferrite, as it is one of a very significant few that can exhibit both ferroics above room temperature.

Techniques used to characterise these materials, range from direct an electromechanical modality, which actually emerges to be non trivial, to indirect measurements such as magnetocapacitance, ac susceptibility, and particularly relevant for this work, neutron diffraction. Neutrons have the unique properties of a magnetic moment and null charge, allowing magnetic and nuclear structures to be probed simultaneously, whilst offering excellent contrast between light and heavy elements.

Temperature, composition and structure dependence is important, as many of the magnetoelectric systems are not coupled linearly; instead relying on strain, or structural coupling, to yield non-linear effects.

Materials based on the $BiFeO_3 - PbTiO_3$ (BFPT) system have been reported previously for their use in high temperature applications, but only powder characterisation has been carried out until recently. This study will investigate some of the first magnetoelectric experiments undertaken on this ceramic in bulk form, predominantly from neutron diffraction to characterise magnetism, phase and structure, as a function of temperature and pressure.

The BFPT system has considerable potential in high temperature piezoelectric and magnetoelectric applications, with a Curie point being some 250°C higher than most PZT based material, and an antiferromagnetic Neél temperature above room temperature. In addition to this, it has a tetragonal phase that exhibits an extremely large spontaneous strain. If not controlled the internal stress upon cooling can destroy the material, such is the case for the $PbTiO_3$ end member. It is this strain structure relationship that is of particular interest.

### Aims and Objectives

The overall aim of this work was to understand the magnetoelectric and magnetoelastic coupling within the bismuth ferrite lead titanate solid solution. This would complement existing literature on the piezoelectric properties to provide a comprehensive analysis of the system, and indicate the feasibility of magnetic 'switching' with an electric field. This could enable optimisation for engineering applications.

To achieve this the project was segregated into smaller 'case studies' focussing initially on compositions of interest to make sensible decisions on where and how to conduct time and funding dependent experiments. Namely neutron diffraction experiments, which require peer assessed proposals.

The case studies employed X-ray, synchrotron and neutron diffraction to characterise the compositional and processing history dependence on resultant phase contributions, which as a solid solution was thought to inherently display stoichiometries with optimum properties from competing structure formation; such as seen in other morphotropic phase boundary materials like PZT.

Alongside to the nuclear structure analysis, neutron diffraction time on various instruments was sought to provide information pertaining to the presence of magnetic iron within the bismuth ferrite end member. The dependence of magnetic order on phase is paramount for comparison to the piezoelectric analogy. Further experiments were envisaged as results suggested the phase could be manipulated to ascertain some level of control on the magnetic arrangements, leading to novel neutron diffraction experiments, which are herein presented.

# 1    LITERATURE REVIEW

## 1.1   CHAPTER OVERVIEW

This chapter aims to cover the principles of atomic structure and how the manipulation of atomic arrangements can present phenomenon such as ferroelectricity and ferromagnetism. It will serve as a basis to describe subsequent experiments, as well as introduce the magnetoelectric effect and magnetoelectric materials.

The history of bismuth ferrite ($BiFeO_3$) and $BiFeO_3$-$PbTiO_3$ its evolution, future and applications will be covered.

## 1.2   STRUCTURE

### 1.2.1  Crystal Structures

Crystallography describes the arrangement of atoms in a material which defines its physical properties. Manipulation of atomic arrangements to enhance favourable properties in the material is the basis of materials science.

A crystal structure is composed of atoms arranged in a particular way to form a lattice, an array of points, or motif, repeated periodically in three dimensions. When these arrays are 'stripped' down to their fewest number of atoms to describe the overall structure and symmetry, a unit cell is formed.

The unit cell of any structure can be categorised by one of seven lattice systems. The different shapes and sizes of these cells are described by the three cell edge lengths, or lattice vectors (Hammond, 1992) $a, b, c,$ and the angles between them $\alpha, \beta, \gamma,$ (Figure 1-1) as well as the presence of a body or face centred atom. The lattice systems that then describe the possible combinations of these lattice parameters are cubic, hexagonal, tetragonal, rhombohedral, orthorhombic, monoclinic and triclinic. Combining this with the various possible lattice centres, we can describe any crystal structure with one of fourteen 'Bravais lattices.' (Figure 1-2).
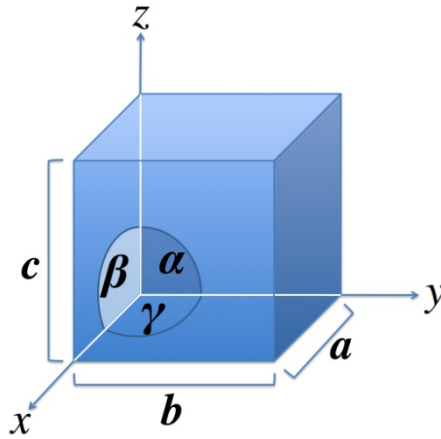
**Figure 1-1 A unit cell with the Cartesian axis' (x,y,z), lattice vectors (a,b,c) and angles between them (α,β,γ) (recreated from Callister, 2000 p.38)**
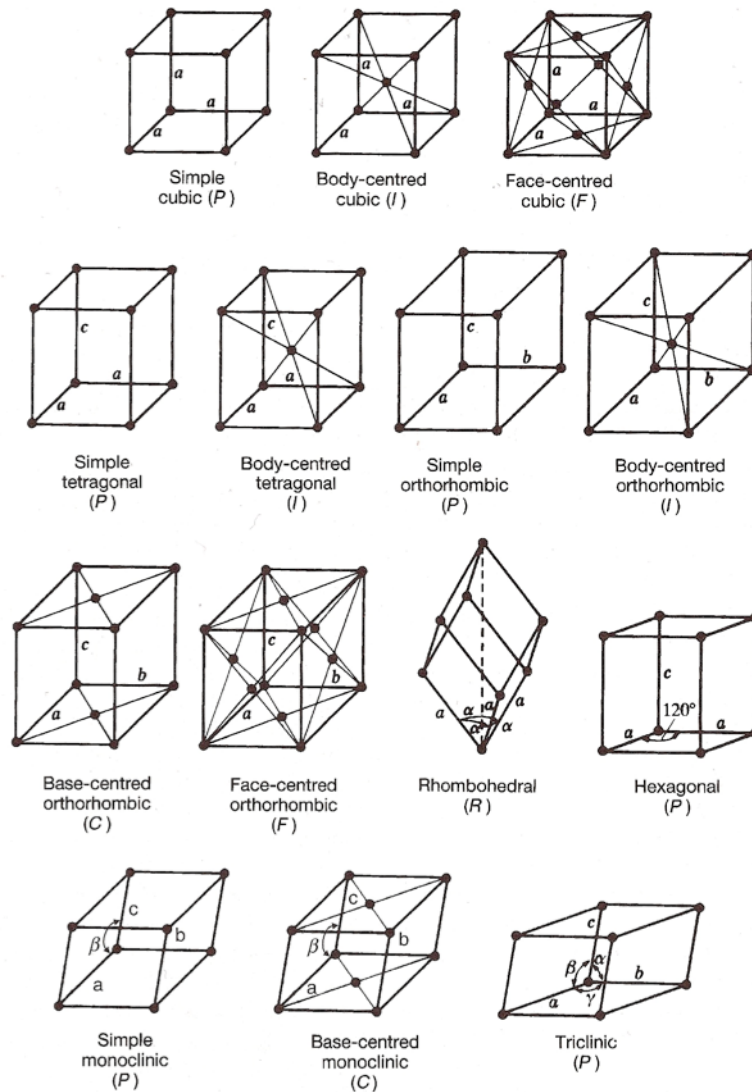


**Figure 1-2 The 14 Bravais Lattices (Hammond, 1992 p.35)**

## 1.2.2  Symmetry & Space Groups

To further define a crystal, a definition of its inherent symmetry is required, for example its appearance after a point symmetry (mirror, rotation, inversion) or a translation operation. These are grouped into seven crystal systems. Combining the lattice parameters and the symmetry of the unit cell gives a full description of the overall structure of a material and can be categorised by one of 230 possible *space groups.* The space groups combine the Bravais lattice with point and translational symmetry elements, the only extra information required to describe the entire lattice is the presence of any point defects, the inclusion or exclusion of atoms within the lattice.

There are many notations for space groups but the two most commonly used are the International Union of Crystallography table number allocation, where all space groups are listed next to an allocated number 1 to 230, and the International Short Symbol (ISS) or Hermann-Mauguin notation (Hammond, 1992), which usually consists of four symbols describing first the Bravais lattice (Table 1-1) and then symmetry. For example, P4mm (ISS#99) describes a primitive cell with a rotation tetrad (4 fold rotation) and two mirror planes, and R3c (ISS#161) exhibits a rhombohedral unit cell with 3 fold rotation and a glide plane translation in the c-axis.

**Table 1-1 The 5 space group symbols and their meanings**

| | |
|---|---|
| P | Primitive    (one lattice point per cell) |
| C | C-Centred or Base Centred (as the faces intersect the c-axis) |
| I | Innenzentrierte  (German for 'Body-Centred') |
| F | Face Centred |
| R | Rhombohedral Primitive |

## 1.2.3  Lattice Points, Planes and Directions

The position of any lattice point may be given in terms of its Cartesian axis coordinates in relation to the origin of the unit cell. For example in Figure 1-3 point **P** can be described in terms of fractions of the lengths along x,y,z  from the origin **O** and then expressed as the ratio of whole numbers (Hammond, 1992), hence **P** is 101.  Again, for a given direction it can be expressed as coordinates, but this time in square brackets. Direction **D** is [110].

When indexing a lattice plane, the fractional coordinates are taken from where the plane intersects the relevant axis and the reciprocal taken. The whole number is then

placed in round brackets, for example plane **M** is (020). This is the Miller index notation. Plane **L** is (010), multiple planes of this type, for example, (100), (010), (001), can be collectively termed {100}, as anyone can be formed by a 4-fold rotation operation (Cullity, 2001).
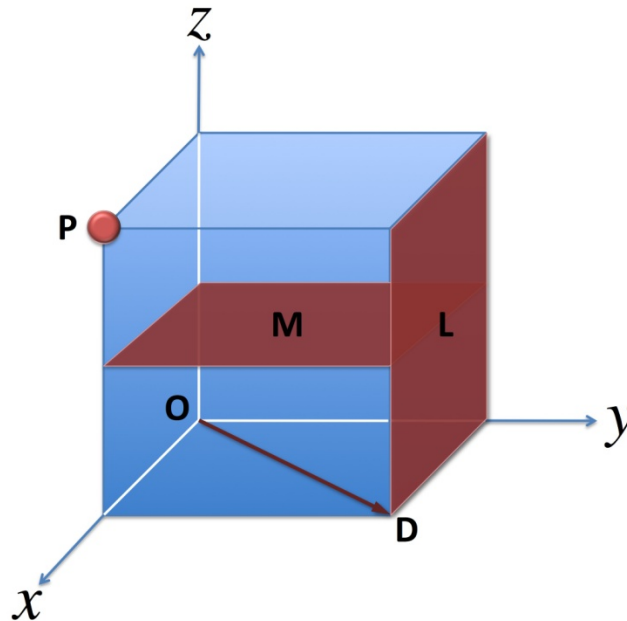


**Figure 1-3 A unit cell labelled with a point (P), direction (D) and plane (L)**

### 1.2.4  Perovskite Structure

A group of materials called ferroelectrics exhibit a spontaneous polarization, the dielectric analogue of ferromagnetic materials which exhibit spontaneous magnetization. There must exist within these materials a separation of charge, which in the case of barium titanate ($BaTiO_3$) originates as a consequence of the positioning of ions within its perovskite structure.

The term perovskite was first used by Gustav Rose in the 1830's to describe $CaTiO_3$ (Mitchell 2002) and in fact all ferroelectric perovskite materials exhibit the $ABO_3$ nomenclature, where A and B are cations, and O is the oxygen anion. Below the temperature termed its Curie point, $T_C$, the perovskite material exhibits a dipole polarization, due to the smaller B cation within the oxygen octahedron assuming a non-centrosymmetric position in relation to the A ion, allowing it to attain a stable bonding pattern. This is shown for barium titanate in Figure 1-4. Above $T_C$ the unit cell becomes cubic and allows the symmetric position of the B ion to be restored and the dipole to disappear as in Figure 1-5. This will be covered in more detail later.

Rather than viewing the perovskite as a cubic closed packed structure with the A ions at the unit cell corners, we can observe the cell with the B ions as the corners in Figure 1-6. This projection allows the oxygen octahedral cage to be seen more readily.
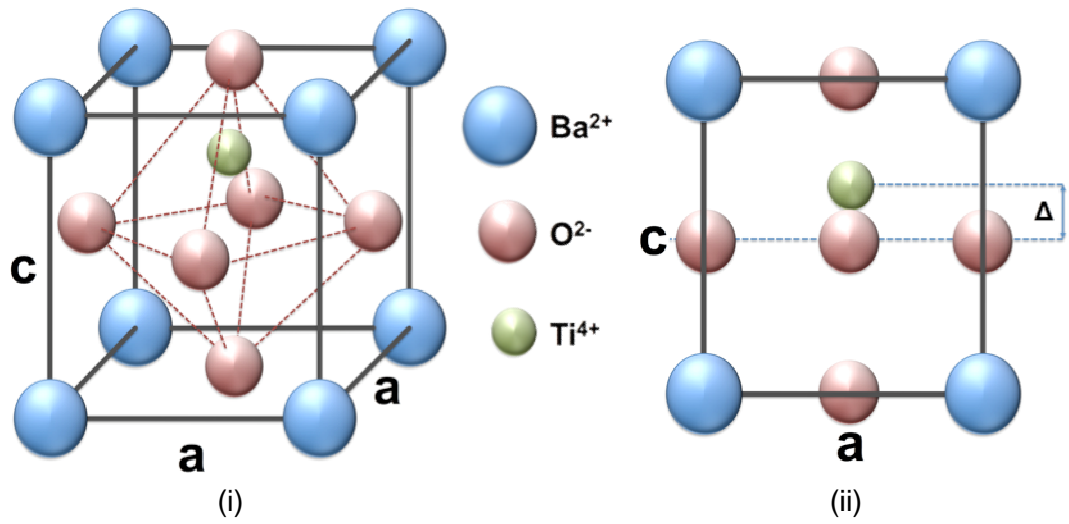
**Figure 1-4 Perovskite structure of BaTiO$_3$ *(i)* in 3d and *(ii)* projected along the [100] exhibiting the non-symmetric position (exaggerated) of the B ion (Ti) below T$_C$**
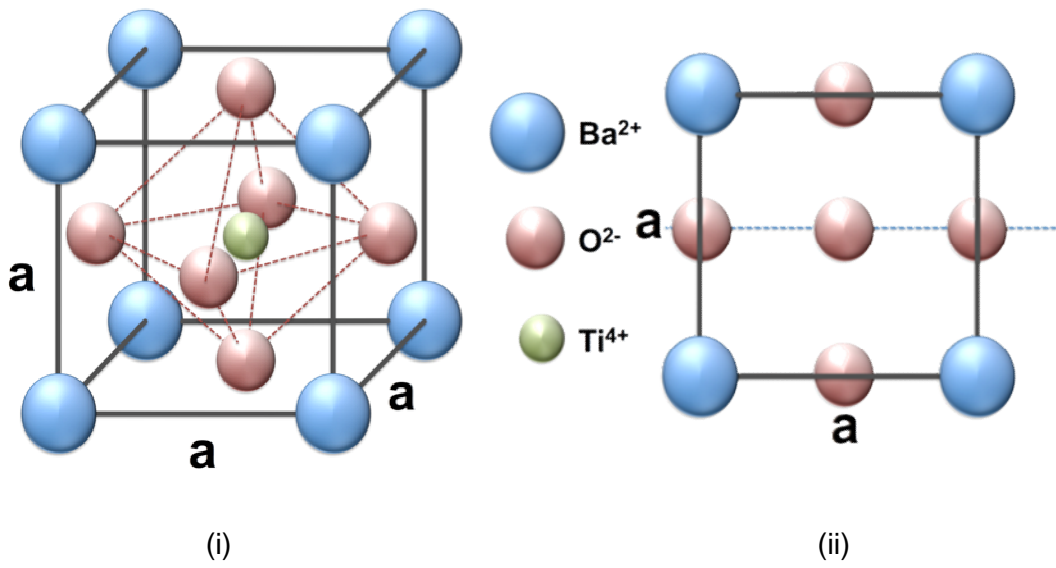


**Figure 1-5 Cubic structure of BaTiO$_3$ *(i)* in 3d and *(ii)* projected along the [100] above T$_C$**
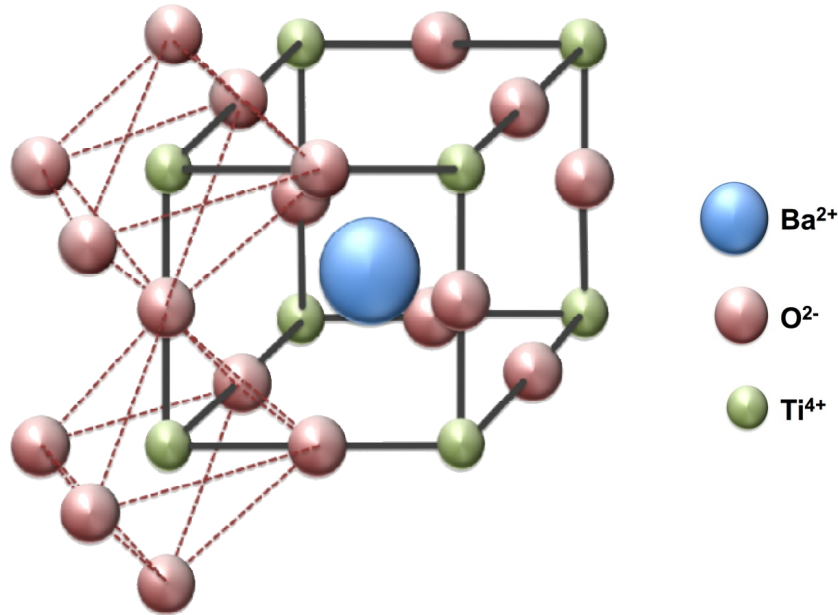
**Figure 1-6 BaTiO$_3$ unit cell with the B site ion at the origin, showing the oxygen octahedral cage in 3 dimensions**

Of 32 point groups in crystal classification, 21 are non-centrosymmetric and 10 are polar (Hammond, 2001 p.86). If these 32 point groups are subject to a time-inversion 122 magnetic point groups are created. These are known as the Heesch groups. This also expands the 230 crystallographic space groups to 1,651 magnetic space groups (Dayanidhi, 1973).

### 1.2.4-1    Oxygen Octahedral Tilt

The perovskite cell can be found in its ideal structure for the case of SrTiO$_3$ at room temperature, but more usually as seen in Figure 1-4 for BaTiO$_3$, the structure is modified by a displacement of a cation which gives rise to the polarization essential to ferroelectricity. Another modification can also be observed such as that in CaTiO$_3$, which exhibits a tilting of the oxygen octahedral and gives rise to a far greater effect on lattice parameters than the cation displacement (Glazer, 1972).

This oxygen octahedral tilt causes subsequent tilting of neighbouring octahedra spreading throughout the lattice. This yields several possibilities for the final structure as successive oxygen cages along an axis can have either the same or opposite sense of tilt (Glazer, 1972). Shown graphically in Figure 1-7 for a generic ABO$_3$ compound where the tilt is along the x-axis, but each axis can contribute in reality to a tilt direction. Figure 1-8 illustrates simply 3 variations of tilt and the effect on its neighbouring cage. There are obviously many more combinations which lead to the

need for a notation system to indicate the type of arrangement observed. This is the Glazer notation. (Glazer, 1972).
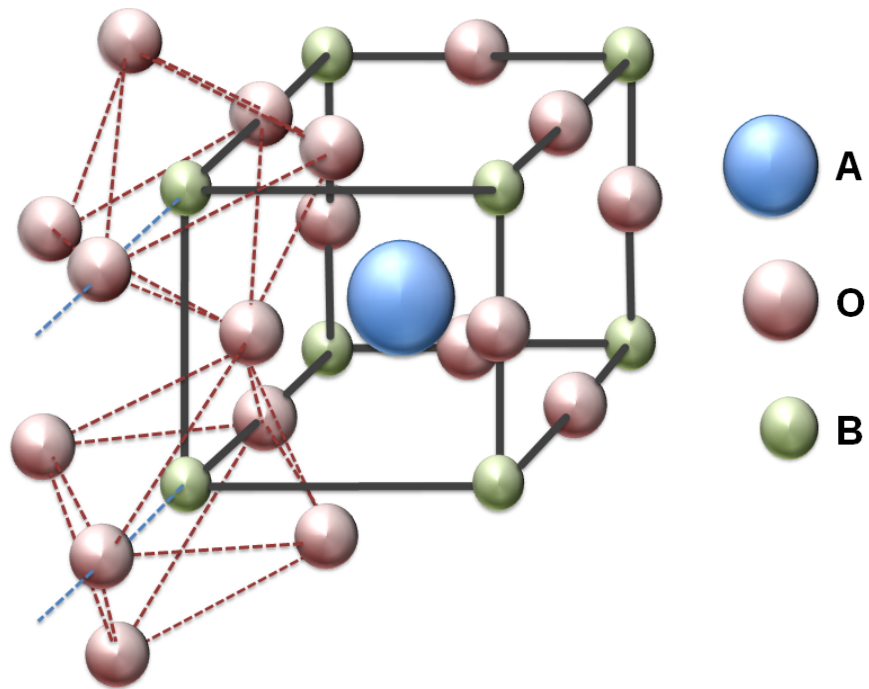


**Figure 1-7 Perovskite unit cell showing an example of the oxygen octahedra tilt and its effect on neighbouring cages**



(a)          (b)          (c)
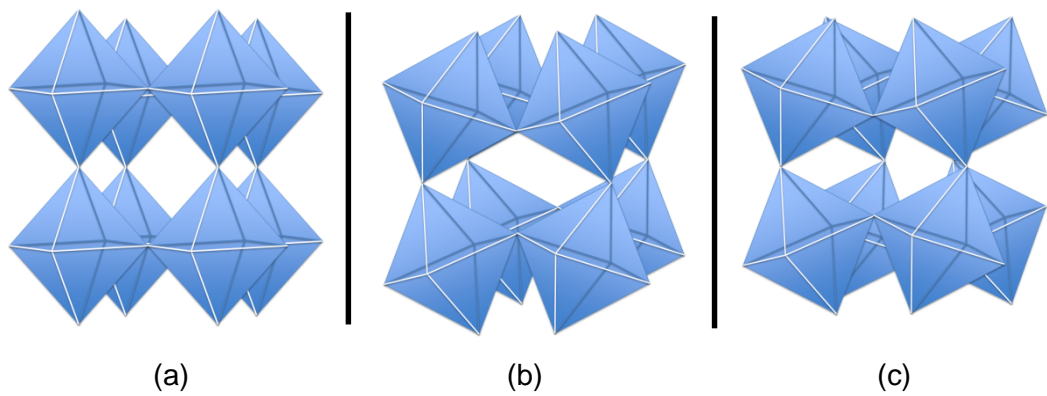
**Figure 1-8 The octahedra tilt in 3 variations. a) No tilt b) In phase tilt c) anti-phase tilt. No tilts are observed on the y and z axis in this illustration.**

1.2.4-2    Tolerance Factor

The perovskite structure is flexible, in that it can accommodate atoms of varying valence. The stability of the resultant structure is often described in relation to the ionic radii, a concept based on Goldschmidt's tolerance factor (Goldschmidt, 1926) ' $t$ '.This is defined in Equation 1-1, where $r_A$, $r_B$ and $r_O$ represent the ionic radii of the A, B and oxygen ions respectively.

$$t = \frac{r_A + r_O}{\sqrt{2(r_B + r_O)}}$$

Equation 1-1-1 (Selbach, 2009)

Tolerance factors have been used in conjunction with ionic electronegativity data to predict difficult–to-prepare systems (Eitel, 2001). By comparing the radii of the contributing ions a cubic structure would result in a t ~ 1, whilst a stable perovskite could range 0.88 < t < 1.09 with the A-site coordination number of 12, or 0.77 < t < 0.99 for an octahedral coordination. (Eitel, 2001).

For values of t < 1, typically a simpler unit cell is formed such as rhombohedral or monoclinic distortions, whereas t > 1 often results in tetragonal or hexagonal symmetry (Eitel, 2001); for example $BaTiO_3$ has a tolerance factor t = 1.06 in its ferroelectric tetragonally distorted phase.

Tolerance factors have also been used to estimate a systems likelihood of being ferroelectric, but this is widely discredited as a method, as the ionic radii is not available for many lanthanide and $Bi^{3+}$ systems, for example $BiFeO_3$. This results in a wide range of possible t values (Selbach, 2009).

## 1.2.5  Rhombohedral Symmetry

It becomes apparent later that it is important to define the nature of a rhombohedrally distorted perovskite. The rhombohedral system can be thought of as a cube stretched along a body diagonal, where $a = b = c; \alpha = \beta = \gamma \neq 90°$.

This distortion is unique as the rhombohedral geometry belongs to one of seven lattice systems, but can be described by two of seven crystal systems. These are the trigonal and hexagonal crystal systems.

Identifying miller indices therefore requires a statement defining which system the rhombohedral cell is indexed by. Throughout this work, reference will be made to the hexagonal or psedo-cubic unit cell by a subscript after the indices. For example $(111)_H$ defines the hexagonal space, and $(111)_R$ defines the primitive rhombohedral,

pseudo-cubic, trigonal crystal system setting. Figure 1-9 depicts the hexagonal unit cell with the smaller primitive rhombohedral unit cell outlined within.
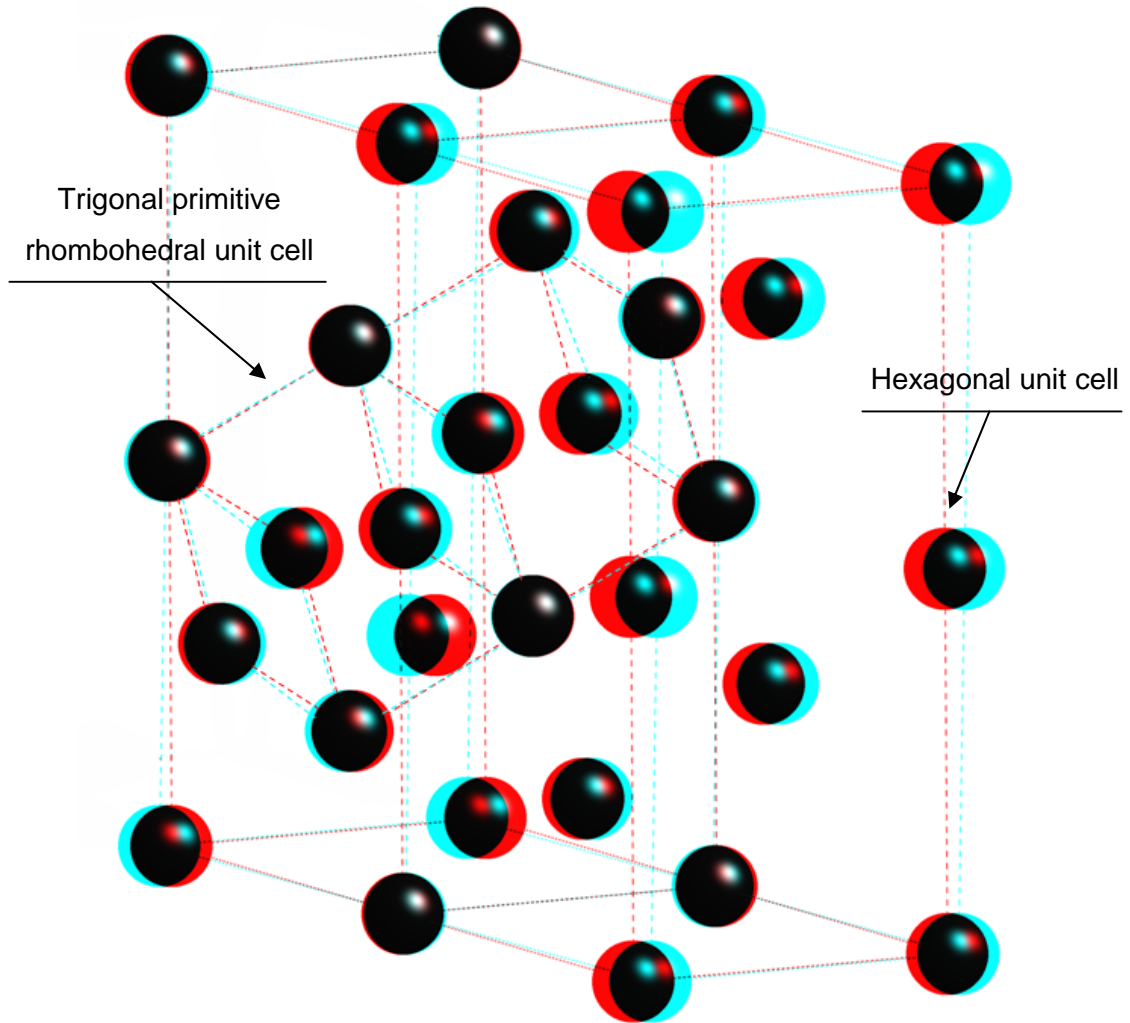


**Figure 1-9 An example of the rhombohedral lattice system whereby the atoms can arrange to be grouped in the hexagonal or trigonal (within) crystal system.**

## 1.3    ELECTRICAL PROPERTIES

### 1.3.1    Dielectrics

A dielectric material is one that is highly electrically insulating but exhibits, or can be made to exhibit, a polar structure. This polar structure is induced when the centre of negative charge in a material is displaced relative to the centre of positive charge. An applied field can induce physical displacement of charge or a material can exhibit these spontaneously, such as in the perovskite structure discussed in the previous section, 1.2.4.

Polarization exists in dielectric materials of which there are four mechanisms. Figure 1-10 illustrates these; atomic, ionic dipolar and diffusional.
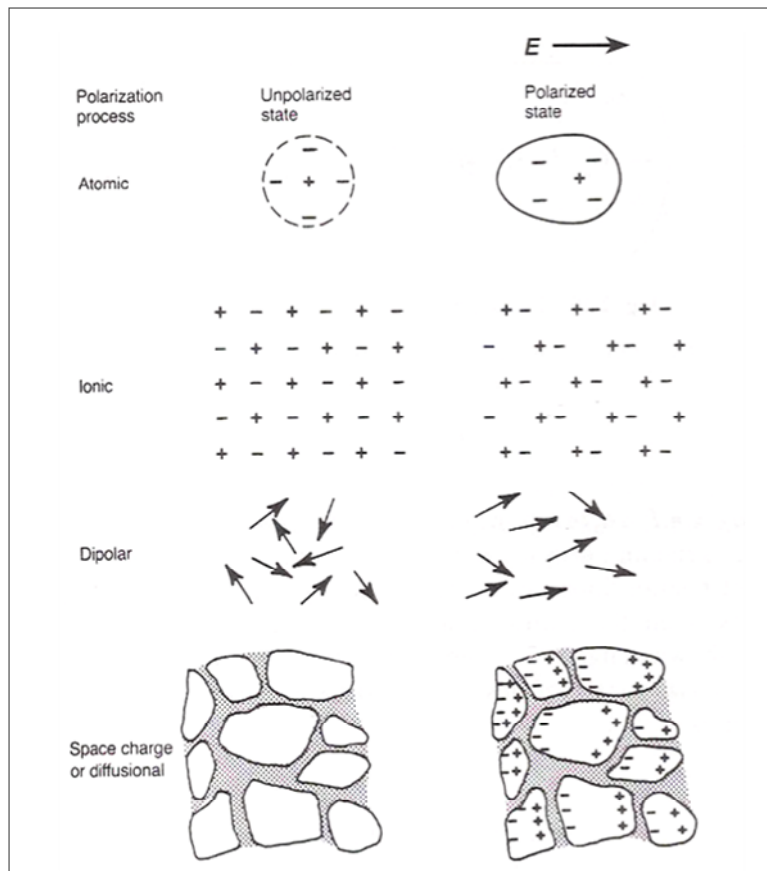


**Figure 1-10 The 4 mechanisms of polarization; atomic, ionic, dipolar and diffusional**
**(Moulson, 2003)**

Atomic polarization, which occurs in all materials, is the small displacement of electrons in an atom relative to the nucleus and occurs most rapidly due to the fast motion of low inertia electrons (Moulson, 2003).

Ionic polarization involves the relative displacement of cation and anion, whilst dipolar polarization occurs when permanent dipoles are already present in the material but present no net charge, as they are randomly orientated due to thermal motion

(Moulson, 2003). The application of an external electric field can cause the dipole moments to align, polarising the material. This is a very temperature dependant mechanism.

As dielectric materials can form dipoles, they exhibit various properties when subjected to an electric field, of which their permittivity is employed as a functional property, and is material characteristic. A common use for these materials is in capacitors, essentially a circuit element formed by placing an insulating layer between two conducting layers; its function is to store electrical charge.

Using a dielectric material as the insulating layer, the capacitance is markedly improved, as the polar nature of the material allows more charge to be stored, compared to a vacuum or air. Equation 1-1 shows the relationship of dielectric permittivity ($\varepsilon$) in a capacitor, with $C$ as capacitance, $d$ the gap between conducting layers, and $A$ the area of a layer.

$$C = \varepsilon \times \frac{A}{d}$$

Equation 1-2 (Moulson, 2003)

### 1.3.1-1    Relative Permittivity

As a dielectric can support an electrostatic field, it can separate charges of opposing polarity. The extent to which a material can support an electric field is given by the relative permittivity ($\varepsilon_r$) (or the relative dielectric constant (K). This relative permittivity is relative to the constant permittivity of free space ($\varepsilon_0$) in Equation 1-2 for a given voltage, where $\varepsilon_r$ is dimensionless and the larger the value the more effective the dielectric (Moulson, 2003).

$$\varepsilon_r = \frac{\varepsilon}{\varepsilon_0}$$

Equation 1-3

### 1.3.1-2    Dielectric Loss

Associated with alternating voltages is the dielectric dissipation factor ($tan\ \delta$), a measure of loss-rate of power from a mode of oscillation, usually in the form of heat for electrical circuits (Moulson, 2003).   An ideal dielectric under a sinusoidal alternating electric field, the current ($I$) is 90° out of phase with the voltage ($V$) and would have $\varepsilon_r = \infty$ and $tan\ \delta = 0$.

As the voltage charges the dielectric capacitor in half a cycle, the current drops to zero, whilst in the second half cycle, the voltage returns to zero as the capacitor releases stored charge, seen as an increase in current to maximum.

However, in a real dielectric the energy between the two states is subject to losses due to resistive leakage or dielectric absorption; this is termed dielectric loss. The current – voltage relationship can then be described using a phasor diagram (Figure 1-11), from which we observe the current for a real capacitor can be resolved in two components; $I_{charge}$ which is in phase with the current (charging current) and $I_{loss}$ which is in phase with the voltage, and responsible for the power loss (loss current) (Moulson, 2003). This is described in Equation 1-4.

$$I_{loss} = I \sin \delta = I_{charge} \tan \delta$$

Equation 1-4

In terms of permittivity, a dielectric has both real ε' and imaginary ε'' components (Equation 1-5) which can be expressed as $I_{charge}$ and $I_{loss}$ respectively. Thus dielectric loss can be defined as the ratio between the real and imaginary components of permittivity in Equation 1-6 (Moulson, 2003).

$$\varepsilon_r = \varepsilon' + j\varepsilon$$

Equation 1-5

$$\frac{I_{loss}}{I_{charge}} = \frac{\varepsilon}{\varepsilon} = \tan \delta$$

Equation 1-6
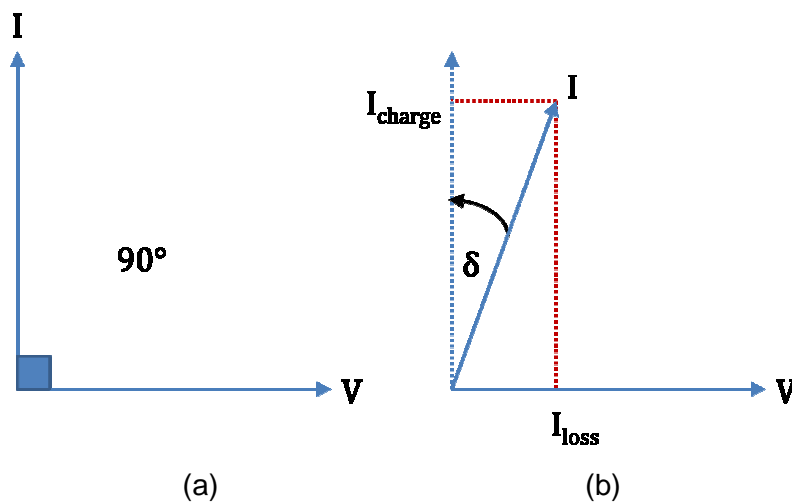


Figure 1-11 Phasor diagram for (a) an ideal dielectric and (b) a real dielectric exhibiting a dielectric loss

## 1.4 FERROELECTRICITY

### 1.4.1 Definition

A ferroelectric is defined as a material that exhibits a spontaneous polarization that can be reversed with the application of an electric field (as long as the field required to reverse the polarization is less than the breakdown field of the material) (Jaffe, 1971). Of the 21 point groups that are non-centrosymmetric (section 1.2.4) and do not possess a centre of symmetry, 20 can exhibit piezoelectricity (section 1.4.7-2) and of those, 10 have a unique polar axis and are anisotropic, exhibiting spontaneous polarization along the polar axis.

In a perovskite $ABO_3$ material the polarization is associated with the relative displacement of the $A^+$, $B^+$ and $O^{2-}$ ions from their symmetrical positions, and exists spontaneously without the presence of an externally applied field, below the Curie point of the material.

### 1.4.2 Domains

As a paraelectric material is cooled through $T_C$ a phase transformation to a ferroelectric phase occurs. The spontaneous polarization that ensues with the transition is a consequence of the alignment of the electric dipoles. The dipoles in a tetragonal unit cell for example can take on 6 different poling directions, each with equal energy contributions and therefore likelihood of forming through the transition.

In order to reduce the energy associated with this onset of polarization and to reduce the number of polarization vectors, 'twinning' a process whereby the polarizations take on antiparallel alignment to form discrete regions of polarization known as domains. The domains in (Figure 1-12) are 180° domains, forming a pattern of positive and negative charges on the surface, acting to reduce the polarization energy required, and to compensate for opposing depolarization fields (Jona, 1993).

The ferroelectric domains are separated by domain walls which have also have an energy associated with their formation. Therefore the process of domain forming cannot continue indefinitely, as the energy related to domain wall formation eventually outweighs the energy reduction achieved by creating new domains.

As well as 180° domains, in tetragonal and rhombohedral crystals, the formation of 90° and 71° / 109° domain walls are also observed respectively (Jaffe, 1971).

In a tetragonal crystal, for example ferroelectric barium titanate, both 180° and 90° domains form (Figure 1-13 (a)) to compensate for the surface charges and depolarization fields, but 90° domains also act to reduce the strain and ferroelastic stresses developed in the ceramic. These 90° domains can be moved and

manipulated through either the application of electric field or stress to allow domains poled in the
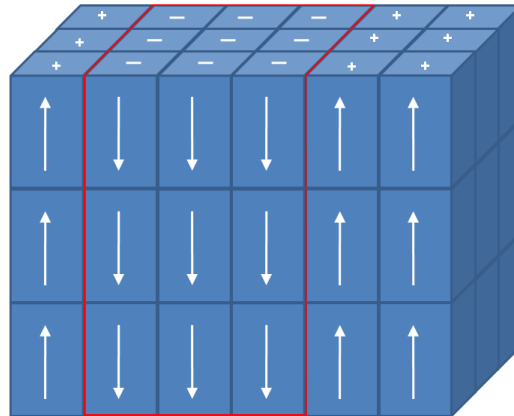


**Figure 1-12  Illustration of 180° domain formation with a single domain of similarly polarised unit cells outlined in red.**



(a)                                    (b)
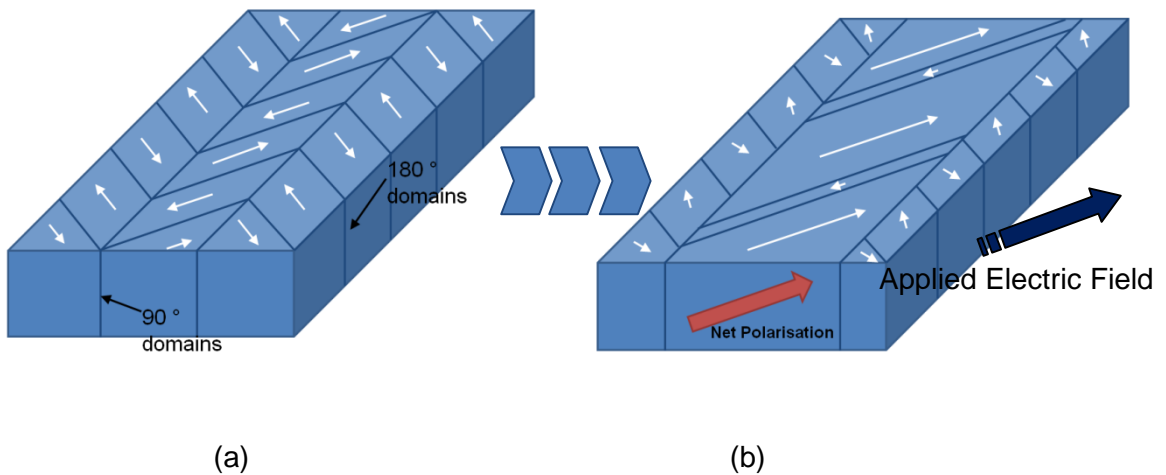
**Figure 1-13 Schematic of a) domain configuration in barium titanate below T$_C$ and b) the effect on domains with applied electric field.**

preferred orientation to grow at the expense of others. This is shown in schematic Figure 1-13.

Although all the domains are polar in nature, the net polarization is zero as there is no unified polarization vector. The material therefore behaves as a non polar material until a static field is applied to orientate the domains so the majority align in a coherent polar direction. The application of an electric field in this way is termed 'poling' and materials can be equally unpoled using mechanical stress and elevated temperatures to re-randomise the domains' polar directions. The characteristics of a ferroelectric and domain configurations can be best described by hysteresis.

### 1.4.3  Ferroelectric Hysteresis

A hysteresis loop (seen in Figure 1-14) is the graphical form of characterising this class of materials. A plot of applied electric field vs. polarization gives rise to a typical loop, where at the origin ($O$) application of an electric field in the positive direction induces a positive net polarization up to a saturation point $P_s$. This happens once as the material is taken from its virgin state where all the domains are randomly orientated to a point whereby no further alignment of the domains can take place. At this saturation limit the material behaves as a typical dielectric with a linear response.

As the field is reversed so too is the polarization. At $E = 0$ the polarization retained is termed remnant polarization, $P_r$. Further decreasing of the field into the negative regime observes a continuing diminishing polarization to zero. This is the coercive field, $E_c$.

The negative field saturation follows, and then upon reversal once more into the positive regime the loop closes and any subsequent change will follow the loop if completed at the same rate.
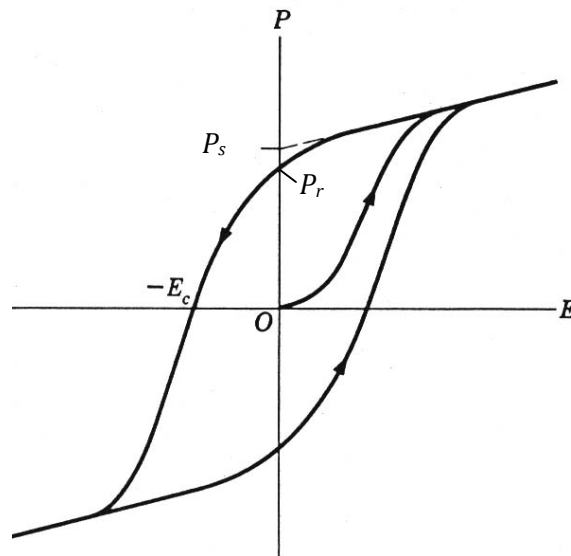


**Figure 1-14 Hysteresis loop schematic of typical ferroelectric behaviour. Origin (O), coercive field (E$_c$) remnant (P$_r$) and spontaneous (P$_s$) polarization are labelled along electric field (E) and polarization (P) axis.**

### 1.4.4  Antiferroelectricity

In the case of a ferroelectric, a decrease in temperature below its Curie point causes a phase transition to occur from a higher to a lower symmetry, leading to the formation of domains, where neighbouring domains align in a direction to give polarization.

In the case of an antiferroelectric, the domain orientations align antiparallel and therefore cancel to produce no net polarization (Känzig, 1957).

### 1.4.5  Paraelectricity

To allow the dipoles to reverse direction in a ferroelectric, the energy associated between the two states must be relatively low. This suggests there is usually a nonpolar state only slightly less stable, consequently raising the temperature will increase the thermal vibrations and relative stability such that the material will transform to the now more favourable non-polar state. The temperature at which this transformation occurs is the Curie point ($T_C$) implying a material can only display ferroelectric properties over a finite temperature range. The Curie point is a specific temperature for a given material that marks a phase transformation to a non-polar form (for example to a cubic structure); this non-ferroelectric structure is termed the paraelectric phase and behaves as a normal dielectric only showing polarization under an applied electric field and no spontaneous polarization.

A paraelectric phase can exist at higher or lower temperatures than a ferroelectric phase although the most common materials such as lead zirconate titanate (PZT) and barium titanate are paraelectric at temperatures higher than the ferroelectric phase.

1.4.5-1    Curie Point and Curie Temperature

The Curie temperature ($T_0$) is a different quantity from the Curie point ($T_C$) and is a material constant determined by extrapolation. The Curie temperature is not equal to the Curie point for first order transitions, but are theoretically equivalent in second order transitions such as magnetism. The magnetic Curie temperature (θ) is similar in definition, and outlined in 1.6.3. Ferroelectric materials generally obey Curie Weiss behaviour (Equation 1-7) above the paraelectric phase transition.

$$\varepsilon_r - 1 = (C/T - T_0)$$

Equation 1-7 (Jaffe, 1972. p.12)

Where $\varepsilon_r$ is the relative dielectric constant, $C$ is the Curie constant, $T$ is the temperature and $T_0$ is the Curie temperature (Jaffe et al 1971. p.12).

### 1.4.6 Ferroelectric Phase Transitions

Heating a ferroelectric material above the Curie point ($T_C$) eradicates the spontaneous polarization, and therefore ferroelectric behaviour. In barium titanate, BaTiO$_3$, above $T_C$ of ~130 °C, a first order phase change from a ferroelectric tetragonally distorted perovskite unit cell (Figure 1-4) to a paraelectric, cubic centrosymmetric form, as previously seen in Figure 1-5, occurs. Ferroelectrics remain polar up until $T_C$ showing an increase in the polarizability of the material until this point.

Cooling below $T_C$ may also show one or several other phase transitions. Again for the case of BaTiO$_3$, a temperature reduction below $T_C$ sees a unit cell distortion from cubic to tetragonal and further transitions occur at 0 °C and -90 °C where the unit cell is orthorhombic with the polar axis parallel to a face diagonal [011], and distorted rhombohedrally with the polar axis along a body diagonal respectively [111]. This is illustrated in Figure 1-15 by Jaffe Cook and Jaffe (1971).
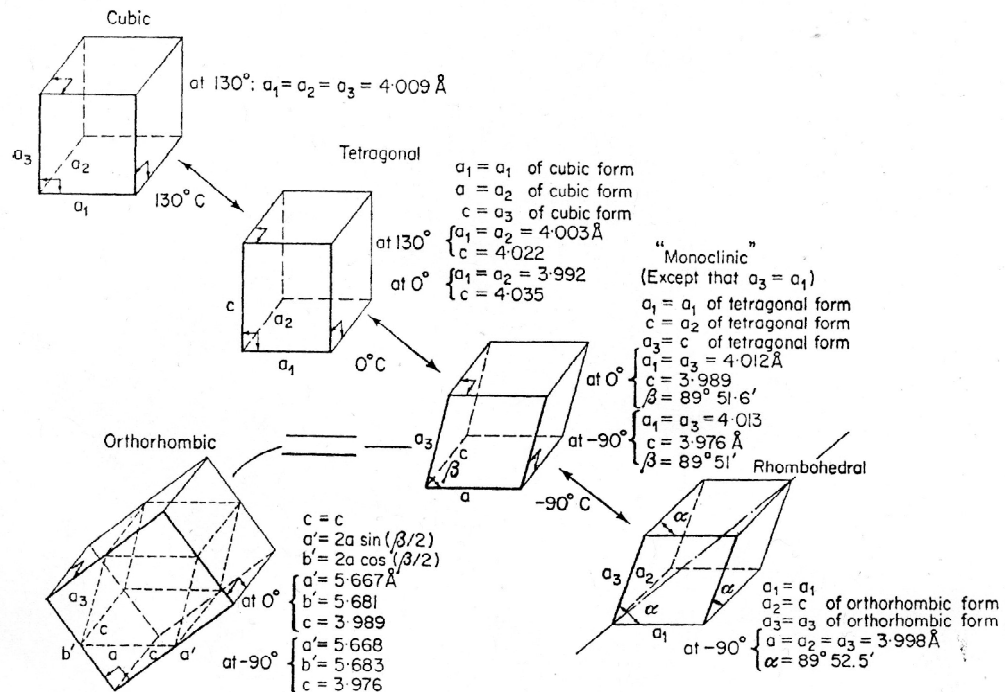


**Figure 1-15 Illustration of the phase changes of barium titanate as a function of temperature, from non-polar cubic, through polar tetragonal, orthorhombic and rhombohedral structures. (Jaffe, 1971. p. 54)**

### 1.4.7 Piezoelectricity

1.4.7-1    Electrostriction

The polarization of dielectrics to produce a dipole consequently induces a mechanical reaction from the material. All non-conducting materials which are placed under an electric field undergo a small change in dimension, or strain. This effect in reality is so minimal however; it is rarely detectable or useful and it is important to note that electrostriction causes a positive strain when the applied field is in either polarity direction. This can be expressed in Equation 1-8 as:

$$x = QP^2$$

<div align="right">Equation 1-8 (Moulson, 2003 p. 339)</div>

Where $x$ relates to strain, $Q$ the electrostriction coefficient, and $P$ the polarization of the material.

1.4.7-2    Piezoelectricity

The word piezo comes from the Greek translation for pressure, and therefore piezoelectricity can be literally translated as pressure electricity. In contrast to electrostriction, the piezoelectric effect exhibits linear coupling between electrical and mechanical parameters, and is observed to change sign with altering polarity (Jaffe, 1971).

Piezoelectric materials' ability to alter polarization with mechanical stress stimuli and to induce a strain with applied electric field can be defined using multiple coefficients that describe the boundary conditions imposed during testing (Trollier-McKinstry, 2004). The most common coefficient used to describe the effect is the piezoelectric charge coefficient, $d_{ijk}$, which can be defined in the direct effect by (Equation 1-9);

$$P_i = d_{ikl}X_{kl}$$

<div align="right">Equation 1-9 (Direct Effect)</div>

where the application of a mechanical stress $(X)$ induces an electric polarization $(P)$. The same coefficient is used in the converse effect, related by Equation 1-10;

$$x_{ij} = d_{kij}E_k$$

<div align="right">Equation 1-10 (Converse effect)</div>

where application of electric field $E$ induces a mechanical strain $x$. Both effects are illustrated in Figure 1-16.

The piezoelectric coefficients are all 3rd rank tensors, hence the piezoelectric response is anisotropic, but symmetry in most piezoelectric systems allows reduced notation (Nye, 1979), discussed in 1.4.7-3.

Piezoelectricity is exhibited in ferroelectrics when in their polarised state, akin to the case of $BaTiO_3$, but there are classes of materials that show piezoelectric effects in the non-polarised state. These materials include Rochelle salt, the first material found to exhibit piezoelectricity and ferroelectricity by Valasek, 1920. These will not be discussed as they are not relevant to this work.



(a)

(b)
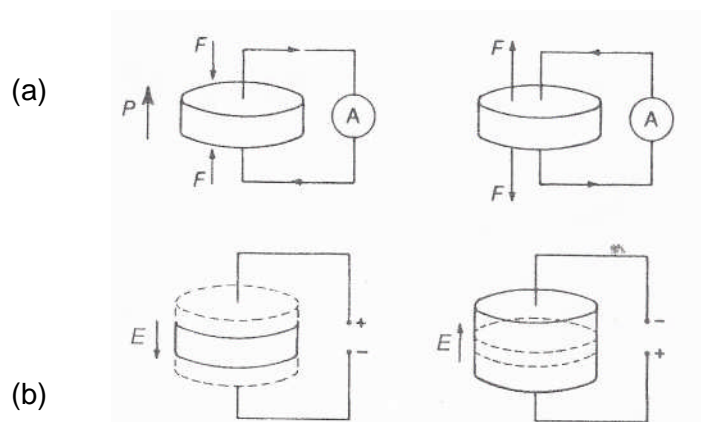
**Figure 1-16 Illustration of the a) Direct and b) Converse piezoelectric effect (Moulson, 2003. p.340)**

1.4.7-3    Piezoelectric Coefficient Notation

The complexity in describing the directions of field, polarization and strain, gives rise to 3rd rank tensor notation. The coefficients are also defined in terms of crystallographic axes; in polycrystalline ceramics, convention is that poling is in the "3" axis.

For the case of the converse effect, $x_{ij} = d_{kij}E_k$, advantageous symmetry in perovskite ceramic structures used throughout this work allows use of reduced notation (Equation 1-11);

$$x_i = d_{ij}E_j$$

Equation 1-11 (Jaffe, 1971)

The expression shows direction of strain and polarization. With $i$ defining the mechanical vector, and $j$ the electric vector. For normal strains, $i$ = 1,2,3, with 3 as the poling direction, and for shear, $i$ = 4,5,6.

Again, due to symmetry, many of the combinations cancel to 0; leaving the only non-zero piezoelectric coefficients as;

$d_{33}$ = applies when the force is in the 3 direction (along the polarization axis) and is impressed on the same surface on which the charge is collected

$d_{31}$ = applies when the charge is collected on the same surface as before, but the force is applied at right angles to the polarization axis

$d_{15}$ = infers charge is collected on electrodes which are at right angles to the original poling electrodes and that the applied mechanical stress is shear

1.4.7-4    Electromechanical coupling factor

Further characterisation of piezoelectric properties can be made by the electromechanical coupling factor, $k$. When an electric field is applied to a piezoelectric body then the mechanical output energy is defined by the effectiveness of the material to transform the electric to mechanical energy. This definition is the 'effective coupling coefficient' $k_{eff}$ (Equation 1-12) and works vice versa to describe the effective mechanical to electrical energy transformation (Equation 1-13), as long as the mechanical stresses do not exceed the materials elastic limit.

$$k_{eff}^2 = \frac{electrical\ energy\ converted\ to\ mechanical\ energy}{imput\ electrical\ energy}$$

Equation 1-12 (Moulson, 2003. p.347)

$$k_{eff}^2 = \frac{mechanical\ energy\ converted\ to\ electrical\ energy}{imput\ mechanical\ energy}$$

Equation 1-13 (Moulson, 2003. p.347)

### 1.4.8  Commercial Ferroelectric Ceramics

Since the discovery of ferroelectrics in 1920 by Valasek and the piezoelectric effect observed in the Rochelle salt he studied, this area of physics was reserved for academic and theoretical interest, being of little use or application due to the complexity of the water soluble and fragile hydrogen bonded structures (Valasek, 1920).

Barium titanate was first reported for its high dielectric constant by Wul in 1945, and the robust, simplistic perovskite structure of the material spurred research for engineering devices (Scott, 2007(a)) thus transforming the ferroelectric oxides field into the electronic ceramics industry producing billions of $BaTiO_3$ capacitors annually (Scott, 2007(a)).

The other two materials of historic note are lead titanate, and most importantly lead zirconate titanate, $Pb(Zr,Ti)O_3$ (PZT), which having after its discovery in 1953 (Sawaguchi, 1953), has proven to be a truly multifunctional piezoelectric, ferroelectric, with a multitude of varying applications.

Prior to 1970 much work was done to model ferroelectric phase transitions and discover new materials (Lines, 1977). Because of the high cost of synthesizing single crystals, bulk polycrystalline materials, particularly of PZT, became the focus and were successfully implemented into piezoelectric actuators and transducers, ferroelectric capacitors and pyroelectric detectors. Sonar was particularly well funded at this time (Scott, 2007).

With the first thin film ferroelectrics being published in 1984, these were then integrated into semiconductor microchips (Scott, 1989) and research into integrated ferroelectrics began and is still the most popular application for ferroelectrics today; with emphasis in research currently on ferroelectric non-volatile random access memories, involving work on film-substrate interfaces, finites size effects, nanostructures and magnetoelectrics (Scott, 2007(a)).


1.4.8-1  Barium titanate ($BaTiO_3$)

Barium titanate, discovered to be ferroelectric over 60 years ago (Wul, 1945) is regarded as the "cornerstone and prototype of the largest family of useful ferroelectrics: the oxide perovskites." (Bell, 2008).

The structure of barium titanate changes from perovskite rhombohedral to orthorhombic at -90 °C, then again at 0 °C to a distorted tetragonal perovskite (Megaw, 1945) (Forrester, 1945) with a transition to a paraelectric cubic structure at 129 °C (Harwood, 1947) as discussed in section 1.4.5 and seen in Figure 1-15. The phase transitions are accompanied by changes in electrical and mechanical

properties. Modification of these phase transition temperatures can be readily done by doping with other elements. Notably partial substitutions of Pb and Ca for Ba lowers the orthorhombic – tetragonal transition temperature, particularly useful for underwater sonar applications, where the more piezoelectrically active P4mm (ISS #99) tetragonal phase is used in an environment close to freezing.

Barium titanate is popular for high-permittivity applications such as capacitors, displaying relative permittivity values of 1,000 – 10,000 over a temperature range of ambient to $T_C$.

### 1.4.8-2    Lead Titanate (PbTiO$_3$)

Lead titanate was reported as ferroelectric in 1950 due to its structural analogy to BaTiO$_3$ and high temperature transition from ferroelectric tetragonal to paraelectric cubic structure at ~490 °C (Shirane, 1950), but it wasn't until 1970 that true polarization reversal by field was accomplished and a spontaneous polarization of 57 μC/cm$^{-2}$ recorded (Remeika, 1970).

The presence of lead is presumed to allow the ferroelectric properties to be cultivated in lead titanate as it is more deformable and polarizable than Ba and Sr in similar ferroelectric titanates (Sani, 2002).

The ferroelectric perovskite structure shows much larger tetragonal (space group P4mm ISS #99) distortion than BaTiO$_3$, with c/a lattice vectors ratio equal to 1.063 (Shirane, 1956) at room temperature, leading to high anisotropy of its piezoelectric and ferroelectric properties; for example a large $d_{33}$ / $d_{31}$ ratio (Sai Sunder, 1995). X-ray (Shirane, 1950) and neutron (Shirane, 1956) diffraction studies confirmed the lattice parameters of lead titanate as a function of temperature as plotted in Figure 1-17 from Shirane et al (1950), and summarized in Table 1-2.

**Table 1-2 Summary of properties for lead titanate**

| Tetragonal Space Group | Ferroelectric Curie Point ($T_C$) | Ambient lattice parameter (a) | Ambient lattice parameter (c) | Ambient c/a ratio |
|---|---|---|---|---|
| P4mm | 490 °C | 3.894 Å | 4.140 Å | 1.063 |
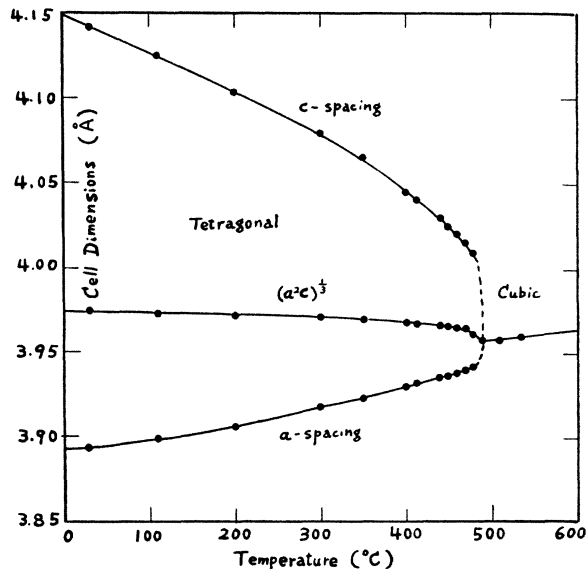
**Figure 1-17 Lattice parameters as a function of temperature for lead titanate sintered powder from X-ray diffraction data (Shirane, 1950).**

Synthesis of lead titanate is made difficult by the large internal strains due to the anisotropic contraction of the unit cell when cooling through $T_C$. Tendency for inter-granular fracture when the grain exceed 1 μm in size (Matsuo, 1966), is prohibitive toward sintering bulk, polycrystalline materials; often resulting in fine particle distributed powders being formed (<5 μm) (Sai Sunder, 1995).

1.4.8-3    Lead zirconate titanate (Pb(Zr,Ti)O₃)

After the discovery of $BaTiO_3$ research was stimulated in to finding materials that exhibited piezoelectric properties over a wider range of temperatures. Over 50 years ago (Sawaguchi, 1953) that came in the form of the perovskite, lead zirconate titanate (PZT), now perceived as the most diversely used and popular commercial piezoelectric with much of its success due to the ability to tailor its properties to specific applications by means of doping. Substitutionally doping on to the A or B site alters the movement of domain boundaries and modifies the electrical properties, at the cost of usually always lowering $T_C$.

PZT forms from the combination of ferroelectric $PbTiO_3$ and antiferroelectric $PbZrO_3$ to create a continuous solid solution with formula $Pb(Zr_x Ti_{1-x})O_3$ where $0 < x < 1$. The solid solutions where x < 0.9 are all ferroelectric, with $T_C$ ranging from 220 – 490 °C depending on composition (x = 0.9 to 0 respectively) (Jaffe, 1954).

The structure of PZT goes through several transitions with varying temperature, but at ambient between 0.52 < x < 0.545 (Moulson, 2003) there lies a phase boundary between two ferroelectric phases. This phase boundary is often termed a

morphotropic phase boundary, the definition of which is discussed in 1.4.9, but this boundary has been a point of contention between researchers for many years. This is reflected in the changes of the phase diagram of PZT over the last 4 decades from Figure 1-18 to Figure 1-20, increasingly showing that the previously thought morphotropic phase boundary, is actually temperature dependent and area of mixed phase at higher temperature, cooling into a monoclinic phase (Noheda, 1999).

The morphotropic phase boundary (MPB), as labelled in Figure 1-18 defines a composition at which an abrupt phase change occurs, irrespective of temperature. In PZT, this occurs between the high temperature rhombohedral (R3m) and tetragonal (P4mm) phases. Even with changes to this MPB toward a narrow mixed phase and monoclinic region, it is agreed that the piezoelectric properties are at an optimum (see Figure 1-21) for most applications at this MPB composition (Bell, 2006). This is due to a peak in permittivity, to which the piezoelectric coefficient is proportional, from the 6 and 8 polarization vectors possible in the tetragonal and rhombohedral phases respectively, allowing 14 possible orientation directions and maximums of polarization at 83% and 87% for each phase, again respectively (Moulson, 2003. p.75).
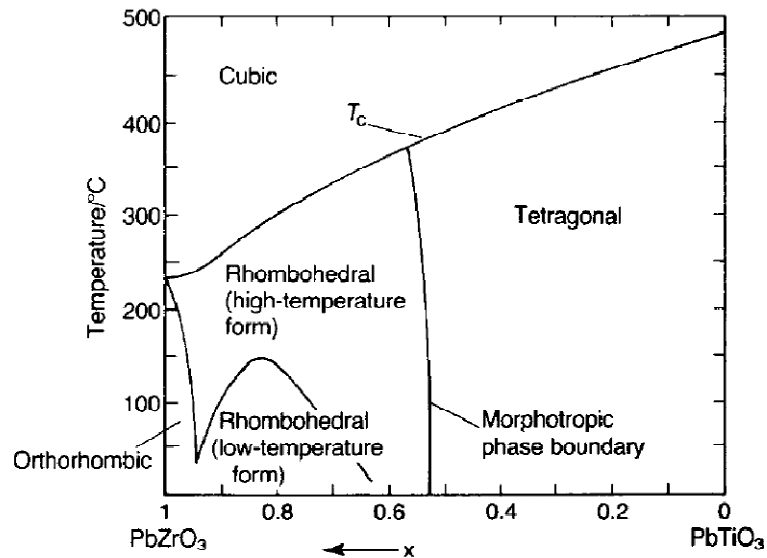


**Figure 1-18 Phase diagram of the Pb ($Zr_x$ $Ti_{1-x}$)$O_3$ system from 1971**
**(Moulson, 2003 p.355)**
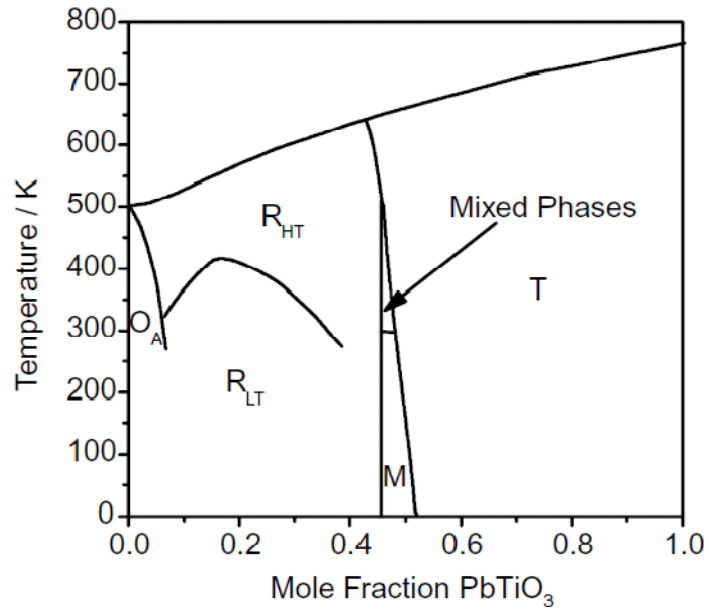
**Figure 1-19 Phase diagram of the Pb (Zr$_x$ Ti$_{1-x}$)O$_3$ system from Noheda et al, 1999 (Bell, 2006).**
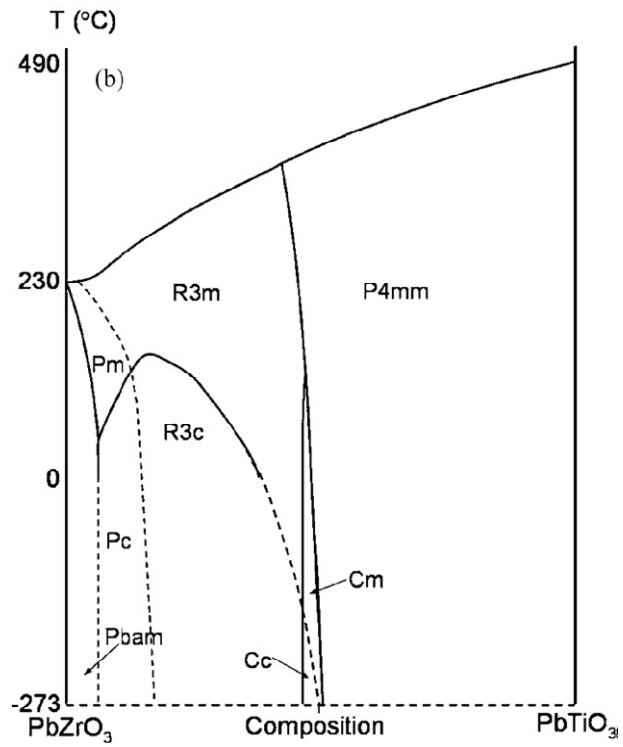


**Figure 1-20 Phase diagram of the Pb (Zr$_x$ Ti$_{1-x}$)O$_3$ system proposed by Woodward et al (2005).**
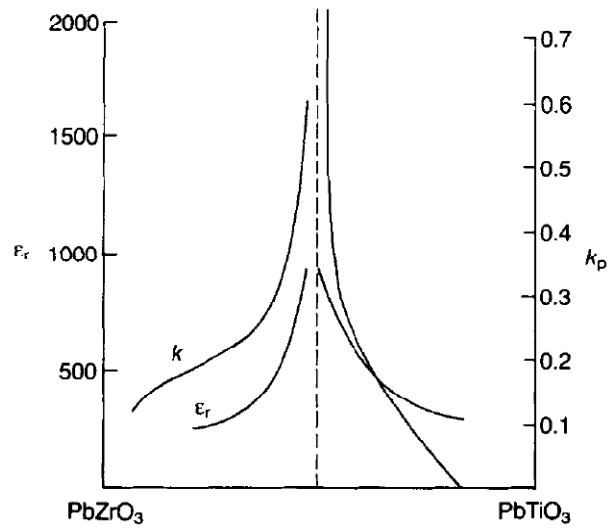
**Figure 1-21 Coupling Coefficient ($k_p$) and permittivity values across the PZT compositional range (Moulson, 2003. p. 356)**

### 1.4.9 Morphotropic Phase Boundary

A morphotropic phase boundary (MPB) is defined by a composition that observes an abrupt phase change that occurs irrespective, or nearly independent of temperature, effectively generating a straight vertical line on a phase diagram.

More recently, this definition has grown to incorporate abrupt crystal structure changes in piezoelectrics where the electromechanical properties are at a maximum (Muhtar, 2008).

## 1.5 MAGNETIC PROPERTIES

### 1.5.1 Principles of Magnetism

Magnetism is perhaps one of the oldest phenomena in history, with records of theory and discussion on the invisible force dating back to the times of Arisotle (Gilbert, 1600) and the first scientific studies conducted by Gilbert, who published the De Magnete in 1600. Until the 1800's however, all magnets and magnetic knowledge was based on iron, either in the smelted pure iron (Fe) form or magnetite ore ($Fe_3O_4$), commonly known as Loadstone (Cullity, 1972). It wasn't until 1820 that electromagnetism was discovered by Ørsted (1820) that other materials could be subject to large enough magnetic fields to be studied for their magnetic properties, and the link between electricity and magnetism was made.

The modern definition of magnetism is a materials' behaviour on the microscopic scale when subject to a magnetic field. Magnetic fields are generated by electric charges in two forms;

- Moving electric charges (electrical current, or changing electric fields) (Maxwell, 1865)
- Intrinsic magnetism from particle spin. ie. electron, neutron (Tipler, 2003)

### 1.5.2 Magnetic Dipole

The well known attractive and repulsive forces of magnets arises from regions called *poles*. Opposite poles attract, and like poles repel.

Poles (almost) always occur in pairs (commonly known as North and South poles based on mariners use of loadstone as the early compass) in magnetized bodies and are impossible to separate. They create fields around themselves, from one pole to the other, and it is this field that interacts with other poles nearby (Cullity, 1972).

The inter-pole field was first quantified in 1785 by Charles Coulomb, and the form of the force between two poles is outlined in Equation 1-14.

$$F \propto \frac{p_1 p_2}{d^2}$$

Equation 1-14 (Cullity, 1972. p.2)

Where $F$ is force (measured in dynes (dyn)), $p$ is the pole strength and $d$, the distance between the two poles.

The force of this field on another pole nearby is reflected in the introduction of the magnetizing force, or field strength, $H$ in Equation 1-15.

$$F \propto pH$$

<div align="right">Equation 1-15</div>

Field strength has the SI units Am⁻¹ or more commonly published in cgs units Oersted (Oe) where 1 Oe exerts 1 µN on a pole of unit strength. The intensity of the field created by a pole is also observed to decrease with increasing distance from the pole by Equation 1-16.

$$H \propto \frac{p}{d^2}$$

<div align="right">Equation 1-16</div>

### 1.5.3 Magnetic Moment

The fundamental principle in magnetism is the *magnetic moment*. The materials discussed herein have intrinsic moments associated with the different classes of magnetism; para-, dia-, ferro-, ferri- and antiferro-magnetism. These classes will be defined later, but at this stage we can state all the moments are generated by the materials atomic electrons. There are two kinds of electron motion as discussed in 1.5.1 that give rise to magnetism; orbital and spin.

The magnetic moment on an atom is associated with its total angular momentum ($J$); the sum of the orbital angular momentum ($L$) and the spin angular momentum ($S$), expressed in Equation 1-17 as;

$$J = L + S$$

<div align="right">Equation 1-17 (Blundell, 2001. p.23)</div>

1.5.3-1    Orbital Moment

In its simplest form, we can equate electron orbital moment to a current $I$, around an elementary loop of area $A$ having no resistance (Blundell, 2001). The magnetic moment $\mu$ is described by Equation 1-18 and illustrated in Figure 1-22.

$$\mu = I.A$$

<div align="right">Equation 1-18 (Blundell, 2001)</div>

If an electron moving is seen as the current, having charge $e$, mass $m$ and a circular orbit of radius $r$ (Bohr 1913) with velocity $v$, then the magnetic moment is given by Equation 1-19;

$$\mu\ (orbit) = I.A = -\frac{1}{2}evr^2$$

This angular momentum can then be quantised in units of $h/2\pi$, where $h$ is Planck's constant, thus realising the lowest non-zero value for an orbital electron moment is;

$$\mu = eh/4\pi m$$
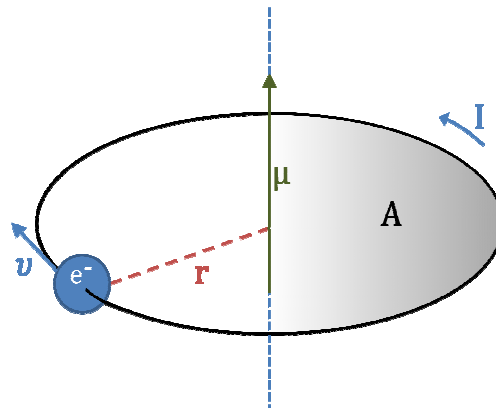
**Figure 1-22 Illustration equating current (I) in a loop of area (A) to an electron orbit with radius (r) and velocity (v) to form a magnetic moment ($\mu$).**

### 1.5.3-2    Spin Moment

An intrinsic magnetic moment is found within an electron due to its spin around its own axis. The magnetic moment due to spin cannot be calculated as multiple single loops of charge precessing around an axis, as the shape and charge distribution of the electron is not known, but it is accepted theoretically that the magnetic moment of an electron due to its spin is equal to the motion in the first Bohr orbit, so follows Equation 1-20.

This fundamental quantity is expressed as the Bohr Magneton, $\mu_B$ (Equation 1-21), and represents the lowest non-zero value for the magnetic moment of an atomic electron.

$$\boldsymbol{\mu_B} = Bohr\ magneton = eh/4\pi m = \mathbf{9.2732} \times \mathbf{10^{-24}\ Am^2}$$

Where the SI units are in Ampere metre squared ($Am^2$), or in mks are Joules per Tesla ($J\ T^{-1}$). (Where 1 Tesla = 1 Weber / $m^2$, 1 Weber = 100,000,000 Maxwells, and 1 Maxwell/$cm^2$ = 1 Oe.)

### 1.5.4  Magnetic Flux

Magnetic flux ($\varphi$) is the measurement of magnetic field strength (H) over a 2 dimensional area with SI units of Weber (Wb).

Magnetic flux density (or magnetic field / magnetic induction, B) is defined as having SI units Wb/$m^2$ = 1 Tesla (T) (0.1 mT = 1 gauss).

### 1.5.5  Magnetization and Susceptibility

When a magnetic field is placed in the proximity of a material, such as iron, the iron becomes magnetized with the extent of the magnetization being dependent on the field strength. The term *magnetization* ($M$) is therefore defined as the *magnetic moment per unit volume* (Equation 1-22);

$$M = \frac{\mu}{V}$$

Equation 1-22

Magnetization has the SI units $Am^{-1}$ (Crangle, 1977).

The amount of magnetization that can occur in a material from the influence of a magnetic field is determined by the materials 'receptiveness' or *susceptibility* to the magnetic field. In magnetism, this susceptibility is termed the volume magnetic susceptibility ($\chi_v$) and is dimensionless. In some types of materials termed paramagnetic (see section 1.6) this relationship is linear defined by Equation 1-23;

$$M = \chi_v H$$

Equation 1-23

Magnetic permeability is a materials ability to support a magnetic field within and is termed relative magnetic permeability ($\mu_r$) which is specific to a material and defined by Equation 1-24;

$$\mu_r = \mu_0(1 + \chi_v)$$

Equation 1-24

where $\mu_0$ is permeability of free space. In free space where there is no magnetization, the magnetic field can be quantified by the vectors *B (magnetic induction)* and $H$, which are related by $\mu_0$ in Equation 1-25:

$$B_0 = \mu_0 H$$

Equation 1-25 (Blundell, 2001)

In a magnetic solid, Equation 1-25 incorporates the term $M$ for magnetization, expressed in Equation 1-26.

$$\boldsymbol{B} = \mu_0(H + M) = \mu_0(1 + \chi_v)H = \boldsymbol{\mu_r H}$$

Equation 1-26

Magnetic susceptibilities are also often described in terms of molar magnetic susceptibility $(\chi_m)$ ($m^3\,mol^{-1}$) and mass susceptibility $(\chi)$ ($m^3\,kg^{-1}$) .These are defined in Equation 1-27 and Equation 1-28.

$$\chi_m = \chi V_m$$

Equation 1-27 (Blundell, 2001)

$$\chi = \chi/\rho$$

Equation 1-28 (Blundell, 2001)

Where $V_m$ is the molar volume ($m^3$) or volume occupied by one mole of the substance ($6.022 \times 10^{23}$ formula units) and $\rho$ is the density ($kg\ m^{-3}$).

Magnetic susceptibilities temperature and field dependence are what characterise the various classes of magnetic materials. These classes are discussed in the following sections.

## 1.6 PARAMAGNETISM AND DIAMAGNETISM

### 1.6.1 Paramagnetism

Paramagnetic materials become magnetized because the ionic magnetic moments align parallel to the direction of an applied external field. This depends linearly on the field, extinguishing the magnetization on removal of the field, expressed in Equation 1-23.

The relationship to mass susceptibility is described by Curie-Weiss Law (Equation 1-30), and the Curie temperature ($\theta$) for a paramagnetic material is positive (Figure 1-23).

### 1.6.2 Diamagnetism

Diamagnetic substances have a negative magnetic mass susceptibility, and diamagnetism exists in all materials. Although weak and nearly always masked by a much larger positive paramagnetic susceptibility, basic diamagnetism is independent of temperature, and follows Curie's Law (Equation 1-29) with a Curie temperature value equal to zero, illustrated in Figure 1-23.

$$\chi = C/T$$

Equation 1-29 Curie's Law (Cullity, 1972. p. 92).

### 1.6.3 Curie Temperature

The first reported measurements of susceptibilities for a large number of materials were conducted by Pierre Curie in 1895 (Cullity, 1972). It was found that the mass susceptibility was independent of temperature for diamagnets but inversely proportional with absolute temperature for paramagnets. This was expanded to become what is termed the Curie-Weiss Law, as defined by Equation 1-30.

$$\chi = C/(T - \theta)$$

Equation 1-30 Curie-Weiss Law (Cullity, 1972. p.93)

Where $\theta$ is a constant termed the Curie temperature (or Weiss temperature) (Néel 1952) which is calculated from extrapolation and $C$ is the Curie constant.

Plotting $1/\chi$ as a function of temperature (Figure 1-23) allows determination of the value $\theta$ which in turn describes the materials behaviour and defines magnetic class; either antiferromagnetic $(-\theta)$, diamagnetic $(\theta = 0)$ or paramagnetic $(+\theta)$.

A positive value of $\theta$ can also indicate a ferromagnet but unlike a paramagnet, a ferromagnetic material exhibits a spontaneous moment at temperatures below $\theta$. This is also true of ferrimagnets, and both of these classes of materials will be discussed next.
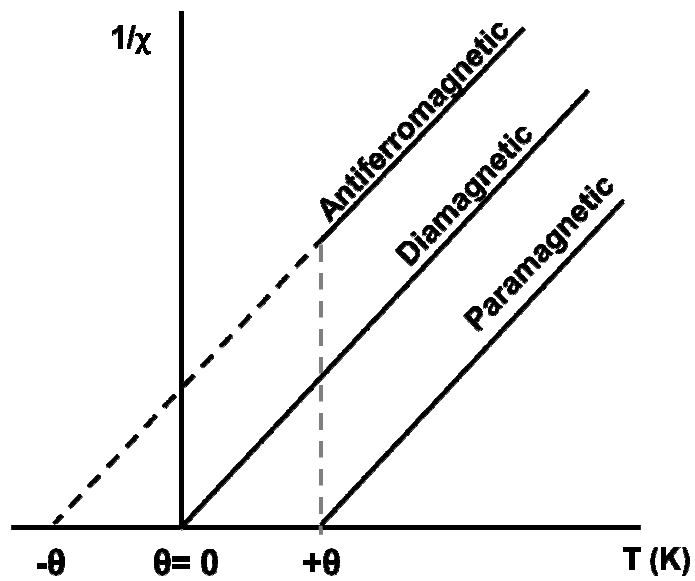


**Figure 1-23 Plot of the inverse of volume susceptibility as a function of temperature. The x intercept value defines the type of magnetism present in the sample (adapted from Blundell, 2001. p. 93)**

## 1.7 FERROMAGNETISM

### 1.7.1 Curie Weiss Theory of Ferromagnetism

A ferromagnetic material possesses a spontaneous magnetic moment, formed from a molecular level magnetization field that when cooled from a paramagnetic state through the materials Curie point, as in Ferroelectrics termed $T_C$, self-magnetizes the material (Cullity, 1972). This molecular field ($H_m$) is expressed by the molecular field constant (γ) in Equation 1-31.

$$H_m = \gamma M$$

Equation 1-31 (Cullity, 1972, p.97)

It is worthy to note that molecular field constant is inversely proportional to susceptibility, expressed in Equation 1-32.

$$\chi = \frac{C}{T - \rho C \gamma} = \frac{C}{T - \theta}$$

Equation 1-32

This molecular magnetic field develops, as previously discussed in section 1.5.3, by the electron orbit around a nucleus plus spin around its own axis. These effects are usually cancelled out by the varying paths of orbit of the multiple energy shells (for example $s$ shells are spherical, $p$ are dumbbell shaped etc) and Pauli's exclusion principle, where in any stable atom, not more than two electrons can occupy the same orbital, and that these electrons will have opposing directions of spin, in turn creating opposite dipoles cancelling out any net effect.

Some elements, particularly transition metals, do not have all orbital energy levels filled, and in particular for this group of elements, the $d$ valence shell is only partially occupied resulting in unpaired electrons allowing a net magnetic moment to exist.

Where electrons occupying multi-orbital sites are unpaired, it is worthy to note Hund's rule (Hund, 1925) which expresses that the electrons will maximize their spin (*i.e.* all electrons take the same spin as they fill orbitals and before any pairing of electrons with opposite spin) to form a high spin state.

## 1.7.2 Exchange Interactions

If we now consider these magnetic moments arranged in a crystal, in most materials the individual magnetic moments will interact so weakly that thermal motion is sufficient to randomise their directions leaving the overall structure with no net magnetic moment, and is therefore paramagnetic.

In some materials such as iron, nickel and cobalt, the partially filled $d$ shells present individual atomic moments through which exchange interactions act to align their moment vectors and reduce their overall energy. This is termed the exchange energy, and is enough to overcome the randomisation effect of thermal motion below the Curie point, seen in Figure 1-24. The alignment through these exchange interactions to give spontaneous magnetization is the formation of ferromagnetism.

The most studied example, iron, is paramagnetic above its Curie point, $T_C$ = 770 °C / 1043 K (Cullity,1972) and below it undergoes a second order phase transition to become ferromagnetic. Instead of a transformation of the crystal structure as seen in ferroelectricity with perovskites (see the example of $BaTiO_3$ in 1.4.6), demagnetized iron remains ferrite (or α-iron) in structure as it forms a ferromagnetic state from the spontaneously magnetized atoms aligned in parallel.

These magnetic moments interact by exchange of magnetic fields, the strength of which is then dependent on the spacing of the magnetic moments. For iron the ideal spacing allows the magnetization to become massive and ferromagnetic. However if the proximity of the moments is too close, the system becomes too rigid to be altered by anything but the strongest of magnetic fields; too far, and the moments are subject to effects from thermal agitation which can cause randomisation to a paramagnetic state (Wadhawan, 2000).

Manganese is a good example of this, as in its natural state at ambient temperature, the magnetic moments fall just outside of the ideal spacing to become ferromagnetic, but with the addition of nitrogen into interstitial sites, or cooling it to below 95 K (-178 °C) (Lawson, 1994) allows ferro and antiferromagnetic ordering respectively to take place from the change in exchange interaction distances.

Conversely, some magnetic moments can influence the symmetry of the crystallographic structure. In the example of manganese, $Mn^{3+}$ ions can distort its octahedral environment. Despite the increase in elastic energy due to the distortion, it reduces the electronic energy to a net energy saving. This is known as the Jahn-Teller effect (Blundell, 2001).
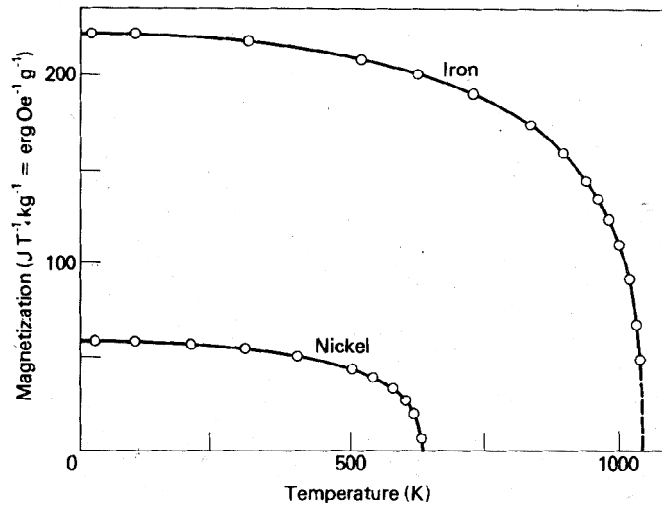
**Figure 1-24 Spontaneous magnetization values as a function of temperature for iron and nickel (Crangle, 1977.)**

Ferromagnets are also characterised by their mass susceptibility response as a function of temperature. Above $T_C$ the spontaneous magnetic moments are free to align in any direction, but the application of an external magnetic field can act to saturate the magnetization of the material by aligning all of the moments in a direction parallel to the field thus exhibiting paramagnetic behaviour. This is perhaps best shown in Figure 1-25, where for ferromagnets θ is positive.
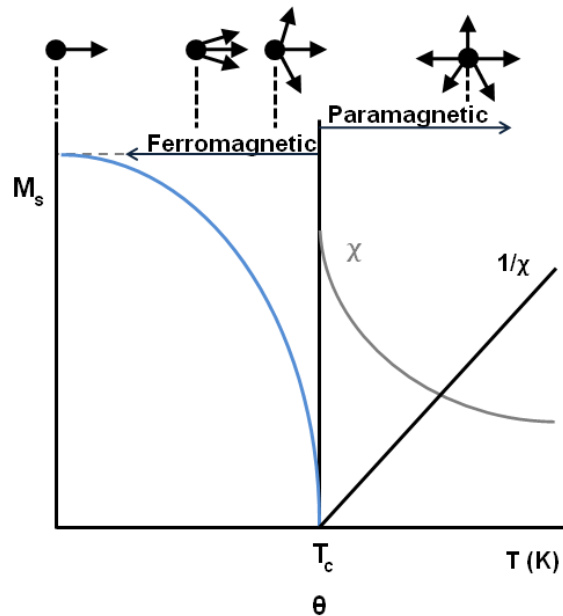


**Figure 1-25 Magnetization and susceptibility curves below and above the Curie temperature with sketches at the top to indicate distribution of magnetic moment direction with zero applied field within a domain (below $T_C$) and a group of atoms (above $T_C$). (Adapted from Cullity, 1972. p.127)**

### 1.7.3 Ferromagnetic Domains

When a ferromagnetic body is placed in a saturating field, the effect at its end surfaces is as though free magnetic poles are present, produced by the discontinuity at the surfaces normal to the magnetisation. The field acting within the material can be expressed as in Equation 1-33.

$$(B_0)_i = B_0 - (B_0)_D$$

Equation 1-33 (Crangle, 1977)

Where $(B_0)_D$ is a demagnetizing field. It is what would be produced by the surface pole distribution, and is present in all materials (Crangle, 1977).

If the magnetic field and the volume of material that the field invades can be reduced, this consequently reduces the amount of associated energy (Equation 1-23).

Forming regions of opposing magnetization reduces the external field and the energy associated, whilst retaining spontaneous magnetization of the material itself and despite of the cost of forming the walls themselves (Crangle, 1977). These discreet regions of aligned magnetic moments are termed *domains* and are separated by domain walls, regions of a few atoms thick in which their atomic moments swing in orientation from one wall to another.

Domains act to cancel the external fields, resulting in no net magnetization of the material volume. Application of an external magnetic field allows those regions which are aligned with the field to grow at the cost of others, as the energy required to move the walls is less than neighbouring domains. The ease at which the domain walls can be moved with the application of a magnetic field or indeed mechanical stress determines magnetic materials properties and ultimately its application. Domains that are relatively difficult to manipulate are termed hard, and consequently have high coercive field ($H_c$) and remnant magnetization ($M_r$) values and are used for 'permanent' magnets. Conversely, easily configurable domains in materials are termed soft, and soft magnetic materials have larger magnetic permeability, lower $H_c$, $M_r$ and require external magnetic fields to energise the magnetism. This however makes them useful in switching devices such as memory.

### 1.7.4 Ferromagnetic Hysteresis

Ferromagnetic hysteresis follows the same form as ferroelectric hysteresis as seen in Figure 1-14, however magnetization ($M$) varies with magnetic field ($H$) and spontaneous magnetization ($M_s$), remnant magnetization ($M_r$) and coercive field ($H_c$) are characteristic features of the loop.

It also illustrates the process of magnetizing demagnetized materials, a process of converting the material from a multi-domain state to 'single' domain, magnetized in parallel to an applied magnetic field. Once all domain walls have moved to allow this single domain state the material is said to be saturated. It is note worthy to mention that during this process, the *magnitude* of the magnetic moment or magnetization of any domain has not changed, merely the vector direction.

### 1.7.5  Stoner Theory of Ferromagnetism

Curie Weiss theory accounts for ferromagnetic moments from a model based on the production of a molecular field. This works very well for almost all magnetic postulations, but where it breaks down is accounting for the magnetic moment per ion. In theory, the magnetic moment magnitude per atom should be equal in a ferromagnetic state, as well as in the same atom's paramagnetic state, just a change in direction should occur. It should also be observed that a magnetic dipole moment should equate to an integer number of electrons. Experimentally however, this is not seen (Hill, 2000(a)).

To explain this, Stoner postulated that ferromagnetism is driven primarily by exchange energies (Stoner, 1933). In an atom, electrons fill an energy shell (given by the *principle quantum number* n = 1, 2, 3, 4…) by first filling various sub shells or orbits (termed, s, p, d, f… corresponding to *angular momentum*  ). As these sub shells are filled, electrons align so that their spin directions align parallel to each other, so as to minimise the exchange interaction energies in that orbit (Hund, 1925). Once the sub shell has been filled it is then energetically favourable to fill the next energy band, unless, the next energy level requires more energy than to oppose the exchange interactions and introduce electrons with spins anti-parallel. This lies true for simple metals where the next energy levels cost more than allowing all the lower states to fill with anti-parallel spins, cancelling any ferromagnetic effect. In transition metals however, the opposite is true, where some of the energy levels become blurred (for example 3d is a higher energy band than 4s, but the energies overlap due to the broad Fermi energy distribution of 4s), making it more efficient to allow partially filled or unpaired parallel spin electrons to exist, hence permitting ferromagnetism (Hill, 2000(a)).

The electron distribution also accounts for the moment distributions that were forbidden in Curie-Weiss theory. For example Ni has 10 valence electrons, of which 9.46 reside in 3d and 0.54 in 4s. Leaving the 0.54 electrons in the 4s is less energetic than forcing an antiparallel spin condition in the 3d. Consequently Ni has a very strong magnetization.

## 1.7.6 Brillouin Function

The Brillouin function arises in the determination of the magnetic dipole moment of electrons in a magnetic field, and is termed after Léon Brillouin (1889-1969) (Thomas, 1985) who published the relationship in 1927 (Brillouin, 1927).

Where $J$ is the total angular momentum per atom (section 1.5.3), which for paramagnets can be allowed to equal infinitum ($J = \infty$) if it is ignored that magnetic moments can only point along certain directions, or $J$ = multiples of ½, if we consider the moments as quantum spins for unpaired electrons.

In the example of materials that have no net orbital contribution ($L = 0$), Brillouin expressed the relationship between $J$ and magnetization ($M$) (Equation 1-34) by using the Brillouin function ($B_j(y)$), which is defined in Equation 1-35, and saturated magnetization ($M_s$) (defined in Equation 1-36).

$$M = M_s B_j(y)$$

Equation 1-34 (Blundell, 2001. p.28)

$$B_j(y) = \frac{2J+1}{2J} \coth\left(\frac{2J+1}{2J}y\right) - \frac{1}{2J} \coth\frac{y}{2J}$$

Equation 1-35 Brillouin function (Brillouin, 1927)

$$M_s = ng\mu_B J$$

Equation 1-36 (Blundell, 2001. p.28)

Where $n$ is the number of atoms per volume and $g$ is the Landau g-factor.

Plotting the Brillouin function as a function of $y$ for different values of $J$, is seen in Figure 1-26 (a). Comparison of this function on plots of magnetic moment as a function of field to temperature ratio (Figure 1-26 (b)) then provides information as to the value of the magnetic moment per ion of the magnetic material. For example iron ($Fe^{3+}$) , has $J = 5/2$ , calculated by its filling of orbitals by Hund's rule, and is given the quantitive value of magnetic moment as ~5 $\mu_B$. (Figure 1-26 (b)).

(a)                                          (b)
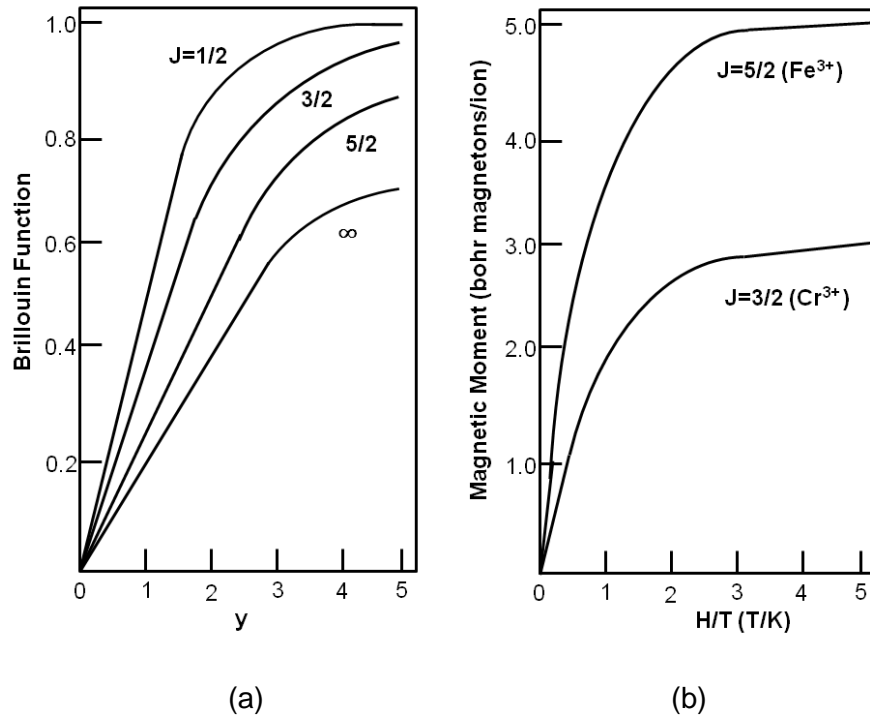
**Figure 1-26 Brillouin function curves where a) Brillouin function vs. small values of y for J = 1/2, 3/2, 5/2 and ∞, and b) Brillouin curves for J= 5/2 and 3/2 for $Fe^{3+}$ and $Cr^{3+}$ respectively on a plot of Magnetic moment vs. Field-Temperature ratio (adapted from Crangle, 1977. p.28-29)**

### 1.7.7 Demagnetisation Effect

The effect of changing the dimensions of a magnetic materials demagnetisation field (Equation 1-33) is shown in Figure 1-27. It is clear that long thin cylinders are the most ideal for minimising the effect, which will become important when testing samples of material using various characterisation techniques. Samples cut so that the ratio of length to width is over 5 minimises the effect to negligible.
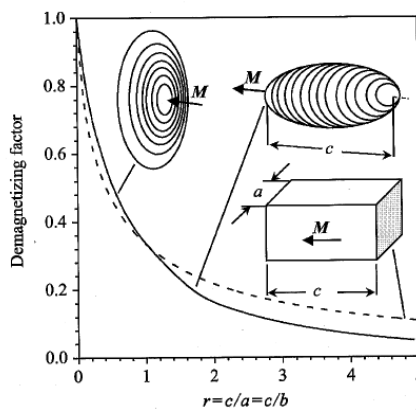


**Figure 1-27 Plot of demagnetizing factor as a function of sample dimension ratio (Fiorillo, 2004)**

## 1.8   ANTIFERROMAGNETISM

Analogous to ferromagnetic materials having the atomic moments aligned in parallel due to exchange interactions, antiferromagnetic materials' atomic moments are aligned antiparallel in a self-compensatory way to give no net magnetization (Blundell, 2001).

Antiferromagnetic (AFM) materials have a small positive susceptibility at all temperatures but this value varies in a fundamentally different way to other magnetic species, so much so they were given their own classification after the theory, developed primarily by Néel a French physicist, was published in a series of articles from 1932 (Néel, 1932) (Néel 1952).

### 1.8.1   Susceptibility above and at $T_N$

The relationship between susceptibility and temperature in an AFM is graphically illustrated in Figure 1-28 showing as the temperature decreases, susceptibility increases to a maximum at a critical temperature termed $T_N$ known as the Néel temperature.

A plot of $1/\chi$ above $T_N$ follows Curie-Weiss behaviour, with extrapolation to a negative Curie temperature (θ) which is equivalent to $-T_N$ (Crangle, 1977).
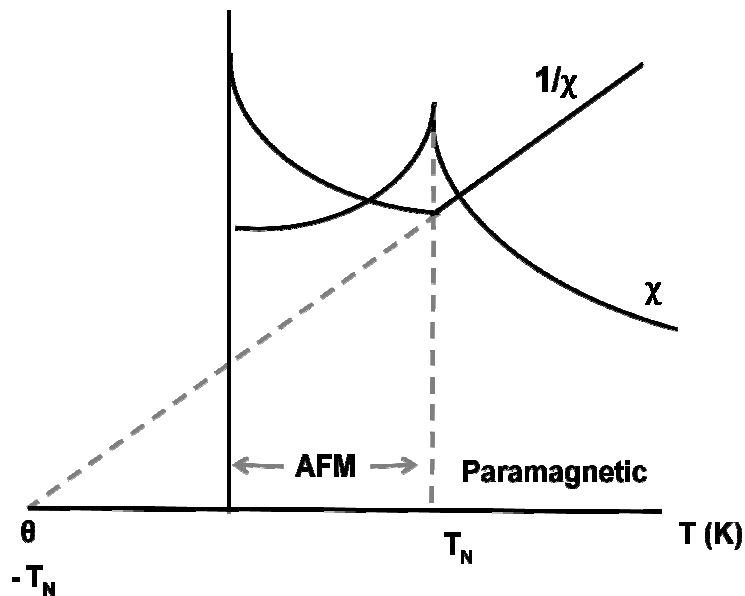


**Figure 1-28 An illustration of magnetic susceptibility as a function of temperature for an antiferromagnetic material (adapted from Cullity, 1972. p.156)**

An AFM that exceeds $T_N$ becomes paramagnetic. Upon cooling through the Néel transition the material is subjected to the same molecular field (γ) to align the spontaneous magnetic moments as in ferromagnetic materials. However, as

described in Equation 1-32, $\theta \propto \gamma$ so that the negative Curie temperature in turn gives a negative molecular field ($H_m$) in the paramagnetic region, which opposes the applied field ($H$).

Whereas the applied field tries to align the ionic moments in a direction parallel to $H$, the molecular field acts in the antiparallel direction to disalign them. The result is that any one ionic moment that has a tendency to align in one direction is simultaneously counteracted to align in the opposite direction by a neighbouring ion.

Below $T_N$ this tendency toward antiparallel alignment is strong enough to act in the absence of an applied magnetic field. The lattice of magnetic ions can then be split into two sub lattices (Blundell, 2001) (Figure 1-29) both with spontaneous magnetizations (Figure 1-30) but having moments approximately opposite, until $T = 0$ K, when the antiparallel alignment becomes perfect (Cullity, 1972).



(a)                    (b)                    (c)
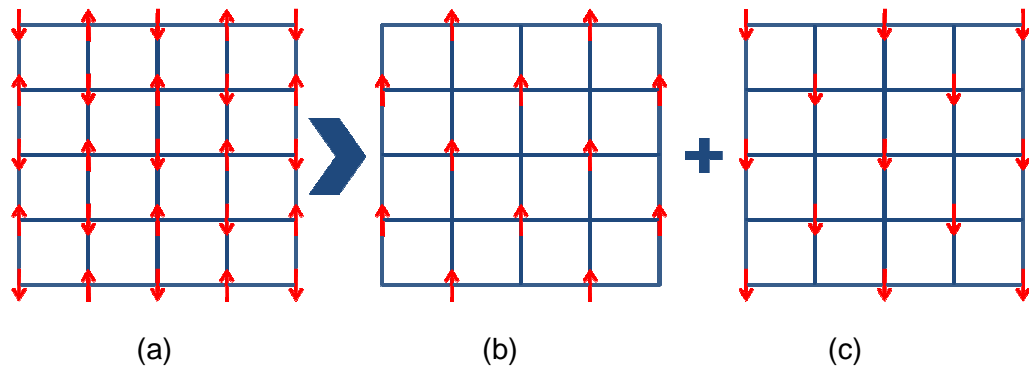
**Figure 1-29 Two sublattices having moments opposite to each other from b) H↑ and c) $H_m$↓ for example, to create a) an antiferromagnetic lattice. (adapted from Blundell, 2001. p. 92)**
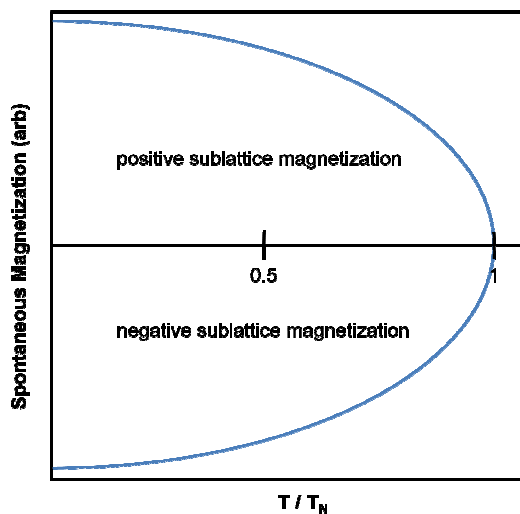


**Figure 1-30 Spontaneous magnetization of the sublattices in a simple antiferromagnet (adapted from Crangle, 1977. p. 63)**

### 1.8.2 Magnetic Susceptibility below T$_N$

When measuring the magnetic susceptibility for an AFM below $T_N$ it is important to consider the direction of the applied field relative to the magnetization direction of the two sub lattices, as there are fundamental differences between an applied field parallel (∥) and perpendicular (⊥) to the spin directions. In a polycrystalline material where these directions will be mixed at random in domains, the behaviour exhibited will lie somewhere in between. These effects can be described by Equation 1-37.

$$\chi = \frac{2}{3}\chi_\perp + \frac{1}{3}\chi_\parallel$$

Equation 1-37 (Crangle, 1977. p.64)

A field applied in the perpendicular direction will present a magnetization in the field direction, as illustrated in Figure 1-31, and would be the same at all temperatures ($T$) from $0 < T < T_N$. This mode of field application causes the spins to be 'canted', or deviate from their ideal antiparallel positions, presenting a 'weak' ferromagnetic effect (Cullity ,1972).

Application of a field parallel to the ionic moments at $T = 0$ K will have no effect on the alignment as the internal fields will be dominant. As temperature or field increases it is expected to increase susceptibility, either up to $T_N$ when the material becomes paramagnetic, or a strong enough field above T = 0 K could cant or realign the antiparallel spins to the field direction (Crangle, 1977) creating an effective 'saturated' ferromagnetic material; however the fields required are unrealistic for modern day devices (>7 T). Expected susceptibilities for parallel and perpendicular fields are shown schematically in Figure 1-32.



(a)                                     (b)
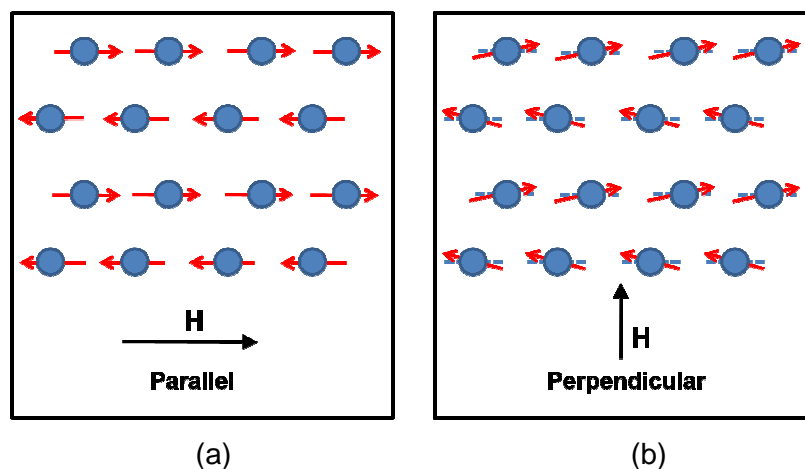
**Figure 1-31 Application of a) parallel and b) perpendicular magnetic fields (H) to a simple antiferromagnetic material (adapted from Crangle, 1977).**
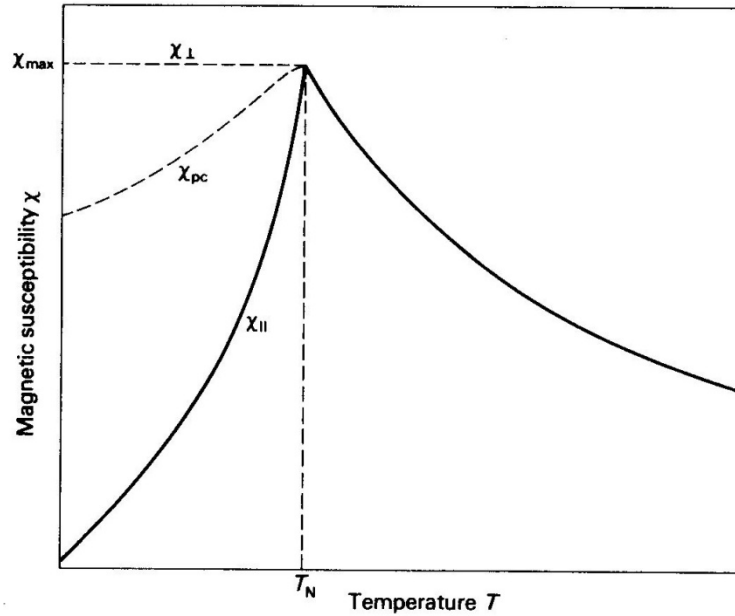
**Figure 1-32 Expected susceptibility of a simple antiferromagnetic single crystal with applied field parallel ($\parallel$) and perpendicular ($\perp$) to spin alignment, and polycrystal (pc) (Crangle, 1977. p.69).**

### 1.8.3 Antiferromagnetic Groups

So far we have only described simple antiferromagnetic materials and defined their spins as anti-parallel; however the order of these spins can occur in several forms, termed magnetic groups. The three main collinear groups are A, C and G. These are represented schematically in Figure 1-33.



(a)                                   (b)                                   (c)
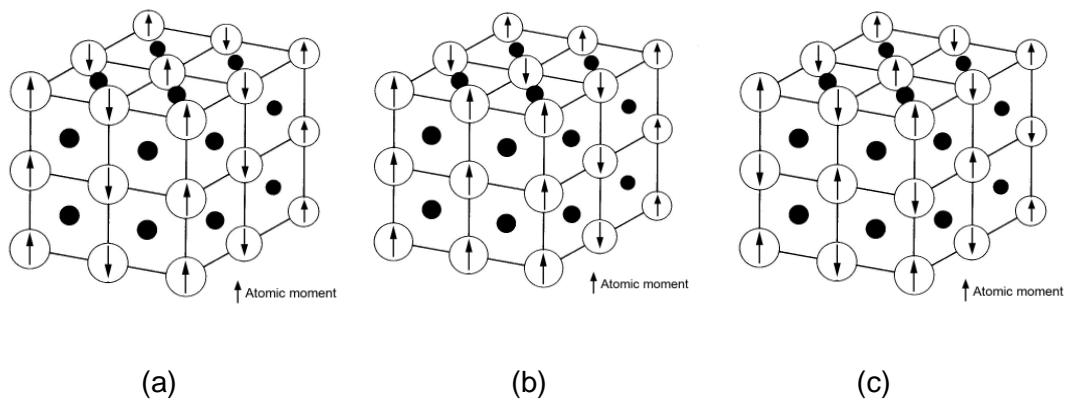
**Figure 1-33 Antiferromagnetic groups a) C-type  b) A-type and c) G-type (adapted from Crangle, 1977).**

C-type antiferromagnetism sees alignment of spins in columns. In A-type the spins are aligned in planes through the structure, and in G-type, each nearest neighbour is antiparallel (Wollan, 1955) (Ranjan, 2007).

### 1.8.4  Canted and Helical Spin Arrangements

Previously, only collinear magnetic systems have been discussed, where all spins lie parallel or antiparallel to a single direction. These systems are common, but there are some that present non-collinear arrangements and form differing helical structures. These are found frequently in rare earth metals and can consist of a helix (cycloidal), cone, antiphase cone and sinusoidally or square-wave moment modulations.

Canted spins in antiferromagnets, whereby the antiparallel alignment is not perfect, giving rise to a small net magnetization or 'weak ferromagnetism' have been reported in many AFM materials. Applications of external fields past critical field strengths can cause canting, but spontaneous weak ferromagnetism occurs frequently in perovskite materials where the polarization breaks the centre of symmetry and introduces canting of the spins via Dzyaloshinkskii-Moriya (DM) interactions. These interactions are based on anisotropic super exchange of electron spin magnetic moments (Moriya, 1960). These are discussed in a material context later.

### 1.9  FERRIMAGNETISM

The treatment for AFM in section 1.8 assumes the two sub lattices are equivalent. If there was some crystallographic reason for this assumption to not hold true, then the magnetizations may be antiparallel in direction but not be equal in magnitude, producing a net magnetization.

Ferrimagnets do not follow Curie-Weiss behaviour for magnetic susceptibilities ($1/\chi$ as a function of temperature plots are often hyperbolic) (Crangle, 1977) as the sublattice magnetizations, if not equal, will have very different and complicated temperature dependencies. For example at low temperature, sub lattice 'a' may be dominant, and at high temperature, sub lattice 'b' takes over (Blundell, 2001).

Overall magnetization however appears ferromagnetic due to the exhibition of a spontaneous magnetic moment at temperatures below $T_C$.

## 1.10 MAGNETIC UNITS

Much of the work done on magnetism was originally conducted and published in cgs (centimetre, gramme, second) units, with systems under the cgs umbrella that included gaussian, electrostatic (esu) and electromagnetic (emu) units. As science and engineering developed and adopted the mks (metres, kilogrammes, seconds) and the international system of (SI) units (Jiles, 2003), the need to translate cgs into SI became apparent. The Sommerfield convention (Sommerfield, 1948) was accepted, with many of the magnetic CGS units converted to SI involving multiples of $4\pi$. Table 1-3 presents a summary of the magnetic quantities and the units relating to them used in this work. It is worth noting that it is still common in the literature to see a mix of cgs and mks/SI units being used.

**Table 1-3 Summary of commonly used magnetic quantities with their SI units *(mks in italics)* and cgs gaussian conversions.**

| SYMBOL | QUANTITY | SI (*mks*)UNIT | CGS, gaussian CONVERSION |
|--------|----------|----------------|--------------------------|
| $\mu_B$ | Bohr Magneton | $9.2732 \times 10^{-24}$ Am$^2$ <br> *(JT$^{-1}$)* | $9.2732 \times 10^{-21}$ ergOe$^{-1}$ |
| $H$ | Magnetic Field Strength | Am$^{-1}$ [*] | Oersted (Oe) <br> (1 Am$^{-1}$ = $4\pi \times 10^{-3}$ Oe) |
| $\varphi$ | Magnetic Flux | Weber (Wb) <br> (1 Wb = *1 V.s*) | Maxwells (Mx) <br> (1 Wb = $10^8$ Mx) |
| $B$ | Magnetic Induction | Tesla (T) <br> (1 T = 1 Wbm$^{-2}$) | Gauss (G) <br> (1 T = $10^4$ G) |
| $M$ | Volume Magnetization | Am$^{-1}$ | emu/cm$^3$ [**] |
| $\chi_m$ | Volume Magnetic Susceptibility | dimensionless | dimensionless |
| $\mu$ | Magnetic Permeability | Henry per metre (Hm$^{-1}$) <br> (1 Hm$^{-1}$ = 1 *Wb/A.m*) | dimensionless |
| $\mu_r$ | Relative Magnetic Permeability | dimensionless | dimensionless |

[*]Often expressed as Ampere-turns per metre for magnetic field strength

[**] emu refers to the term "electromagnetic unit" and is in reference to the cgs subset where the Ampere force constant = 1, rather than Gaussian.

## 1.11 MAGNETOELECTRIC MULTIFERROICS

### 1.11.1 Multiferroics

1.11.1-1   Primary Ferroics

A crystal is referred to as being "ferroic" when "it has two or more orientation states in the absence of an external magnetic field, electric field or mechanical stress" (Aizu, 1970).

As previously discussed, any of these orientation states are identical or symmetrical in structure but are different in respect to their direction of arrangement of atoms that posses electric or magnetic dipole moments. These are ferroelectrics, whereby the orientation states are spontaneous electric polarization ($P$) vectors; Ferromagnets (and antiferromagnets) where the orientation states are spontaneous magnetization ($M$) vectors; and ferroelastics, whose orientation states are spontaneous strain ($x$) tensors. Any of these components may be switched to another equivalent state by the application of the external fields ($E, H$) or stresses ($\sigma$) described above, and are also defined as *Primary Ferroics* (Schmid, 1994(a)).

There is another Primary ferroic termed Ferrotoroidicity, but it is not within the scope of this work.

1.11.1-2   Secondary Ferroics

In the thermodynamic classification (Schmid, 2003), as well as the three primary ferroics, defined in Equation 1-38, there also exists three *Secondary Ferroics,* termed Ferrobielectrics, Ferrobimagnetics and Ferrobielastics (Schmid, 2003), with coefficients of electric permittivity ($\varepsilon_{ij}$), magnetic permeability ($\mu_{ij}$) and elastic compliance ($s_{ijkl}$) respectively (Schmid, 1994(a)). These are expressed in terms of free enthalpy ($g$) as functions of electric ($E$) and magnetic ($H$) field at constant temperature ($T$) in Equation 1-39;

$$-g(E, H: \boldsymbol{T}) = P_i E_i + M_i H_i + x_{ij}\sigma_{ij}$$

Ferroelectric + Ferromagnet + Ferroelastic

Equation 1-38 Thermodynamics of Primary Ferroics (Rivera, 1994)

$$-g(E, H: \boldsymbol{T}) = P_i E_i + M_i H_i + x_{ij}\sigma_{ij}$$
$$+\frac{1}{2}\varepsilon_0\varepsilon_{ik}E_i E_k + \frac{1}{2}\mu_0\mu_{ik}H_i H_k + \frac{1}{2}s_{ijkl}\sigma_i\sigma_j$$

Ferrobielectric + Ferrobimagnetic + Ferrobielastic

Equation 1-39 Thermodynamics of Secondary Ferroics (Schmid, 2003)

1.11.1-3   Mixed Secondary Ferroics

The term 'multiferroic' is applied to those materials which can exhibit two or more of the primary ferroics, united in the same phase (Schmid, 1994(a)). In this instance, we can observe properties of mixed secondary ferroics, where coupling between two of the primary ferroics takes place. This is seen in Equation 1-40:

$$-g(E,H{:}\boldsymbol{T}) = \ldots + \boldsymbol{d_{ijk}E_i\sigma_{jk}} + \boldsymbol{Q_{ijk}H_i\sigma_{jk}} + \boldsymbol{\alpha_{ij}E_iH_j} \ldots$$

Piezoelectric + Piezomagnetic + Magnetoelectric

Equation 1-40 Mixed Secondary Ferroics (Glazer, 2007)

The mixed secondary ferroics are termed Ferroelastoelectrics (Piezoelectrics), Ferromagnetoelastics (Piezomagnetic) and Ferromagnetoelectrics (Magnetoelectrics) with piezoelectric coefficient $(d_{ijk})$, piezomagnetic coefficient $(Q_{ijk})$ and magnetoelectric $(\alpha_{ij})$ coefficient respectively.

The coupling of one ferroic to the other is illustrated in Figure 1-34 , where for the example of the magnetoelectric effect highlighted, the application of an electric or magnetic field, acts to modify the magnetic magnetization or electric polarization respectively.
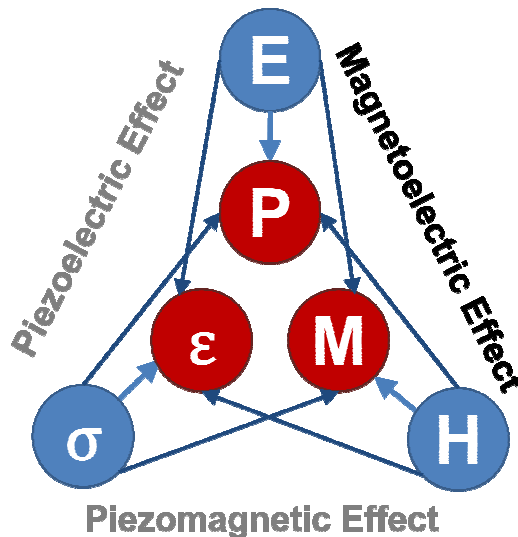


**Figure 1-34 Multiferroic coupling illustration. The magnetoelectric effect is highlighted as per the example given in the text.**

## 1.11.2 Magnetoelectrics

Materials that exhibit both ferroelectric and ferromagnetic (or antiferroelectric and antiferromagnetic (Fiebig, 2005)) behaviour *and* where these ferroics are coupled, are termed magnetoelectrics (ME). They are described thermodynamically in Equation 1-40.

Two independent observations marked the birth of magnetoelectrics. The first in 1888, Röntgen discovered that a moving dielectric became magnetized when placed in an electric field (Röntgen, 1888). The reverse, polarization of a moving dielectric in a magnetic field, was discovered 17 years later.

Secondly, Pierre Curie in 1894 showed the possibility of intrinsic ME behaviour in non-moving crystals through symmetry (Curie, 1894) which later Peter Debye set out in a series of magnetoelectric terminologies (Debye, 1926), but for some time science failed to show the effect experimentally.

Landau and Lifshitz reported in 1960  that time reversal asymmetry was required  for magnetoelectric effects (Landau, 1960) (Schmid, 1994(b)), resulting in the linear magnetoelectric behaviour being predicted in the antiferromagnet $Cr_2O_3$ by Dzyaloshinskii in 1957 (Dzyaloshinskii, 1959) which was later confirmed experimentally by Astrov by measuring electric field induced magnetization (Astrov, 1960). This marked the first observed behaviour experimentally of the magnetoelectric effect, and followed with the inverse magnetic field induced electric polarization (Folen, 1961), launching a decade of experimental and theoretical research trying to utilise the potential of coupled magnetic and electric properties (Fiebig, 2005).

The work completed over this time was culminated in a book by O'Dell (O'Dell, 1970) and started a series of conferences on the magnetoelectric effect interaction phenomena in crystals (MEIPIC) (Freeman, 1975) (Schmid, 1994(c)).

The magnetoelectric effect was generally weak in the fact that electric control of magnetic fields worked with relative ease and relatively small electric fields, but the reversal, using a magnetic field to influence and electric polarization required fields in the order of $10^4$ Oe, or Teslas, much greater than the order of magnitudes modern day consumer devices can produce. This weak effect, the rare nature of these materials, and the limited understanding of microscopy techniques to observe this phenomenon, eventually lead to a decline in research efforts from its peak in 1973 (Fiebig, 2005).

At the start of the millennium, with increased understanding of the theory behind multiferroics and ME behaviour (Hill, 2000) (through density functional theory (Hill, 2002)) and the miniaturization culture of modern electronics (Prinz 1999), the requirement for these advanced materials once again sparked a new research trend in the 1990's, illustrated in Figure 1-35.
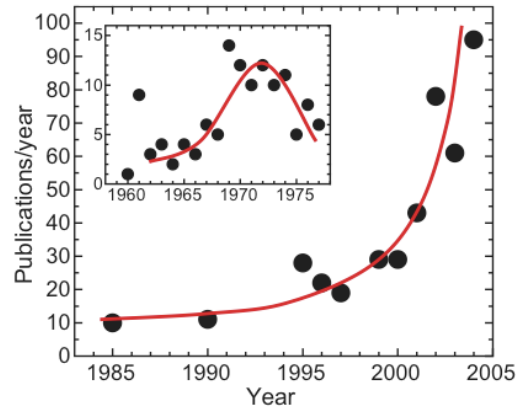


**Figure 1-35 Publications per year with "magnetoelectric" as a keyword according to web of science, http://isiknowledge.com. (Reprinted by permission from Macmillan Publishers Ltd; Nature (Fiebig, 2005).**

1.11.2-1  Why are they so rare?

One group in particular at the University of California in Santa Barbara, USA, undertook a complete overhaul on multiferroic theory and tried to clear up the fundamental physics involved. Nicola Hill (now Spaldin) completed the first of many publications on the subject beginning with "first  principles of multiferroic magnetoelectric manganates" in 2000 (Hill 2000(b)) which was quickly followed by density functional theory modelling in 2002 (Hill, 2002).

In these pivotal publications, Hill reported that in most magnetic materials the magnetic dipole is formed by the partial filling of 'd' electron shells allowing unpaired electrons to exist with an uncancelled spin component due to Hund's rule and Stoner's theory (Hund, 1925) (Stoner, 1933); but this contradicts the requirement for ferroelectricity. In perovskite structures below $T_C$, the central ion displaces and hybridizes its orbits with the oxygen octahedra, stabilizing the ferroelectric distortion (Hill, 2000(a)). For the example of $PbTiO_3$ the $Ti^{4+}$ ion hybridizes such that it mixes its 3d orbitals with that of the oxygen 2p orbitals making the lowest unoccupied energy level states in the d-shell. Consequently empty 3d ($3d^0$) shells are created, contradictory the necessary $3d^n$ shells required for magnetism (Hill, 2000(a)).

Symmetry also plays a small role in the scarceness of these systems. There are 31 Heesch point groups that can sustain spontaneous electric, and the same again for magnetic, polarizations. 13 exist in both sets allowing simultaneous ferroic properties to exist (Hill, 2000(a)), which is a small but significant number of the total 122 possible Heesch crystal structures (Dayanidhi, 1973).

### 1.11.2-2   Magnetoelectric Multiferroics

The definition of a multiferroic states that the material must exhibit two or more of the primary ferroics. The magnetoelectric definition does not require primary ferroics to exist together, just that the material must exhibit their behaviour. From Equation 1-40, we can determine that magnetoelectricity is formed from mixing secondary, not primary ferroics.

Therefore the relationship between magnetoelectrics and multiferroics is not commensurate and there can exist magnetoelectrics that are not by definition multiferroic. This is illustrated graphically in Figure 1-36.
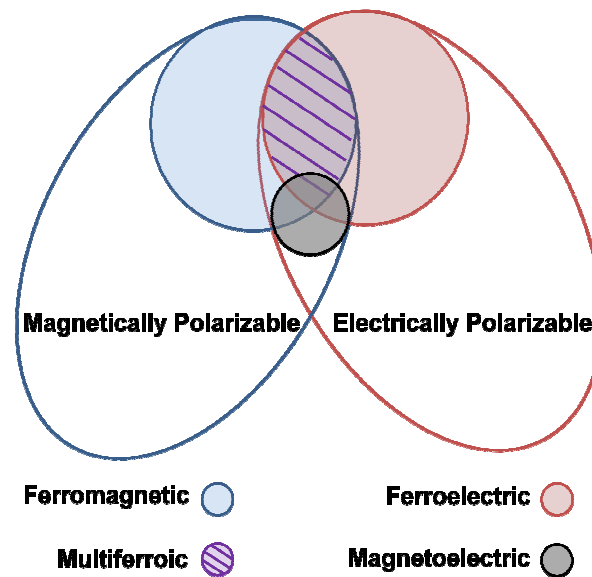


**Figure 1-36 The relationship between magnetoelectric and multiferroic materials (Reprinted by permission from Macmillan Publishers Ltd; Nature. (Eerenstein, 2006).**

Magnetoelectric coupling may exist whatever nature of magnetic and electric order parameters are present, including paraelectric and paramagnetic materials (Eerenstein, 2006).

An example of this is demonstrated in $Cr_2O_3$ which is a magnetoelectric but does not possess any spontaneous electric polarization, although with the application of an electric field, polarization is induced (Astrov, 1960).

Another addition to the separation of the two definitions lies in $YMnO_3$ which is a ferroelectric antiferromagnet. This proves that not all magnetic-electric multiferroics are magnetoelectric as in this compound the linear ME effect is forbidden by symmetry (Fiebig, 2007).

### 1.11.2-3  Linear Magnetoelectric Effect

The coupling between the two ferroics shown in Figure 1-34 is termed the *linear magnetoelectric effect* as it describes the direct response $(P, M)$ of an external field stimulus $(E, H)$ and is quantified by the magnetoelectric coefficient $(\alpha_{ij})$ which can be defined by Equation 1-41.

$$P_i = \alpha_{ij}H_j \quad M_j = \alpha_{ij}E_i$$

<div align="right">Equation 1-41 (Zvezdin, 2006)</div>

The magnetoelectric coefficient is however bound by upper limits due to its relationship to the electric $(\kappa)$ and magnetic susceptibilities $(\chi)$ (Brown, 1968). (Equation 1-42);

$$(\alpha_{ij}/4\pi)^2 \leq \chi_{ii}\kappa_{jj} \text{ or } {\alpha_{ij}}^2 \leq \mu_{ii}\varepsilon_{jj}$$

<div align="right">Equation 1-42 (Brown, 1968)</div>

where $\mu$ and $\varepsilon$ are of magnetic permeability and electric permittivity respectively.

The linear ME effect however is relatively small, principally due to the maximum values of magnetic and electric susceptibilities being relatively small and $\alpha_{ij}$ appears as a product in Equation 1-42 of the two properties. There are no such limits however on higher order, non-linear, couplings, demonstrated in 1.11.2-5 (Eerenstein, 2006).

The ME coefficient can only be non-zero for materials that have no centre of symmetry and are time-asymmetric; this is because $\alpha_{ij}$ is a derived from elements of the materials symmetry (Eerenstein, 2006).

### 1.11.2-4  Quadratic Magnetoelectric Effect

Expanding the mixed secondary ferroic relationship (Equation 1-40) we can incorporate higher order couplings of magnetic and electric polarizations defined by

Equation 1-43 which introduces third rank tensors $\beta_{ijk}$ and $\gamma_{ijk}$ that represent quadratic magnetoelectric coefficients (Schmid, 2003).

$$-g(E, H : \boldsymbol{T}) = \cdots + \tfrac{1}{2}\varepsilon_0\varepsilon_{ik}E_iE_k + \tfrac{1}{2}\mu_0\mu_{ik}H_iH_k + \alpha_{ik}E_iH_k + \tfrac{1}{2}\beta_{ijk}E_iH_jH_k + \tfrac{1}{2}\gamma_{ijk}H_iE_jE_k + \cdots$$

Equation 1-43 (Schmid, 2003)

These third rank tensors can offer much higher values than the linear effects alone.

## 1.11.2-5   Indirect Coupling

The magnetoelectric terms discussed so far only include contributions from the ferroelectric and ferromagnetic parts. If we refer back to Equation 1-40 it is apparent that strain can play a pivotal role by cross coupling the magnetic and electric mechanisms through piezomagnetic and piezoelectric components.

There are two methods of introducing strain coupling, through mixed ferroic phase systems, or composite magnetoelectrics.

### 1.1.1-1.1   Single Phase Strain Coupling

The term single phase in this context is taken to describe a non-composite structure, or one that is made up of a single material or system such that it consists of both ferroic parameters within one unit cell, from which ME effects are attributed.

An example of this can be seen in the following sections for systems such as $BiFeO_3$, $BiMnO_3$ and rare earth manganites.

### 1.1.1-1.2   Composite Strain Coupling

The alternative to 'single phase' coupling is the composite, or pseudo-multiferroic, modality. Figure 1-37 presents two types of coupling through strain, intergranular and multilayers.

Intergranular composites utilise a mixture of grains as shown in Figure 1-37 a) (Eerenstein, 2006). In this example the material consists of a piezoelectric and piezomagnetic / magnetostrictive phase grains intimately dispersed through the microstructure so that any electric or magnetic stimulus imparts a strain response from the relevant piezoelectric or piezomagnetic grain which in turn transforms to a mechanical stress that is transmitted to a neighbouring, alternate ferroic grain to modify the magnetic or electric polarization state respectively.

In laminar multilayers a piezomagnetic or magnetostrictive and piezoelectric layer or layers, are bonded together so that the ME effect can be exhibited through transmission of strain.

This type of composite structure can take form in a range of dimensions from polycrystalline sintered ceramics to thin film heterostructures (Wang, 2003) (Eerenstein, 2006), and some composites have even been formed from nanostructured spinel pillars which have shown high interface to volume ratios and exhibit strong ME coupling (Martin, 2008).
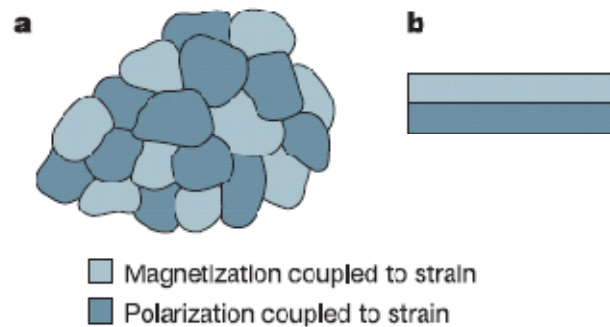


**Figure 1-37 Magnetoelectric strain coupling by mixing two phases of piezomagnetic and piezoelectric material as a) a mixture of grains or b) as composite layers (Reprinted by permission from Macmillan Publishers Ltd; Nature. (Eerenstein, 2006).**

1.11.2-6   Time Reversal and Space Inversion Symmetry

Landau and Lifshitz reported in 1960 that time reversal asymmetry was required for magnetoelectric and piezoelectric effects (Landau, 1960).

Time reversal symmetry is present in ferroelectrics as a spontaneous electrical polarization has no time dependence. Conversely, a magnetic dipole would reverse polarity with a reversal of time, as the electron spin and orbit would consequently be counter - rotated. Spatial inversion symmetry is present in ferromagnetics as dipole moments from electron spin and orbit rotate in the same direction irrespective of the inversion operation, whereas ferroelectrics would see a switch in polarity.

Multiferroics present neither spatial inversion nor time reversal symmetry. summarized in Table 1-4.

**Table 1-4 Summary of time reversal and space inversion symmetry in ferroics (Eerenstein, 2006. p. 760).**

| Ferroic | Spatial Inversion Symmetry | Time Reversal Symmetry |
|---------|---------------------------|------------------------|
| Ferroelastic | Yes | Yes |
| Ferroelectric | No | Yes |
| Ferromagnetic | Yes | No |
| Multiferroic | No | No |

### 1.11.3 Measurement of the Magnetoelectric Effect

The measurement of magnetoelectric effects is not a trivial matter. There lies experimental issues as well as the major challenge of making samples insulating enough to prevent leakage currents contributing to the recorded signal, a problem found frequently in ferroelectric polarization loops (Eerenstein, 2006).

ME coupling can be measured directly; a magnetic response to an applied electric field, or electric response to an applied magnetic field, or indirectly, by recording changes in either polarization (dielectric constant) or magnetization at or near a ferromagnetic or ferroelectric transition temperature respectively.

Indirect measurements are relatively simple but only give comparative values, rather than explicitly define the magnetoelectric coupling. Examples of this are magneto capacitance (Catalan, 2006), or magneto dielectric measurements (Scott, 2007(b)). Care must be taken with magneto capacitance measurements however as magneto resistance and surface (Maxwell-Wagner) effects can give similar results without the presence of ME coupling (Catalan, 2006).

Direct measurements provide intrinsic, quantitative values of ME effects, and methods typically include recording electric data, voltage or current, inside a (sometimes cryogenically cooled & superconducting) magnetometer applying bias magnetic fields (to reduce hysteresis to get linearity), whilst AC oscillating Helmholtz coils provide the moving magnetic field to induce the ME effect (Figure 1-38) (Ryu, 2002).
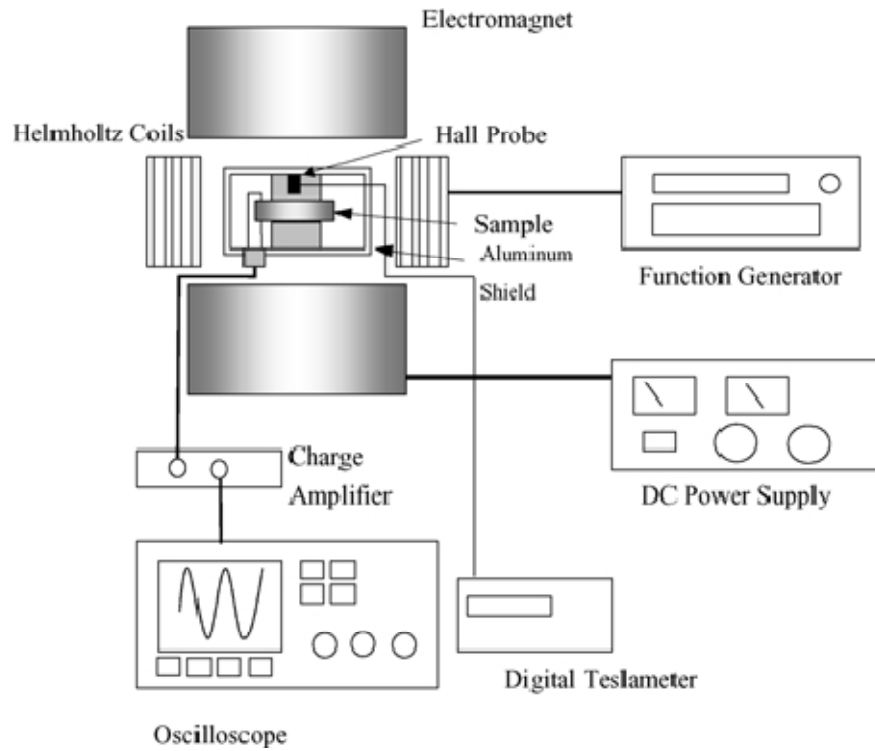
**Figure 1-38 Schematic of a ME measurement system (Reprinted by permission from Springer; J. Electroceramics. (Ryu, 2002. p.112)**

1.11.3-1  Magnetoelectric Coefficient Values

In the example of Figure 1-38, the electrical response can be measured as current or voltage (Eerenstein, 2006), where the time-integrated current per unit area represents the magnetically induced polarization in Equation 1-41 and Equation 1-43 where ignoring higher order terms (Eerenstein, 2006) we see Equation 1-44.

$$\alpha_{ij} = \Delta P_i / \Delta H_j$$

Equation 1-44 (Eerenstein, 2006)

Where voltage is measured however, we can observe empirical coupling coefficients, also denoted as α which again, assuming linearity is expressed in Equation 1-45.

$$\alpha = \Delta E / \Delta H$$

Equation 1-45 (Eerenstein, 2006)

## 1.11.4 Magnetoelectric Multiferroic Materials

Stimulated by the announcement of perovskite $Pb(Fe_{0.5}Nb_{0.5})O_3$ displaying both antiferromagnetic and ferroelectric properties (Smolenskii, 1958) plus reports of the ME effect being observed in antiferromagnetic $Cr_2O_3$ (Astrov, 1960), a flurry of research originated reporting ME effects in numerous compounds, including higher order effects.

The result of the research was summarized by O'Dell (1970) and for single phase studies can be categorized into compound types. The most popular are the boracites, rare earth manganites, and perovskites; namely bismuth based perovskites (Suryanarayana, 1994).

There are other systems that make up fractions of the 100 or so magnetoelectric multiferroic compunds that will not be discussed. These include rare earth molybdates (Ponomarev, 1994) and phosphates (i.e. $KNiPO_4$) (Lujan, 1994).

### 1.11.4-1   Boracites

The boracites are a large family of crystal structures bearing the general formula $Me_3B_7O_{13}X$ where Me is bivalent metal ion and X a monovalent anion (Suryanarayana, 1994).

These complex structured systems contain many atoms per formula unit and more than one formula unit per unit cell, bound by numerous inter-ionic interactions which prevent isolation of individual ferroics, causing multiferroicity (Prellier, 2005).

The first of the multiferroic boracites was reported by Ascher et al in 1966 for the bulk Nickel-Iodine compound, $Ni_3B_7O_{13}I$ (Ascher, 1966). Ni-I-Boracite is paraelectric antiferromagnetic (space group $P\bar{4}3c$, ISS# 219) below $T_N$ = 120 K (Schmid, 1965) becoming ferroelectric and weakly ferromagnetic (space group $Pca2_1$, ISS# 29) (Tolédano, 1985) below $T_C$ = 64 K (Ascher, 1966). The onset of ferroelectricity is thought to modify the antiferromagnetic order sufficiently to give a net magnetization (Schmid, 1965), a consequence of the coupling between the electric and magnetic ferroics being due to symmetry. This symmetry condition allows a magnetic field induced 90 ° reorientation of the magnetization direction to drive a 180 ° reversal of the electric polarization direction (Schmid, 1994(b)). Conversley, a 180 ° electric field induced polarization reversal causes a 90 ° magnetization reorientation (Schmid, 1994(b)). This giant ME effect (Fiebig, 2005) is realised by a reduction in the magnetic symmetry to lower the free energy which can only operate (based on the parent paramagnetic dielectric phase symmetry, a $\bar{4}$ operation) when a simultaneous magnetic and electric reorientation occurs (Fiebig, 2005).

Hans Schmid completed magnetic susceptilibity measurements on a comprehensive list of bulk 3d transition metal boracites through the late 1960's (Schmid, 1965) summarised in Table 1-5, where all were found to have high and low temperature structure modifications, with the high temperature relating to negative Curie-Weiss temperatures, purporting to them being antiferromagnetic (Figure 1-23).

**Table 1-5 Some Boracites and their Curie Temperatures (Schmid, 1965)**

| BORACITE | Curie Temperature θ (K) |
|---|---|
| $Fe_3B_7O_{13}Cl$ | 37 |
| $Co_3B_7O_{13}Cl$ | 85 |
| $Ni_3B_7O_{13}Cl$ | 108 |
| $Co_3B_7O_{13}Br$ | 10 |
| $Ni_3B_7O_{13}Br$ | 133 |
| $Cu_3B_7O_{13}Br$ | 35 |
| $Cr_3B_7O_{13}I$ | 302 |
| $Mn_3B_7O_{13}I$ | 88 |
| $Fe_3B_7O_{13}I$ | 130 |
| $Co_3B_7O_{13}I$ | 25 |
| $Ni_3B_7O_{13}I$ | 325 |

1.11.4-2   Rare Earth Manganites

A-site cation engineering in perovskite manganese oxides, $REMnO_3$ (where RE is a rare earth ion) started in 1955 with lanthanum (Yakel, 1963) and quickly grew to incorporate neodynium, praseodymium and dysprosium (Vickery, 1957). Throughout the 1960's the list grew, much to the credit of Bertaut who investigated most of the systems and found that the structure of the resulting oxides were dependent on ionic radii (Prellier, 2005).

A reduction in cation radii causes an instability in the Jahn-Teller distortion of orthorhombic (space group $Pnma$, ISS# 62) centrosymmetric unit cells to a hexagonal (space group $P6_3Cm$, ISS#185)  non-centrosymettric perovskite, with the cross over lying between Y and Ho. This is summarized graphically in Figure 1-39.
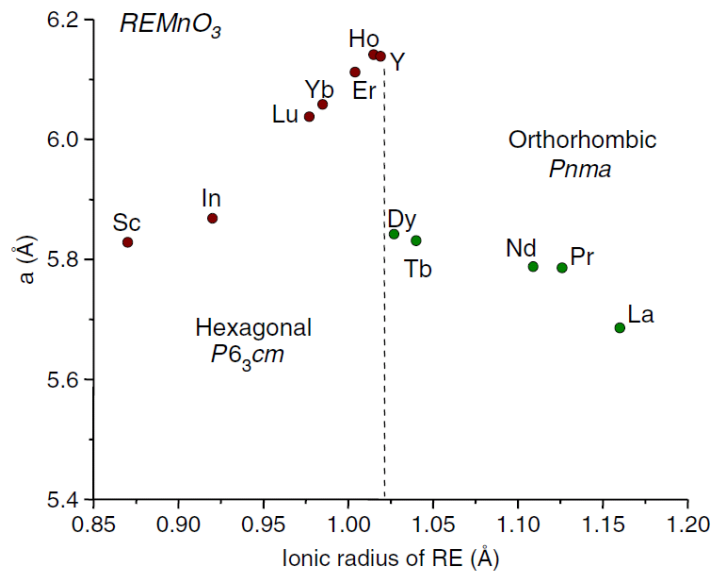
**Figure 1-39 Structure of REMnO$_3$ as a function of RE ionic radius.**
**(Reprinted by permission from Institute of Physics Pub.; (Prellier, 2005. p.810).**

The bulk orthorhombic structure exhibits spontaneous magnetization but not ferroelectricity as the centrosymmetric nature does not allow a spontaneous polarization (Figure 1-5, section 1.2.4). This encompasses the ions Dy, Tb, Nd, Pr and La.

The bulk hexagonal systems, which include Sc, In, Lu, Yb, Ho, Er and Y present a non-centrosymmetric perovskite and can exhibit 4 long range orders; Ferroelectric polarization up to $T_C$ = 570 - 900 K (Venevstev, 1994) (Fiebig, 2005); A-type antiferromagnetism from the antiparallel alignment of Mn$^{3+}$ up to $T_N$ = 70-130 K (Fiebig, 2005) and up to 2 rare earth magnetic orders ~5 K (Sugie, 2002).

Interestingly DyMnO$_3$ is stable in both orthorhombic and hexagonal forms, the latter exhibiting AFM $T_N$ ~ 100 K and FE $T_C$ ~ 900 K. YMnO$_3$ is also anomalous as its hexagonal structure forms a cubic perovskite unit cell, but does not exhibit ferroelectricity like others. Instead it is observed to be antiferromagnetic from indirect exchange between the Mn ions through the O ions at low temperatures (termed super exchange) < 80 K (Huang, 1997), and ferroelectric as a consequence of the Y site fivefold coordination and triangular layered MnO$_5$ tilting (Longkai, 2004). This results in frustrated Mn - O - Mn and Mn – O – O - Mn in plane and interplane exchange paths respectively (Fiebig, 2005) subsequently providing strong coupling between the magnetic, electric and elastic properties (Fiebig, 2005).

The structural phase transition from paraelectric to this frustrated pseudo-ferroelectric state is at a temperature termed $T_{pt}$ (related to the polyhedral tilting) which exists at a higher temperature ($T_{pt}$ = 1207 K) than another ferroelectric transition to the typical B

ion - O ion displacement in the perovskite, without a change of symmetry, termed $T_{FE}$ (Lonkai, 2004). The linear ME effect in this $P6_3Cm$ space group is forbidden by symmetry (O'Dell, 1970) thus higher order effects occur from electric and magnetic domain coupling (Fiebig, 2002). $YMnO_3$ can only be synthesized in the bulk by using extreme pressure (>6 GPa) (Fiebig, 2005).

### 1.11.4-3   Composite Multiferroics

Single-phase materials exhibiting strong magnetoelectric effects are limited (Hill, 2000(a)) but two-phase composites of ferroelectric and magnetic materials became apparent when van Suchtelen combined piezomagnetic and piezeoelectric phases in 1972 (van Suchtelen, 1972), an idea which lead to Boomgaard (1974) preparing $Ni(Co,Mn)Fe_2O_4$ and $BaTiO_3$ composites.   By coupling these highly magnetostrictive and piezoelectric materials respectively, through uniaxial cooling, mechanical stress is transmitted between grains (Boomgaard, 1978) (Hanumaiah, 1994) (Figure 1-37(a)).

The physical properties of a material formed from two or more constituent compounds are determined by these constituents and the interactions between them. These can be classed in to 'Sum', 'Scaling' and 'Product' properties (Ryu, 2002).

Sum and scaling result from a sum and averaging effect of the constituents properties, however product properties result from the interaction of the two constituents to present novel effects giving a two-phase system a synergetic approach, allowing the ME effect to be generated from two constituents that do not exhibit any magnetoelectricity alone (Fiebig, 2005).

A crude display of the ME effect from the bonding of a piezomagnetic and piezoelectric material is given in Equation 1-46.

$$ME\ Effect = \frac{electrical}{mechanical} \times \frac{mechanical}{magnetic}$$

Equation 1-46 (Fiebig, 2005).

The ME interaction between two phases however is much more complex than defined in Equation 1-46. In the $Ni(Co,Mn)Fe_2O_4$ / $BaTiO_3$ composite, the mechanical stresses being transversed between grains was hugely lossy, but even in early experiments, Boomgard et al achieved an ME response over an order of magnitude larger than single-phase compounds with a ME voltage coefficient ($dE/dH$) = 80 mV cm$^{-1}$ Oe$^{-1}$ (Hanumaiah, 1994) and ME coefficient $\alpha_{ij}$ = 722 x10$^{-10}$ s m$^{-1}$ (Ryu, 2002).

To reduce the loss, laminar instead of particulate composites were successfully implemented (Fiebig, 2005) of which there are 2 classes to consider; horizontal multilayers and nanostructures.

### 1.1.1-1.3   Horizontal Multilayer Composite Magnetoelectrics

Research in this area is currently focussed on thin film technology, with the most popular system in literature for thin film multilayers being $BaTiO_3 - CoFe_2O_4$. However magnetoelectric measurements in these epitaxial systems are not forthcoming (Eerenstein, 2006) due to bonding of the layers becomes a limiting factor.

Thin films can be matched much more precisely with fine tuning of surface roughness with pulsed laser deposition, or molecular beam epitaxy for example, but fixation to a substrate forces elastic interactions to become negligible due the clamping effect of the substrate (Zheng, 2004) producing ME voltage coeffiecients of only a few tens of mV cm$^{-1}$ Oe$^{-1}$ (Martin, 2008). This is a prominent reason for research into nanostructured composites.

Thick film laminate layers are dominated by PZT – Terfenol-D (Spaldin, 2005) (Ryu, 2001). PZT has already been discussed in section 1.4.8-3 as a popular commercial piezoelectric. Terfenol D is an alloy of Terbium and Iron (Fe) (*TerFe*) developed by the Naval Ordnance Laboratory (*NOL)*, United States, in the 1980's. It also contains dysprosium (-*D*) with formula $Tb_xDy_{1-x}Fe_2$ where x ~ 0.3. It has the highest magnetostrictive properties of any alloy (Etrema, 2003).

Ryu et al (2001) reported the ME effect in Terfenol-D - PZT - Terfenol-D thick film sandwich laminates by bonding with silver epoxy and applying a 0.45 T bias field to allow linearity by removing the hysteresis component (Ryu, 2002) achieving ME voltage coefficient of 5900 mV cm$^{-1}$ Oe$^{-1}$. The same group also published ME voltage coefficients of 10300 mV cm$^{-1}$ Oe$^{-1}$, replacing PZT for single crystal <001> orientated piezoelectric PMN-PT (lead manganese niobate – lead titante) under a 0.4 T bias (Ryu, 2002).

There are three major hurdles to overcome in multilayers, namely geometric ratios, resonance effects and layer bonding. In composite samples, the magnetoelectric voltage coefficient increases with magnetostrictive to piezoelectric thickness ratio ($t_m$ / $t_p$) (Fiebig, 2005) as the compressive stress is increased in the piezoelectric with reduced thickness. Contrary to this, output voltage decreases.

Resonance matching of the two layers also becomes important to tune the optimum ME coupling between the two layers, and importantly to remove noise and prevent loss (Ryu, 2002).

Bonding in thick film devices needs to resist environments in which they would operate. In ambient, neutral environments, this is relatively easy, but extreme environments could be challenging.

### 1.1.1-1.4   Nanostructured Composite Magnetoelectrics

To remove the clamping effect from the substrate in classical thin film multilayering, Zheng et al (2004) grew nanostructured hexagonal pillars of magnetostrictive $CoFe_2O_4$ (CFO) in a matrix of piezoelectric $BaTiO_3$ (BTO). Because of the immiscibility of the two phases, CFO is a spinel structure and BTO forms a perovskite, the phases spontaneously separate to form pillars in the order of tens of nanometres (Martin, 2008) which allows high interface to volume ratios, important for coupling the two materials through strain. This also allows epitaxial matching in 3 directions and reduced substrate imposed mechanical clamping as the layer interfaces are now vertical. This is presented schematically in Figure 1-40.

Zavaliche (2005) et al have subsequently shown ME voltage coefficients $dE/dH =$ 100 V cm$^{-1}$ Oe$^{-1}$ at room temperature (Martin, 2008) for CFO pillars in a $BiFeO_3$ (BFO) matrix, using the ME properties of BFO to create the bias.
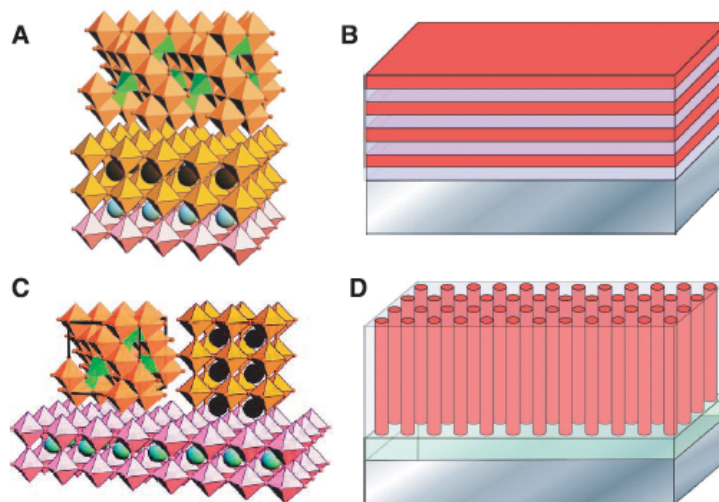


**Figure 1-40 a) Mulitlayer heterostructured spinel (top)and perovskite (middle) on a perovskite substrate (bottom) b) A schematic of thin film multilayers on a substrate  c) Epitaxial nanostructures of a spinel and a perovskite on a perovskite substrate d) Schematic of a self-assembled nanostructure on a thin film and substrate. (Reprinted by permission from AAAS; Science. (Zheng, 2004).**

1.11.4-4   Bismuth Based Perovskites

The first known and perhaps most studied multiferroics lie within the perovskite umbrella, with the general formula $ABO_3$. With substitution of both A and B site ions cultivating an extensive list of systems (Fiebig, 2005).

Perovskites are popular as the non-centrosymmetric nature of the central B ion allows spontaneous polarization, a necessity for ferroelectricity that has already been seen in the rare earth manganites (1.11.4-2).

There are two Bi perovskite structured compounds that represent major landmarks in ME research; the first being $BiMnO_3$.

$BiMnO_3$ has been synthesized in the bulk, as theory suggested it was likely to be both ferromagnetic and ferroelectric due to its simple B site cation perovskite arrangement and its ionic radii (1.24 Å) (Kimura, 2003) being similar to La (1.22 Å) in the RE manganite (Prellier, 2005). Experimentally, $BiMnO_3$ displays ferromagnetism rather than AFM like the RE Manganites, with a $T_C$ = 105 K and ferroelectric $T_C$ = 750 K (Kimura, 2003) below which presents a polar space group C2 (ISS# 5) (Atou, 1999). Substitution of the Bi ion with Sr reduces electrical resistance, but quickly eradicates ferromagnetism. This indicates that double exchange Mn − O − Mn interactions through the oxygen does not occur in this system, but instead FM occurs via superexchange (SE) interactions.  Every trivalent $Mn^{3+}$ cation is observed to reveal Jahn-Teller distortion placing the Mn − O − Mn bonds close to 180 °; For every Mn ion there are four 90 ° ferromagnetically favourable SE angles, and two 180 ° antiferromagnetically favourable SE angles. As two thirds of the SE interactions favour FM, they overcome the AFM interactions (Atou, 1999).

Bi-O offer strong covalent bonding causing the off-centred displacement (Prellier, 2005) in the perovskite, alluding to strong coupling between electric and magnetic ferroics through the oxygen structure, which is observed from an anomaly in the dielectric constant and specific heat at the onset of the ferromagnetism (Kimura, 2003).

Like $YMnO_3$, $BiMnO_3$ can only be synthesized in the bulk at high pressure (6 GPa, (Atou, 1999)), but can be readily deposited onto a substrate as thin films by nebulized spray pyrolosis (Moreira dos Santos, 2002).

Substitutions on the B site cation aimed at trying to induce spontaneous magnetization using iron instead of manganese have also been researched. This led to the development of $BiFeO_3$, which is discussed next.

1.11.4-5   Bismuth Ferrite

Bismuth ferrite has undoubtedly been studied more extensively than any other magnetoelectric multiferroic (Figure 1-41), being hailed the most promising candidate for multiferroic devices in a single phase (Shvartsman, 2007) due to its multiferroic nature above room temperature and simple structure. This opens the door to devices and applications without the need for sub-ambient temperatures.
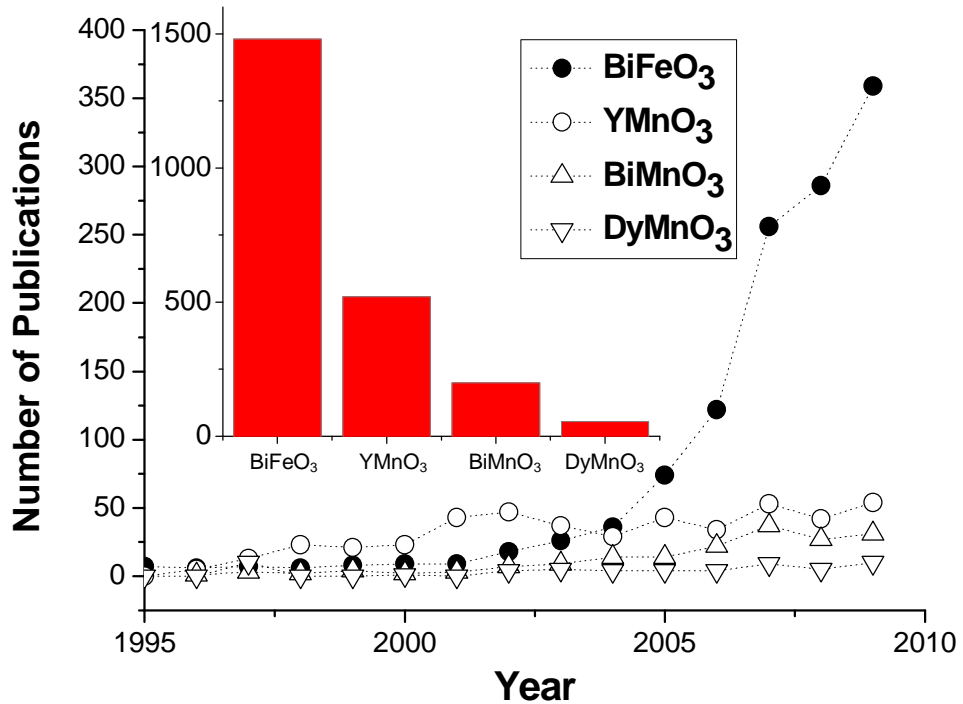


**Figure 1-41 Plot: Graphic illustration of the number of publications per year of different magnetoelectric compounds 1995-2009. Inset: Total number of publications since 1930 (according to http://wok.mimas.ac.uk/ under "*compound* AND multiferroic* OR magnetoelectric*" search parameters.)**

1.11.4-6   Bulk Polycrystalline $BiFeO_3$

Bismuth ferrite was first reported in 1957 (Royen, 1957), exhibiting antiferromagnetism in a cubic perovskite structure with a rhombohedral distortion (Zaslavskii, 1960) (Tomashpol'skii 1964).

Over the decades, there has been extensive research from both ferroelectric and magnetic based communities. This is summarized in Table 1-6, and shows that whilst it has never been disputed that bismuth ferrite exhibits a rhombohedral distorted perovskite, the space group has been changed over the years, with the ensuing advancement in diffraction techniques, but is now accepted as R3c (ISS# 161).

**Table 1-6 Summary of BiFeO$_3$ research over 5 decades**

| Reference | Perovskite Distortion | Space Group | Ferroelectric | Oxygen Distortion | Magnetic | Magnetic Structure | FE T$_C$ | AFM T$_N$ | ME Coupling |
|---|---|---|---|---|---|---|---|---|---|
| Zaslavskii (1960) | Rhombohedral | R-3m | | | AFM | | | | |
| Fedulov (1961) | Rhombohedral | | ✔ | | AFM | | 850 °C | | |
| Smolenskii (1963) | Rhombohedral | | ✔ | | AFM | | | 370 °C | |
| Tomashpol'skii (1964) | Rhombohedral | R3m | ✔ | | | | | | |
| Kiselev (1964) | Rhombohedral | R3m | ✔ | | AFM | G-Type | | 380 °C | |
| Roginskaya (1966) | Rhombohedral | | ✔ | | AFM | | 830 °C | 370 °C | |
| Michel (1969) | Rhombohedral | R3c | ✔ | ✔ | AFM | G-Type | 830 °C | | |
| Tutov (1970) | Rhombohedral | R3c | ✔ | ✔ | AFM | | ~900 °C | 372 °C | |
| Fischer (1980) | Rhombohedral | R3c | ✔ | ✔ | AFM | G-Type | 830 °C | 370 °C | |
| Sosnowska (1982) | Rhombohedral | R3c | | | AFM | IC* G-Type | 830 °C | 370 °C | |
| Kubel (1990) | Rhombohedral | R3c | ✔ | ✔ | AFM | | 830 °C | 370 °C | |
| Schmid (1994a) | | | ✔ | | AFM | | | | ✔ |
| Ederer (2005) | Rhombohedral | R3c | ✔ | ✔ | AFM | IC* G-Type | 850 °C | 370 °C | ✔ |

*IC = Incommensurate

X-ray and neutron diffraction have been used throughout the literature on bulk polycrystalline and single crystal bismuth ferrite (BFO) to construct its rhombohedral R3c structure (Michel, 1969) and characterize its ferroelectric and magnetic classifications. Ferroelectricity and antiferroelectricity was accepted to exist by symmetry (Michel, 1969) (Moreau, 1971) until it was proven by hysteresis (Teague, 1970) and polarized light microscopy (Tabares-Munõz, 1985) to be solely ferroelectric, with a spontaneous polarization along the [111]$_{pseudo\ cubic}$ / [001]$_{hexagonal}$ of $P_S \sim 6.1$ μC cm$^{-2}$ in bulk polycrystalline and $P_S \sim 80$ μC cm$^{-2}$ (Shvartsman, 2007) with piezoelectric strain coefficient $d_{33} = 60$ pm V$^{-1}$ (Shvartsman, 2007) for a single crystal. An octahedral oxygen distortion was observed with a tilt (a$^-$ a$^-$ a$^-$), perceived from ensuing diffraction reflections, rotating ± 13.8 ° around the three fold axis, between − 269 °C (4 K) and the ferroelectric curie point $T_C = 830$ °C (Kubel, 1990).

Magnetic characterization was also completed by neutron diffraction (Michel ,1969) (Fischer, 1980). In the first approximation, it can be described by local magnetic ordering as collinear G-type AFM with each Fe$^{3+}$ surround by six nearest Fe nearest neighbours with antiparallel spin (Figure 1-33) (Kiselev, 1964) (Michel, 1969) (Fischer, 1980) below a Néel temperature accepted as $T_N = 370$ °C (Catalan, 2009) from neutron diffraction and Mössbauer techniques (Fischer, 1980).

This antiparallel alignment is inconsistent however. The non-centrosymmetric distortion of the perovskite that dictates ferroelectricity in the compound also causes anisotropy in the magnetic superexchange interactions between the Fe$^{3+}$ ions (Lebeugle, 2008), termed Dzyaloshinskii-Moriya (DM) interactions (Moriya, 1960)(1.8.4), resulting in a weak canting of the AFM moments with many groups having reported 'weak ferromagnetism' (Smolenskii, 1963) (Michel, 1969) a consequence developing a net magnetization.

Sosnowska et al (1982) observed a long range order of the canted AFM spins from splitting of the AFM peak using high resolution neutron diffraction, alluding to the magnetic moments exhibiting incommensurate (IC) ordering in the bulk with a period of 620 (±20) Å (Sosnowska, 1982). This incommensurate ordering is described as chiral, cycloidal or helical magnetic ordering (Sosnoska, 1997) (Sosnowska, 2002) (Przenioslo, 2006(a)) and acts to cancel the 'weak ferromagnetism' as it is averaged out to zero by a full rotation period (Figure 1-42). The chiral is observed from 5 K to $T_N$ (640 K / 370 °C ) (Przenioslo, 2006(a)). The determination of the modulation model remains in discussion, as the observed splitting in neutron diffraction can be attributed to circular cycloid (described), ellipsoidal cycloid and spin density wave models (Przenioslo, 2006(a)) (Lebeugle, 2008). For clarity it is simply termed incommensurate modulation.
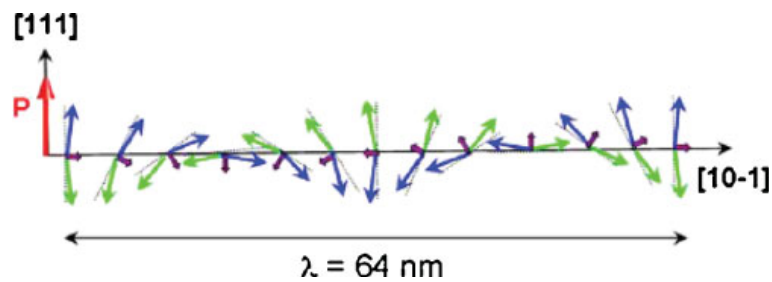
**Figure 1-42 Schematic representation of the spin cycloid. Canted antiferromagnetic spins (blue and green) give rise to a net magnetic moment (purple) that is averaged out to zero due to the incommensurate modulation. The spins are contained within the plane defined by the polarization vector (red) and the cycloidal propagation vector (black) (Lebeugle, 2008).**

A change of the periodicity of the IC structure is observed when doping on the A or B site with metal ions such as lanthanum or manganese respectively (Sosnowska, 2002) (Przenioslo, 2006(b)). The addition of Mn shows an increase of the periodicity until in $Bi(Mn_xFe_{1-x})O$ restoration of the collinear structure occurs for x > 0.2 (Sosnowska, 2002).

Despite the ferroelectric structure being intimately linked to the antiferromagnetism, the incommensurate order prohibits the linear magnetoelectric effect because of symmetry (Kubel, 1990) (Przenioslo, 2006(b)), but does allow higher order effects (quadratic), with the underlying mechanism based on complex Dzyaloshinskii-Moriya (DM) interactions.

Applying a magnetic field of a few Tesla witnesses a relationship with polarization such that $P \propto H^2$ (Zvezdin, 2006). Above a critical field, typically ~20 T (200,000 Oe) (Zvezdin, 2006) spin flop occurs (a rotation of the magnetization direction by 90° (Morrish, 1965)) (Lebeugle, 2008) and $P$ responds to $H$ linearly, with a jump increase in magnetization (Zvezdin, 2006) alluding to a breakdown of the IC modulation, allowing the linear ME effect and recovering the canted state induced magnetization.

There have been no published reports of ME effects in bulk samples of BFO, mainly due to the averaging out of some effects due to the polycrystalline nature (Catalan, 2009) and the fact it is relatively difficult to synthesize BFO without forming second, non-perovskite, phases (namely $Bi_2Fe_4O_9$) that nucleate at grain boundaries (Catalan, 2009). BFO is also readily decomposed at high temperatures ca. 1000 °C and under high electric fields >200 kV cm$^{-1}$ (Catalan, 2009).

Observations of the coupling effects between the ferroelectric and antiferromagnetic ferroics is communicated in literature however for thin films, where the complexity of the IC order is relinquished by epitaxial strain (Catalan, 2009.)

**Table 1-7 Summary of properties for bismuth ferrite in the hexagonal setting**

| Rhombohedral Space Group | Ferroelectric Curie Point ($T_C$) | Antiferromagnetic Néel Temperature ($T_N$) | Ambient lattice parameter (a) | Ambient lattice parameter (c) | AFM Type |
|---|---|---|---|---|---|
| R3c | 830 °C | 352 °C | 5.579 Å | 13.868 Å | IC* period 620 Å G-type |

*Incommensurate

### 1.11.4-7 Thin Film $BiFeO_3$

Freestanding films were prepared in the mid 1980's by H. Schmid that are akin to single crystals, such that at ambient temperature their crystal structure is rhombohedral (Catalan, 2009).

In 2003, a paper focussing on the growth of BFO on heteroepitaxially constrained thin films on $SrTiO_3$ substrates by pulsed laser deposition (Wang, 2003), stimulated discussion (Eerenstein, 2005) (Wang, 2005) and research as it presented enhancements of polarization (up to ~ 90 $\mu C$ $cm^{-2}$ (Wang, 2003)), piezoelectric strain coefficient ($d_{33}$= 70 pm $V^{-1}$ (Wang, 2003)), magnetoelectric effect (Zhao, 2006) ($dE/dH$= 3 V/cm Oe (Wang, 2003)), thickness dependent magnetization and an observation of a monoclinic (Li, 2004) or tetragonal (Qi, 2005) structure, rather than rhombohedral as seen in bulk materials, due to the epitaxial strain from the cubic $SrTiO_3$ substrate. Rhombohedrally structured films can be formed with growth from a (111) orientated $SrTiO_3$ substrate (Li, 2004).

The thin films (< 600 nm) cannot sustain the incommensurate modulation observed in the bulk, so exhibits 'collinear' G-type AFM throughout (Zhao, 2006), but with weak ferromagnetism from the canted alignments that are no longer averaged out by the period contributing to an increased magnetization (0.5 $\mu_B$ per unit cell (Ramesh, 2007) / 70 emu $cm^{-3}$ (Wang, 2003)) compared to the bulk (~8 emu $cm^{-3}$ (Martin, 2007)).

BFO is also observed to show relatively small sensitivity of polarization to epitaxial strain confirmed by increasing film thickness, thereby reducing epitaxial strain effects, leaving the polarization constant (Kim, 2008). This reduced sensitivity stems from the piezoelectric constant of BFO (60 pm $V^{-1}$), which links stress to polarization, being substantially smaller compared to other perovskite ferroelectrics (100-1000 pm $V^{-1}$) (Catalan, 2009).

A summary of the magnetoelectrics discussed is given in Table 1-8.

**Table 1-8 Summary of magnetoelectric compounds and composites in section 1.11.4.**

| Composition | Ferroelectric $T_C$ (°C) | Ferromagnetic $T_C$ (°C) | Anti-Ferromagnetic $T_N$ (°C) | ME Voltage Coefficient (mV cm$^{-1}$ Oe$^{-1}$) |
|---|---|---|---|---|
| $Cr_2O_3$ | n/a | - | 37 [1] | 20 [2] |
| $YMnO_3$ | 647 [3] | - 228 [3] | -198 [3] | 0.000002059 [4] |
| $CoFe_2O_4$ + $BaTiO_3$ Intergranular | 130 [5] | | - | 130 [2] |
| $CoFe_2O_4$ + $BaTiO_3$ Laminar Thin Film Multilayer | 130 [5] | - | - | < 50 [6] |
| $BiFeO_3$ + $CoFe_2O_4$ Nanostructure | 1100 [7] | - | - | 100,000 [8] |
| Terfenol-D + Polycrystalline PZT | 220 - 490 [9] | 380 [10] | - | 5,900 [2] |
| Terfenol-D + Single Crystal PMN-PT | - | 380 [10] | - | 10,300 [2] |
| $BiMnO_3$ | 177 [11] | -168 [11] | - | unknown |
| $BiFeO_3$ Thin Film | 850 [12] | - | 650 [7] | 3,000 [7] |

[1](Kumar, 2007) [2](Ryu, 2002) [3](van Aken, 2001) [4](Sekher, 2006) [5](Moulson, 2003) [6](Martin, 2008) [7](Wang, 2003) [8](Zavaliche, 2005) [9](Jaffe, 1954) [10](Etrema, 2003) [11](Kimura, 2003) [12](Kubel, 1990)

## 1.12 BISMUTH FERRITE LEAD TITANATE

### 1.12.1 Nomenclature

To remove the need to express bismuth ferrite lead titanate compositions by lengthy formula descriptions a simplified nomenclature will be used. Bismuth ferrite lead titanate, $xBiFeO_3 - (1-x)PbTiO_3$, may be expressed as the abbreviated BFPT followed by 4 numbers which are allied to the composition. The first two numbers relate to the percentage content of bismuth ferrite, and the last two, lead titanate content. For example BFPT 7030, or 7030 relates to the composition $0.7BiFeO_3 - 0.3PbTiO_3$. The nomenclature x = 0.7 would also describe the same composition.

### 1.12.2 Structure

Rhombohedral bismuth ferrite (space group R3c) (Michel, 1969) forms a solid solution with tetragonal lead titanate (space group P4mm) (Shirane, 1956) to form $xBiFeO_3 - (1-x)PbTiO_3$ (Venevstev, 1960) (or BFPT), which as a polycrystalline ceramic exhibits a morphotropic phase boundary (MPB) (an area of mixed R3c and P4mm phases) at ca. x = 0.7 (Fedulov, 1964) where ferroelectric $T_C$ = 908 K / 635 °C (Sai Sunder, 1995).

As is observed in lead zirconate titanate (PZT), the morphotropic phase boundary in BFPT displays an increase in electrical permittivity and piezoelectric activity (Comyn, 2005). This is attributed to the relatively large internal lattice strain c/a ratio = 1.187 for x = 0.7, which when compared to barium titanate (c/a = 1.01 (Yagnik, 1971)), PZT (c/a=1.02 (Jaffe, 1971)) and the lead titanate end member (c/a = 1.063 (Sai Sunder, 1995)) as well as compositions with increasing $BiFeO_3$ content (Figure 1-42, 1-43) it is easy to see how this could have effect on the physical properties.

In fact this distortion, plus analysis of the work by Smith (1968) presenting the molar volume of the tetragonal and rhombohedral forms as being significantly different, 39.4 and 37.5 $cm^3$ respectively (a difference of ca. 5%); has such an effect on the system that much of the literature reports difficulty in producing dense bulk ceramics. This is due to the huge anisostropic strain induced lattice distortion and mismatch, causing the material to intergranularly fracture upon cooling from the sinter (Fedulov, 1964) (Sai Sunder, 1995).

The width and position of the MPB has been a point of debate by researchers since the first publication of the phase diagram by Fedulov, 1964 (Figure 1-45). The controversy stems from the lack of information on the form of the ceramics being investigated as various levels of internal stress feature in ceramics through differing
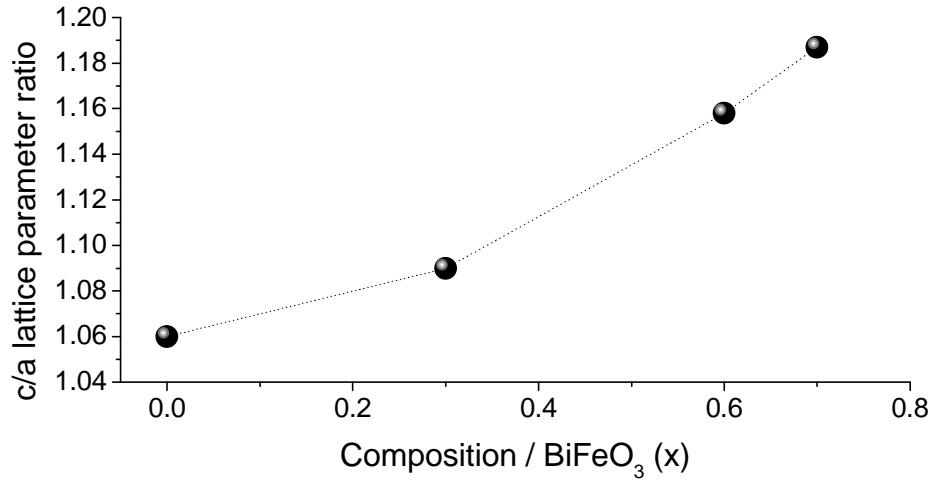
**Figure 1-43 Plot of c/a lattice parameter ratios with increased additions of bismuth ferrite to the solid solution (values taken from Sai Sunder, 1995).**
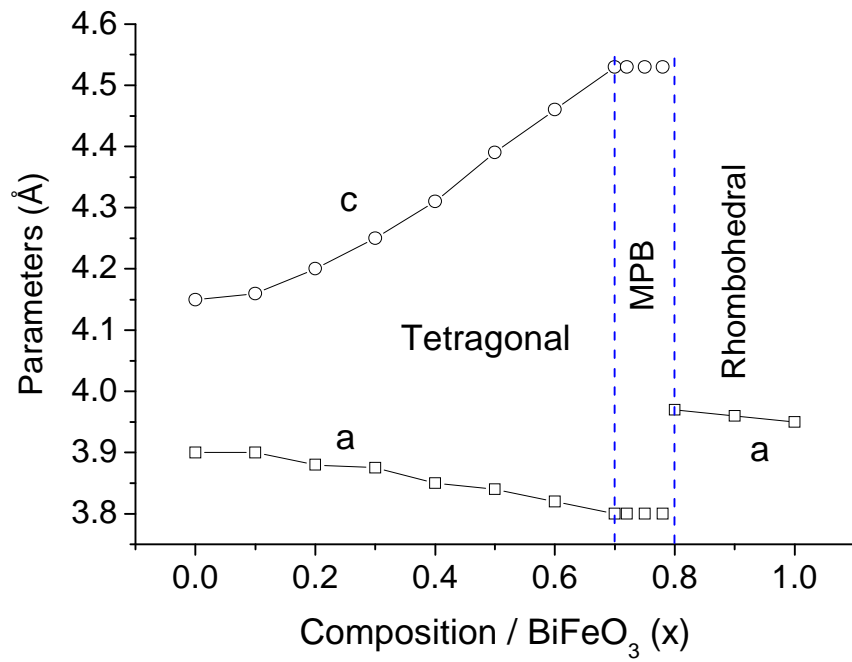


**Figure 1-44 Lattice parameters in the $BiFeO_3$ – $PbTiO_3$ solid solution (values taken from Smith, 1968).**
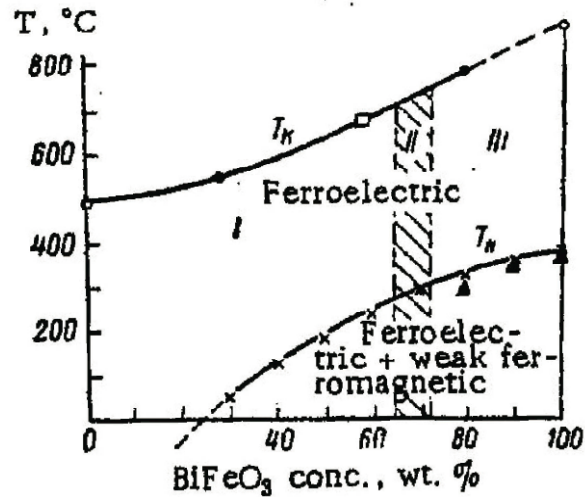
**Figure 1-45 Ferroelectric and magnetic phase diagram for the BiFeO₃ – PbTiO₃ system, by Fedulov, 1964. Where I) is the tetragonal region, II) tetragonal + rhombohedral region and III) rhombohedral region (Fedulov, 1964).**

process routes, which techniques like X-ray diffraction would struggle to present reproducible results.

The range of techniques that have been used to characterise various other properties and identify their respective transitions have also had contrasting values.

For example, the phase diagram by Fedulov is constructed using experimental data from X-ray diffraction and Faraday method magnetometry (Fedulov, 1964) where as work by Sai Sunder (1995), Woodward et al (2003) and Bhattacharjee (2007) was undertaken again using XRD but on a range of bulk and crushed bulk (to powder) ceramics. The most recent phase diagram construction by Zhu (2008) contributes to the controversy by using solely XRD on sintered bulk samples and SQUID magnetometry.

The results of the crystal structure and MPB as a function of composition is summarised in Table 1-9.

Criticisms made on the formation of the phase diagrams referenced in Table 1-9 centre around the use of powder XRD for the study of the systems crystallography (Arnold, 2009) (Lightfoot, 2010). X-rays, and even synchrotron radiation, suffer from the proportionate relationship between scattering power and atomic number (Z) (see Section 2.4.1-2 and 2.5.1-3) preventing the characterisation of the oxygen tilt within the BFPT system. The oxygen octahedra are well established at playing a vital role in the structural transitions and magnetic properties of bismuth ferrite and other bismuth perovskites, like BiMnO₃ (section 1.11.4-4), so it is widely accepted that only neutron diffraction can categorically map the structure (Lightfoot, 2010).

**Table 1-9 Summary of publications on (x)BiFeO$_3$ – (1-x)PbTiO$_3$ reporting compositionally dependent phase distribution and techniques used.**

| Author | Sample Form | Crystallographic Technique | Magnetic Technique | Width of MPB xBiFeO$_3$ – (1-x)PbTiO$_3$ | 7030 T$_C$ (°C) | 7030 T$_N$ (°C) |
|---|---|---|---|---|---|---|
| Fedulov (1964) | Not described | Powder XRD | Faraday Method | 0.65 < x < 0.72 | ~ 700 | ~280 |
| Sai Sunder (1995) | Crushed Pellets | Powder XRD | - | 0.7 < x < 0.8 | ~630 | - |
| Woodward (2003) | Annealed Crushed Pellets | Powder XRD | - | 0.6 < x < 0.7 | 632 | - |
| Bhattacharjee (2007) | Not described | Powder XRD | - | 0.69 < x < 0.73 | - | - |
| Zhu (2008) | Bulk pellets | Powder XRD | SQUID | 0.69 < x < 0.83 | - | ~300 and ~250 |

1.12.2-1  Mixed Phase Region

The definition of a morphotropic boundary is given in section 1.4.9 and defines a compositionally independent phase boundary. This term is widely used within the literature to define the much wider, certainly composition independent region in the BFPT system, where the BiFeO$_3$ rich rhombohedral phase is first found to coexist with the tetragonal phase until the rhombohedral phase is diluted out.

Throughout this work there are instances which need to separate the original definition of an MPB from the region that describes phase coexistence. For this the MPB is used to define the composition at which the first instance of tetragonal phase is found within the rhombohedral. For example in Table 1-9, for Fedulov, 1964, this would be x = 0.72.

A second term, mixed phase region (MPR), will be subsequently used to describe the composition range within both phases occur simultaneously. Again for the example of Fedulov in Table 1-9, this would be between x = 0.65 and 0.72.

## 1.12.3 Ferroelectric Properties

Many works that have published data on the ferroelectric properties of the BFPT system are incomplete or do not span the entire compositional range (Smith, 1968), (Comyn, 2004), (Zhu, 2006), (Zuo, 2009). Smith et al (1968) for example completed dielectric constant and dissipation measurements on only 4 compositions, x = 0.2, 0.4, 0.6 and 0.8.

However work completed by Comyn and Stevenson (2005) during Stevenson's masters dissertation, produced the first measurements across the entire compositional range, from x = 0.1 to 0.9 in 0.1 steps (plus 0.65, 0.75), of polarization, $d_{33}$ and strain with applied electric field to dense bulk sintered ceramics (summarised in Comyn, 2005).

Polarization experiments carried out using charge measurements from the setup described by Comyn (2005) on bulk polycrystalline pellets show that BFPT 7030 allows significantly more polarization at equivalent applied fields, up to nearly 6 times at 10 MVm$^{-1}$ compared to 6040 (Figure 1-45 and 1-46), however no compositions loops show coercive field or saturation, which is regarded as typical ferroelectric behaviour.

1.12.3-1   Polarization Measurements
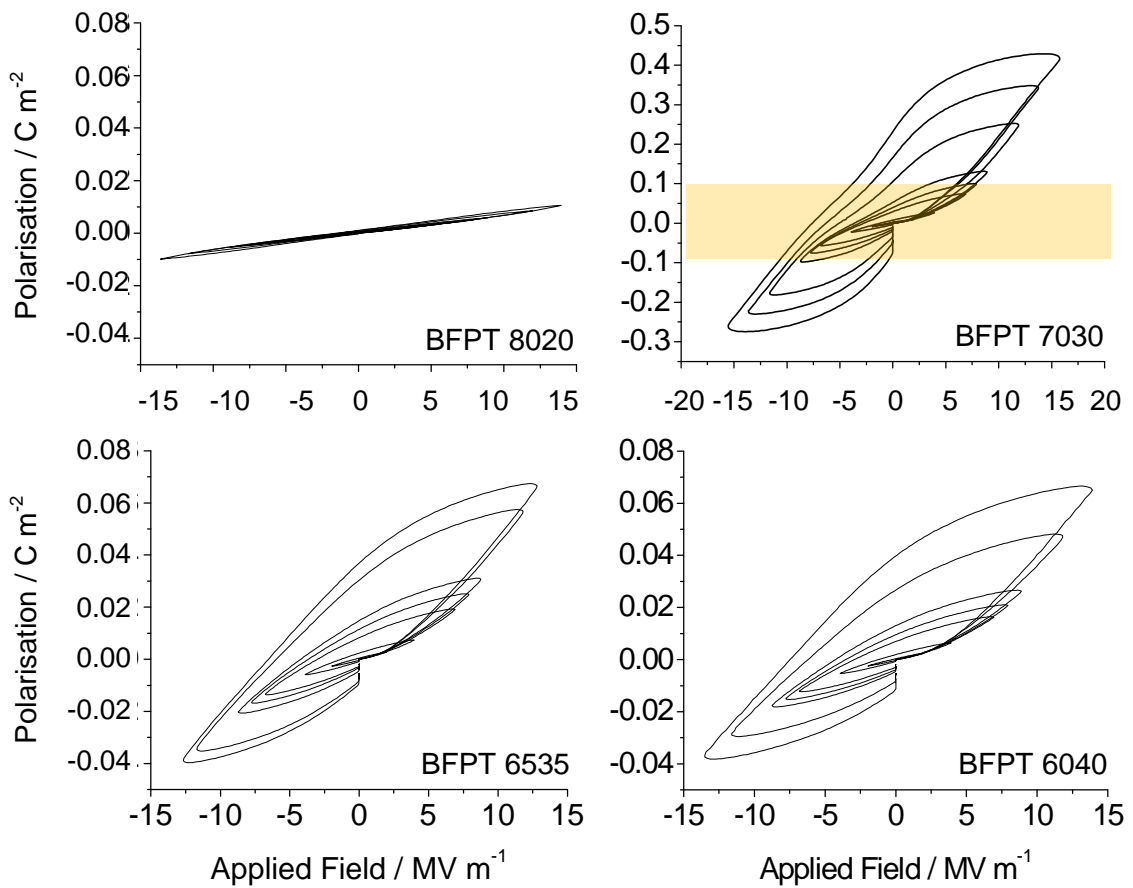


**Figure 1-46 Polarization – Field data for compositions BFPT 8020 – 6535 (x=0.8 – 0.65) where the yellow section in 7030 indicates the relative scale of polarization compared**
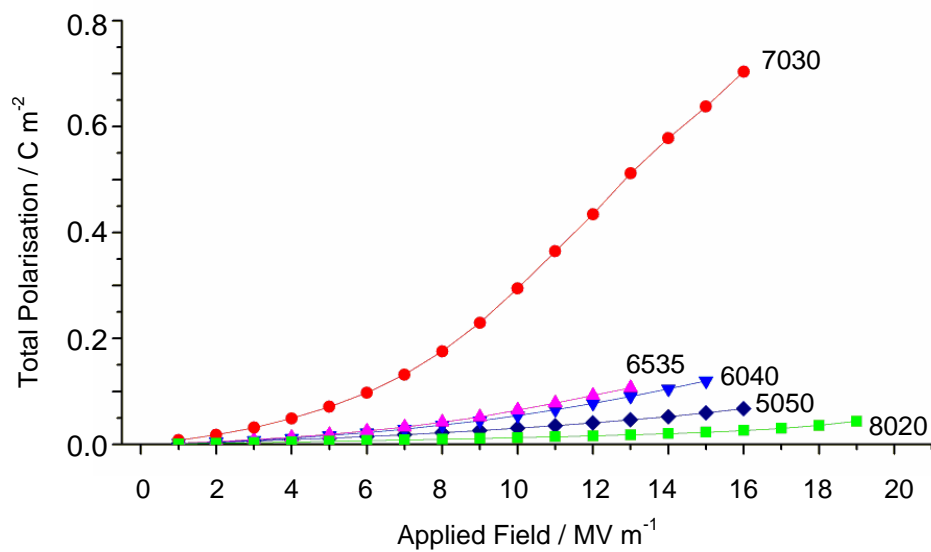


**Figure 1-47 Total (peak to peak) polarization as a function of applied electric field for compositions x= 0.5, 0.6, 0.65, 0.7 and 0.8.**

1.12.3-2  Piezoelectricity

Strain-Field (Figure 1-48) and $d_{33}$ measurements (calculated from the slope at zero field) on the same bulk samples show similar maxima in properties for the BFPT 7030 composition.

The strain field measurements indicate more obvious ferroelectric and piezoelectric behaviour than the polarization measurements, where at low fields no strain develops until application of high enough electric field, generates a piezoelectric strain response in both positive and negative regimes and non-zero gradient at zero field (Comyn, 2005).

It is worthy to note that the onset of the piezoelectric response for each composition changes radically, measured by the onset of strain and piezoelectric response $d_{33}$. Comparing the data in Table 1-10 however shows that the strain is onset by electrostriction before the piezoelectric effect. This is particularly pertinent in 6535. A maximum in high field $d_{33}$ is seen in BFPT 7030 of 160 pm V$^{-1}$.
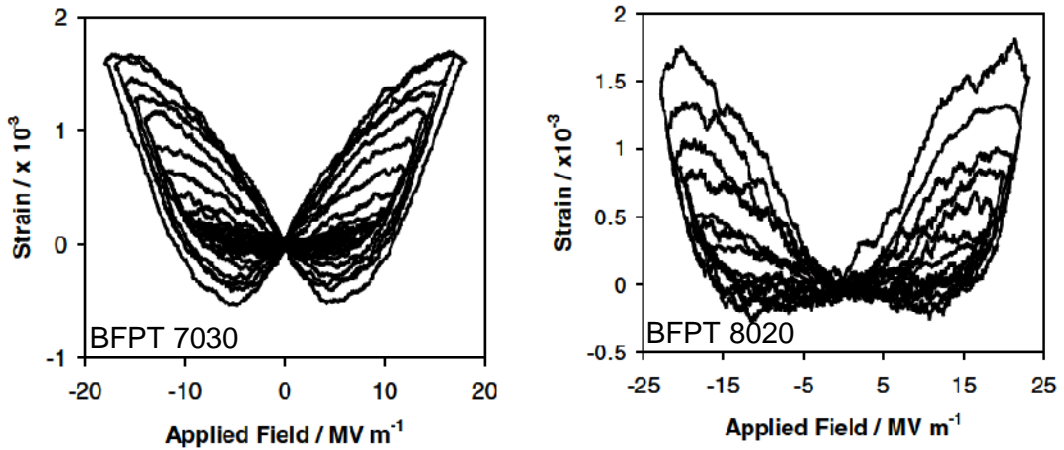


**Figure 1-48 Strain – Field data for compositions BFPT 7030 & 8020 (x = 0.7 & 0.8) (Comyn, 2005).**

**Table 1-10 Onset fields for strain and d$_{33}$ in the (x)BiFeO$_3$-(1-x)PbTiO$_3$ compositions x=0.6, 0.65, 0.7 and 0.8.**

| Composition | Onset Field ($d_{33}$) / MV m$^{-1}$ | Onset Field (Strain) / MV m$^{-1}$ |
|---|---|---|
| BFPT 6040 | 11 | 10 |
| BFPT 6535 | 10 | 7 |
| BFPT 7030 | 9 | 8 |
| BFPT 8020 | 20 | 17 |

## 1.12.4 Magnetic Properties

Bismuth ferrite lead titanate is reported to exhibit G-type (Comyn, 2009) antiferromagnetic order analogous to bismuth ferrite, and indeed present due to the arrangement of the iron ions in the end member compound (Fedulov, 1964).

The Néel temperature of BFPT is composition dependent, as the dilution of the antiferromagnetic $BiFeO_3$ phase increases with concentrations of lead titanate (Zhu, 2008). This is again subject to differing reports as the magnetic behaviour is linked to phase contributions and methods of measuring the magnetic order which as summarised in Table 1-9 is inconclusive. Neutron diffraction however once again is widely accepted to be the only form of characterisation that can classify a magnetic structure and identify its class. For example Superconducting Quantum Interference Devices (SQUID) and Vibrating Sample Magnetometry (VSM) can readily characterise the magnetic group, either ferro- antiferro- or para- magnetic, but solely neutron diffraction, through the interaction of the neutrons with the magnetic spins of the ions can define A, C or G type AFM.

## 1.12.5 Non Bulk Forms

As well as the bulk, monolithic sintered ceramics which is the focus of this work, bismuth ferrite lead titanate has been fabricated in numerous other forms including single crystals, thin and thick films. These are discussed next.

### 1.12.5-1  Single Crystal

Single crystal synthesis of BFPT has been carried out and published in several papers and thesis by Burnett et al (2005, 2006, 2008) using the flux growth method. In this form it has been difficult to grow crystals above >5 mm across or to complete comprehensive electrical and magnetic characterisation due to the internal strain causing a large degree of cracking, and all the crystals formed have deviated to become purely paramagnetic and tetragonal in phase, irrespective of composition.

### 1.12.5-2  Thin Film

Much work has, and continues to be done on thin films of the BFPT system. Particularly synthesis by pulsed laser deposition and electrical characterisation has been well reported in several articles by Khan et al (2005 to 2008), including his Thesis, in which the whole topic is covered in great detail. The reader is directed to Khan (2008) for further reading.

## 1.12.6 DOPING

Conductivity is a well reported problem in the literature for bismuth ferrite (Catalan, 2009). Many groups have tried to remedy this using various doping regimes on the A and B site ions. In BFPT, dopants including Ga, La and Sc have been substitutionally added to the system to increase the resistivity and improve ferroelectric properties, however these always come at the cost of lowering the ferroelectric $T_C$ (Cheng, 2003 (a, b, c)) (Zhu, 2006).

## 2   CHARACTERISATION TECHNIQUES

### 2.1   CHAPTER OVERVIEW

This chapter serves to introduce the various techniques that have been used to investigate the magnetic properties of bismuth ferrite lead titanate, and correlate the relationship between magnetism and structure. Details of the apparatus, their operating parameters and their output are discussed.

### 2.2   ELECTRON MICROSCOPY

Scanning electron microscopy (SEM) is a similar technique to optical microscopy but offers much higher resolution at higher magnification due to the Rayleigh criterion; a relationship which describes the limit of resolution or the smallest distance between two points which can be clearly resolved, as being proportional to the incident wavelength (Goodhew, 2001).

The limit of resolution for light microscopy using blue ($\lambda$ = 450 nm) light for example is 200 nm, whereas electrons can achieve sub nanometre de Broglie wavelengths after acceleration attributing to resolutions of a few nanometres after electromagnetic lens aberrations, apertures and  spot sizes have been considered (Goldstein, 2003).

In its primary mode of operation an SEM continuously rasters an electron beam across the surface of a conducting sample, controlled by speed and step size, whilst detectors identify either back scattered electrons or secondary electrons that are emitted as a result of interactions between the incident beam and illuminated sample volume.

Secondary electron (SE) imaging provides topographical information with a large depth of field (>10 μm) and resolution 1 – 20 nm. Back scattered electrons are also used to conduct 'in lens' imaging, where a detector sits as a halo around the incident beam above the sample surface, to image higher resolution and contrasting images at the cost of topography and depth of field (Goldstein, 2003).

As the nature of ceramics are non-conducting, ceramic samples imaged are prepared by sputter coating a thin (few nm) layer of platinum or carbon to prevent charging of the sample, an effect which is detrimental to electron imaging.

## 2.3 VIBRATING SAMPLE MAGNETOMETRY

Vibrating sample magnetometry, or VSM, relies on the principle that the motion of a magnetic material in a uniform applied magnetic field induces an electromotive force or *emf* in a sensing coil (Fiorillo, 2004).

According to Faraday's law of induction, if the sample is vibrating at a constant frequency, then the emf produced in the sensing coils will be proportional to the rate of change of magnetic flux due to the motion of the sample (Al Jawad, 2004).

At its simplest, this involves measuring the current induced from an applied magnetic field in a pair of counter-wound pickup coils from a sinusoidally oscillating sample parallel to the magnetic field, mounted on a rigid rod. This is shown schematically in Figure 2-1.
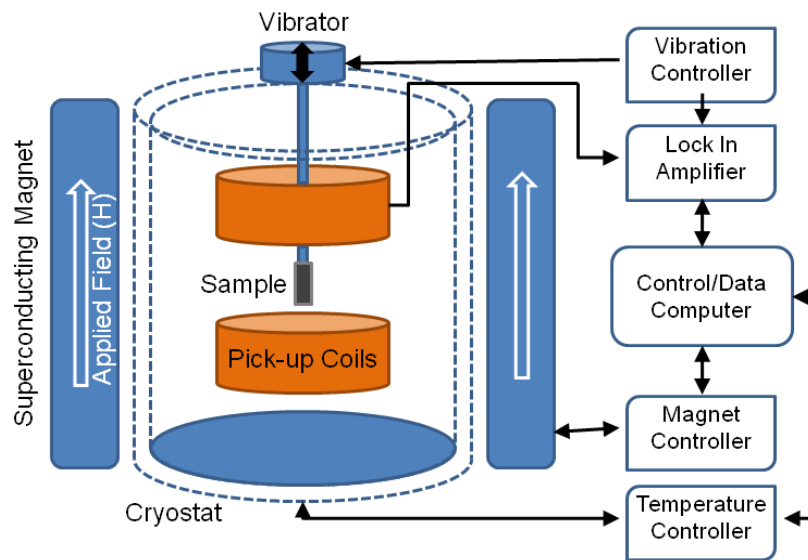


**Figure 2-1 Schematic of a vibrating sample magnetometer**

Counter winding of the pickup coils nulls their emf and eddy current contributions when the magnetic fields are applied.

The main advantages of VSM is that it performs bulk magnetization measurements over the entire sample volume. The magnetic field can also be swept to measure hysteresis and characterize the magnetic nature of the material.

It must be noted however, that the VSM measures the sample as well as the sample rod and substrate. Being that the latter two are carbon fibre and polyethylene respectively, the diamagnetic response must be taken in to consideration for subtraction by running the VSM sample-less first.

Some example data is shown below (Figure 2-2) for Co/Ru multilayers, presenting ferromagnetic and antiferromagnetic signals.

(a)                                     (b)
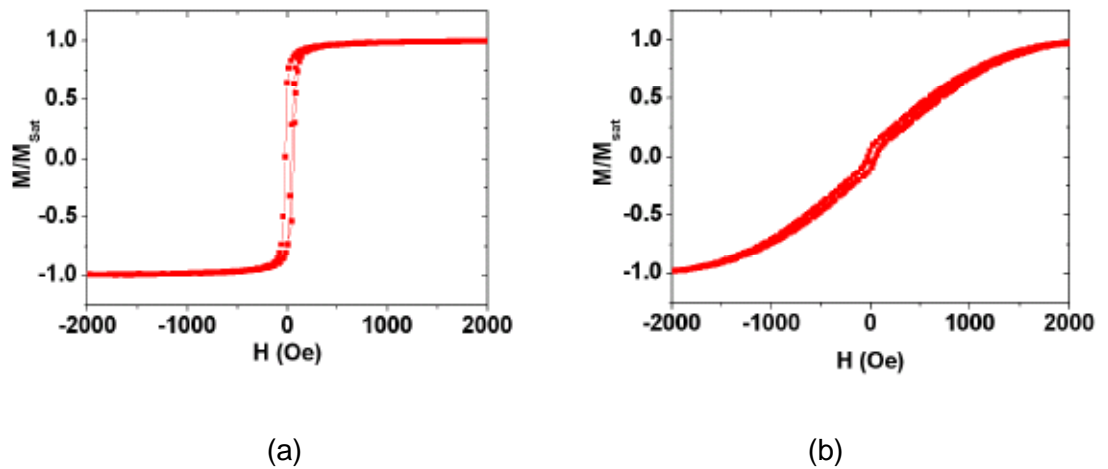
**Figure 2-2 Examples of VSM hysteresis loops of thickness dependent magnetic Co/Ru multilayers. Thick samples are a) ferromagnetic, whilst thinner films present b) antiferromagnetism (Kinane, 2008).**

## 2.4 X-RAY DIFFRACTION

Diffraction of light, or electromagnetic (EM) radiation, has been long studied and used as a powerful technique to characterise the structure of crystalline materials.

The next 2 sections are dedicated to the diffraction of EM radiation with wavelengths of 10 – 0.1 Å; X-rays.

X-rays are produced when any electrically charged particle of sufficient kinetic energy rapidly decelerates, termed Bremsstrahlung in German meaning 'braking radiation' (Cullity, 2001). The most popular particle is the electron, and section 2.4.1 and 2.4.2 describe the varying geometries and experimental parameters associated with diffraction of X-rays of different energies based on electron deceleration.

Diffraction itself occurs when a condition is met where two or more waves of EM radiation are 'reflected,' in this case from planes of atoms, and the path differences between reflections from successive planes is equal to an integer number of wavelengths. This condition was discovered and named after W. H. Bragg and son, W. L. Bragg, termed Bragg's Law (Equation 2-1);

$$n\lambda = 2d_{hkl}sin\theta$$

Equation 2-1 Bragg's Law

where $d$ is the distance between successive planes, and $\theta$ is the incident/diffracted angle of the X-ray beam.

Interactions between X-rays and atoms occur predominantly through interactions with the electron cloud, thus making X-ray scattering dependent on the atomic number of the element it interacts with. Materials such as lead, bismuth and tungsten for example are strong absorbers and scatterers of X-rays, and are often used for shielding, whereas light elements such as hydrogen and oxygen, diffract poorly as the X-ray – electron cloud interaction is weak.

X-ray diffraction (XRD) is used in view of this study for phase analysis, including identification, and resolution of unit cell parameters, crystal structure and strain.

### 2.4.1 Laboratory X-ray Diffraction

2.4.1-1 Production of X-rays

In laboratory X-ray diffraction (XRD) the radiation is produced by X-ray tubes (Figure 2-3) (Coolidge, 1913), with power ratings based on the amount of heat they can dissipate, given in maximum allowable tube current (mA) for a given voltage (kV). Inside the tube a tungsten filament is heated by electrical current, which emits electrons drawn to the anode target by the high potential difference (Figure 2-3). The allowable tube current is based on the flow of electrons to target (Cullity, 2001).

The moment the electrons strike the anode metal target, the deceleration causes X-ray emission in all directions of a broad spectrum of wavelengths (termed the continuous spectrum), which escape through one or more beryllium windows, which are 'transparent' to X-ray radiation.

The continuous spectrum is superimposed by a characteristic spectrum, a sharper, more intense line spectrum unique to the anode metal. The characteristic lines are labelled K, L, M (in reference to the electron orbital shells principal quantum number 1, 2, 3 respectively) and relate to the shell at the end of a transition caused by an electron interaction with an orbital electron, as shown in Figure 2-4.
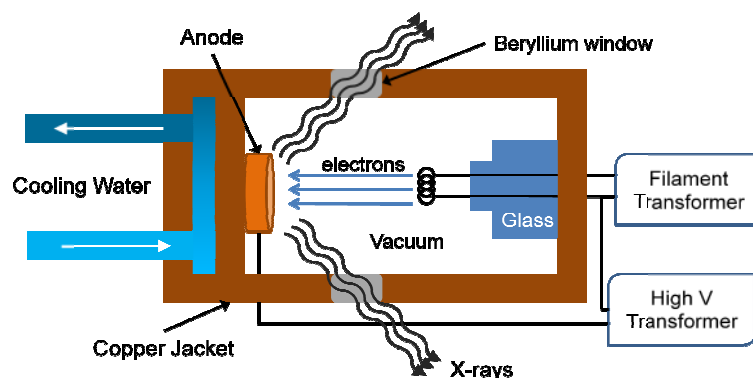


**Figure 2-3 Schematic of an X-ray tube (adapted from Cullity, 2007).**

A summary of typical wavelengths for common tube anodes are shown in Table 2-1. Some systems operate with a monochromater, a crystal or grating which only allows reflections or photons pass of a particular wavelength (or very narrow range), to remove the effects of the continuous spectrum and focus on the most intense radiation from the characteristic spectrum.
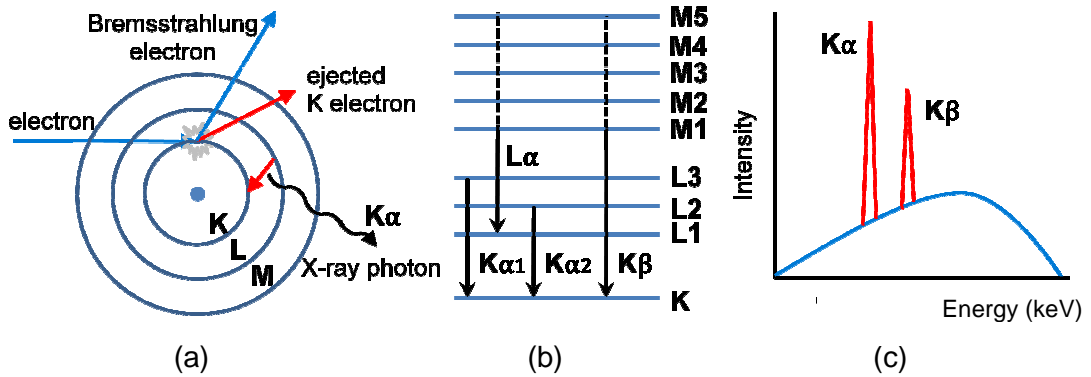


**Figure 2-4 Illustration of the production of the characteristic X-ray spectrum from a) electron interaction, b) the relative shell energy c) and the profile superimposed over the continuous spectrum.**

**Table 2-1 Typical wavelengths encountered for the transition metals chrome, copper and molybdenum.**

| Anode Element | Wavelength / λ (Å)* | | |
|---|---|---|---|
| | $K\alpha_1$ | $K\alpha_2$ | $K\beta_2$ |
| Chrome (Cr) | 2.8976 | 2.2937 | 2.0849 |
| Copper (Cu) | 1.5406 | 1.5444 | 1.3923 |
| Molybdenum (Mo) | 0.7093 | 0.7136 | 0.6323 |

*Values taken from Hölzer et al (1997)

### 2.4.1-2    Laboratory X-ray Diffraction Geometry

There are several geometries in which Bragg's law can be satisfied for diffraction, these include the Laue method, rotating crystal, and powder (polycrystalline) diffraction (Cullity, 2001). The latter of which can be split into two systems, Debye-Scherrer and the most popular, Bragg-Brentano. The Bragg-Brentano focussing geometry (seen in Figure 2-5) keeps the source of monochromatic X-rays and diffracted radiation detector symmetrical (of equal distance to the specimen surface)

about the sample, and sweeps through angles of 2θ, within a focussing circle (Hammond, 1997).
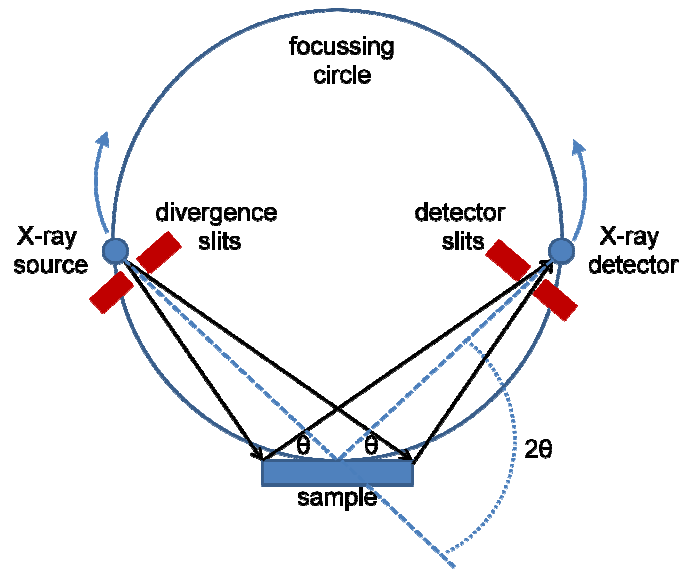


**Figure 2-5 Schematic of Bragg-Brentano geometry for powder XRD.**

The XRD instrument, Philips X'Pert MPD (Almelo, The Netherlands), used within the Institute for Materials Research at Leeds is typical of this geometry with a stationary sample and rotating source / detector arms. Diffracted X-ray intensities are recorded in a 1D plot against angle 2θ to produce a diffractogram.

### 2.4.1-3    Structure Factors, Peak Broadening and Temperature Factors

The electric part of electromagnetic radiation, such as X-rays, interacts with an electron by imparting the sinusoidal oscillating charge fluctuation. The result is an electron that itself oscillates, accelerating and decelerating in phase with the absorbed incident radiation. The subsequent change in acceleration ultimately releases 'scattered' X-rays that match the properties of the incident beam. Although these scattered X-rays are released in all directions, the intensity ($I$) is dependent on the scattering angle.

The nucleus of an atom has a relatively massive mass ($m$) compared to an electron and makes any charge oscillation from an X-ray difficult to the extent it is negligible (Equation 2-2), and does not contribute to scattering. However, an atom with multiple electrons now has multiple points of scatter, as each individual electron scatters part of the radiation.

$$I_{scattered\ radiation} \propto \frac{1}{m^2_{scattering\ particle}}$$

<div align="right">Equation 2-2 (Cullity, 2001)</div>

In fact, at $2\theta = 0$ an atom of atomic number $Z$, scatters $Z$ times the amplitude of the incident wave scattered by one electron. Other directions ($2\theta \neq 0$) introduces phase mismatch, which results in partial interferences. These variations can interfere constructively with other diffracted waves to present intense diffraction peaks, or can interact destructively, so as to annihilate a peak entirely related to a plane of atoms. The scattering efficiency of a given atom is therefore described by the atomic scattering factor ($f$) for a given atom, in a given direction. $f = Z$ when $2\theta = 0$.

$$f = \frac{amplitude\ of\ incident\ wave\ scattered\ by\ an\ atom}{amplitude\ of\ incident\ wave\ scattered\ by\ one\ electron}$$

As $2\theta$ increases, more scattered waves become out of phase, decreasing $f$. This occurs independent of wavelength, but has the effect of reducing the intensity of diffracted radiation at higher scattering angles.

This can be described for a unit cell by summing the scattering over all atoms in a unit cell. Termed the structure factor ($F$), this describes how the atomic arrangement, given by fractional coordinated $u, v$ and $w$ for each atom affects the scattered beam. If a unit cell contains atoms 1,2,3....n, then $F$ for the reflection $hkl$ is described as;

$$F = f_1 e^{2\pi i(hu_1+kv_1+lw_1)} + f_2 e^{2\pi i(hu_2+kv_2+lw_2)} + .. f_n e^{2\pi i(hu_n+kv_n+lw_n)}$$

Or

$$F_{hkl} = \sum_{1}^{N} f_n e^{2\pi i(hu_n+kv_n+lw_n)}$$

<div align="right">Equation 2-3 (Cullity, 2001)</div>

Coherent scattering from an atom in regular periodicity reinforces coherent scattering in some directions, and cancels in others. This phase difference effect is the basis of diffraction.

So far we have only considered the instance that the arrangements of atoms in the lattice are perfectly spaced apart at fixed points so that diffraction can occur. In reality this is not true, as thermal vibrations, crystallite size and strain all alter this perfect crystallographic motif.

The temperature factor is multiplied by the intensity to take into account the thermal vibration of the atoms within the lattice, which increases with increasing 2θ, or decreasing d-space, as the smaller distances suffer from higher positional error with increasing agitation.

For fixed atoms of exact planar distances, the peaks represented on a diffractogram will appear as vertical lines at the precise value of d-spacing for that plane. Distortions of these lattice positions gives rise to peak broadening, as the d-spacing is now over a distribution of values. Strain is a typical property that causes broadening, as it acts to distort the unit cells and their subsequent lattice spacing. Small crystallite sizes also purport to peak broadening, as the smaller crystallites (< 100 nm) have less successive planes to interact with, increasing the likelihood of destructive interference occurring from deeper within the crystal, allowing a larger distribution of angular divergence. This is also relevant to defects within the crystal that introduce a break in the successive planes and would show similar broadening to that of small crystallites.
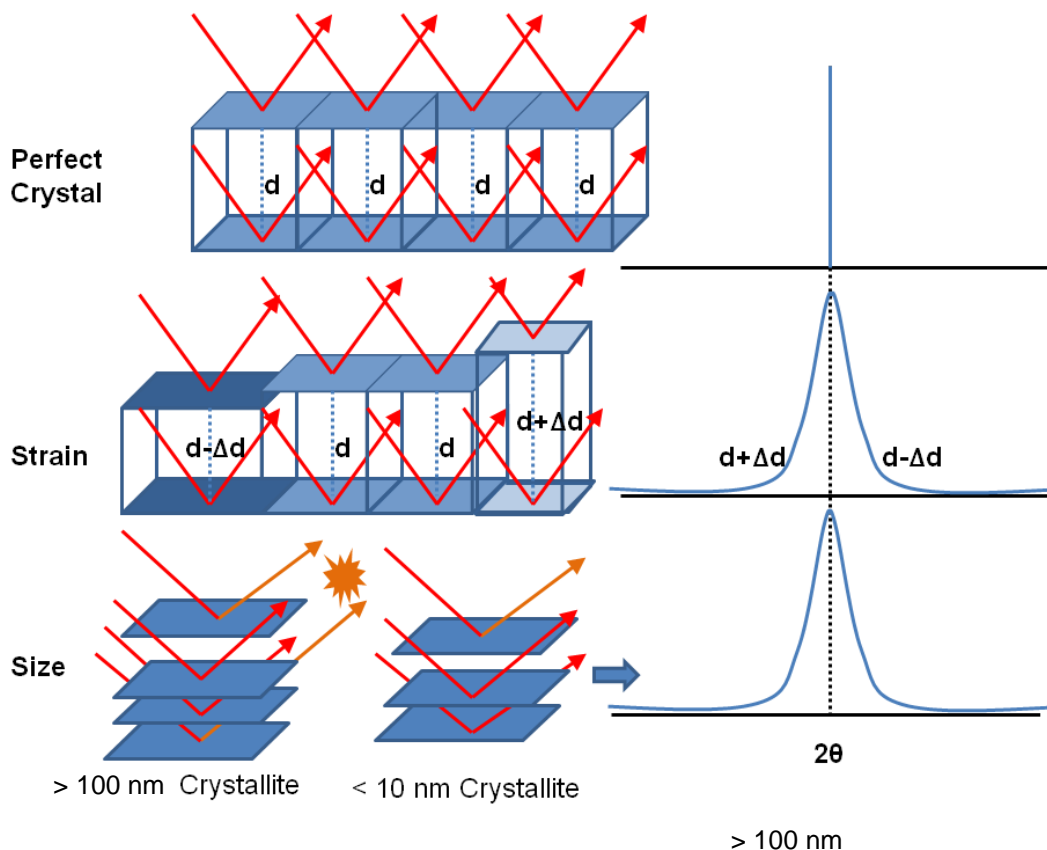


**Figure 2-6 Illustration of peak broadening in a diffractogram from strain and crystallite size. X-rays (red) diffract from unit cell planes (blue) in phase to form constructive interference peaks or destructive interference annihilation (orange).**

Particle size and strain analysis from X-ray diffraction can be done easily for either case from a single peak, but where contributions from both effects occurs, a more robust method is required, involving multiple peaks from the pattern.

The extent of the broadening can be measured for any peak as the full width at half maximum intensity (FWHM). This value can then be substituted in to Scherrer's equation to calculate the average particle size and strain contributions, as each source can be described by a different angular dependence. This is shown in Equation 2-4.

$$(FWHM)^2 = \underbrace{\left(\frac{0.9\,\lambda}{D\,cos\theta}\right)^2}_{size} + \underbrace{(4\varepsilon\,tan\theta)^2}_{strain} + b_0^2$$

Equation 2-4

Where FWHM is in radians, $\lambda$ is wavelength in angstroms (Å), $D$ is average particle size in angstroms, $\theta$ is theta in degrees, $\varepsilon$ is the strain term and $b_0$ is the instrumental broadening contribution, again in radians.

## 2.4.2  Synchrotron Radiation

2.4.2-1    Production of Synchrotron X-rays

There are over 40 particle synchrotrons in the world (Diamond, 2009) with facilities ranging in circumference and energy from the MAX-Lab, Sweden at 30 m and 0.55 GeV to the Large Hadron Collider at 26.7 km and 7 TeV respectively. However they all share the same basic operational layout (Figure 2-7). For the production of X-rays, electrons are used, produced by a cathode ray tube and accelerated through a linear accelerator (linac) into a smaller booster synchrotron. This speeds up the particles to energies high enough to be injected into the main storage ring.

The storage ring is made up of a many sided polygon in which the electrons are accelerated in bunches around an orbit at a constant energy until they reach relativistic speeds by radio frequency cavities. The electrons release high intensity X-rays at each corner of a polygon where a 'bending magnet,' utilizing Lorentz forces on the negatively charged particle, applies a field perpendicular to the direction of the electron causing a rapid deceleration in the particles previous vector, emitting light tangentially (Diamond, 2009). There are multiple bending magnets which provide multiple 'beams' of X-rays, which are then used for experimental diffraction, termed 'beamlines.' Over time the electron density reduces due to degradation of the orbit or gas molecule collisions, requiring the storage ring to be routinely re-filled.

The advantages of synchrotron light over laboratory sources are that the brilliance and high intensity of the X-rays often allows transmission through bulk, relatively large samples, rather than surface diffraction from the laboratory counterpart, or further penetration through heavily X-ray absorbing elements like lead.

Synchrotrons emit a continuum of photon energies allowing the varying beamlines to select energies or wavelengths per experimental requirements.
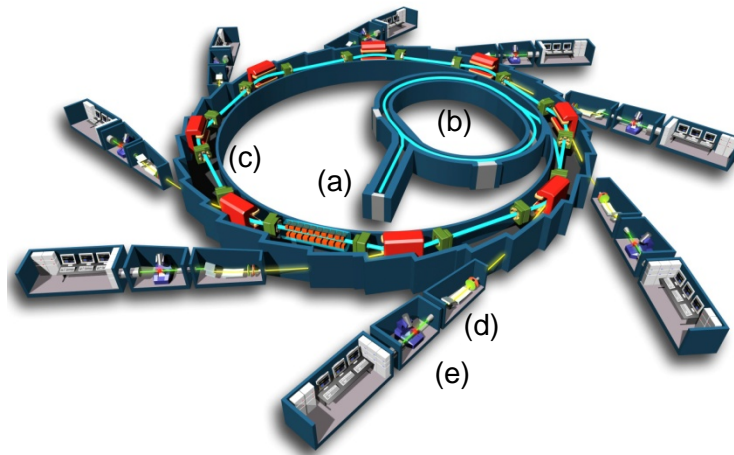
**Figure 2-7 Schematic of a synchrotron illustrating the path of electrons (blue) through a) the linear accelerator, b) booster ring, c) storage ring with bending magnets (red) and the resultant X-ray photons emitted (yellow) to d) the beamlines optics and e) experimental hutches (reproduced with permission, Chaix & Morel, 2005.)**

2.4.2-2    Laue transmission &  Debye – Scherrer Geometry

Work within this project was completed using high energy synchrotron X-ray radiation on the Materials Science beamline ID11 at the European Synchrotron Radiation Facility (ESRF) in Grenoble, France.

The reader is referred to the ESRF website <http://www.esrf.eu/> for more details on the facility.

ID11, as with most other beamlines, can operate using the Laue transmission geometry or Hull/Debye-Scherrer geometry. The laue geometry allows a beam of white X-rays to incident on the sample and uses a bank of position sensitive detectors (PSD) to collect diffracted patterns that have transmitted through the sample as a function of angle. The range of wavelengths acts as rotation of the source and detector in lab XRD, to satisfy Bragg's Law.

In the Debye-Scherrer geometry the white beam is mono-chromated, in the case of ID11 by a Silicon crystal cut through the (111), and once again a bank of PSDs is used to collect transmission diffraction.

## 2.5   NEUTRON DIFFRACTION

Neutrons were discovered by James Chadwick (1981-1974) in 1932 (Shull, 1995) for which he won the Nobel Prize in 1935. Enrico Fermi later showed that neutrons could be used in fission to support a chain reaction and neutrons that were slowed, or moderated, were more efficient at producing further fission (Bacon, 1953). The properties of these moderated particles became suitable for detecting the positions and motions of atoms, leading to the Nobel Prize, 1994 in Physics, awarded to Bertram Brockhouse and Clifford Shull to the development of neutron scattering techniques (Bennington, 2006).

Modern day neutron diffraction is typically carried out in large scale facilities around the world from dedicated nuclear reactors and spallation sources.

### 2.5.1   Neutron scattering

2.5.1-1   Properties of the Neutron

A neutron is an uncharged subatomic particle that when bound with protons form the entire mass of atomic nuclei. Neutrons can be split from the nuclei, and survive approximately 1000 seconds as a free particle, with a mass, magnetic spin and magnetic moment summarised in Table 2-2.

**Table 2-2 Basic Properties of a Neutron**

| Neutron Property | Value* |
|---|---|
| Mass ($m_N$) | $1.675 \times 10^{-27}$ kg |
| Charge | 0 |
| Spin | 1 / 2 |
| Magnetic Dipole Moment ($\mu_n$) | -1.913 $\mu_N$ |

\* taken from (Squires, 1978)

The de Broglie wavelength of a neutron is related to its velocity by (Equation 2-5);

$$\lambda = \frac{h}{mv}$$

Equation 2-5

where $h$ is Plancks constant,  $m$ is the mass and $v$ is the velocity of the neutron. The velocity is proportional to the square root of the kinetic energy, which in turn relates to temperature through Boltzmanns constant ($k_B$) expressed in Equation 2-6;

$$E = \frac{1}{2}mv^2 = k_B T$$

Thus for any neutron;

$$E = k_B T = \frac{1}{2}mv^2 = \frac{h^2}{2m\lambda^2} = \frac{\hbar^2 k^2}{2m}$$

where $k$ is the wavevector with magnitude $k = 2\pi/\lambda$.

Thermal neutrons (60-1000 K) therefore have a de Broglie wavelength ca. 1-4 Å and energy range ca. 5-100 meV (Squires, 1978). Energies are selected by moderation of the neutrons.

### 2.5.1-2    Neutron Interactions

Unlike X-rays, which scatter through interactions with the electron cloud of an atom, neutrons mainly scatter by atomic nuclei interactions, and their scattering power (cross-section) is thus not related to the atomic number of the element.

The interactions with atomic nuclei is weak allowing them to penetrate deeply or transmit through the material being examined, reducing the surface contributions and allowing the bulk of the material to be probed, as well as allowing complex sample environments such as cryostats, furnaces and pressure cells to be applied.

The unique property of neutrons however is the magnetic moment of the particle due to its spin. These moments can couple directly to spatial and temporal magnetizations on the atomic scale (through the electron cloud) and allow neutron diffraction to be the only technique that can categorically characterize magnetism and probe nuclear structure simultaneously.

Neutron diffraction is analogous to X-ray diffraction hence the majority of scattering theory such as Bragg's Law for nuclear interactions still remains applicable, but there are some subtle differences which will be introduced.

### 2.5.1-3    Cross-sections

When a beam of neutrons is incident on a material sample with a flux, $\Phi$, the result of complex interactions (Bacon, 1953) (Breit, 1936) with the scattering system is defined by its cross section ($\sigma$) (with units of barns, 1 barn = $10^{-28}$ m$^2$). The differential cross

section is defined by counting all the neutrons scattered into the solid angle $d\Omega$, at a point $r$ in the direction $\theta, \varphi$  (Figure 2-8) by;

$$\frac{d\sigma}{d\Omega} = \frac{number\ of\ neutrons\ scattered\ per\ second\ into\ d\Omega}{\Phi\ d\Omega}$$

Equation 2-8

The total scattering cross section then simply integrates Equation 2-8 for all directions;

$$\sigma_{total} = \int_{all\ directions} \left(\frac{d\sigma}{d\Omega}\right) d\Omega = 4\pi b^2$$

Equation 2-9 (Bacon, 1953)

Where $b$ is the scattering length (in fm), a constant dependent on the elemental isotope and describes the attractive or repulsive potential of the element on the neutron. This is shown in the difference between the wavefunction (ψ) for incident neutrons on the scattering system and scattered neutrons  at  the point $r$ in Equation (2-10 & 2-8);

$$\psi_{incident} = \exp(ikz) \qquad\qquad \psi_{scattered} = -\frac{b}{r}\exp(ikr)$$

Equation (2-10), (2-11)

where $k$ is the wavevector of the incident neutrons and $b$ the scattering length. The value of the scattering length depends on the particular nucleus and the spin state of the nucleus (I) plus neutron (±½) system (Bacon, 1963). Thus every nucleus with a non-zero spin has two values of scattering length. The relationships between scattering length and nuclei are determined experimentally, and unlike X-rays with atomic number (Z), have no correlation and vary erratically from nuclide to nuclide, summarised in Figure 2-9. The scattering in Bragg reflections arises from interference effects with similar radiation from other nuclei, termed coherent scattering length ($\sigma_{coh}$) (Bacon, 1963). There is also an incoherent scattering length ($\sigma_{inc}$) due to disorder from scattering from the various isotope contributions however this is beyond the scope of this work and is omitted for simplicity.
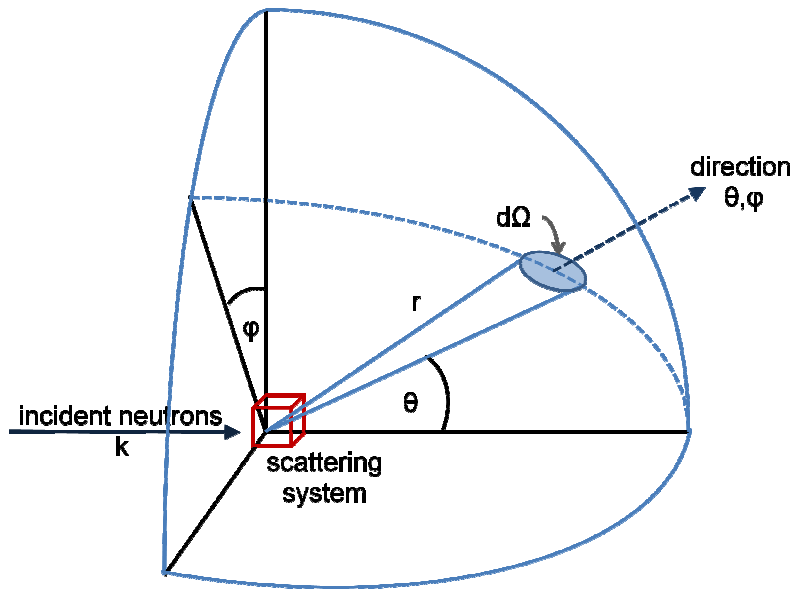
**Figure 2-8 Geometry of scattering experiment (adapted from Squires, 1978. p.5.)**
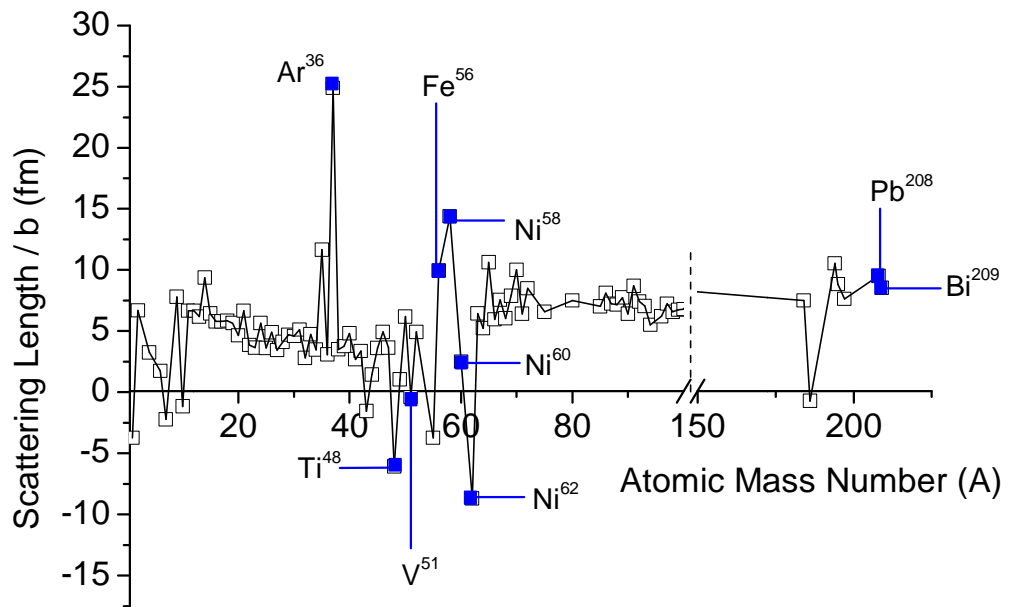


**Figure 2-9 Plot of coherent neutron scattering lengths as a function of atomic mass. Elements of interest have been highlighted (values taken from Sears, 1992).**

## 2.5.2 Reactor sources

From the 1940's onwards, neutron diffraction experiments were performed using a beam of neutrons from a $U^{235}$ fission reactor (Hannon, 2006). Today many facilities such as the French Institute Laue-Langevin (ILL, http://www.ill.eu) and Laboratoire Léon Brillouin (LLB, http://www-llb.cea.fr/) in Grenoble and Paris respectively, and Germanys Berlin Neutron Scattering Centre (BENSC, http://www.helmholtz-berlin.de) in Berlin utilise a 58 MW (HFR), 14 MW (Orphée) and 10 MW (BER II) fission reactor to produce hot through thermal to cold neutrons by using moderators around the core to mediate the neutrons to the desired energies.

2.5.2-1    Moderators

The high flux reactor (HFR) at ILL for example employs 25 litres of liquid deuterium to inelastically interact and absorb energy from the epithermal neutrons direct from the core and emit cold neutrons (T ~ 25 K); water is used for thermal neutrons (T ~ 300 K) and a block of hot graphite to moderate for hot neutrons (T ~ 2000 K) (Squires, 1978). The Maxwellian distribution of flux from the various moderators is shown schematically in Figure 2-10.
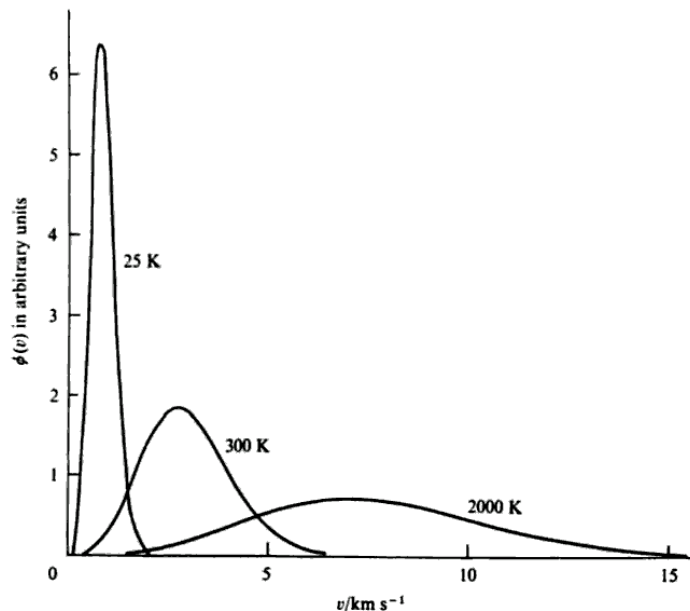


**Figure 2-10 Neutron flux distribution as a function of velocity for T = 25, 300 and 2000 K (Squires, 1978. p. 4).**

2.5.2-2    Constant Source Diffraction

The neutrons emitted from a reactor source are commonly termed constant source as the flux is constant as a consequence of the reactor being held in a critical, chain reacting, state.

Once the neutrons have been moderated to an energy range, a crystal is often used to monochromate the neutrons to a select wavelength. The diffraction is then analogous to monochromated X-ray diffraction discussed earlier, with large surface area position sensitive detectors to detect scattered neutrons.

The resolution of constant wavelength instruments using neutrons or X-rays, is described by the variation of a Bragg peaks full width half maximum (FWHM) and scattering angle, described by Caglioti et al (1958) reduced to (Equation 2-12);

$$\frac{FWHM^2}{8log_e 2} = Utan^2\theta + Vtan\theta + W$$

Equation 2-12 (Caglioti, 1958)

where $U > 0$, $V < 0$, $W > 0$ and are dependent on instrumental contributions. This suggests that with decreasing d-space, the resolution decreases from a maximum as it tends to smaller and smaller d-spacings.


## 2.5.3  Spallation sources

In more recent years, experimental neutrons have come from using particle accelerators to produce ions for neutron spallation, a process whereby neutrons are ejected from a target due to impact from accelerated particles.

The majority of the experiments within this project were conducted using spallated neutrons for diffraction, in particular, the ISIS spallation neutron source at the Rutherford Appleton Laboratory (Chilton, UK).


2.5.3-1    ISIS Spallation Source

The ISIS spallation neutron source operates as illustrated in Figure 2-11. Rather than electrons, electric discharge techniques create negatively charged hydrogen ions (H⁻) which are bunched by a radio frequency (RF) quadrupole, are then accelerated through a linear accelerator (linac) (a series of RF copper drift tubes) to 37% of the speed of light (665 keV)  (Bennington, 2006).

These bunches of ions are then injected into a synchrotron by passing through a thin foil of alumina which strips the electrons from the hydrogen ions, creating protons.

These are subsequently directed by electromagnets and accelerated around a 163 metre circumference ring in two bunches to 84 % the speed of light (800 MeV) (Bennington, 2006).

After 10,000 cycles of the synchrotron, powerful 'kicker' electromagnets (0 to 5000 Amps in 100 ns) eject the relativistic particles into a collision course with a tungsten target. As the proton bunches strike the target, spallation occurs, knocking highly energetic neutrons out of the tungsten atoms in all directions. Moderators are used to attain thermal energy ranges of the neutrons, which are then transported by neutron guides to 20 instruments in the experimental hall to pass through samples for diffraction or spectroscopy. The entire process occurs 50 times per second.
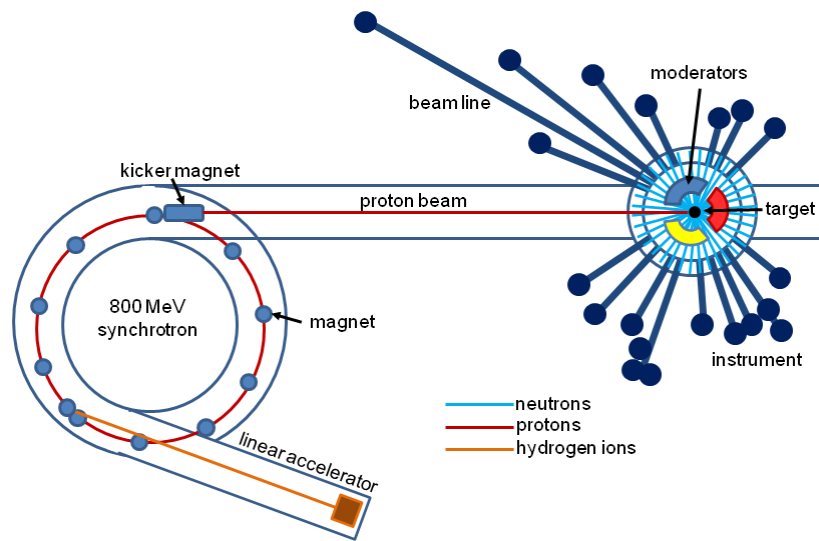


**Figure 2-11 Illustration of ISIS neutron spallation source (adapted from Bennington, 2006. p.11)**

### 2.5.3-2    Moderators

Moderators placed around the tungsten target, range from liquid hydrogen (T ~ 20 K) for cold neutrons, liquid methane (T ~ 100 K) for cool neutrons and ambient water for thermal neutrons (T ~ 300 K). The moderators give rise to a characteristic peak asymmetry, born by the rapid build up neutron flux as the protons strike the target, followed by an extended, longer tail from moderators introducing intensity decay (Figure 2-12). Spreading, from an otherwise sharp peak, also occurs over time spent in the moderator as the neutrons undergo more collisions, thus moderator volumes at ISIS are small, ~ 0.5 L.
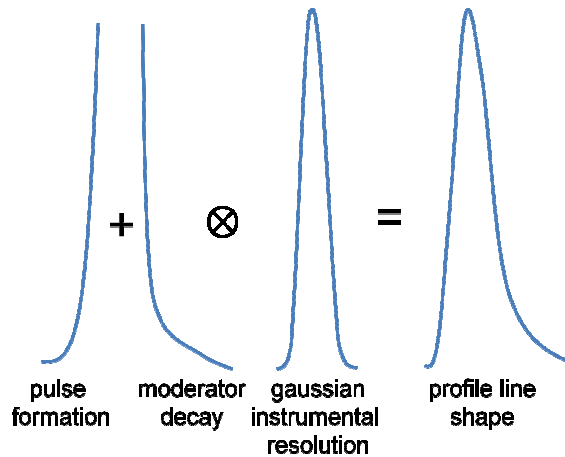
**Figure 2-12 Illustration (exaggerated) of the complex peak line shape as a result of spallation source neutron formation and moderation (adapted from Bennington, 2006. p. 38).**

2.5.3-3    Time of Flight Powder Diffraction

As discussed previously, thermal neutrons have associated wavelengths in the order of interatomic spacings, thus can be used for diffraction by an arrangement that satisfy Bragg's law for diffraction.

In the case of a polycrystalline material, the sample can be considered as a statistically large enough number of randomly orientated crystals such that for any reflection there will be a finite number of planes at the Bragg angle. Introducing white radiation, in the form of thermal neutrons of a range of energies or wavelengths, to this sample creates discrete cones of scattered radiation where the various wavelengths satisfy the Bragg angle simultaneously for all $hkl$ reflections. The white beam of neutrons travel a known distance 'L' from the source to the sample, to a fixed detector at an angle 2θ, with the neutrons arrival times being recorded. This is termed time of flight (TOF) diffraction.

As the neutron momentum is related to wavelength by Equation 2-7, it is then possible to calculate d-spacing by combining it with Bragg's law to give;

$$t = 505.56 \, L \, sin\theta \, d$$

Equation 2-13 (Smith, 2006. p.35)

where TOF ($t$) is measured in microseconds, flight path ($L$) in metres and d space in angstroms.

The unique geometry of TOF allows a complete pattern to be recorded by one fixed detector, but counting times can be greatly reduced by employing multiple numbers

of detectors, often arranged in to banks surrounding the sample, with each bank having its own characteristic ranges of d-space and resolution.

The banks can then be normalised by 'monitoring' the neutron pulses. That is a detector after the moderator counts the number of neutrons incident on it which is statistically relative to the number of neutrons being incident on the sample. This allows a record of flux fluctuations during experimentation.

Resolutions of TOF detectors become functions of time ($t$), flight path length ($L$) and $cot\,\theta$. From Equation 2-14 these can become very high with back scattered detectors (θ~180°) and long path lengths (HRPD Manual).

$$\frac{\Delta d}{d} = \left(\left(\frac{\Delta t}{t}\right)^2 + \left(\frac{\Delta L}{L}\right)^2 + (\Delta\theta cot\theta)^2\right)^{1/2}$$

Equation 2-14 (Smith, 2006)

Where $\frac{\Delta d}{d}$ describes the resolution as the d-space ($d$) spread in the Bragg reflection for a given instrumental setup. The highest resolution instrument is the high resolution powder diffractometer (HRPD) at ISIS, with a $\frac{\Delta d}{d} \sim 4 \times 10^{-4}$.

Some instruments however utilise 'choppers' to select only a small range, or monochromate incoming neutrons to act as CW machines. The choppers range in size and shape, but popular designs are based on a spinning disc with a slit that depending on the frequency of it being rotated allows only certain energies of neutrons to pass into the sample area. It is not uncommon to use multiple choppers to select fine wavelength ranges, and in some cases to remove frame overlap. Choppers are also used on many beam lines to remove the 'prompt pulse,' a term given to the fastest most energetic neutrons from spallation that would act to saturate the detectors and cause frame overlap by overtaking slower neutrons from previous pulses.

## 2.6   STRUCTURAL REFINEMENT OF DIFFRACTION DATA

Powder diffraction had a growing importance during the 1960's owing to the lack of large single-crystal specimens (Rietveld, 1966), but the averaging, isotropic and extinction effect of many artefacts from polycrystalline samples, as well as the inherent presence of overlapping reflections, prevents the full use of available information compared to its single crystal equivalent (Rietveld, 1967).

A series of publications focussing on research into uranium compounds in the early 1960's lead to a requirement for powder neutron diffraction patterns to be convoluted into individual peaks to access the full amount of crystallographic information stored within the patterns (Rietveld, 1966). A "structure factor least squares" computer programme was written by Hugo Rietveld (Rietveld, 1966) that took into account the overall isotropic temperature factors, scale factors, background, atomic coordinates, scattering factors and instrumental factors to obtain a model based on a least squares fit between the calculated and observed integrated intensities, measured at regular angular intervals from powder neutron diffraction for alkaline earth metal uranates (Rietveld, 1966).

This quickly developed (Rietveld, 1967) to form a robust method using profile intensities rather than integrated intensities to allow the maximum amount of information to be retrieved from overlapping peaks, and was expanded to become applicable to both nuclear and magnetic structures. This is named after Hugo Rietveld, and is termed "Rietveld Refinement" (Rietveld, 1969).

The actual procedure is relatively complex, but can be broken down into several key areas that are considered for the least-squares operation. These include peak width, based on CW parameters U, V, W (halfwidth parameters) by Caglioti (1958), orientation correction, peak profile (ie. Gaussian, Lorentzian, pseudo-Voight), structure factors and least square parameters (inc. space group, lattice parameters, asymmetry, scale factor, background and temperature factors) (Rietveld, 1969).

Because of its complexity, several software packages have been written and made available to the diffraction community. The two most popular examples are the freeware packages, General Structure and Analysis Software (GSAS) (Larson, 2004) and the FullProf suite (Rodriguez-Carvajel, 1993), the latter of which includes a host of various programs which complement the refinement process, such as a visualisation program WinPlotR.

Another program implemented throughout this work is X'Pert HiScore Plus (PANalytical B.V., Almelo, The Netherlands), which is packaged as part of the X'Pert MPD X-ray diffractometer used at the University of Leeds. This software has a highly intuitive graphical user interface (GUI) and carries out many processes automatically such as $K\alpha_2$ peak removal.

For any Rietveld refinement, there must be appropriate data collected (McCusker, 1999). For Bragg Brantano geometry powder diffraction this includes ensuring a constant-volume condition, that is at all angles of 2θ the divergence slits remain constant so that at low angles the X-rays illuminate a large area with minimal penetration, and at high angles the same volume is illuminated by the reduction in area but increased penetration depth (McCusker, 1999). The X'Pert MPD diffractometer at Leeds utilises programmable divergence slits (PDS) which maintain a constant surface area of illumination and not constant volume. Software such as HiScore Plus however can convert the data to simulate the constant volume solution. Preferred orientation effects need also to be addressed as texture leads to incorrect peak intensity measurements for the observed – calculated intensity least square comparison.

All types of diffraction require a standard reference material to be first run with the same diffraction parameters as the sample to be examined (McCusker, 1999). This allows an initial refinement against reference data held in the Inorganic Crystal Structure Database (ICSD) hosted by the UK Chemical Database Service (CDS, 1996) ([www.cds.dl.ac.uk](www.cds.dl.ac.uk)), at STFC Daresbury Labs, Warrington, UK. The reference can be refined using the set material properties (for lattice parameters, space group etc) to solve the instrumental effects which can then be applied for the sample to be measured. For X-ray diffraction this is often polycrystalline silicon and for synchrotron lanthanum hexaboride ($LaB_6$).

Once a model has been generated by refinement of the parameters appropriate to the phases being examined, the quality of the agreement between the observed and calculated profiles can be expressed in terms of the weighted profile factor ($R_{wp}$) and expected weighted profile ($R_{exp}$), both of which are determined by functions of profile intensity, standard deviation of the profile intensity, calculated counts, number of points and the latter also includes the number of refined parameters (Rodriguez-Carvajel, 1993)

A conventional indicator of "goodness of fit" is chi$^2$ (Appendix A), which is ($R_{wp}$ / $R_{exp}$) (McCusker, 1999) and should approach 1. However these values are affected by counting statistics and should not be over interpreted, instead careful examination of a difference plot is accepted to be the most accurate guide (McCusker, 1999).

The full description of the Rietveld method and the guidelines surrounding the process are detailed and to describe it all is not within the scope of this work, but the reader is directed to the work of McCusker et al (1999) from which the refinement guidelines have been followed and Lutterotti (1990) and Enzo (1988) for direction on fitting strain induced peak broadening.

# 3   EXPERIMENTAL

## 3.1   CHAPTER OVERVIEW

This chapter details the methods of sample synthesis and specific experiments used to determine the magnetic and structural characteristics of the bismuth ferrite lead titanate system and how they compare to the ferroelectric properties, highlighting any coupling between the ferroics.

Details of instruments, apparatus and parameters are subsequently reported here.

The objectives of the experiments conducted as highlighted in the introduction are to;

- Synthesize high density bulk polycrystalline ceramics in a range of compositions
- Complete laboratory magnetometry and neutron diffraction to characterise magnetism as a function of composition and temperature.
- Complete diffraction experiments as a function of composition and temperature to characterise the structure.
- Complete a phase diagram for bulk polycrystalline BFPT.

## 3.2   SYNTHESIS OF BISMUTH FERRITE LEAD TITANATE

As described by Comyn (2005) and Stevenson (2007), the synthesis of dense polycrystalline sintered $xBiFeO_3 - (1-x)PbTiO_3$ ceramics is well practiced due to fabrication for previously reported electrical measurements. Appropriate proportions of $Bi_2O_3$, $Fe_2O_3$, $PbO$ and $TiO_2$ (99.9% purity, Aldrich) to make up compositions $0.3 \leq x \leq 0.9$ in 0.1 steps (including x = 0.62, 0.65, 0.68, 0.75), were attrition milled in 2-propanol for 30 minutes. The resultant slurry was dried under heat lamps, sieved and calcined in covered alumina crucibles for 4 hours at 800 °C. Subsequently the powder was sieved and milled for a second time with 2-propanol and 2 vol % Glascol HA40 binder, dried and sieved.

For laboratory XRD, 15 mm dia. pellets and 12 mm dia. cylinders were uniaxially pressed at 50 MPa, followed by cold isostatic pressing at 200 MPa. The binder was burnt out by slow heating to 500 °C, followed by sintering.

Compositions $0.3 \leq x \leq 0.75$ were sintered in batches at 1000 °C and $0.8 \leq x \leq 0.9$ at 950 °C according to density measurements (Bell, 2007), on a same composition calcined powder bed. The powder bed, or atmosphere powder, creates a positive partial pressure within the alumina crucible of the volatile bismuth and lead compounds resulting in a weight loss no greater than 0.1 %, in keeping with other publications (Woodward, 2003).

### 3.2.1  Bulk Polycrystalline Ceramics

For bulk ceramics that do not crack or disintegrate due to internal strain developed through the ferroelectric $T_C$, slow cooling at 20 °C /hr is necessary. During sintering, shrinkage occurs by approximately 15 - 20 %. The cylinders are then mechanically thinned and polished using silicon carbide paper to 10.0 mm and the discs to 400 $\mu$m thick (P2500 Grit, Buehler, Germany). These discs were used for geometric density measurements, calculated as between 7.03 – 7.79 kg m$^{-3}$ (90.2 – 94.5 % of theoretical) for x = 0.4 to 0.9 respectively, and for phase analysis by laboratory X-ray diffraction and microstructure imaging by Scanning Electron Microscopy (SEM).

For electrical measurements, other as-fired pellets were lapped and polished to 200 $\mu$m, and silver electrodes (silver paint) applied with a diameter of 6 mm. By using electrodes with a diameter smaller than that of the ceramic test specimens, it ensured that dielectric breakdown occurred through the ceramic rather than the sample edges. For magnetometry measurements separate batches of pellets were cut into 2 x 2 x 10 mm bars.

### 3.2.1-1  Annealing

A selection of the disc compositions, including x = 0.7, were subsequently annealed after sintering and polishing at 750 °C for 30 minutes under alumina crucibles, again to minimize volatile metal loss.

### 3.2.2  Spontaneously Disintegrated Powders

As the formation of the tetragonal ferroelectric phase introduces a large spontaneous strain, described in section 1.8.2 (c/a = 1.187 for BFPT 7030), inducing this effect by fast cooling (> 900 °C /hr )from a sintering temperature of 1100 °C (for x ≤ 0.7) and 1000°C (for 0.8 ≤ x ≤ 0.9) in 15 mm dia. cylindrical batches of the various compositions, leads to complete cylinder self-disintegration of some compositions to a fine powder (Comyn, 2008) (Stevenson, 2010). The thermal routine is summarised in Figure 3-1.
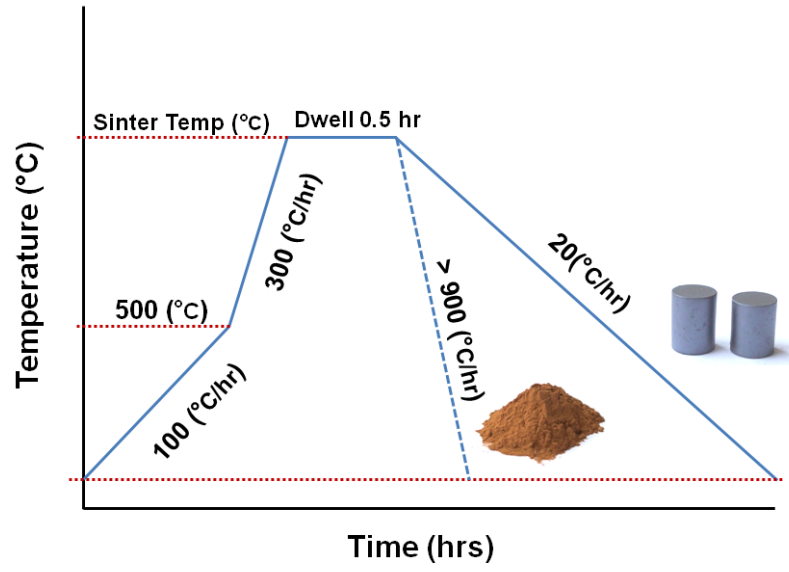
**Figure 3-1 Furnace routine for synthesis of various forms of BiFeO$_3$ – PbTiO$_3$**

## 3.3  EXPERIMENTAL SAMPLE PREPARATION

### 3.3.1  Scanning Electron Microscopy (SEM)

3.3.1-1    Bulk

Ceramic samples for SEM were mounted onto aluminium stubs, fixed with an adhesive carbon pad to ensure a conductive path from the sample to the stub which is then ground in the microscope to prevent charge build up due to the insulating nature of ceramics.

To further increase the conductivity, carbon paint was applied to the edges down to the carbon pad, and the samples were coated with a thin (5 nm) layer of platinum using an Emscope TB500 Pt sputter coater (Emscope Labs, Ashford, UK).

3.3.1-2    Powder

Powder samples were prepared by drop-casting. Again adhering a carbon pad to an Al stub and applying a solution of sample powder and (minimum amount of) 2-propanol, mixed and deposited by pipette. Once the solvent has evaporated, Pt coating can then be completed.

### 3.3.2  X-ray Diffraction (XRD)

3.3.2-1    Bulk

Ceramic pellets were mounted to clean glass slides using modelling clay and flattened so the sample surface matched the reference surface of the surrounding aluminium mask. This was done using a dedicated mechanical device supplied with the XRD. The slide could then be mounted on to the XRD stage and diffraction started in 'flat plate' geometry.

3.3.2-2    Powder

Powders and particulate samples were back filled into an aluminium block which has an aperture on the reference surface. Once the block is filled with powder, taking care not to impart any texture, it is inverted to present a powder surface in line with the reference surface. This can again be mounted into the diffractometer, but with the option of using a spinning stage.

### 3.3.3 Vibrating Sample Magnetometry (VSM)

Samples used were cut in to standard bars of 2 x 2 x 10 mm so as to keep the demagnetisation factor to a minimum (see 1.7.7).

Only bulk ceramics were possible to mount into the VSM due to the carbon fibre rod utilised. The ceramic bars were placed onto a polyethylene stick and fixed by wrapping with polyethylene tape. The sample stick was then attached to the carbon fibre rod which is then lowered into the cryostat.

### 3.3.4 Large Scale Facility Diffraction Samples

These are generally specific to the experiment and tailored to the desired parameters and specifications of the individual instrument. The sample preparation in these cases will be discussed per experiment in later sections, but are based on monolithic or powdered samples taken from the batches described in section 3.2.

## 3.4 LABORATORY CHARACTERISATION TECHNIQUES

### 3.4.1 Scanning Electron Microscopy

Secondary and in-lens electron microscopy was carried out on a LEO 1530 Field Emission Gun (FEG) with Gemini column (Carl Zeiss ltd, Cambridge, UK) scanning electron microscope (SEM). Specific recording conditions vary per sample and image, so are presented with each micrograph in the results as they are discussed.

### 3.4.2 Laboratory X-ray Diffraction

X-ray diffraction was undertaken using primarily the X'Pert Pro MPD by PANalytical (Almelo, The Netherlands) unless otherwise stated, utilising Bragg Brantano geometry with a copper tube, $\lambda = Cu\ K\alpha_1 = 1.5406\ \text{Å}$.

The diffractometer employs a line focus source attenuated by a 10 mm mask, soller slits and programmable divergence slits (PDS) to illuminate a 10 x 5 mm area of the sample in either flat plate or spinner mode. The diffracted beam is then passed through programmable antiscatter slits (PASS) and a nickel filter to a X'Pert X'celerator detector.

The spinner stage is particularly useful for small amounts of powder, or simply to improve diffraction statistics, as spinning a powder sample increases the likelihood of diffracting planes.

The sample stage can be removed and replaced with an alumina hot stage (Anton-Paar DHS 1200) with a temperature range from ambient to 1200 °C. This allows in situ annealing and phase transition monitoring.

Rietveld analysis of XRD patterns was conducted using X'Pert HiScore and FullProf for complementary and comparative analysis using constraints to fix the atomic positions of Fe and Ti to be equivalent and maintaining positive temperature factors. Other variations and constraints are presented with refined data in the results section.


### 3.4.3 Vibrating Sample Magnetometry

Magnetometry conducted in the Department of Physics at the University of Leeds was employed to conduct magnetic characterisation to aid in presenting a scientific case for large scale facility neutron diffraction beam time.

The VSM is an Oxford instruments 3001 capable of magnetic fields up to ± 7 Tesla via a superconducting magnet immersed in a liquid helium cryostat. The temperature range available is from 4 K to 330 K using cryogen flow and the variable temperature inserts, although the experiments were all done at ambient.

Samples were loaded and vibrated at 55 Hz. The signal response is typically low, and any noise induced from local domestic 50 Hz sources was reduced by using a lock in amplifier to detect the reference frequency.

A set routine is initiated with the following parameters;


± 2.0 Tesla (Wb.m$^{-2}$)

Rate of 0.005 T.s$^{-1}$ (50 Gauss.s$^{-1}$)

5 quadrant loop. (0 field $\rightarrow$ +2.0 T $\rightarrow$ 0 field $\rightarrow$ -2.0 T $\rightarrow$ 0 field $\rightarrow$ +2.0 T)

## 3.5 LARGE SCALE FACILITY DIFFRACTION EXPERIMENTS

Use of the large scale facilities is controlled by a peer assessed proposal system, under the European Framework (6 and 7) protocol.

For each experiment a beam time proposal outlining the scientific case must be submitted under various deadlines based on the times of the facilities run schedule.

The 8 large scale facility experiments undertaken for the scope of this work (although 14 have been completed in total) can be found attributed to supervisor T. P. Comyn as the listed principal investigator in all.

### 3.5.1 Neutron Experiments

3.5.1-1    Magnetic order, moment and structure dependence on bulk composition and temperature. *Polaris Instrument at ISIS, Chilton, UK.*

Experiment number: RB 520125. Instrument Scientist: R. I. Smith.

The characterisation of magnetic ordering and structure over the various compositional range $0.2 < x < 0.9$ for bulk ceramics as a function of temperature was undertaken through 2 neutron experiments on the medium resolution time of flight instrument Polaris (Hull, 1992).

In both instances, iso-compositional cylindrical samples of BFPT were stacked intimately into Suprasil (high purity fused silica, Heraeus, USA) glass tubes to allow a large enough volume to intersect the full cross section of the incident neutron beam (20 x 40 mm at maximum aperture) (Smith, 1997).

The glass tubes were not sealed to enable ambient pressure into the sample area. This was intentional to reduce the volatility of the Bi and Pb when heated in the experiment.

The high flux Polaris instrument employs 316 K Gd poisoned water to moderate spallated neutrons. Choppers allow an incident wavelength of 0.1 – 6.59 Å at the sample position, 12.0 m from the water moderator (Smith, 1997). Diffraction data is collected through 4 banks (A to E) of detectors ranging in position angle, resolution and d-space range, summarised in Table 3-1. The layout of the instrument is presented in Figure 3-2.

A liquid helium flow cryostat and vacuum furnace (AS Scientific, Abingdon, UK) was used to house a sample stick that fixed the Suprasil glass sample tube to one end and cool the material to > 4 K or heat to < 700 K respectively. The sample tank can then be evacuated ($< 10^{-4}$ mbar) to remove scattering by air. Although the cryostat and furnace are fabricated from steel and other metals, a vanadium window is aligned to the incident neutrons path, as vanadium has a very small negative scattering length (b = -0.402) and appears 'transparent' to neutrons (Sears, 1992).

**Table 3-1 Summary of detector banks used on the Polaris instrument at ISIS. The detectors are arranged in to 4 banks labelled A to E with increasing resolution.**

| Bank Position | Very Low Angle (A) | Low Angle (B) | 90 degrees (E) | Back Scattered (C) |
|---|---|---|---|---|
| Detector | ZnS scintillator | $^3$He gas tubes | ZnS scintillator | $^3$He gas tubes |
| No. of detectors | 80 | 80 | 216 | 58 |
| Resolution ($\Delta$d/d) | $3 \times 10^{-2}$ | $1 \times 10^{-2}$ | $7 \times 10^{-3}$ | $5 \times 10^{-3}$ |
| d-space range (Å) | 0.5 – 21.0 | 0.5 – 8.15 | 0.3 – 4.1 | 0.2 – 3.2 |

\* taken from Smith (1997)
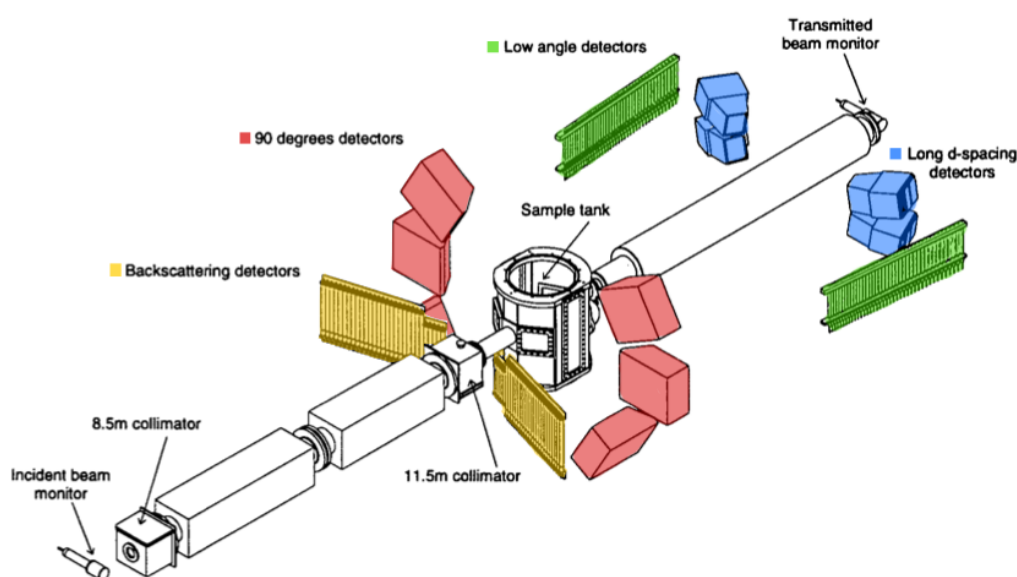


**Figure 3-2 Schematic of the Polaris neutron powder diffractometer instrument at ISIS, Oxford, UK (Smith, 1997).**

Diffraction patterns for each composition were collected in the cryostat and furnace during cooling and heating respectively in 20 K steps from 4K to 700 K.

Because each bank of detectors varies with scattering angle, they must be normalised by dividing through the neutron count collected by the incident beam monitor. The flux of neutrons is measured in microAmp hours (mA.h), so to standardise collection times, each run was set to collect for 50 μA (~ 20 mins) negating effects from flux fluctuation during the experiment.

An individual bank however can be assumed to have the same resolution across the detectors that form it, so to produce a diffractogram each bank is 'focussed' to improve the counting statistics, as previously mentioned in 2.5.3-3.

WinPlotR visualisation software as part of the FullProf Suite (Rodriguez-Carvajal, 1993), was employed to fit multiple peaks and Rietveld refine a model to fit the resultant data, implementing an instrument resolution function (IRF) for Polaris, which can be defined in FullProf.

*3.5.1-2*    Magnetic order, moment and structure dependence on disintegrated powder composition and temperature. *G4.1 at LLB, Paris, France & Polaris at ISIS, Chilton. UK.*

Experiment number: 9092. Instrument Scientist: G. André.

The two-axis powder diffractometer G4.1 independently funded by the Commissariat à l'énergie atomique (CEA) at the Laboratoire Léon Brillouin (LLB) near Paris, France, operates a constant wavelength of neutrons sourced by the 14 MW Orphée reactor. The epithermal neutrons leave the reactor core and are moderated by 300 K heavy water, followed by further moderation by 300 K water to produce cold neutrons. Monochromation is achieved by pyrolytic graphite orientated in the (002) to produce a constant wavelength of 2.4226 Å.

The samples used were spontaneously disintegrated samples of BFPT, or where the sample had not fully disintegrated, remaining sintered ceramic material was crushed with pestle and mortar to fit and pack into the sample holder.

The incident neutrons are shone through these powders loaded into 10 mm dia. vanadium cans again within a liquid helium flow orange cryostat. Measurements were taken at room temperature, at 4 K, then upon continuous heating back to room temperature with each temperature point presented as the average of a temperature range of ca. 20 K. Typical collection times were of the order of 40 minutes per temperature point.

The 800 cell position sensitive boron fluoride scintillator ($BF_3$) multidetector covered a 80 ° 2θ range with 0.1 ° between 2 cells and collecting diffraction patterns over an equivalent d-space range of 1.7 to 13.8 Å. This is illustrated in Figure 3-3.
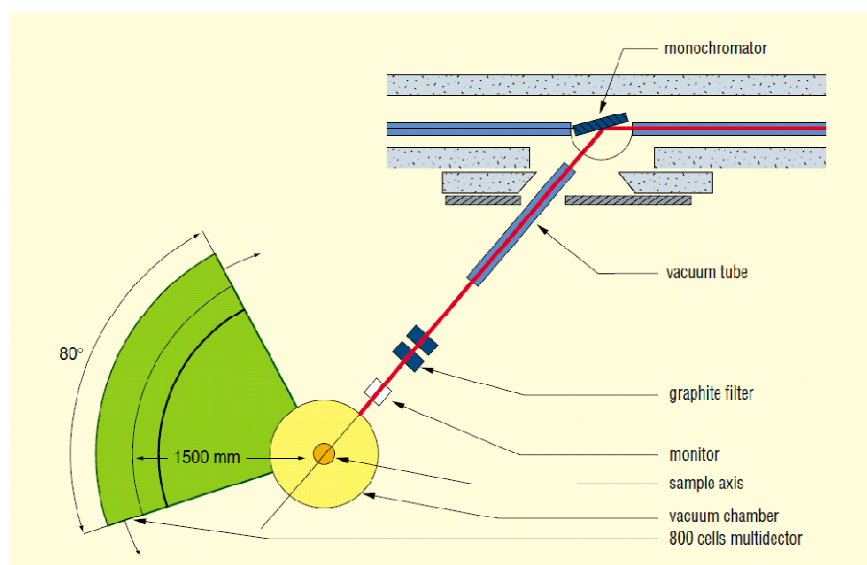
**Figure 3-3 Schematic of the G4.1 constant wavelength diffractometer at LLB (André, 2003)**

### 3.5.1-3 Study of G-type antiferromagnetic order to ascertain the presence of any incommensurate order. *HRPD Instrument at ISIS, Chilton, UK.*

Experiment number: RB920306. Instrument Scientist: Kevin Knight.

The time of flight neutron high resolution powder diffractometer (HRPD) at ISIS is moderated by 100 K liquid methane and situated ~100 m from the neutron target achieving $\Delta d/d$ resolution of up to ~4 x$10^{-4}$ (Ibberson, 1992), allowing fine changes in lattice and the antiferromagnetic diffraction peak to be resolved and probed for any splitting that is consistent with satellites when collinear G-type antiferromagnetic order becomes incommensurate such as seen in $BiFeO_3$ (Sosnowska, 1982) (Section 1.11.4-6).

Polycrystalline samples of x = 0.7, 0.75 and 0.9, $xBiFeO_3 - (1-x)PbTiO_3$ were prepared by fast (900 °C/hr for x = 0.7) and slow (20 °C/hr for x = 0.75, 0.9) cooling from the sinter as described previously. This resulted in either dense ceramic bodies for x = 0.75 and 0.9, or a self-disintegrated powder for x = 0.7. The dense ceramic bodies (x = 0.75 and 0.9) were subsequently crushed using a press and pestle and mortar, to form a powder. The samples are summarised in Table 3-2.

Diffraction data were collected for each sample in a flat plate can of 15 x 20 mm placed in an orange cryostat cooled with liquid He (helium-flow) to 7.5 K. Choppers were set so as to prevent frame overlap and deliver pulses 100 ms and 40 ms to cover 2-4 Å and 4.18 – 5 Å in real space respectively. This is summarised in Table 3-3.

**Table 3-2 Composition, form and phase of $xBiFeO_3 – (1-x)PbTiO_3$**

| Composition (x) | Form | Predominant Phase |
|---|---|---|
| x = 0.7 | *Self-disintegrated Powder* | Tetragonal (P4mm) |
| x = 0.75 | *Crushed Ceramic* | Rhombohedral (R3c) |
| x = 0.9 | *Crushed Ceramic* | Rhombohedral (R3c) |

**Table 3-3 Summary of chopper settings for HRPD (Stevenson, 2010)**

| d-space range | Chopper 1 (6 m from source) | Chopper 2 (12 m from source) | Pulse length (ms) |
|---|---|---|---|
| 2.0 – 4.0 Å | 50 Hz | 10 Hz | 100 ms |
| 4.18 – 5.0 Å | 50 Hz | 25 Hz | 40 ms |

A 2 hour collection over 2-4 Å (100 – 200 ms TOF) d-spacing was used to examine nuclear structure in detail and an 8 hour collection for 4.18 – 5.0 Å (200 - 240 ms TOF) was required to see the antiferromagnetic peak at ~ 4.6 Å. Ariel software (V.3.2, ISIS, Oxford. UK), was employed to focus the data into a diffractogram. The data reduction also removes the 'prompt pulse', high energy, high speed neutrons that can pass through the choppers and give a 'spike' on the detectors.

HRPD houses 3 detector positions, a low-angle (30°) bank, a 90° bank, and the highest resolution back-scattered bank (168°) (Ibberson, 1992)(Figure 3-4). Only the highest resolution data from the latter are presented in this work. WinPlotR visualisation software as part of the FullProf Suite (Rodriguez-Carvajal, 1993), was employed to fit multiple peaks to the antiferromagnetic peaks and satellites, using an IRF for HRPD.
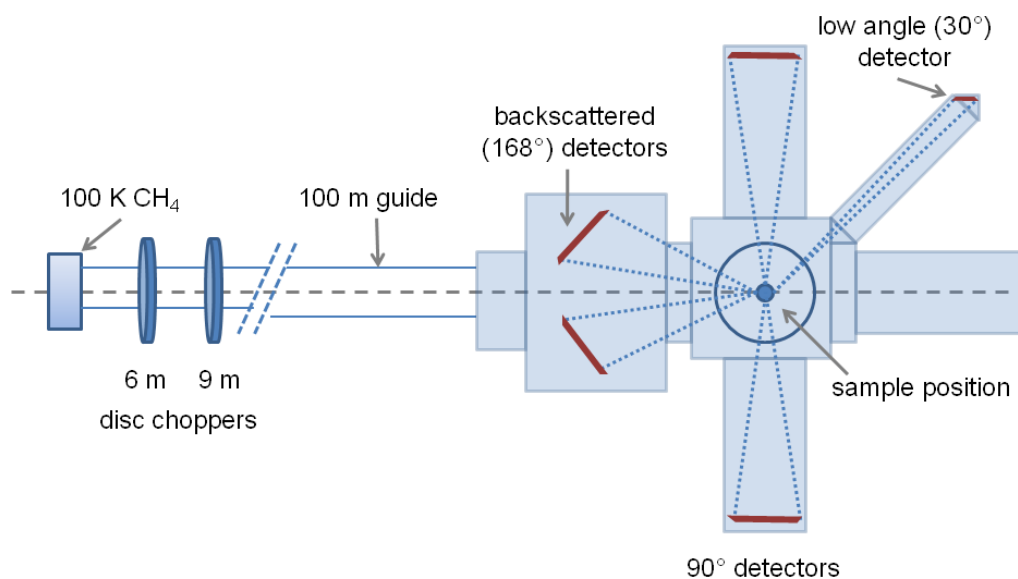
**Figure 3-4 Schematic of the high resolution neutron powder (HRPD) diffractometer at ISIS, Oxford, UK.**

3.5.1-4    Response of magnetic order and structure to externally applied isostatic pressure. *PEARL Instrument at ISIS, Chilton, UK.*

Experiment number: RB910102. Instrument Scientist: W. G. Marshall.

The Paris-Edinburgh (PE) cell At Rutherford Labs (PEARL) (Godec, 2004) is a medium resolution, high pressure (HiPr) beam line (Figure 3-5(a)) capable of delivering up to ~ 25 GPa (Klotz, 1995) with a diamond anvil, or more routinely ~ 10 GPa (Besson, 1992) with tungsten carbide anvil variants.

The PE-cell itself (Figure 3-5(b)) is a collaborative result of the Université Pierre et Marie Curie, Paris, and the University of Edinburgh, fabricated from steel (50 kg) (Godec, 2004) and used within an evacuated sample tank similar to Polaris, but housed on the PEARL instrument beam line.

Anvils used in the experiment were tungsten carbide driven by a hydraulic ram piston against a steel breech to compress a thin Ti-Zr (null scattering) split gasket containing either a small bulk, or powder sample up to 10 mm$^3$ with a small volume of liquid perdeuterated methanol-ethanol (4:1 by volume) pressure transmitting medium as well as a pure lead sphere (ca. 0.8 mm dia.) pressure marker. This is pinched with 6 tonnes of uniaxial pressure to seal the gasket sides but not apply any internal pressure.

The methanol-ethanol mix is used as it resists freezing with high pressures, and the lead acts a pressure marker as the $a$ unit cell parameter once refined (from (200) peak) can be related to isostatic pressure (Fortes, 2004) within the gasket at room temperature by the relationship in Equation 3-1. Circulated cooling water and the

50 kg steel cell thermal mass maintain 300 K through out to allow accurate pressure measurement.

$$Isostatic\ Pressure \propto \frac{1}{a\ lattice\ parameter\ (Pb)} = \frac{1}{\sqrt{3} \times (d - space(\text{Å}))}$$

Equation 3-1

Pressure was increased by 0.5 tonne uniaxial ram increments from 6 to 12 tonnes which covered a range of 0 – 1.2 GPa internal gasket isostatic pressure.

Neutrons enter the PE cell through a boron nitride collimator into a 14° cutaway aperture in the anvils and incident directly on to the gasket. Cadmium (highly neutron absorbing) shielding prevents scattering from the cell in 360° perpendicular to the incident beam direction (Figure 3-6). PEARL employs a 100 K liquid methane moderator situated 12.6 m from the sample position. It again uses multiple detector banks positioned at 30° (module 5) and 90° (module 9) (Figure 3-5(a)) with a maximum $\Delta d/d$ resolution in the latter angle of 8 x 10$^{-2}$.

Time of flight diffraction was collected between 1 and 19.5 µs using module 9 corresponding to a d-spacing range of 0.3 – 4.15 Å. In order to observe the antiferromagnetic only peak at ~4.6 Å, the PE cell is rotated and tilted at a range of pressure steps to collect from the low angle module 5 detectors. This configuration collects 1 - 8.5 Å at lower resolution (Equation 2-14) and with poorer statistics, so substantially longer collection times are necessitated.

(a)                                           (b)
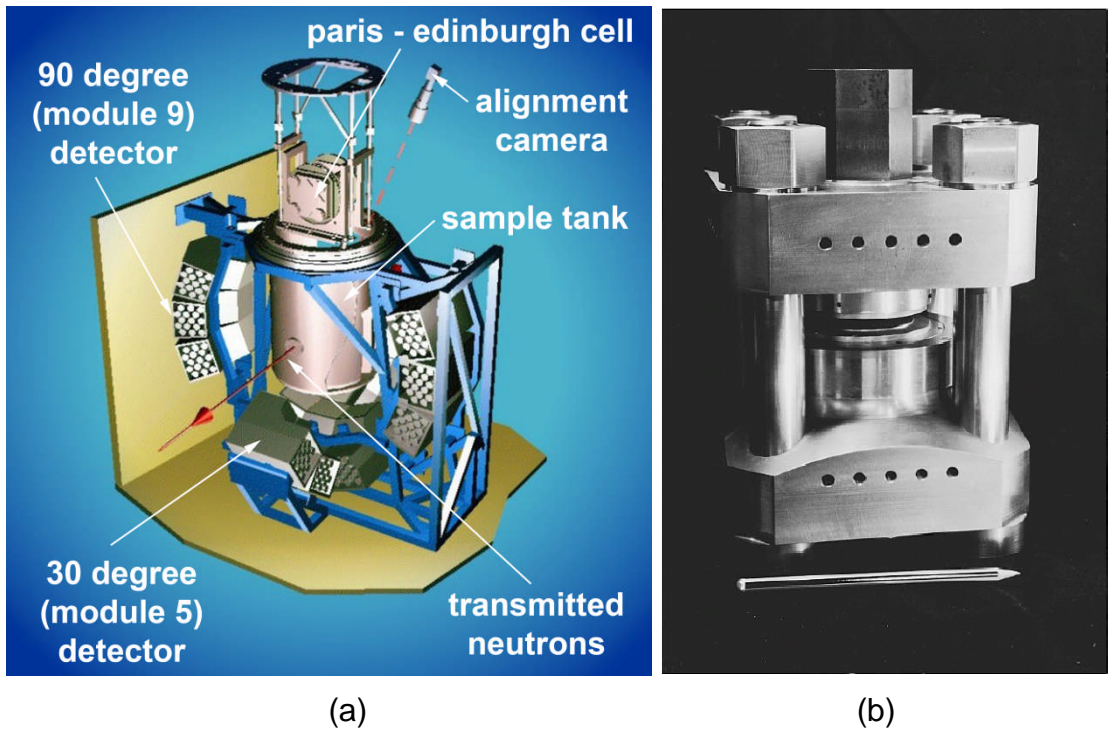
**Figure 3-5 (a) The PEARL beam line and instrument setup at ISIS, Oxford, UK. (Pearl, 2010) (b) The Paris Edinburgh cell used at PEARL (pencil shown for scale) (Klotz, 1995)**
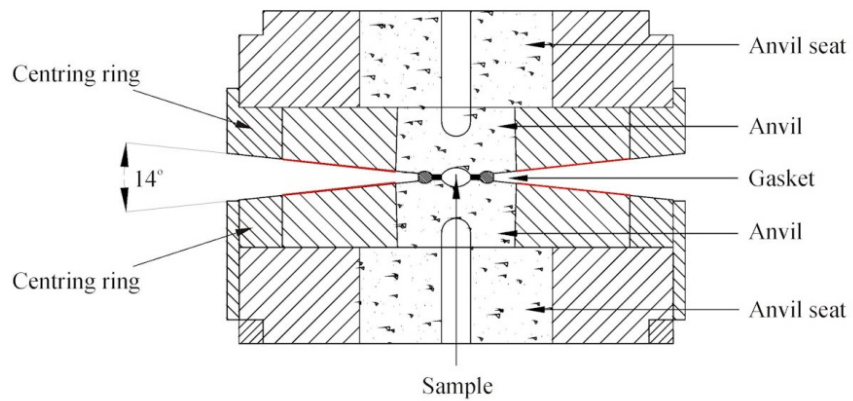


**Figure 3-6 Schematic of the Paris Edinburgh cell gasket and anvil setup. The red lines indicate presence of cadmium shielding, and the incident beam enters from the top. (Godec, 2004.)**

3.5.1-5    Response of magnetic order and structure to externally applied electric
            field. *E2 Instrument at BENSC, HMI, Berlin, Germany.*

Experiment number: MAT-01-2487. Instrument Scientist: I. Glavatskyy.

Dense polycrystalline bulk discs, 28 mm in diameter mechanically thinned and polished to 500 µm (P2500 Grit, Buehler, Germany) and electroded on both sides using silver paint (Demetron 6200 0007) were used to collect neutron diffraction using the E2 powder diffractometer at HMI (Hahn-Meitner-Institut, Berlin).

The BER II 10 MW reactor at HMI delivers epithermal neutrons to a 166 K pyritic graphite crystal for moderation and monochromation, giving a constant wavelength of 2.39 Å.

Electric field was applied parallel to the incident beam across the electroded discs using a modified cryostat sample stick. A Teflon block was mounted at the sample end to provide insulation from the sample to the stick and cryostat. From the Teflon an aluminium paddle and Teflon coated copper wire protruded to introduce an electric field to the sample, from a 6.5 kV amplifier (FUG HCN 140-6500 V). The electrodes were adhered to the paddle and wire using silver paint (Figure 3-7).

To prevent breakdown of and around the sample, the modified stick was placed within a cryostat (nitrogen-flow) and evacuated to $< 5.0 \times 10^{-4}$ mbar (0.05 Pa) to reduce arcing from Paschen curve effects, and cooled to 250 K ($\pm$ 1°). This relatively small drop in temperature saw the effect of increasing sample resistance by nearly 4 orders of magnitude to allow a greater field to be achieved for longer periods (up to 12 hours), without significant changes to phase contributions, strain or magnetic arrangements due to the decreased temperature.

Data was collected by a 2D wire position sensitive multidetector spanning 80° with 0.2° between wires (intermediate angles can be collected by rotating the detector bank on an air stage) obtaining 400 points simultaneously between 1.5 and 8.5 Å over 4 hour periods per step in voltage applied. Voltages ranged from 1 – 5 kV in 1 kV steps, applying an effective field of 2 – 10 MV m$^{-1}$. Parasitic scattering from the sample environment is reduced by employing a radial oscillating collimator.

Software "TVNexus" was used to normalise and focus the data over 32° (1.5 to 5 Å) to create diffractograms from the raw data.
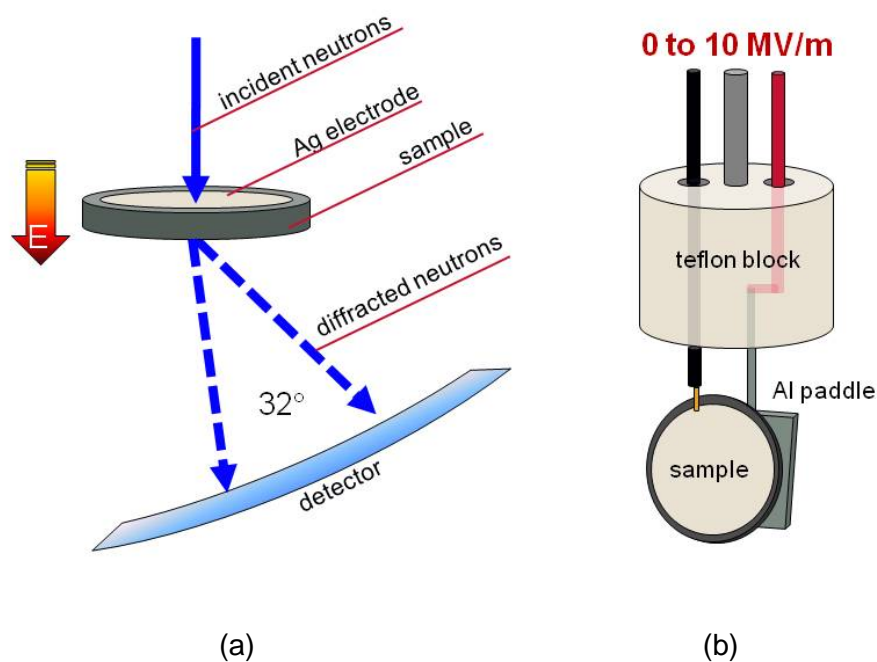
**Figure 3-7 (a)Schematic of the experimental geometry and (b) modified sample stick with sample for the E2 instrument at HMI, Berlin, Germany.**

### 3.5.2 Synchrotron Experiments

*3.5.2-1*     Response of structure to externally applied electric field.
            *ID11 at ESRF, Grenoble, France.*

Instrument Scientist: J. Wright

A single synchrotron experiment has been conducted at the European Synchrotron Radiation Facility (ESRF) on beam line ID11, the set up of which has been previously discussed.

The aim was to collect high resolution diffraction patterns relating to the structure of BFPT as a function of applied electric field to compare to the neutron data collected in 3.5.1-5. This was completed in a collaborative experiment with Dr. David Hall of Manchester University.

Thin (300 μm) disc samples of 7030 composition 28 mm in diameter were electroded by gold sputtering (40 nm) and placed in the synchrotron beam monochromated by a (111) orientated silicon single crystal to an energy 80.734 keV, or wavelength = 0.15372 Å.

The experiment was undertaken at room temperature and ambient pressure (as field application times are greatly reduced) and applied electric fields of 0 – 15 MV m$^{-1}$ in 0.5 MV m$^{-1}$ steps parallel to the 100 x 100 μm incident synchrotron beam for 10 minutes at a time.

The position sensitive Frelon CCD camera detector records the cone of diffracted X-rays emergent from the samples. This is then binned in to 10° sections and averaged. In this experiment 1 – 5 Å was represented by 2.4° span of the detector.

A powder of lanthanum hexaboride ($LaB_6$) was run as a reference for refinement of the instrumental parameters such as wavelength.
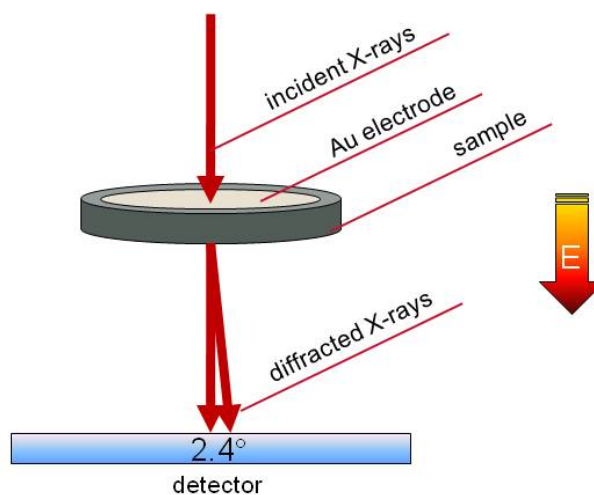


**Figure 3-8 Schematic of the experimental geometry on the E2 synchrotron instrument at the ESRF, Grenoble, France.**

# 4   RESULTS AND DISCUSSION

## 4.1   CHAPTER OVERVIEW

In this chapter the microstructure and phases of the BFPT system are investigated as a function of composition and temperature to create a comparative phase diagram to that of previous publications.

Microscopy and X-ray diffraction are used to develop a scientific case for using large scale facilities and the success or deficiencies of the techniques used are discussed.

Subsequent neutron and synchrotron experiments are investigated using structure refinements to convolute the data; characterising the magnetic structure per composition and temperature, presenting a magnetic phase diagram and any incommensurate order, as well as the systems response to elastic and electric external stimuli.

## 4.2   SAMPLE APPEARANCE

### 4.2.1   Bulk Polycrystalline Ceramics

Bulk samples used, synthesised using the mixed oxide method described in section 3.2.1, are shown below in Figure 4-1. Compositions $0.3 \leq x \leq 0.6$ are noticeably softer and browner than $x \geq 0.7$.



10 mm                    15 mm

(a)                              (b)
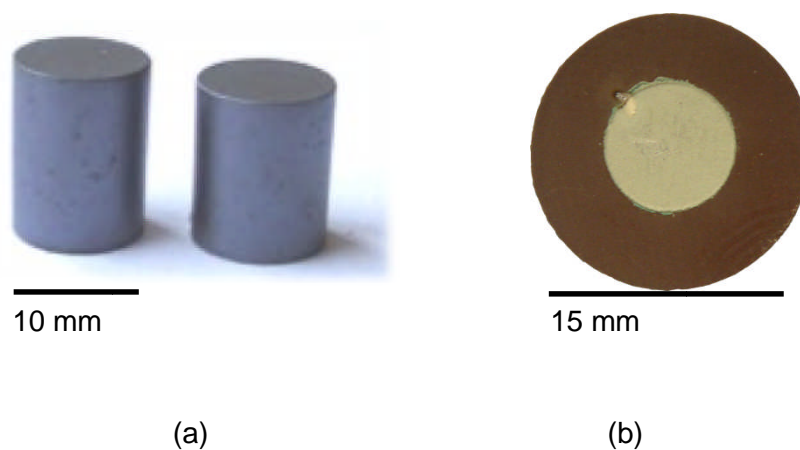
**Figure 4-1 Photographs of bulk polycrystalline ceramics in a) cylindrical form and b) disc (pellet) form. The disc is shown with a small silver electrode for electrical measurements.**

## 4.2.2  Self Disintegrated Powders

Upon fast cooling from the bulk sintering temperature (1000 °C) as described in section 3.2.1, it was observed that the 7030 BFPT composition spontaneously disintegrated. Other compositions also underwent micro cracking or disintegration to large agglomerates but the results were not reproducible. The sinter temperature was increased to 1100 °C for $x \leq 0.75$ and 1000 °C for $x \geq 0.8$ (much above this led to melting or evaporation of the sample) in an attempt to increase grain size and stimulate constant spontaneous fracture, as seen for the $PbTiO_3$ end member (Matsuo, 1966).

At the elevated temperatures, compositions where $0.3 \leq x < 0.60$ crumbled into powder featuring agglomerates of material. Compositions $x \geq 0.75$ failed to disintegrate but rather cracked or fractured, at most breaking apart into sintered blocks. Composition $x = 0.9$ was subsequently crushed for comparison. BFPT 6040 and 7030 however self disintegrated entirely into very fine, flour like consistency powder. The evolution of which is illustrated in the series of screen shots (Figure 4-2) for 7030,  taken from a video recording of a cylinder being placed on an alumina plate from the sinter at 1000 °C over 2.5 minutes, cooling in ambient air.



| | |
|---|---|
| 10 mm | 10 mm |
| 0 seconds (from furnace at 1100 °C) | 10 seconds at ambient temperature |
| 10 mm | 10 mm |
| 20 seconds | 30 seconds |
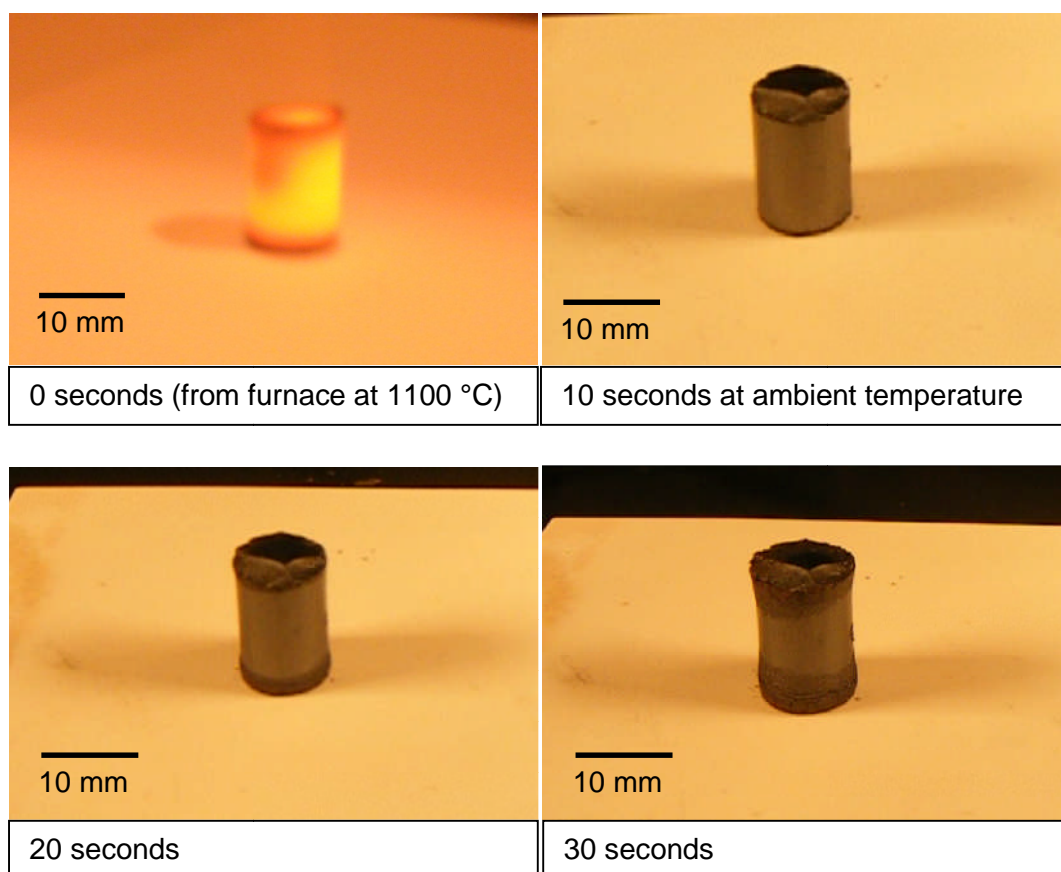
Continued overleaf...
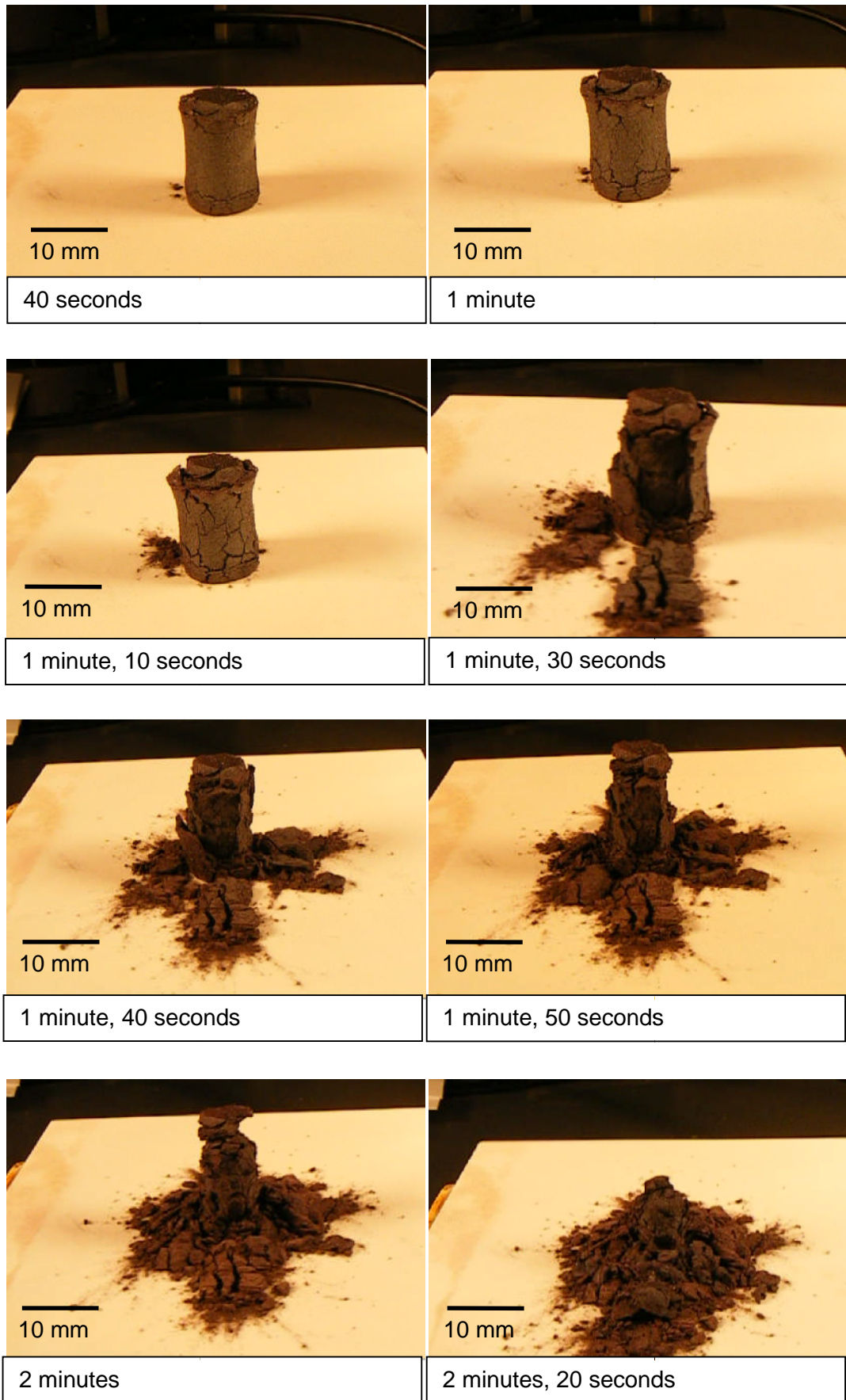
**Figure 4-2 A series of screen shots taken from a video recording over 2.5 minutes of a BFPT 7030 10 mm dia. cylinder cooling from 1100 °C after sinter.**

## 4.3   SURFACE VS. BULK INTERNAL STRESS COMPARISON

It is clear from previous publications that internal stresses and the tetragonal strain (Figure 1-43) within the BFPT system plays a significant part in its synthesis and properties (section 1.12.2).

To characterise the microstructure and to conduct phase analysis, scanning electron microscopy and XRD was employed respectively. This offered data to contribute to the overall project, and was also good experimental practice to ensure that the composition after the sinter was in keeping with the starting ratios for each batch.

Comparison of the X-ray patterns conducted on as-fired ceramics observed discrepancies from sample to sample. Diffraction data collected after annealing the ceramic samples, and with further comparisons made with disintegrated powders, presented clear evidence that the samples were heavily influenced by the internal stresses reported and a study to characterise this was completed. Examples of diffraction patterns from laboratory XRD can be seen in Figure 4-3 and Figure 4-4 for polycrystalline and disintegrated powders respectively.

It is note worthy that a trace amount of a non BFPT phase is seen in 9010, matched to a non-perovskite contribution which is known to plague synthesis of the BFO end member by destabilising the ferroelectric distortion (Catalan, 2009).

To remove the effects of stoichiometry, a composition independent case-study is presented on the largest c/a ratio contributing fraction x = 0.7 (Sai Sunder, 2005).

Table 4-1 shows the samples and their physical state from the differing processing routes used for the study, as well as the type of diffraction pattern collected.

**Table 4-1 Summary of samples of 0.7 $BiFeO_3$ – 0.3 $PbTiO_3$ for case study**

| Sample | Form | Dimensions | Thermal Routine | Diffraction Source |
|--------|------|------------|-----------------|--------------------|
| *0.7 $BiFeO_3$ – 0.3 $PbTiO_3$* |
| 1 | Self-disintegrated powder | Particulates | 1100 °C Sinter + Fast Cool (900 °C/hr) | Lab X-ray (Cu) |
| 2 | Dense Ceramic | 0.4 mm thick disc | 1000 °C Sinter + Slow Cool (20 °C/hr). Polish. | Lab X-ray (Cu) |
| 3 | Dense Ceramic | 0.4 mm thick disc | 1000 °C Sinter + Slow Cool (20 °C/hr) + Anneal 750 °C after polish. | Lab X-ray (Cu) |
| 4 | Dense Ceramic | 10 mm thick cylinder | 1000 °C Sinter + Slow Cool (20 °C/hr). Polish | Synchrotron (0.1536 Å) |
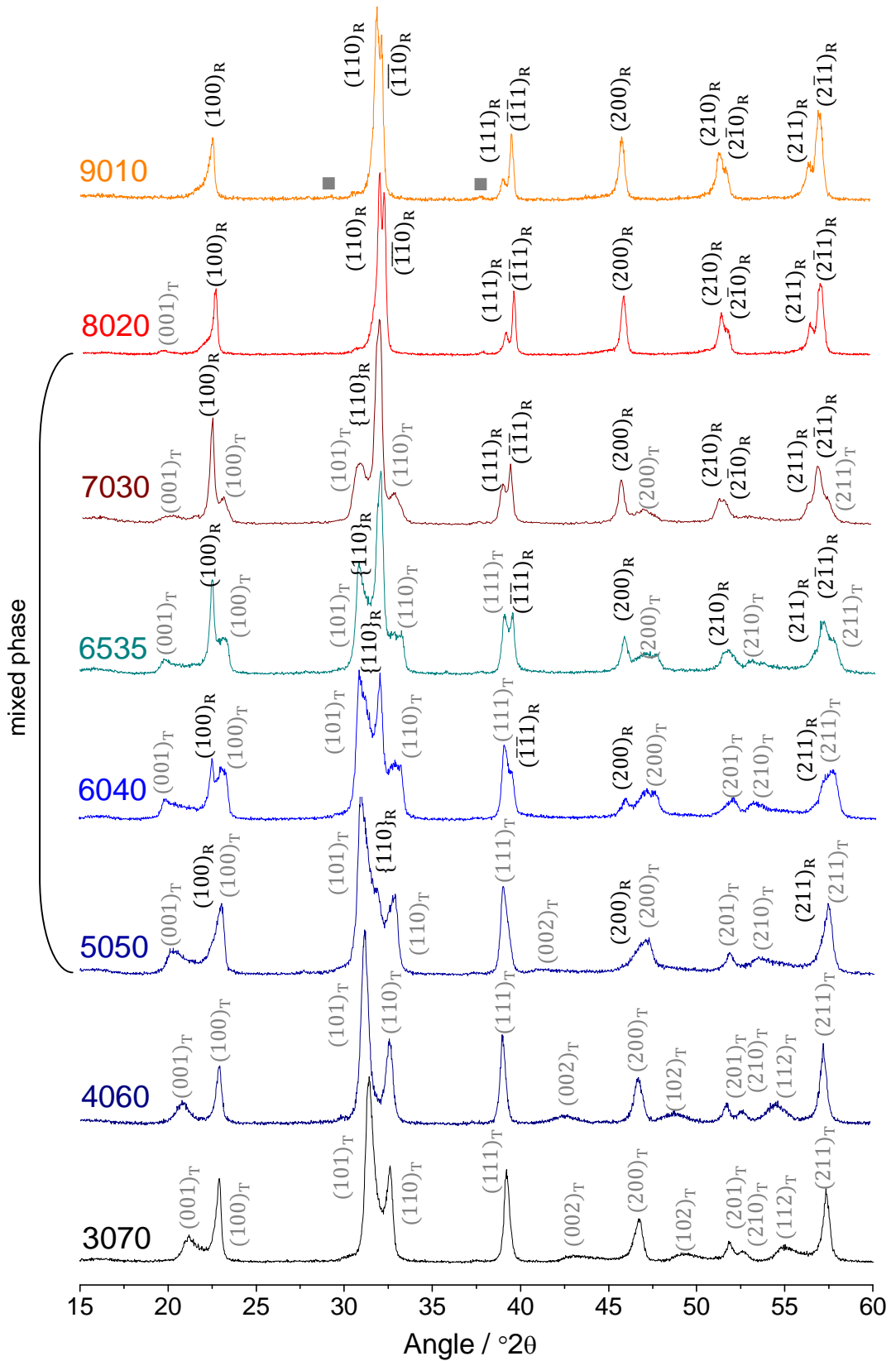
**Figure 4-3 X-ray diffraction traces taken from the surface of bulk polycrystalline ceramics xBiFeO$_3$ – (1-x)PbTiO$_3$ where 0.3 ≤ x ≤0.9. The patterns have been indexed using P4mm (T) and R3c (R) space groups in the pseudo-cubic setting. ■ represents a non-perovskite phase (Catalan, 2009).**
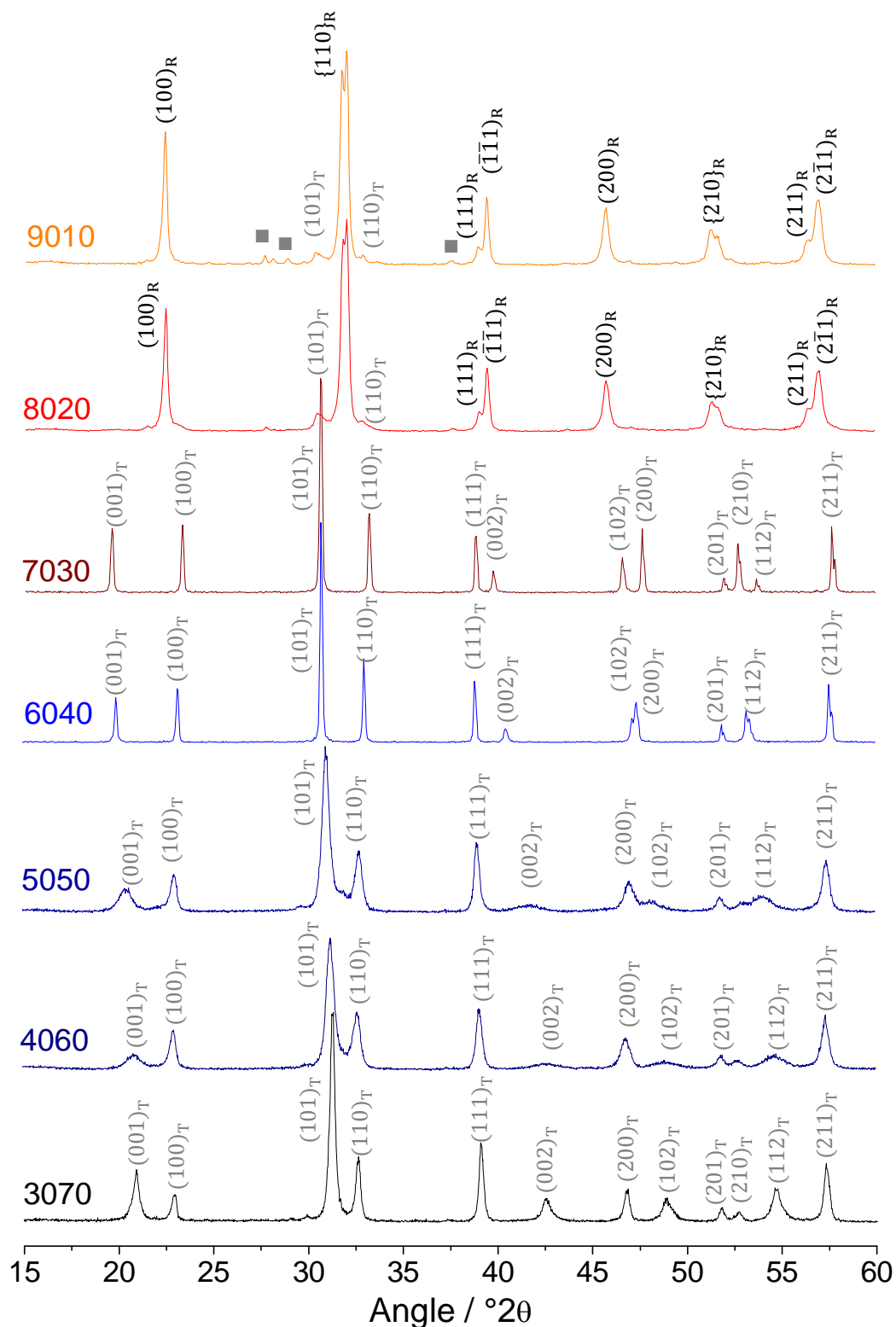
**Figure 4-4 X-ray diffraction traces from fast cooled ceramics (>900 °C/hr) of xBiFeO3 – (1-x)PbTiO3 where 0.3 ≤ x ≤0.9. The patterns have been indexed using P4mm (T) and R3c (R) space groups in the pseudo-cubic setting. ■ represents a non-perovskite phase (Catalan, 2009).**
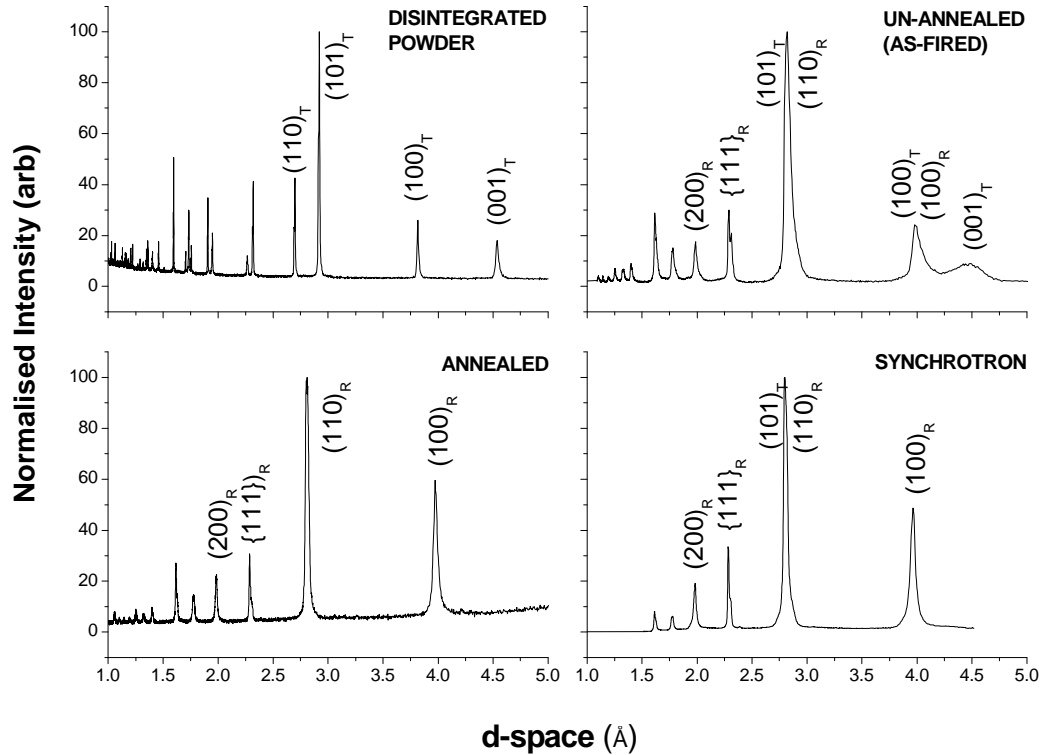
**Figure 4-5 Diffraction data collected for the four samples of BFPT 7030 in various forms, normalised to the highest peak intensity.**

The patterns in Figure 4-5 illustrate the diffraction data collected for the 7030 BFPT case-study. They clearly show contrasting peak broadening, attributed to various levels of internal stress present in each sample. Structure refinement for each sample using FullProf was conducted for quantitative phase analysis, using R3c (hexagonal setting) and P4mm space groups, and to calculate inherent microstrain ($X$) within the material. Initially, refinement of a standard "stress free" polycrystalline sample of silicon for XRD, and $LaB_6$ powder for synchrotron, was completed with the same experimental setup to equate the effects of instrumental optics.

Qualitatively, the disintegrated (DS) powder is observed to exhibit purely tetragonal reflections with negligible broadening due to strain, concluded by the particularly sharp peaks corresponding to the P4mm space group. The as-fired disc however suggests mixed tetragonal and rhombohedral phases with large internal stresses developing within the material observed by the broadening of the peaks, particularly in the tetragonal phase from the $(001)_T$ thought to relate to the large lattice distortion and mismatch.

This was confirmed by structure refinement, using the Rietveld method, of the disintegrated powder (Figure 4-6) and as-fired samples (Figure 4-7). Using the

methodology in Appendix A, it was possible to successfully fit (chi$^2$ = 9.85) a wholly tetragonal P4mm phase with relatively negligible strain to the powder pattern ($X$ = 0.38 %), whilst the as-fired disc XRD analysis calculates ~ 25.8(5) % tetragonal phase concentration.

The annealed reflections compared to that of the as-fired disc, are observed to have lost the tetragonal contributions and structure refinement (Figure 4-8), again using constraints outlined in Appendix A, results in good agreement indices (chi$^2$ = 2.59) for the presence of a purely rhombohedral phase, with lesser effects of microstrain ($X$ = 0.87 %) compared to the as-fired sample ($X$ = 1.17 %)).

Results of the synchrotron model refinement (Figure 4-9) yields a microstrain ($X$ = 1.66 %). However inaccuracies lie within making quantitative evaluations for the as-fired and synchrotron samples, such as phase ratios or strain values, from structure refinement. The large degree of broadening in the diffraction reflections made refinement of the models for these two samples particularly difficult, as the broadening tended to exceed the limits the model would accept for almost all reflections. Subsequently the program often struggled to refine the atomic isotropic temperature factors (B$_{iso}$) yielding unrealistic, large negative values.

The strain calculations in general must be used cautiously, and perhaps only relatively, as not only were the some of the refinements conjectural, but the values and errors associated with the evaluated strains are not comparable to other diffraction experiments on other instruments (Von Dreele, 2009). Varying optics, in terms of XRD and synchrotron radiation, prohibit any accurate, absolute value correlation in associated strains; as well as the definition of microstrain calculated by FullProf is ¨Lorentzian isotropic strain.¨ This is unique to the Thomson-Cox Hastings pseudo-Voigt profile shape function (Finger,1994) which allows line broadening to be more accurately modelled (McCusker, 1999) taking into account the axial divergence seen in the peak edges of the XRD patterns. This isotropic strain coefficient, describes only strain independent of crystallographic orientation, but in reality could develop preferably in certain directions. Tentatively, the results of the calculated microstrain from the most dominant phase are plotted in Figure 4-10 for comparison. A trend is observed with the largest strains being present in the synchrotron and XRD as-fired samples, and the least being present in the spontaneously disintegrated powder.

Strain aside, the synchrotron sample that has been exposed to the same synthesis route as the as-fired disc, shows other considerable differences, such as observing greater concentration of rhombohedral phase. The parameters from all the structure refinements are summarised in Table 4-2.
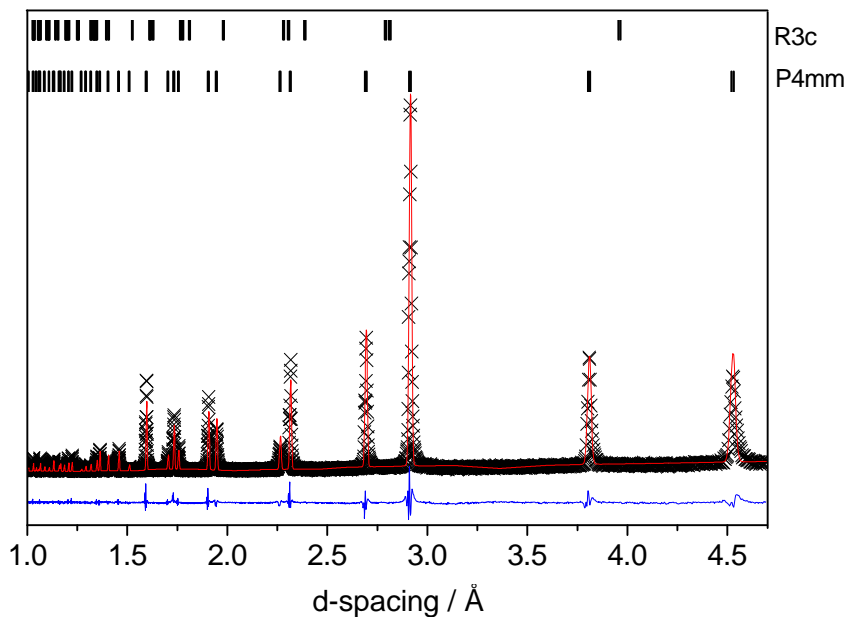
**Figure 4-6 FullProf structural refinement for the 7030 BFPT disintegrated powder from laboratory X-ray diffraction data. A number of points have been removed for clarity. Observed data is shown by crosses (black), and the (red) line the refined model. The (blue) line below shows is the difference plot (chi$^2$ = 9.85).**
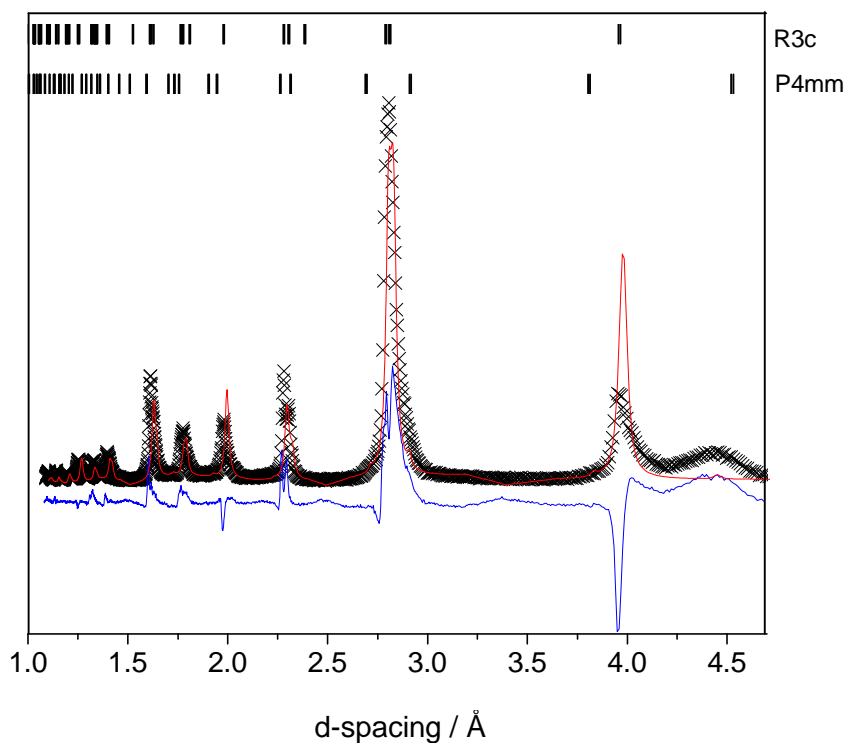


**Figure 4-7 FullProf structural refinement for the 7030 BFPT as-fired disc from laboratory X-ray diffraction data. A number of points have been removed for clarity. Observed data is shown by crosses (black), and the (red) line the refined model. The (blue) line below shows is the difference plot (chi$^2$ = 35.6).**
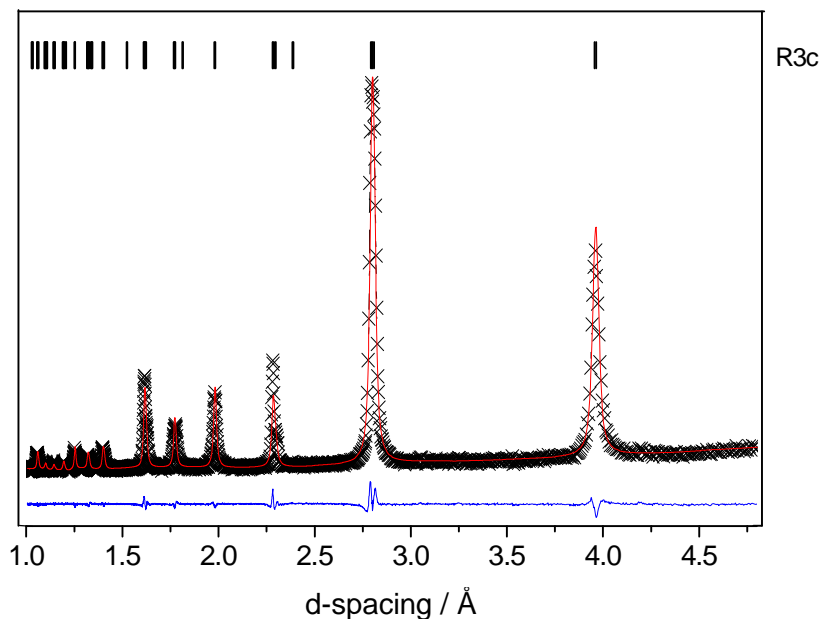
**Figure 4-8 FullProf structural refinement for the 7030 BFPT annealed disc from laboratory X-ray diffraction data. A number of points have been removed for clarity. Observed data is shown by crosses (black), and the (red) line the refined model. The (blue) line below shows is the difference plot (chi$^2$ = 2.59).**
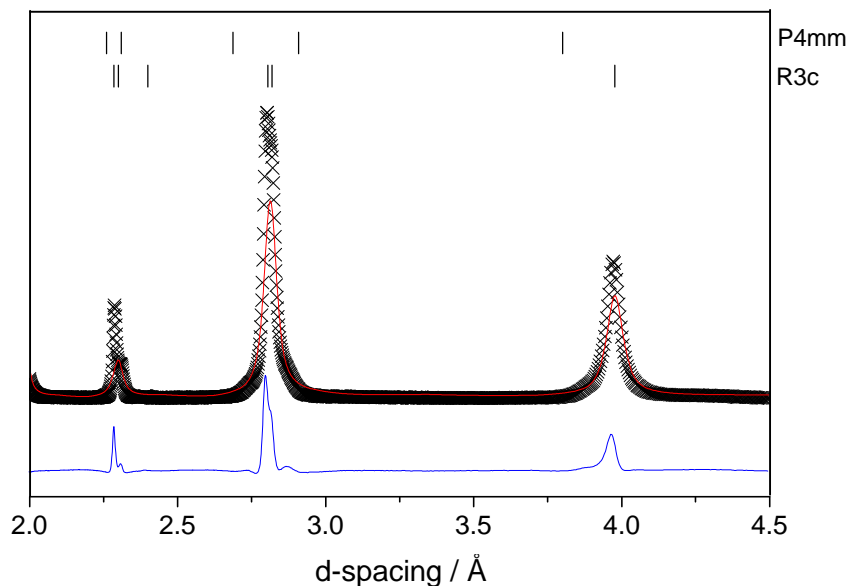


**Figure 4-9 FullProf structural refinement for the 7030 BFPT cylinder from synchrotron diffraction data. A number of points have been removed for clarity. Observed data is shown by crosses (black), and the (red) line the refined model. The (blue) line below shows is the difference plot (chi$^2$ = 10.6).**
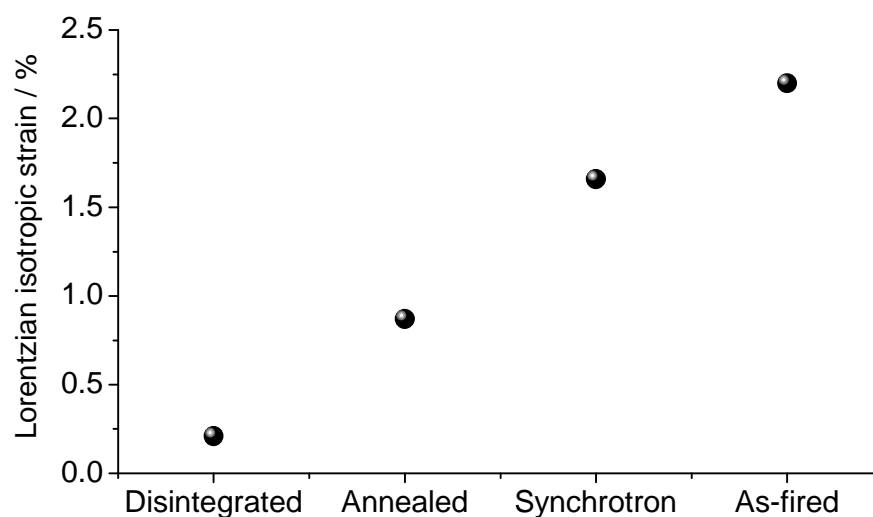
**Figure 4-10 Lorentzian isotropic strain calculated from FulProf structure refinement for 7030 BFPT from various diffraction experiments.**

**Table 4-2 Parameters generated from structure refinement of 7030 BFPT in bulk and powder forms, of various X-ray diffraction experiments**

| Experimental sample / technique | Parameter | | | | |
|---|---|---|---|---|---|
| | $a$ / Å | $c$ / Å | Primitive unit cell volume / Å$^3$ | $c$ /$a$ ratio (P4mm) | R3c / P4mm phase fraction |
| Disintegrated powder / XRD | 3.813(7) | 4.531(6) | 65.88 | 1.19 | 0.00 |
| As-fired disc / XRD  P4mm | 3.824(3) | 4.489(2) | 65.64 | 1.17 | 0.742(9) |
| As-fired disc / XRD  R3c | 5.577(1) | 13.651(1) | 61.28 | | |
| Annealed disc / XRD | 5.591(4) | 13.810(2) | 62.29 | - | 1.00 |
| As-fired cylinder / synchrotron  P4mm | 3.892(2) | 4.311(5) | 65.30 | 1.11 | 0.876(5) |
| As-fired cylinder / synchrotron  R3c | 5.593(6) | 13.851(1) | 62.74 | | |

* R3c is in the hexagonal setting except the primitive unit cell volume, which is in pseudocubic space.

Penetration depth of the incident radiation, calculated using the HighScore Plus mass-absorption calculator (based on data from Kluwer, 1995), predicts for synchrotron light of λ = 0.1536 Å is up to 3.215 mm, where as for Cu Kα radiation to be between 2.7 and 15.7 µm perpendicular to the surface over the 15-60° 2θ range. This suggests that the higher energy synchrotron, and therefore increasingly penetrative, radiation diffracts with more of the sample that is representative of the bulk crystallography, whereby XRD can only be attributed to diffraction solely from the top layer of grains on the sample surface (Figure 4-11).

Surface morphology has been shown to be easily effected by processes such as mechanical polishing in ferroelectric ceramics (Bogardus, 1965), increasing residual stresses in the material imparted from the mechanical energy. This is perhaps a prominent reason in the large discrepancies in the BFPT phase diagram presented in Table 1-9, as all of the crystallographic data was collected with copper anode laboratory XRD and would have only been able to detect diffraction from the top ~3 grains, based on previous microstructural analysis (Bell, 2007).
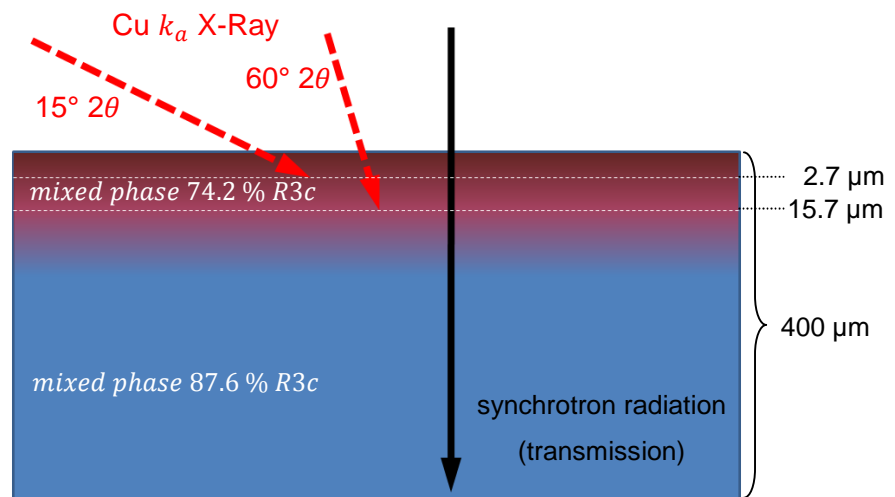


**Figure 4-11 Graphic illustrating the penetration of X-ray radiation normal to the sample surface.**

The large spontaneous strains seen in the as-fired discs tetragonal phase, both from probing the bulk with synchrotron and the surface with XRD, inherently yields a larger volume change from the paraelectric cubic structure than the rhombohedral phase. Thus on cooling through the ferroelectric Curie point, to relieve the spontaneous strain energy at the onset of the structural transition, the materials on the tetragonal side of the MPB (x < 0.8 from Figure 4-3) see some individual grains assume the smaller volume rhombohedral symmetry. This transformation of phases is seen in thin films of the $BiFeO_3$ end member where epitaxial clamping to a $SrTiO_3$ substrate

causes a tetragonal structure distortion rather than the rhombohedral form found in the bulk (Wang, 2003) due to little difference in the energy associated in forming either phase (Bell, 2007).

The transformation from tetragonal to rhombohedral is more dominant in the bulk, as seen from the synchrotron data, where the grains have limited space due to competing neighbouring grains. On the surface, the grains are not clamped and are therefore free to take on the larger volume phase. This is expected to be exacerbated by mechanical grinding and polishing imparting stress energy.

Annealing the ceramic further acts to relieve stress within the mixed phase surface crystal structure. Where the rhombohedral volume is highly compressed (Table 4-2) from lattice mismatch, the highly distorted and constrained tetragonal phase present in the as-fired sample, is transformed to a wholly rhombohedral crystallography with reduced microstrain.

These stresses could equally result in microcracking (as seen in x $\geq$ 0.75 from section 4.2.2) or spontaneous disintegration from thermal shock, resultant from fast cooling through the ferroelectric Curie point. This is well documented for the $PbTiO_3$ end member, due to the tetragonal symmetry generating anisotropic contraction of the unit cell on cooling (Sai Sunder, 1995), and the results for the disintegrated sample support this for the BFPT system.

### 4.3.1 Conclusions

The large range of phase coexistence seen from X-ray diffraction patterns is proposed to be due to an internal stress relief mechanism, associated with the large spontaneous strain inherent in the tetragonal phase on cooling through $T_C$ transforming to the smaller volume rhombohedral phase.

This is pronounced in the bulk which has been probed with penetrative synchrotron radiation, where as surface crystallography is observed to exhibit higher concentrations of tetragonal phase, as the grains at the surface are unclamped.

However, changes in surface crystallography are readily induced by mechanical grinding and polishing imparting stress into the lattice, the effects of which can be relieved by annealing the sample. This also helps to explain the reason for the fluctuations in the reported MPB position in Table 1-9 previously.

Conjectural structure refinement only allows comparison to other experiments to be qualitative, but it does serve as a warning that laboratory XRD is not enough to characterise the crystallography of this highly stress dependent BFPT system. It is important that future work be completed using synchrotron or neutron radiation, which can penetrate the material and collect data from the volume of the sample.

## 4.4   MICROSTRUCTURAL ANALYSIS

Microstructure of both the polycrystalline and disintegrated powders has been imaged using scanning electron microscopy in both secondary electron (SE) and backscattered (InLens) mode.

Average grain size was calculated by employing image processing software ImageJ (National Institutes of Health, U.S. Dept. of Health (www.nih.gov), Maryland, USA). After an image has been loaded and a contrast threshold set, the software can be used to identify and quantify particles.

### 4.4.1   Bulk Polycrystalline Ceramics

From secondary electron images, made into 3 dimensional anaglyphs in Figure 4-12 (standard images can be found in Appendix B), it is evident that there is a relationship between grain size and composition in the BFPT system. Summarised in Figure 4-13, a general, small increase with increasing bismuth ferrite contributions is observed with a step change present at 8010 and again for 9010, where the previously sub microns grains increase by nearly 6 times, and a perturbation from the higher BFO content trend is presented at 7030, having an average grain size of 0.78 μm and a maximum grain size of 1.23 μm.

It is important to raise here the difference in sintering temperature for the 8020 and 9010 compositions is 50 °C lower than the rest of the samples at 1000 °C. This was chosen due to density measurements indicating the higher bismuth content compositions required lower temperatures to minimise volatility and improve density (Bell, 2007). Despite this change, the 8020 follows the trend of grain sizes, with good agreement to that of 7525, but the 9010 step can probably be explained by the presence of a non-perovskite phase. These are described in the literature as $Bi_{46}Fe_2O_{72}$ (Kumar, 2000), $Bi_2O_{2.75}$ (Komarneni, 1996) and most commonly $Bi_2Fe_4O_9$ (Catalan, 2009). This is only seen significantly in the x = 0.9 composition and could be attributed to the large grain size, although there is little literature to support this.

With the presence of wholly or predominantly rhombohedral phase in the bismuth ferrite rich 8020 and 9010 compositions, the increased grain size can be attributed to a lower stress state within the lattice, reducing the likelihood of dislocations and defects within the crystallography that could act to pin the grain boundaries and encourage growth.

Within the other compositions however, where the concentration of tetragonal phase is not negligible, it has already been seen how spontaneous tetragonal strain can affect the crystallography within the mixed phase region.
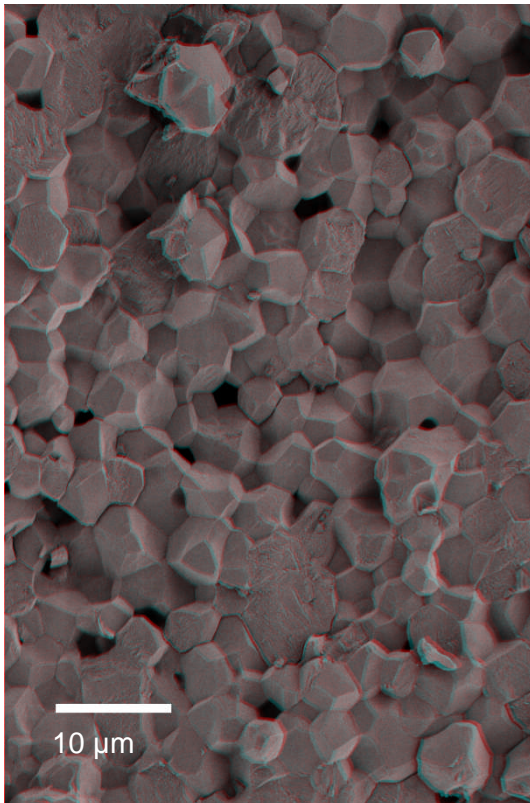
9010 | SE, 3 kV
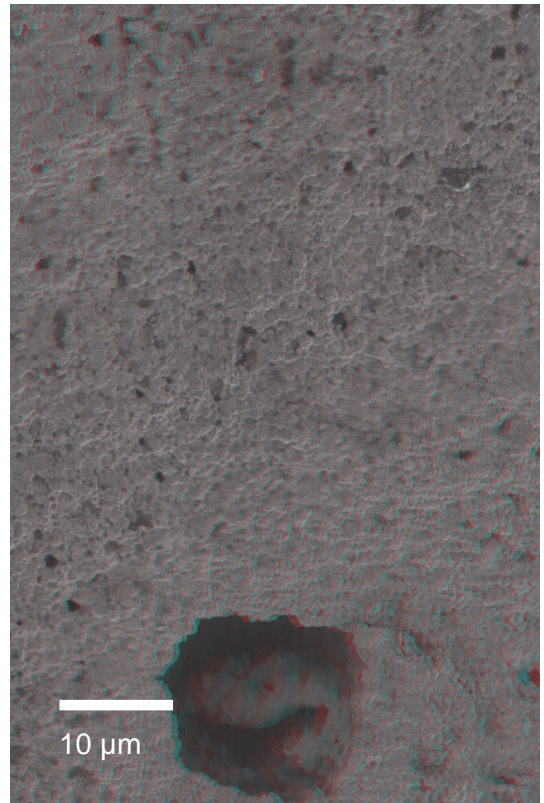
8020 | SE, 3 kV
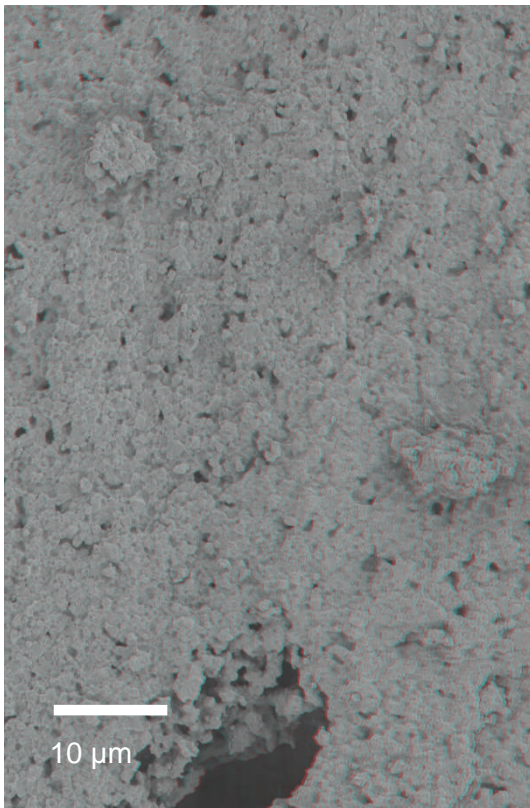
7525 | SE, 3 kV
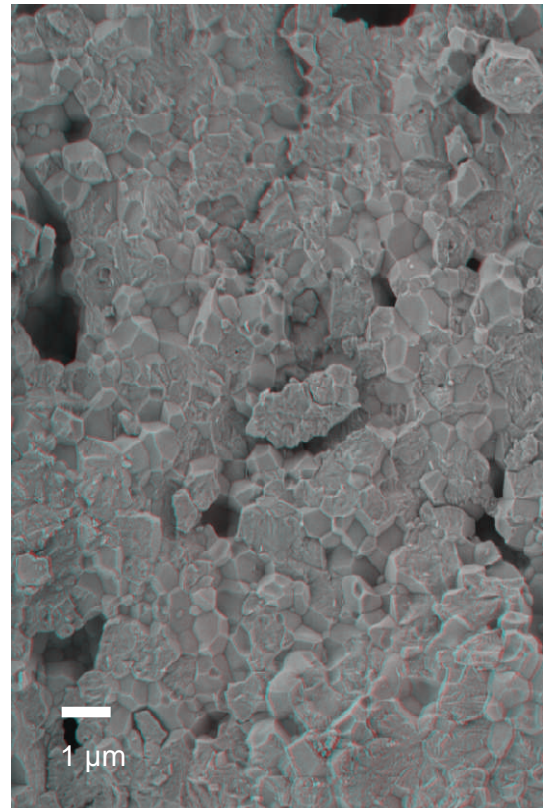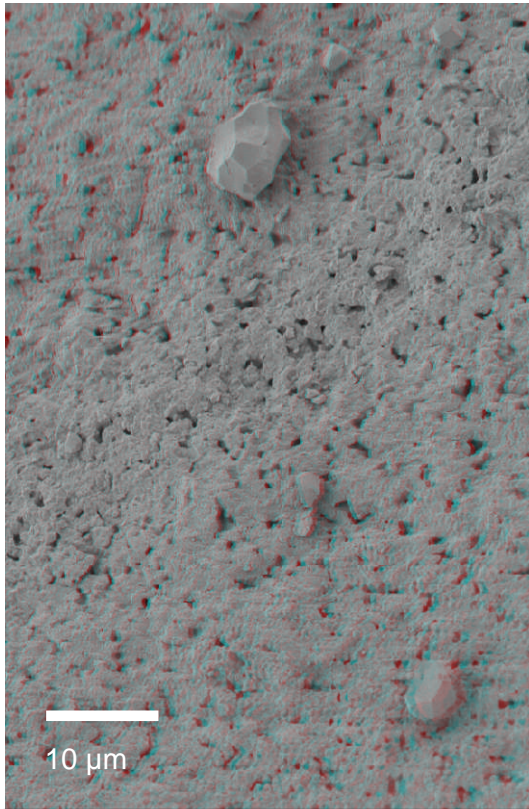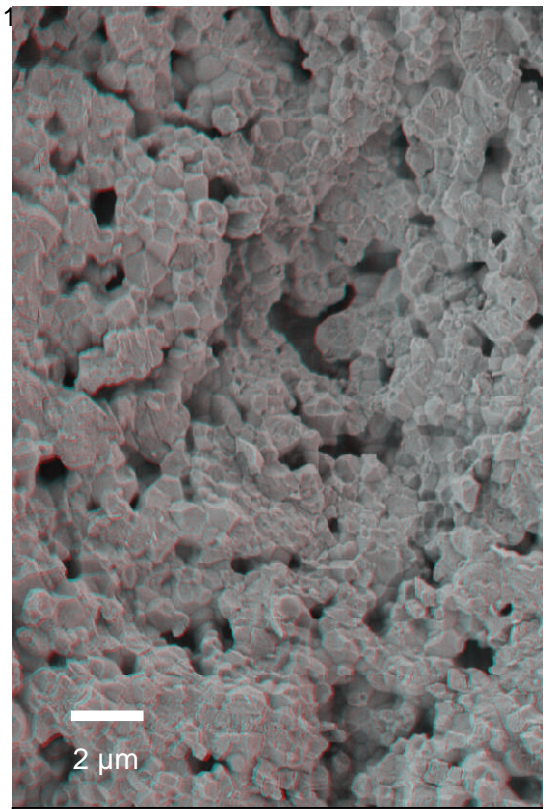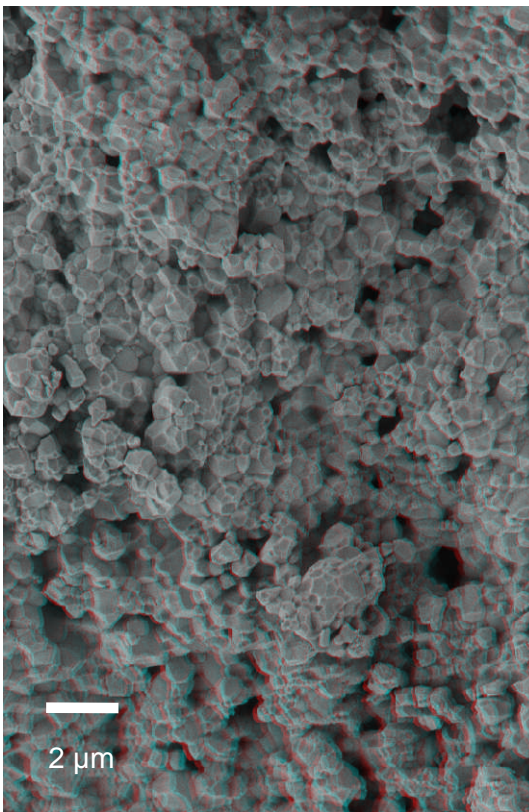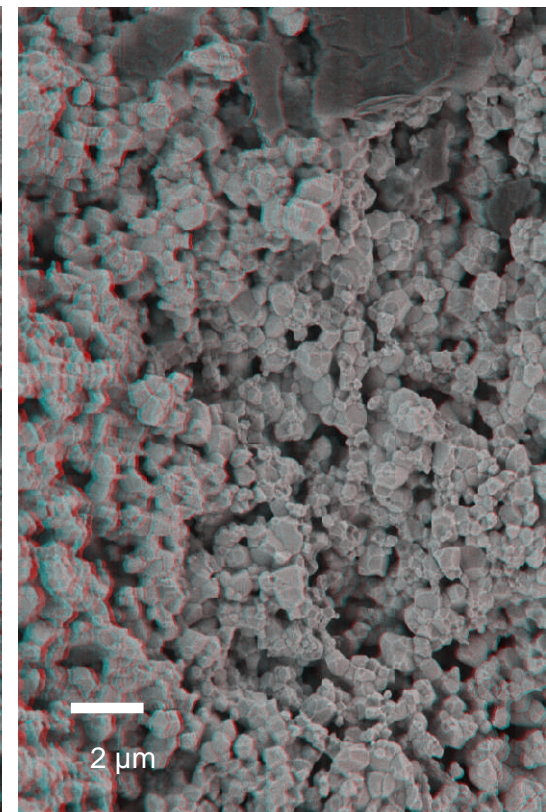
7030 | SE, 3 kV

**Figure 4-12 Scanning electron anaglyphs of fractured BFPT sintered ceramics using secondary electron (SE) imaging.**
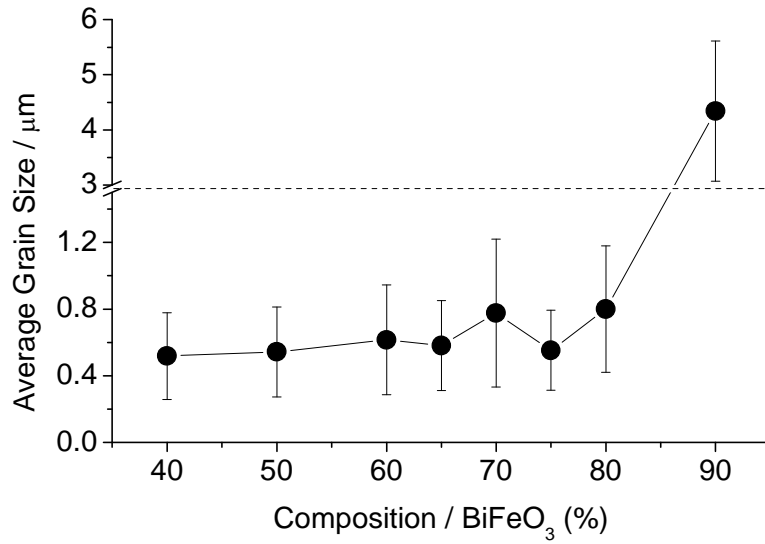
**Figure 4-13 Plot of average grain size as a function of composition for slow cooled from the sinter, bulk polycrystalline ceramics determined from SEM image analysis. The vertical bars represent the minimum and maximum grain sizes present in each micrograph.**

This tetragonal strain is shown to be at maximum in the 7030 composition (Sai Sunder, 1995) (Smith, 1968) from Figure 1-42, with the increased volume associated with the tetragonal phase.

## 4.4.2 Disintegrated Powders

As discussed in section 4.3, whilst the slow cooled samples compensate internal stress by transformation into the smaller primitive cell volume R3c (Comyn, 2008) and form solid ceramics. The driving force behind the disintegration is thought to be tetragonal distortion introduced when cooling through $T_C$, applying sufficient stress that the increased energy can no longer be compensated for by transformation to the rhombohedral phase; so is relieved by self-disintegration (Sai Sunder, 1995) (Bell, 2007). Characterisation of the various degrees of disintegration was again conducted with SEM, illustrated in Figure 4-14. Average grain size was also calculated by employing ImageJ and plotted with the maximum and minimum grain sizes, illustrated in Figure 4-15.

A similar trend is seen in grain size compared to the bulk ceramics but in reverse, and for compositions x ≤ 0.7, grain sizes are ca. 10 times larger. Here the smaller grain sizes exist in the higher BFO concentrations, 0.75 ≤ x ≤ 0.9, which are also seen to be in the form of fractured sintered ceramic. The fast cooling from the sinter has failed to fully disintegrate these materials, and has undergone limited grain growth from the elevated sinter temperature compared to the monolithic samples in 4.4.1 previously (the x = 0.9 ceramic due to manual crushing with pestle).

Little or no disintegration is seen in the x = 0.8 and 0.9 compositions respectively. The average grain sizes yielded for these samples are 1.19 μm for 8020 and 0.87 μm for 9010 with a relatively small size distribution compared to the more lead titanate rich compositions. This is in excellent agreement with the observations of pure lead titanate sintered ceramics (Matsuo, 1966), which suggests that it is the tetragonal phase driving the intergranular fracture.

A distribution of grain sizes is seen through 0.3 ≤ x < 0.6 from 6.7 to 10.1 μm over a steady gradient with a perturbation again seen at x = 0.7. This composition is seen to develop intergranular separation through fast cooling from an elevated sinter temperature, yielding large, 13.2 μm (average) grains but with some as large as 20 μm in diameter. The process (Figure 4-2) is shown to happen completely independently and in a period of less than 2.5 minutes. It is suggested this is due to the large tetragonal distortions developed when cooling through $T_C$, but also on exceeding a critical grain size (Matsuo, 1966) by increasing the temperature of the sinter. This is seen in the literature for the $PbTiO_3$ end member. Sub 1 micron grains in lead titanate ceramics are reported to remain intact from the sinter, whereas samples where grains exceed 10 μm become dissociated by intergranular fracture. This is clearly a mechanism that can be extracted from the data in Figure 4-15, as the larger grain size samples exhibit increased levels of disintegration (or decreased level
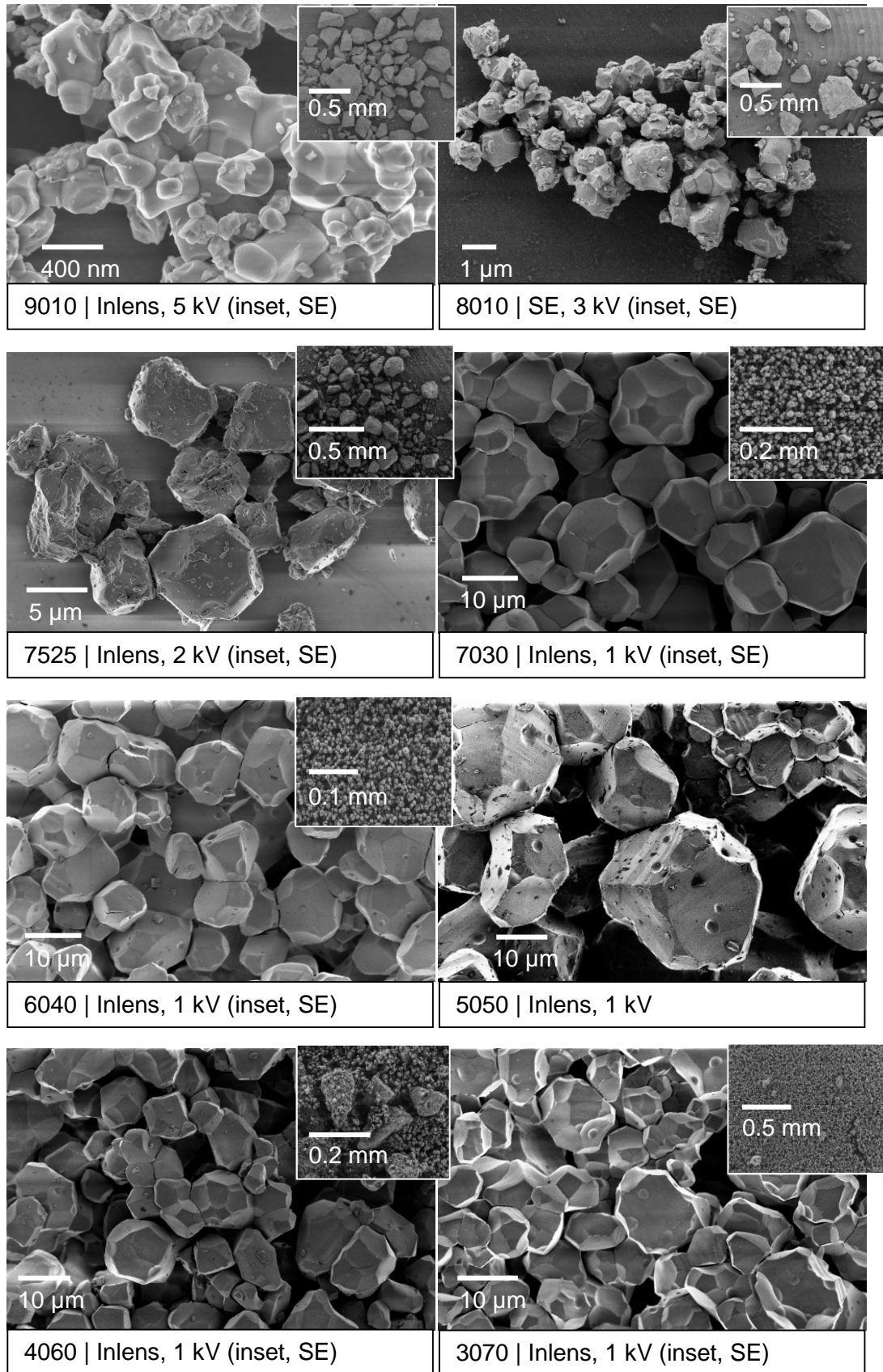
**Figure 4-14 Scanning electron micrographs of BFPT fast cooled ceramics using In lens and secondary electron (SE) imaging. The inset images are lower magnification to observe the form of the ceramic.**
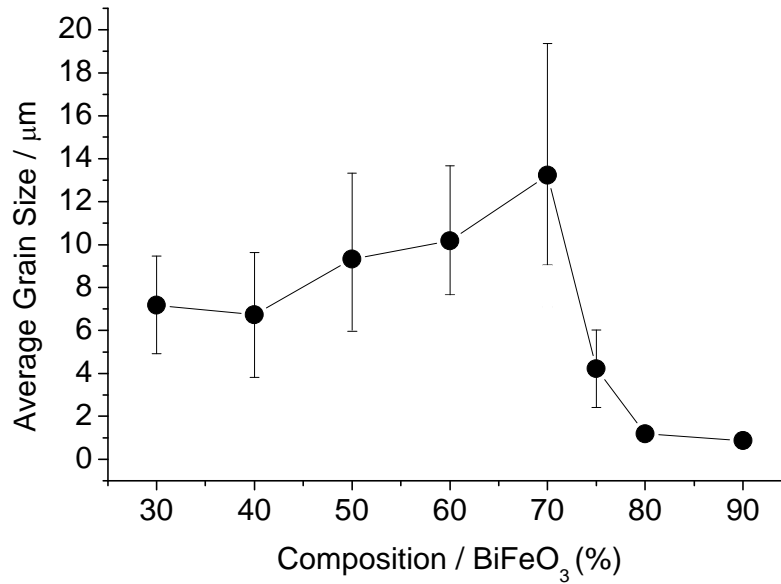
**Figure 4-15 Plot of average grain size as a function of composition for fast cooled ceramics from the sinter. Disintegrated powders (0.3 ≤ x ≤ 0.7) and fractured ceramics (0.75 ≤ x ≤ 0.9) grain size is determined from SEM image analysis. The vertical bars represent the minimum and maximum grain sizes present in each micrograph.**

of observed agglomerates) is observed.

A critical grain size could then be envisaged for BFPT, above which it is energetically favourable to relieve the stress by intergranular fracture (Matsuo, 1966) (Evans, 1978) (Bell, 2007) in the tetragonal phase. Evans, 1978, discusses this and can be summarised in Equation 4-1;

$$l_c = \frac{2\gamma}{3U_s}$$

Equation 4-1

where $l_c$ is critical grain facet length, $\gamma$ is the grain boundary fracture energy and $U_s$ the magnitude of the strain energy at the criticality. Intergranular separation is therefore most likely to occur in the compositions with larger grain sizes (Bell, 2007), as this decerases the energy required at which fracture can occur.

For the system of BFPT, the critical grain size can be approximated to ca. ~ 7 µm, as none of the sintered ceramics are seen to exhibit grains larger than this, but the fast cooled compositions show disintegration from 0.3 ≤ x ≤ 0.7, where below x = 0.6 the average grain sizes are above 7 µm, but the range of crystallite sizes below average cross this critical size resulting in only partial disintegration. At x = 0.6 and 0.7

however, all of the grains are above the 7 μm threshold resulting in complete spontaneous disintegration to crystallite size particles.

### 4.4.3 Conclusions

It is apparent that the microstructure of BFPT is sensitive to composition due to the spontaneous strain in the tetragonal lattice. On cooling through $T_C$, the lattice crystallography transforms from a cubic perovskite paraelectric phase, to a ferroelectric tetragonally distorted structure.

The tetragonal distortion induces a stress within the system by constraining the neighbouring unit cells, exacerbating the internal strain. The fracture energy of the forming grains is then related to their size, where above a critical dimension, the grain boundary fracture energy is sufficiently decreased (Equation 4-1) that it is exceeded by the stress energy on the lattice. This results in spontaneous intergranular disintegration, and is observed in the x ≤ 0.7 compositions, which are sintered at an elevated temperature to their bulk sample counterparts, increasing the grain size past the proposed ~ 7 μm critical grain size.

In the instance that the grain size is reduced, the grain boundary fracture energy is increased, resulting in the energy considerations for fracture to not be fulfilled. Instead the system is driven to relieve the internal stress, developed by the tetragonal strain, by partial phase transformation to the smaller primitive volume rhombohedral phase. This allows dense, sintered ceramics to form, but the lattice mismatch within maintains a constant level of increased internal strain and stress which is observed by line broadening in X-ray diffraction patterns.

This mechanism is observed in the $PbTiO_3$ end member in the literature (Matsuo, 1966).

The stress state can be further modified by imparting energy into the system by mechanical grinding and polishing. This increases the strain in the surface grains, inducing a preferentially tetragonal phase as the surface is unclamped and can overcome the energy associated; observed in bulk samples by surface X-ray diffraction. Highly penetrative synchrotron radiation however allows a significant increased ratio of the bulk to surface to be probed, and is shown to exhibit a higher fraction of rhombohedral phase, where the competing phases are clamped by neighbouring grains. Annealing relieves the surface stresses, encouraging transformation of the system to adopt an increased rhombohedral phase concentration.

The whole process is summarised graphically in Figure 4-16.

It is evident therefore that the structure is highly dependent on internal stress conditions, and it is proposed that this is the reason for the discrepancies in the

literature for the observed morphotropic phase boundary, as each author describes varying processing routes which will adopt different states of stress, and therefore phase.
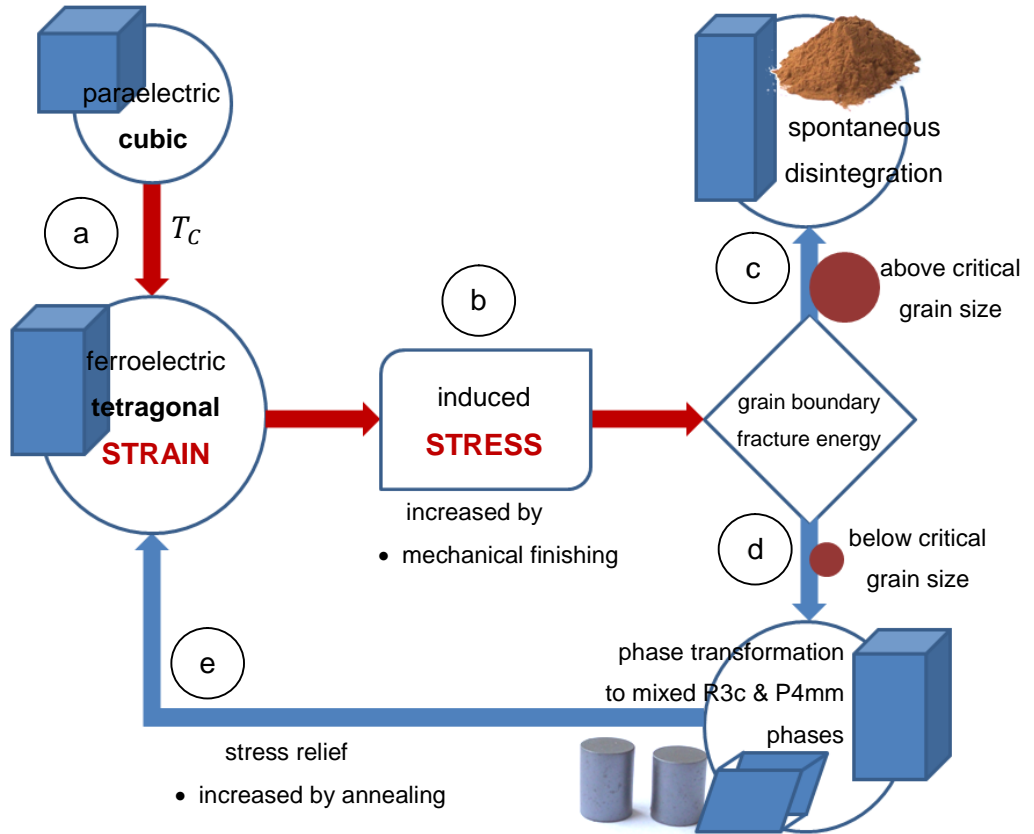


**Figure 4-16 Graphic summarising the mechanism of internal strain influencing the synthesis and crystallography of the BFPT system.**

## 4.5   STRUCTURAL PHASE ANALYSIS

### 4.5.1   Motivation

Neutron diffraction has been used to complete phase analysis of the BFPT system, principally due to the penetrative nature of neutrons reducing the proportion of diffraction representative of the surface and allowing a probe of the bulk crystallography of sintered polycrystalline samples, as well as be able to observe reflections pertaining to lighter titanium and oxygen atoms as well as magnetic contributions.

### 4.5.2   Bulk Polycrystalline Ceramics

Neutron diffraction of the polycrystalline samples imaged using the higher resolution structural C-bank of Polaris is presented in Figure 4-17, and indexed using the space groups P4mm for tetragonal, and R3c (pseudocubic) for rhombohedral phase contributions. The pseudocubic setting is used for easier comparison of planes.

It is clear from the traces broad peaks that internal strain within the lattices is still present in the bulk. Contributions from particle size can be considered negligible as grain size is known to be larger than 100 nm (2.4.1-3), however defects within the material may well give broadening contributions simulating sub 100 nm crystallites, but would not show the level of broadening observed in the lower d-spaces seen in Figure 4-11 (Williamson, 1953).

The broadening of the diffraction peaks prevents accurate structure refinement using the Rietveld method as discussed previously in the 7030 case-study (section 4.3).

Instead least squares profile fitting (WinPlotR), employing an instrument resolution function for the Polaris C-bank, of the (200) and (002) reflections (confirmed by (100) and (001) data that is discussed later) to determine $a$ and $c$ lattice parameters respectively, as well as peak area integration of relevant rhombohedral and tetragonal reflections has been conducted to estimate phase fractions. These are summarised in Table 4-3. The composition 7525 shows tetragonal peak presence but too weak in concentration for peak fitting.

Figure 4-18 illustrates the difference in lattice parameters between the surface X-ray diffraction patterns, published by Sai Sunder (1995) and from experiments discussed previously in Figure 4-3, and with the neutron data collected from the Polaris instrument (Figure 4-17) on bulk polycrystalline samples.

The $a$ lattice parameter for the rhombohedral phases are in good agreement; with the bulk, represented by the penetrative neutron diffraction, being only slightly larger. The tetragonal phase $c$ parameter however is observed to be significantly larger in the surface crystallography, where both X-ray values are in excellent agreement, than in
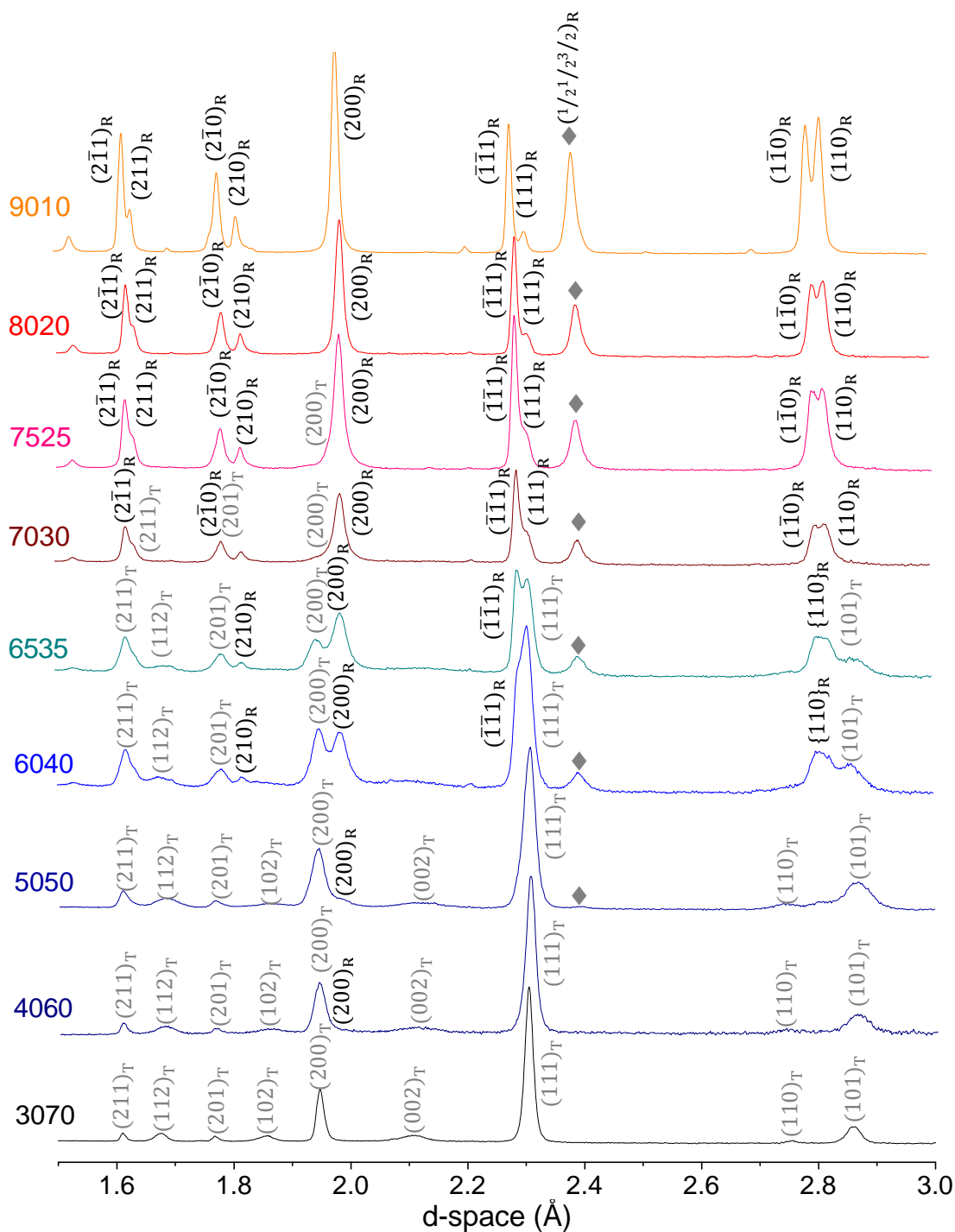
**Figure 4-17 Normalised indexed neutron diffraction patterns collected from the C-bank on Polaris for sintered polycrystalline ceramics of xBiFeO$_3$ – (1-x)PbTiO$_3$ where 0.3 ≤ x ≤ 0.9 at ambient temperature. The patterns are indexed using the P4mm and R3c space groups in the pseudocubic setting. ◆ represents magnetic contributions.**

**Table 4-3 Lattice parameters of xBiFeO$_3$-(1-x)PbTiO$_3$ measured from least squares profile refinement of Polaris neutron data for bulk polycrystalline samples.**

| Composition (x) | a (Å) | c (Å) | c/a ratio (P4mm phase) | R3c phase (%) | P4mm phase (%) |
|---|---|---|---|---|---|
| 0.9 | 3.9866(2)* | - | - | 100 | 0 |
| 0.8 | 3.9978(5)* | - | - | 100 | 0 |
| 0.75 | 3.9923(4)* | - | - | ~100 | trace |
| 0.7 | 3.8915(6) | 4.3012(1) | 1.105 | 87.6(3) | 12.4(3) |
| 0.65 | 3.8927(8) | 4.2631(1) | 1.095 | 52.1(2) | 47.9(2) |
| 0.6 | 3.894(5) | 4.2454(6) | 1.090 | 26.1(6) | 73.9(6) |
| 0.5 | 3.8857(6) | 4.2351(8) | 1.090 | trace | ~100 |
| 0.4 | 3.8877(6) | 4.2270(1) | 1.087 | trace | ~100 |
| 0.3 | 3.8947(2) | 4.2122(4) | 1.082 | 0 | 100 |

*based on R3c pseudo-cubic setting
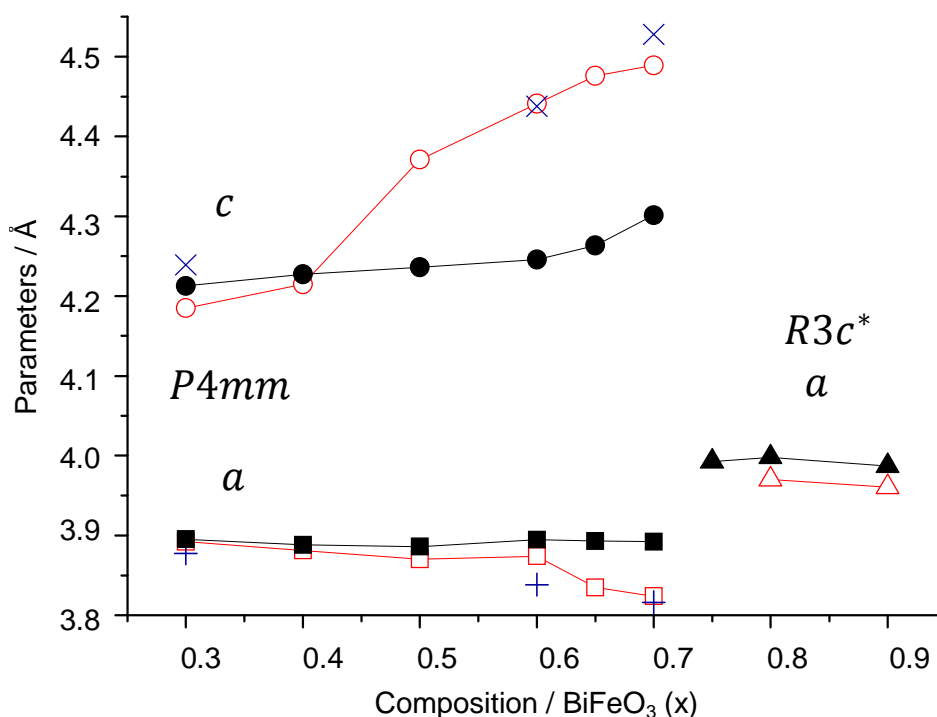


**Figure 4-18 Lattice parameters of sintered polycrystalline xBiFeO$_3$ – (1-x)PbTiO$_3$ ceramics calculated from (black) neutron (bulk) and XRD (surface) diffraction (red). A comparison is also made to (blue) XRD data from Sai Sunder, 1995. *R3c in pseudocubic space.**
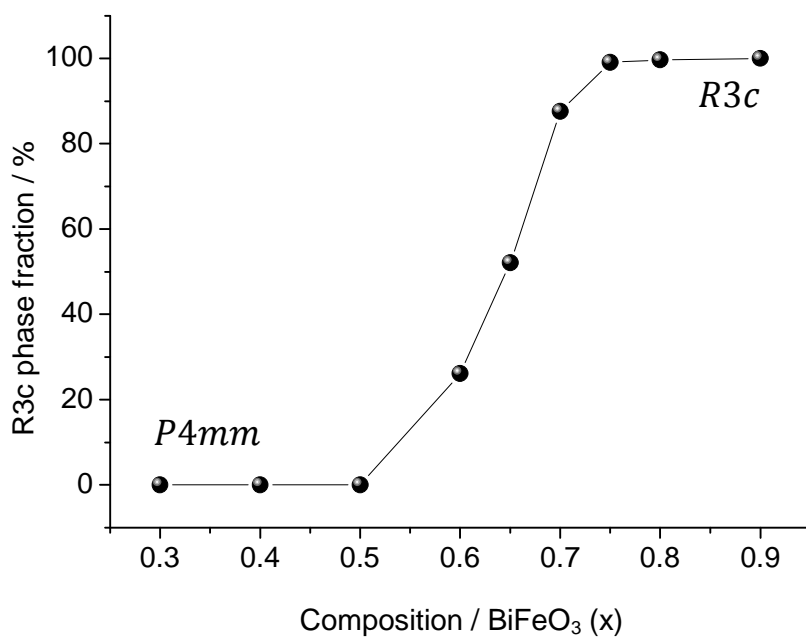
**Figure 4-19 Rhombohedral phase fraction as a function of composition in sintered polycrystalline xBiFeO$_3$ – (1-x)PbTiO$_3$ ceramics, calculated from neutron diffraction data. Error bars appear smaller than the points used.**
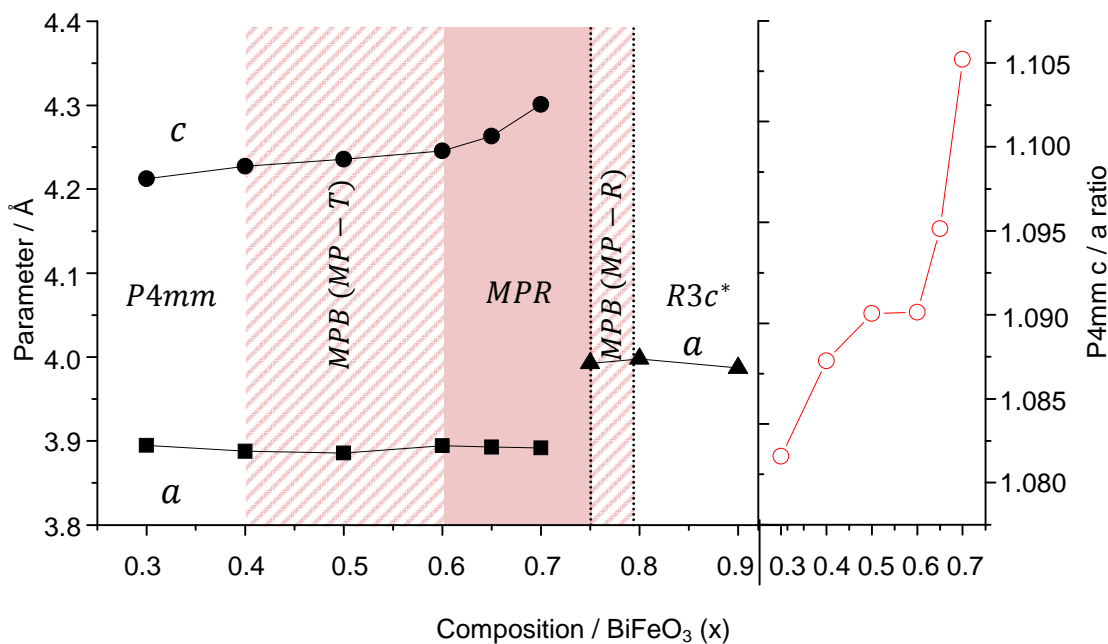


**Figure 4-20 Summary of parameters calculated from neutron diffraction. Unit cell parameters (*R3c in pseudocubic space) are overlayed with phase fraction information to define the mixed phase region (MPR) (red shade) and morphotropic phase boundary (MPB) (red hatch) in the BFPT system. Tetragonal c/a ratio (right) is also shown.**

the bulk. This reinforces the conclusions of 4.3, providing further evidence that the surface tetragonal distortion is much larger than observed for the bulk.

It can clearly be seen from Figure 4-19 that the region of significant mixed phase is similar to the MPB range reported for all the authors in Table 1-9, with considerable contributions from both R3c and P4mm phases observed in compositions $0.6 < x \leq 0.75$. However, there are also subtle contributions from the rhombohedral phase in the predominantly P4mm materials $0.4 \leq x \leq 0.5$ that the increased resolution of the Polaris C-bank, over typical laboratory diffraction, can resolve. More work is required to probe the intermediate compositions between $x = 0.4$ and $0.6$ to determine the MPR tetragonal side boundary (technically a MPB from mixed phase to tetragonal P4mm). The rhombohedral rich boundary, defined as the first instance of tetragonality being introduced, or the common use of morphotropic phase boundary (1.12.2-1) (MPB) definition for this system, is observed to be between $0.75 \leq x < 0.8$.

A summary of the neutron diffraction data discussed above is illustrated in Figure 4-20, illustrating the lattice parameters, c/a ratio and phase fractions as a function of composition. The c/a ratio is observed to show a rapid increase in the *c* axis parameter where the mixed phase ratios are equivalent ($x = 0.6$), with a continuing trend in an expanding tetragonal *c* axis with increased $BiFeO_3$, indicating increased distortion in the tetragonal phase as the rhombohedral content increases to reduce the clamping effects. This confirms the highest level of tetragonal distortion to be present in the 7030 composition, where it is expected the largest internal stresses are expected to exist.

A reflection at ~2.4 Å, denoted by ♦, is indexed as the $(^1/_2{}^1/_2{}^3/_2)_R$ which represents contributions in the rhombohedral phase from the oxygen octahedra tilt within the perovskite unit cell, as well as antiferromagnetic order. The intensity of the peak increases dramatically with increased $BiFeO_3$ content, attributed to the increased concentration of magnetic iron ions within the system.

The oxygen octahedra reflection is only seen in the rhombohedral phase and is assumed to be due to $a^-a^-a^-$ antiphase tilting (Figure 1-8 (c)) as seen in the bismuth ferrite end member (Michel, 1969) (Kubel, 1990). In the tetragonal phase, no tilting occurs, and the oxygen contributions are masked by the dominant nuclear peaks.

### 4.5.3  Disintegrated Powders

Fast cooling the ceramics as previously discussed acts as a driving force to spontaneously disintegrate most of the ceramic compositions. Neutron diffraction patterns were initially collected using the G4.1 instrument at LLB. These were subsequently done again from the C-bank of Polaris at ISIS, as the increased resolution allowed excellent peak definition. The patterns from Polaris are shown in Figure 4-21.

Upon fast cooling from the sinter, compositions x ≤ 0.75 failed to disintegrate but rather cracked or fractured, at most breaking apart into sintered blocks. These were crushed using a pestle and mortar for the experiment here, as the experiment required uniform filling of the vanadium sample can. Compositions 0.3 ≤ x < 0.60 crumbled into powder featuring agglomerates of material. The agglomerates tended to be large enough to pick out, but were easily removed by passing through a 20 micron sieve to allow only the powder that had undergone disintegration to be probed.

Whilst the slow cooled samples have time to compensate internal stress by transformation into the smaller primitive cell volume R3c and form solid ceramics, the accelerated cooling prevents this relief mechanism, driving the ceramics to undergo spontaneous disintegration to relieve the same stress that occurs on passing through the ferroelectric structural phase transition.

The diffraction patterns suggest agreement with the proposed mechanism, observed as a sharpening of the diffraction peaks due to the lack of strain broadening effects, and is perhaps the most noticeable difference in a comparison between the patterns shown in Figure 4-19 for fast cooled and Figure 4-18 for bulk.

The lack of mixed phase in the fast cooled ceramics is also noticeable, except for traces of tetragonality in the 7525 composition. For compositions x ≤ 0.7 the material is observed to be 100 % P4mm tetragonally distorted perovskite, with shifts in peak positions as a function of composition. The $(002)_T$ and $(200)_T$ are perhaps the most obvious, increasing and decreasing respectively with $BiFeO_3$ content; indicating an increase in $c$ and decrease in $a$ lattice parameters pertaining to an increase in tetragonal distortion. Least squares profile fitting (WinPlotR), employing an instrument resolution function for the Polaris C-bank, confirm this, with a maximum chi$^2$ for the fits = 3.23. This is summarised in Figure 4-22.

Extrapolation of the $c$ and $a$ axis to the $PbTiO_3$ end member (x =0) observes excellent agreement with the $c/a$ ratio = 1.06 in the literature ($PbTiO_3$ $c/a$ = 1.063) (Shirane, 1950).
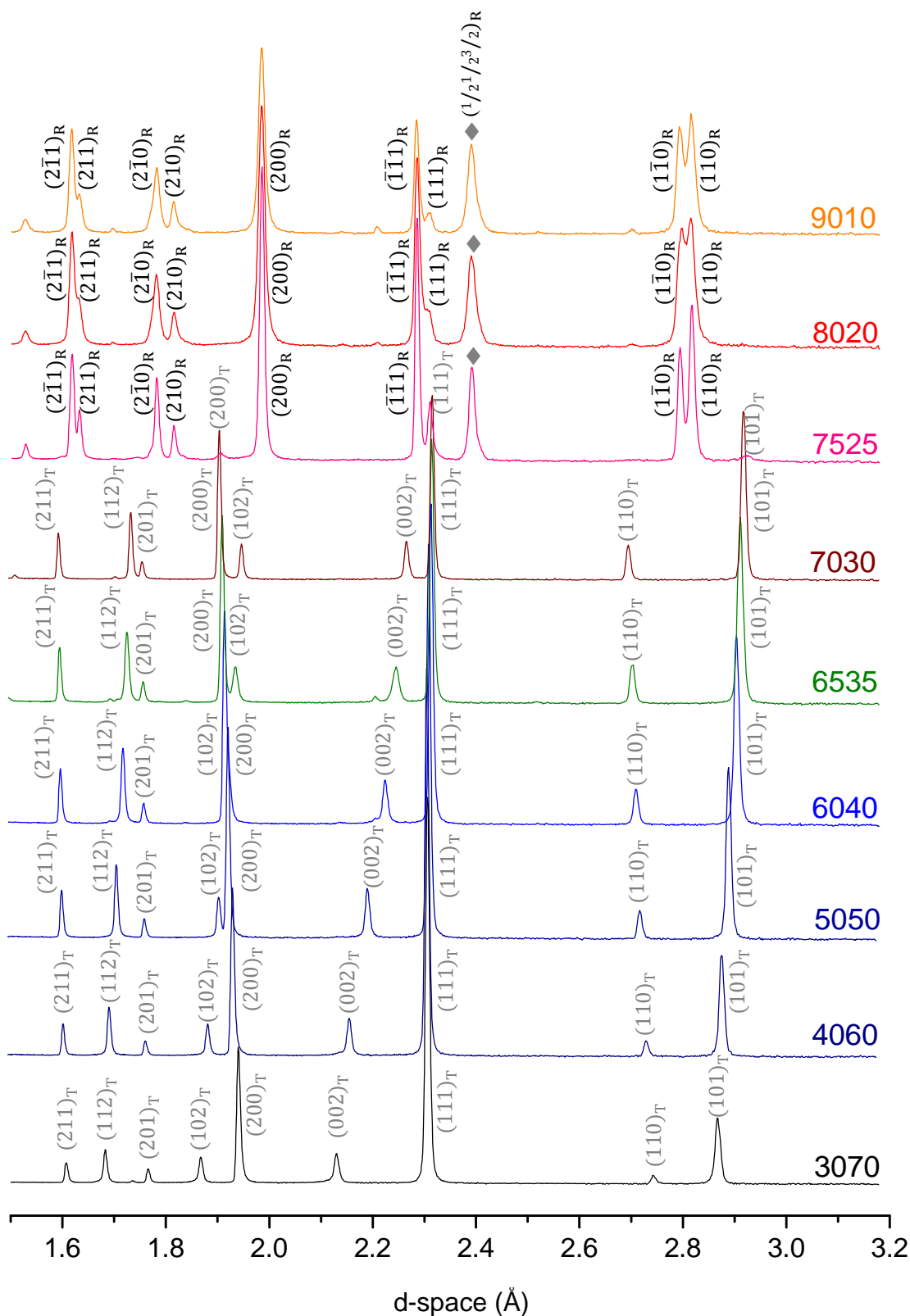
**Figure 4-21 Normalised neutron diffraction patterns collected from the C-bank on Polaris for fast cooled ceramics (>900 °C/hr) of xBiFeO$_3$ – (1-x)PbTiO$_3$ where 0.3 ≤ x ≤ 0.9. The patterns are indexed using the P4mm and R3c space groups in the pseudocubic setting. ◆ represents magnetic contributions.**

**Table 4-4 Lattice parameters of $xBiFeO_3$-$(1-x)PbTiO_3$ measured from least squares profile refinement of Polaris neutron data for fast cooled powder samples.**

| Composition (x) | a (Å) | c (Å) | c/a ratio (P4mm phase) | R3c phase (%) | P4mm phase (%) |
|---|---|---|---|---|---|
| 0.9 | 3.9805(4)* | - | - | 100 | 0 |
| 0.8 | 3.9807(4)* | - | - | 100 | 0 |
| 0.75 | 3.9812(4)* | - | - | ~100 | trace |
| 0.7 | 3.8273(2) | 4.5509(2) | 1.189 | 0 | 100 |
| 0.65 | 3.8392(3) | 4.5088(1) | 1.174 | 0 | 100 |
| 0.6 | 3.8354(6) | 4.4671(5) | 1.165 | 0 | 100 |
| 0.5 | 3.8505(2) | 4.4044(5) | 1.144 | 0 | 100 |
| 0.4 | 3.8843(5) | 4.3324(6) | 1.112 | 0 | 100 |
| 0.3 | 3.8961(1) | 4.2729(1) | 1.097 | 0 | 100 |

*base on R3c pseudocubic setting
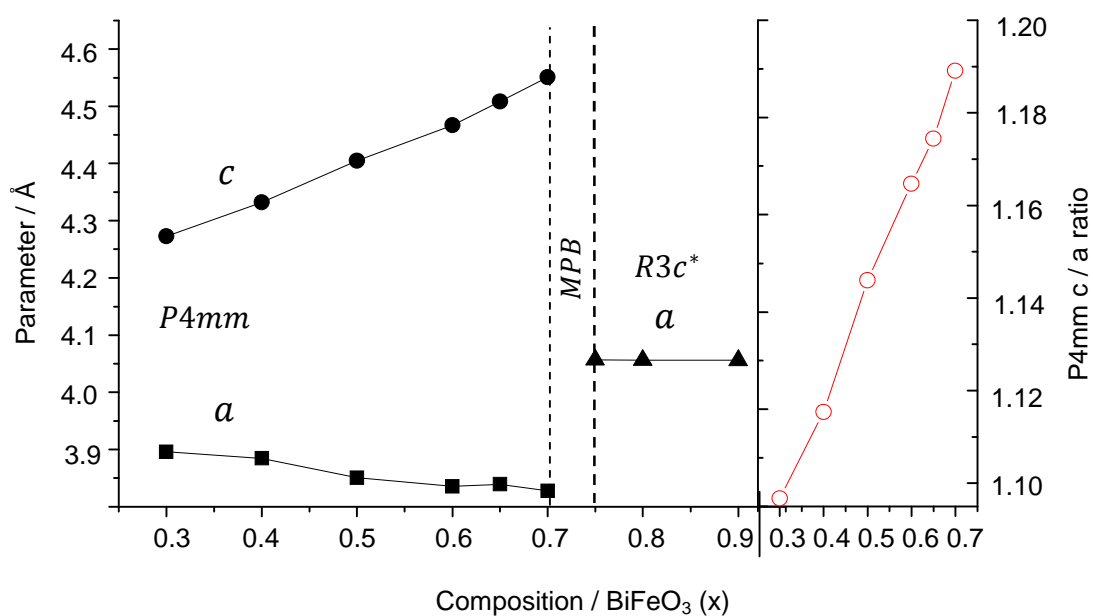


**Figure 4-22 Summary of parameters (R3c in pseudocubic space) calculated from neutron diffraction for fast cooled powders. Tetragonal c/a ratio (right) is also shown.**

For x > 0.7 materials, purely rhombohedral reflections are seen. They are observed to show the same relative FWHM as their bulk equivalent, indicating the act of fast cooling or crushing the materials has not influenced the crystallography.


### 4.5.4  Conclusions

The evidence here supports the critical grain size and stress relief mechanism discussed in the previous sections as the sintered ceramics are observed to have transformed to a mixed phase material (Figure 4-16 (d)) throughout the compositional range except for the extremities below x = 0.3 and above x = 0.8, where the materials are phase pure to their end member P4mm and R3c space groups respectively.

With increased mixing of the phases from the tetragonal PbTiO$_3$ end, the P4mm $c/a$ ratio is observed to increase dramatically, as the phase transformation stress relief mechanism is thought to proportionately increase due to increasing lattice mismatch exacerbating the spontaneous strains.

The $c/a$ ratio is significantly lower than observed from laboratory X-ray diffraction traces, further validating the surface stress model.

All of the either fully or partially spontaneously disintegrated samples 0.3 ≤ x ≤ 0.7, have grain size distributions which exceed the proposed ~ 7 μm threshold, and are observed to display fully tetragonal crystallography akin to the PbTiO$_3$ end member, from which the disintegration model by Matsuo (1966) and Evans (1978) is based.

The spontaneous tetragonal strain, represented by the $c/a$ ratio can also be extrapolated back to observe a value at x = 0 to be ~ 1.06. This is in excellent agreement again with the PbTiO$_3$ end member.

Fast cooled ceramics with sub micron grains do not fracture and are observed to exhibit rhombohedral distortions where induced stress from the tetragonal phase has been partially relieved by full transformation to the lower volume phase.

## 4.6   MAGNETIC PHASE ANALYSIS

### 4.6.1   Motivation

Two techniques are presented to characterise the magnetic order within the BFPT system. These are laboratory magnetometry and neutron diffraction. Vibrating sample magnetometry offers a relatively quick and easy method for characterising magnetism into its para-, ferro- and antiferro- magnetic classes, but falls short of determining types of antiferromagnetism or helical structures for example.

Based on magnetometry measurements however, a scientific case for neutron time at ISIS could be made, and was successfully applied for. These results allow the magnetic structure to be probed simultaneously to the nuclear structure, whilst varying external parameters such as temperature.

### 4.6.2   Vibrating Sample Magnetometry

Vibrating sample magnetometry (VSM) was conducted as per the setup in section 3.4.3, using compositions $0.6 \leq x \leq 0.9$ and $x = 0.3$ formed by the description in 3.3.3. These were selected as the most structurally interesting range of compositions from the previous chapter, plus $x = 0.3$ for comparison.

The data recorded (Figure 4-23) is magnetic moment per unit mass of the sample as a function of applied magnetic field, calibrated by a known volume sample of nickel. The gradient is directly related to the magnetic mass susceptibility, as previously discussed, and can detect contributions from short range magnetic ordering.

A sample of pure $BiFeO_3$ was measured for comparison to the reported magnetic characteristics, as well as a PZT ceramic to ensure that the sample mounting process did not induce magnetic effects from external sources.

The magnetic response from the PZT sample is flat and only shows fluctuations from noise due to the electromagnet. The $BiFeO_3$ however suggests the presence of antiferromagnetism, characterised by its generally linear open loop susceptibility response, but also points toward a ferromagnetic influence based on the hysteresis seen in the low magnetic field regime.

This is in keeping with reports of $BiFeO_3$ that describe its magnetic order as weakly ferromagnetic, from canting of the antiferromagnetic alignment.

The BFPT samples 9010 and 8020, which are shown by diffraction to be rhombohedral in structure, present an almost linear response with a slight opening in the loop but with no ferromagnetic hysteresis.
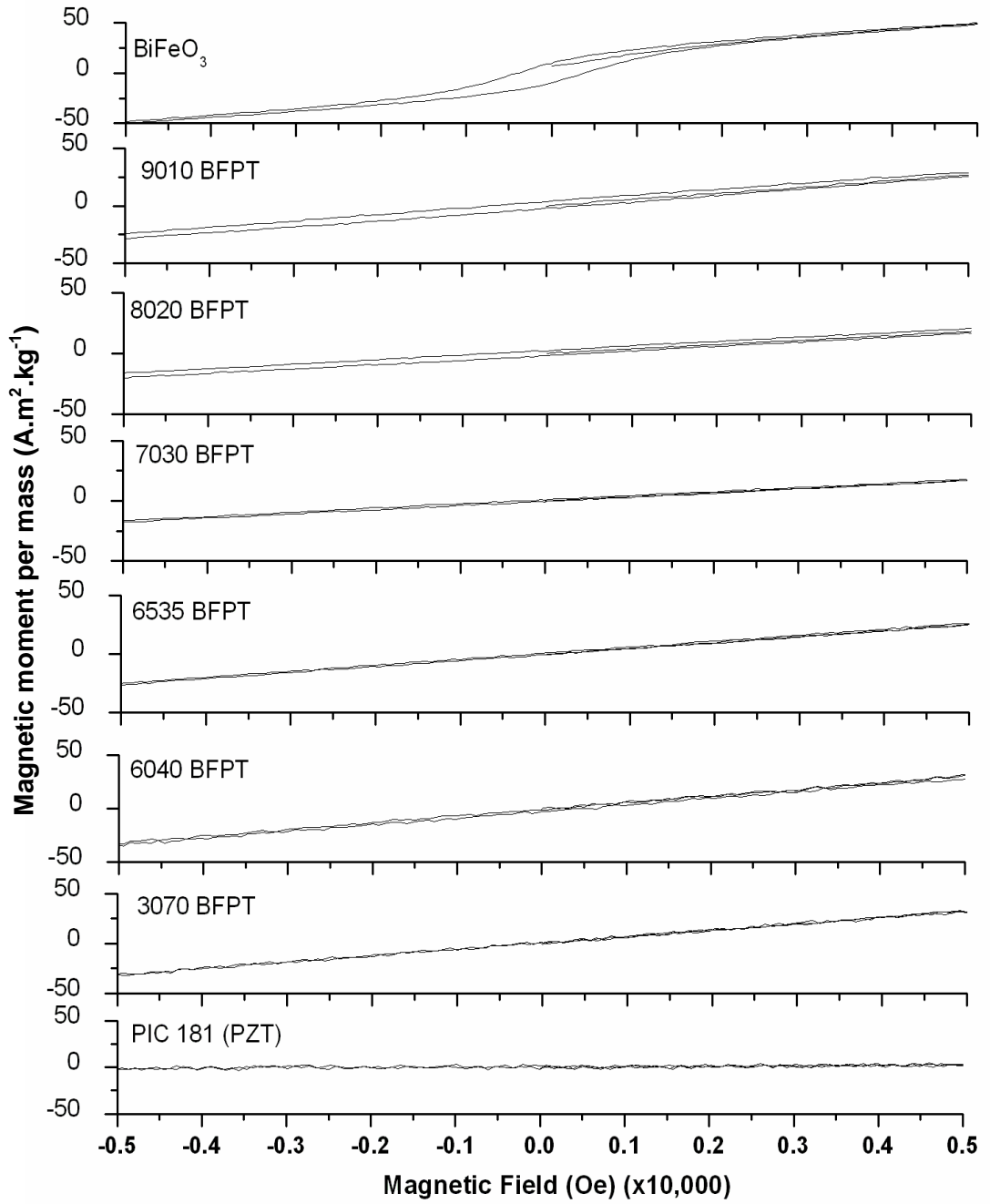
**Figure 4-23 Vibrating Sample Magnetometry (VSM) data plotted for bulk polycrystalline ceramics of BFPT.**

- 153 -

This is indicative of antiferromagnetism, with the opening representing the loss of energy developed by the opposing lattice. 7030, again predominantly rhombohedral is also seen to exhibit a very slight opening, but is within the thickness of the lines drawn in Figure 4-23.

All compositions below 7030 are subsequently observed to show no opening, and purely linear response to the magnetic field. This constant susceptibility over applied field is in keeping with paramagnetic behaviour. This suggests that the increased level of tetragonal phase has diluted the magnetism, a connotation that perhaps the antiferromagnetism in the BFPT system can only be associated with the rhombohedral phase.

This hypothesis is strengthened by analysis of the volume magnetic susceptibility (Figure 4-24), calculated from the gradient of the magnetization vs. field data in Figure 4-23. This shows a steady decrease in magnetic susceptibility from the BFO end member to x= 0.7, as the concentration of antiferromagnetic rhombohedral phase is reduced. This then increases as the tetragonal phase is no longer biased by the rhombohedral AFM presence, and exhibits paramagnetic behaviour, allowing the magnetic field to have a greater influence on the magnetic moments. This is thought to continue up until there is no magnetic iron left by dilution, as per the PZT sample, which has no susceptibility contribution.
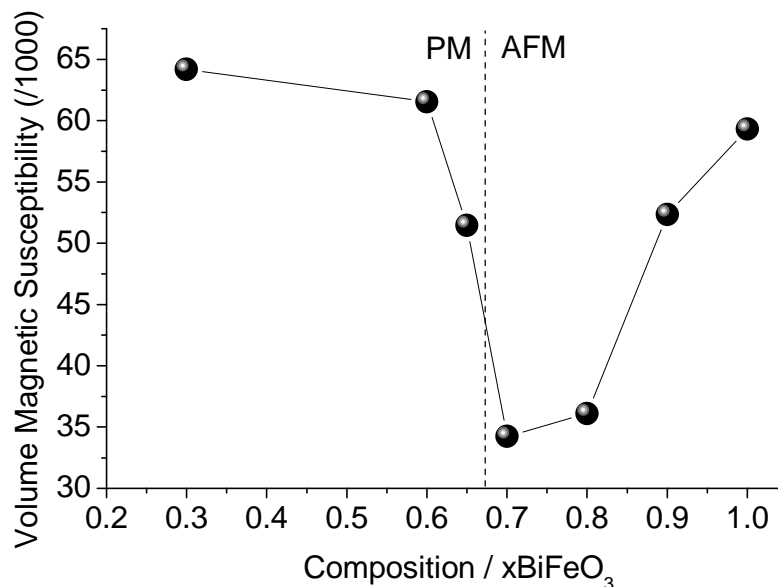


Figure 4-24 Gradients of VSM data plotted as volume magnetic susceptibility as a function of composition for BFPT. The dashed line represents the transition from antiferromagnetic to paramagnetic observed in Figure 4-9.

### 4.6.3 Neutron Diffraction

4.6.3-1    Bulk Polycrystalline Ceramics

Neutron diffraction data collected on the Polaris instrument, as per the experimental methods described in section 3.5.1-1 is presented in Figure 4-25 for bulk polycrystalline ceramics as a function of composition ($0.3 \leq x \leq 0.9$) at ambient temperature. To characterise the magnetic order and compare to the structural differences that the compositional variations induce, the lower resolution but higher d-space range A-bank is plotted.

The reflection observed at $\sim$ 4.6 Å in all compositions at room temperature except 3070, is indexed as the $(\frac{1}{2}\frac{1}{2}\frac{1}{2})_R$. This is double the d-space of the $(111)_R$, which represents the polar direction in the rhombohedral phase, associated with the iron ions arrangement in the bismuth cage.

In hexagonal space, this reflection is indexed as the $(101)_H$, and actually overlaps the $(003)_H$, a second purely magnetic reflection (Sosnowska, 1997), however the resolution limitations of Polaris are unable to resolve this. This is discussed further later.

In X-ray data, the $(\frac{1}{2}\frac{1}{2}\frac{1}{2})_R$ is not visible, pertaining to its nature as a purely long range magnetic order contributing peak. This can subsequently be classified as antiferromagnetic, due to its reflection representing every other iron, where the neutrons diffract with the atoms magnetic moment in either a parallel or anti-parallel magnetization vector.

Antiferromagnets that exhibit nearest neighbours with antiparallel spins are characterised as G-type antiferromagnetism (Figure 1-33 (c)). This is in agreement with the models in the literature for the $BiFeO_3$ end member (Kiselev, 1964) (Michel, 1969) (Fischer, 1980).

The concentration of the magnetic ion reduces with increased $PbTiO_3$, which is reflected in the diminishing intensity of the peak at 4.6 Å. This trend is in partial agreement with the magnetometry data, however the more sensitive neutron experiment is observed to extent the presence of long range AFM order to 4070 BFPT. It may be that the VSM is dominated by short range contributions that cannot be detected by diffraction.
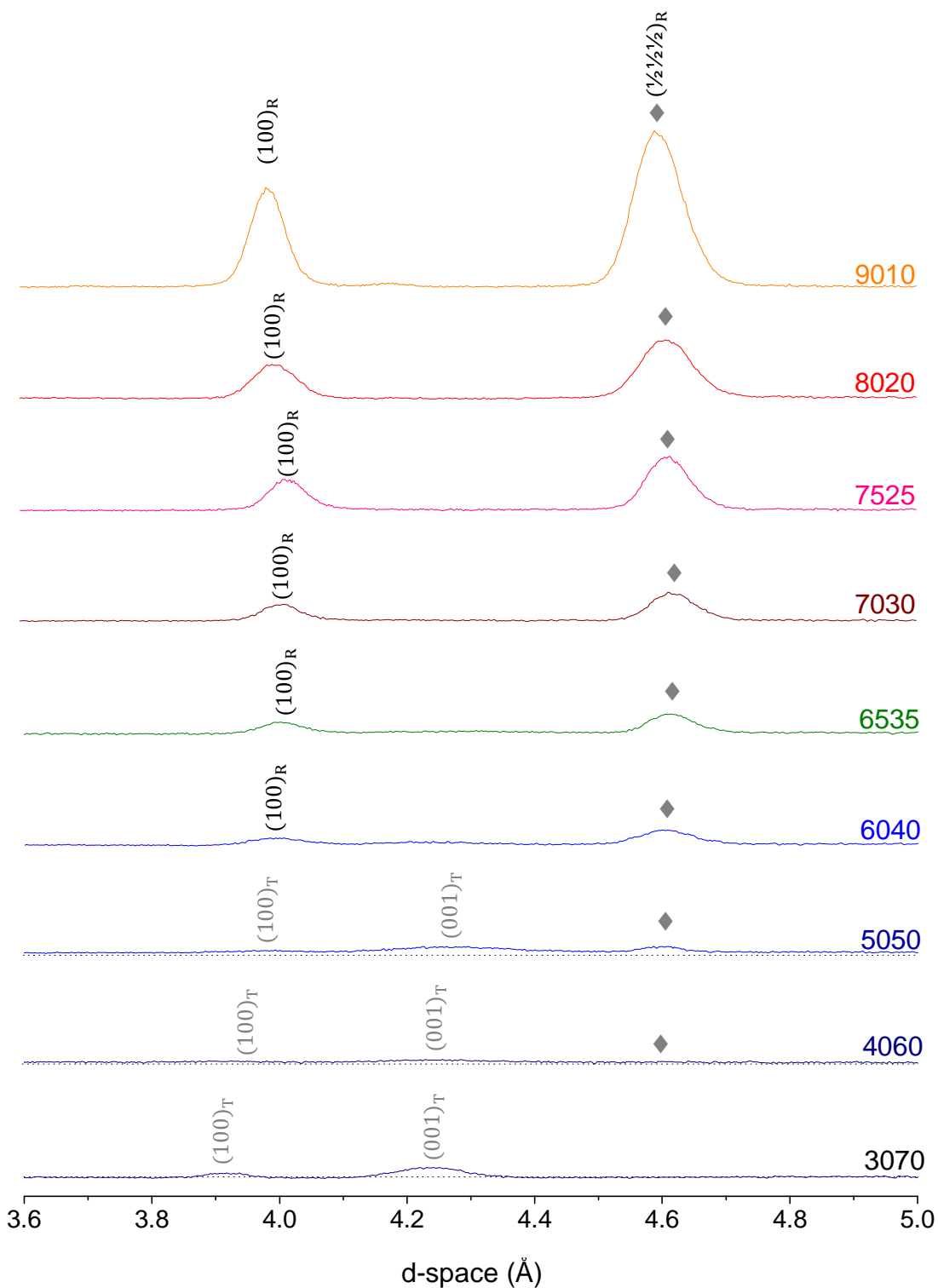
**Figure 4-25 Normalised neutron diffraction patterns collected from the A-bank on Polaris for sintered polycrystalline xBiFeO$_3$ – (1-x)PbTiO$_3$ ceramics where 0.3 ≤ x ≤ 0.9 at ambient temperature. ♦ represents magnetic contributions.**

## 4.6.3-2    Néel Temperature

The compositional range 0.4 ≤ x ≤ 0.9 (excluding 8020) has been studied at ambient and at base (4 K) temperature, as well as through a range of temperatures in between and up to 700 K (427 °C) to observe changes in the magnetic peaks and realise a Néel temperature per composition. Examples of the resultant patterns are shown in Figures 4-24, 4-25 and 4-26 for the compositions x = 0.9, 0.7 and 0.4 respectively. The composition x = 0.4 has been normalised to $x10^6$ greater intensity for clarity.

In the $BiFeO_3$ end member, the sum of intensities ($I$) of the (½½½) ($101_H$ + $003_H$) reflection is reported to be proportionate to the square of magnetic order parameter $R$ (Haumont, 2005). $R$ in turn is related to the observed physical properties of the magnetic phase; magnetization. (Haumont, 2005).

This is expressed in Equation 4-2:

$$R = \sqrt{(I(101) + I(003)} \approx M/M_0$$

Equation 4-2 (Palewicz, 2007)

Calculated least squares profiles, refined to model the peak intensity of the $(½½½)_R$ reflection to good agreement indices (WinPlotR) using an instrument resolution function file for Polaris A-bank, has been conducted over the temperature range for each composition. The resultant peak intensities are normalised by the intensity at base temperature, which represents the absolute spontaneous magnetization, or magnetic moment per ion, as temperature factors are considered to be negligible. The values are then represented as $M/M_0$. Normalising the temperatures at which the relative peak intensities are measured to an initial value of $T_N$ presents a $T/T_N$ series.

Expansion of the Brillouin function (Equation 1-35) in the form of a Bessel function (Arfken, 2001) as a series where $J = 5/2$, the quantum spin for unpaired electrons in $Fe^{3+}$, and for $y = T/T_N$ produces a value per temperature equivalent to the spontaneous magnetization $M/M_0$ (Darby, 1967). This is completed for $n$ number of temperatures measured. Combining the calculated points from the Brillouin function for the temperatures measured with the points from the table of values by Darby (1967), and plotting the two data series and varying the value of Néel temperature in the matrix until the observed and Brillouin function values of $M/M_0$ (below $T/T_N$=1) yield the best agreement by a least square calculation tending to 0. This is expressed by Equation 4-3;
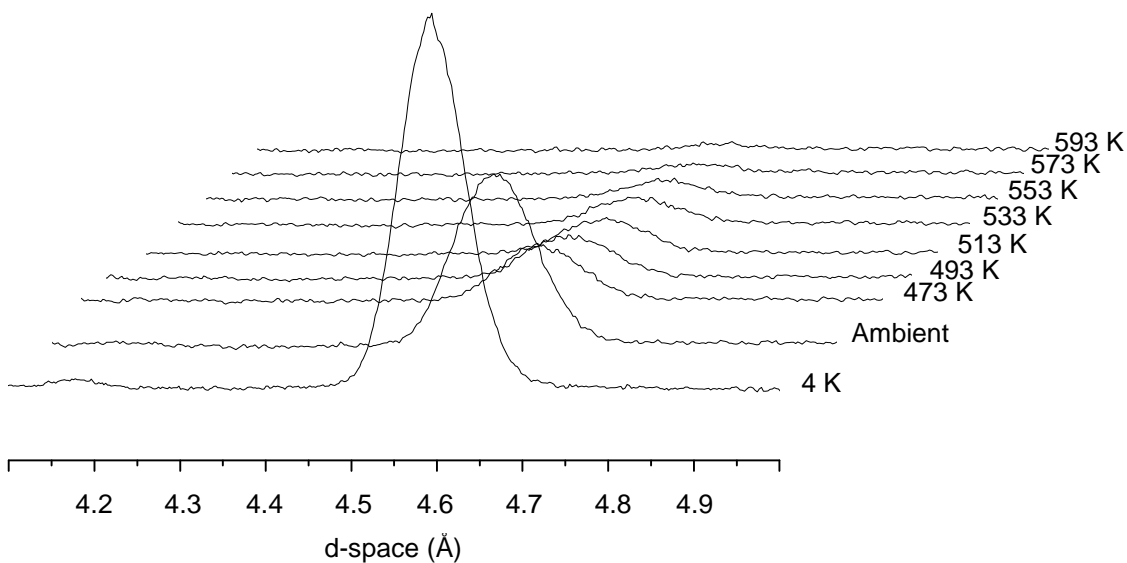
**Figure 4-26 Plot of the antiferromagnetic peak with increasing temperature for the 9010 BFPT polycrystalline sintered ceramic.**
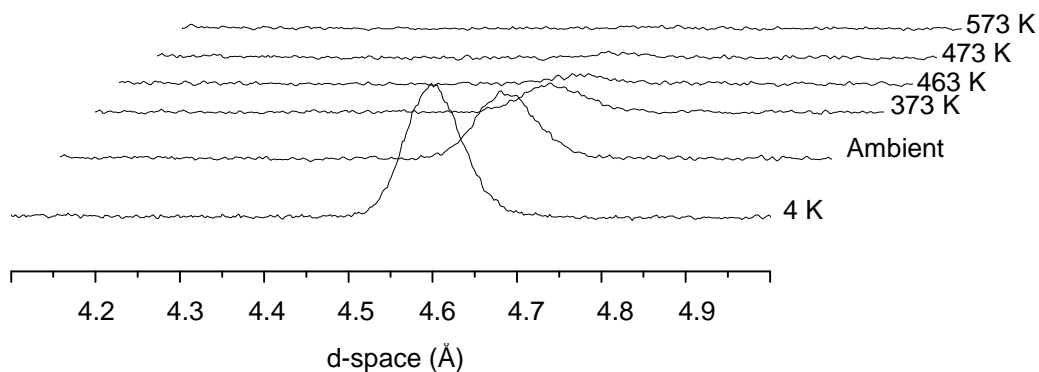


**Figure 4-27 Plot of the antiferromagnetic peak with increasing temperature for the 7030 BFPT polycrystalline sintered ceramic.**
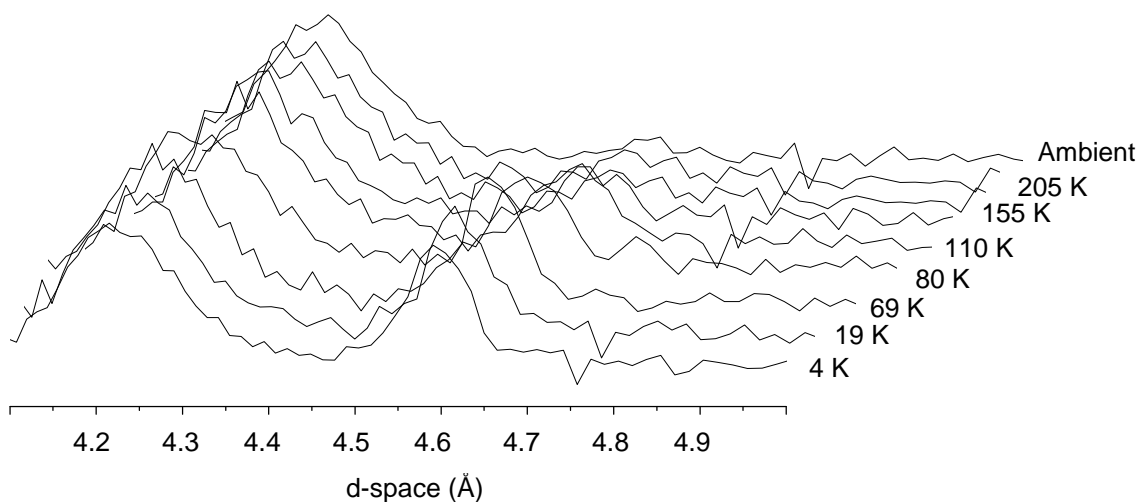


**Figure 4-28 Plot of the antiferromagnetic peak with increasing temperature for the 4060 BFPT polycrystalline sintered ceramic (intensity x 10$^6$ for clarity).**
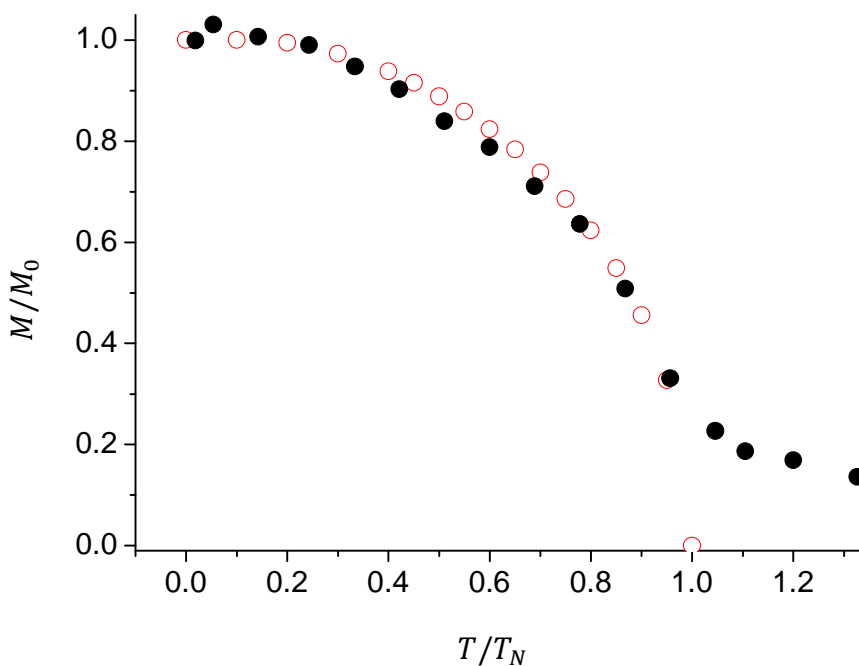
**Figure 4-29 Plot of the Brillouin function (red, open) (where $J = 5/2$), compared to the observed $M/M_0$ (black, closed) from profile fitting of x = 0.9 BFPT AFM peak intensity after normalisation. The fit yields a lowest agreement factor of 0.0122, at a value $T_N$ = 323 °C / 596 K. Some points are omitted for clarity.**
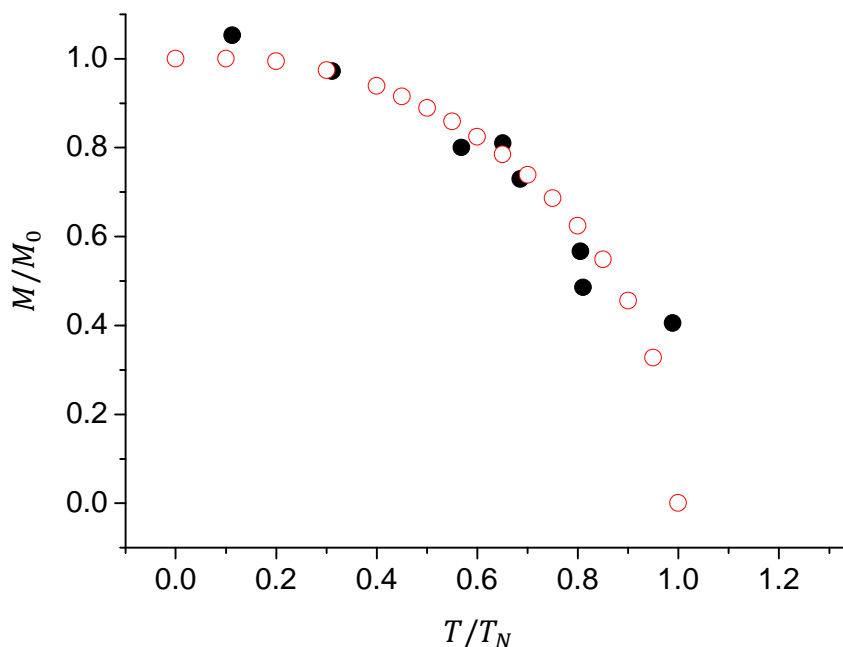


**Figure 4-30 Plot of the Brillouin function (red, open) (where $J = 5/2$), compared to the observed $M/M_0$ (black, closed) from profile fitting of x = 0.6 BFPT AFM peak intensity after normalisation. The fit yields a lowest agreement factor of 0.345, at a value $T_N$ = 247 °C / 530 K. Some points are omitted for clarity.**

$$agreement\ factor = \frac{1}{n} \cdot \sum_{i=1}^{n} ((M/M_0)_{brillouin} - (M/M_0)_{obs})^2$$

<div align="right">Equation 4-3</div>

Only the range of $M/M_0$, where $T/T_N < 1$ are used for the agreement factor, as they offer the least error (sigma) from profile fitting. The magnetization data after $T/T_N > 1$ represent the background contributions from peak fitting and is discounted.

The relationship between observed and calculated magnetization for the range of temperatures are illustrated in Figure 4-29 and Figure 4-30 as examples, and are associated to the compositions 9010 and 6040 respectively. The 9010 yields an excellent approximation to the Néel temperature (596 K) when comparing the values calculated by structure refinement (592 K) (Comyn, 2009) validating the method. Estimation by refinement reduces the need for fractional temperature changes during neutron experiments, which are extremely time costly. The calculated Néel temperatures and their agreement factors are listed in Table 4-5. Although the 6040 is seen to exhibit erroneous agreement indices, a consequence of reduced peak intensity and increased error in profile refinement, the model is seen to follow qualitatively well in Figure 4-28, as well as follow an expected trend when the Néel temperatures yielded are subsequently plotted against composition, in Figure 4-31.

From this plot a general trend is observed, where a decrease in $T_N$ with decreasing $BiFeO_3$ content, due to the reduction in concentration of magnetic iron ions occurs.

However there is an unexpected perturbation between x = 0.6 and 0.7. This is perhaps a result of error in the peak profile and Brillouin function fitting, but as it is known that large internal stresses are inherent in these compositions, it is not inconsistent with these forces influencing the magnetic order through the lattice. It is seen at x = 0.5 - 0.6 that the onset of the rhombohedral phase oxygen tilt begins to emerge, and as the oxygen bonding within bismuth based perovskites is well reported to play a part in the magnetic structure (Atou, 1999) (Kimura, 2003) (Prellier, 2005) (Eitel, 2007), this could well be a mechanism for this discrepancy.

**Table 4-5 Calculated Néel temperatures and their agreement factors from refinement to the (5/2) Brillouin function.**

| Composition (x) | Calculated $T_N$ (K) | Agreement factor ($a$) |
|---|---|---|
| 0.9 | 590 | 0.0122 |
| 0.7 | 528 | 0.0681 |
| 0.65 | 516 | 0.1543 |
| 0.6 | 515 | 0.3450 |
| 0.5 | 468 | 0.3236 |
| 0.4 | 392 | 0.5561 |
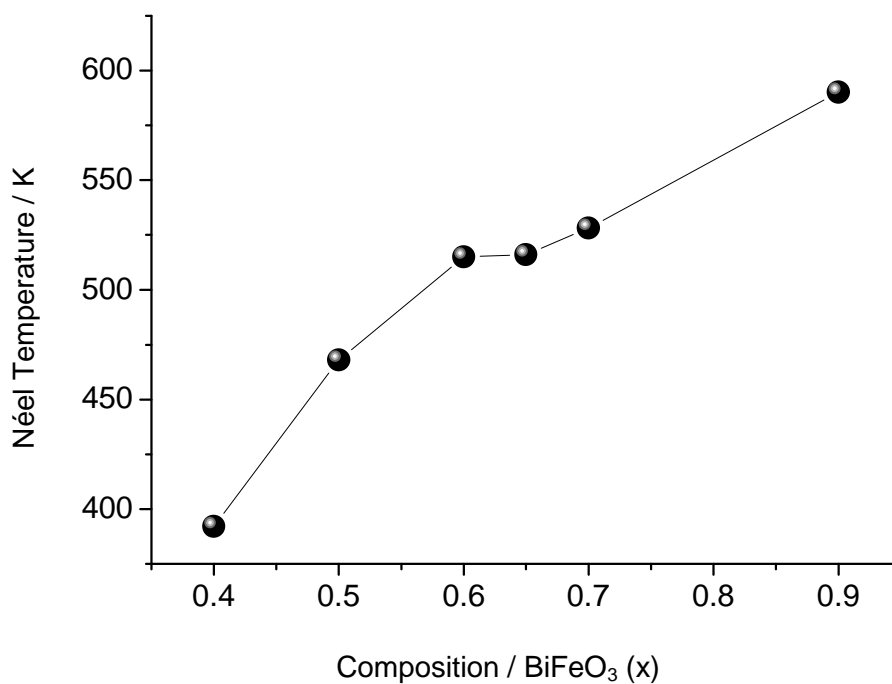


**Figure 4-31 Néel temperature as a function of composition for bulk polycrystalline ceramics of BFPT.**

4.6.3-3    Disintegrated Powders

Neutron diffraction data collected on the A-bank from the Polaris instrument, from the same experiment presented in Figure 4-21, is plotted as over the 3.6 to 4.8 Å range to probe any contributions from the antiferromagnetic peak in Figure 4-25

The compositions that were observed to be rhombohedrally distorted in Figure 4-19, $0.75 \leq x \leq 0.9$ are observed to exhibit G-type antiferromagnetism. The tetragonal materials however show an absence in antiferromagnetic order, instead portraying increased tetragonal distortion with increased $BiFeO_3$ content up to $x = 0.7$, evident by the separating of the (001) and (100) reflections.

This suggests that at ambient temperatures, only the rhombohedral phase can sustain antiferromagnetism.


In keeping with the comparison to the sintered ceramics, the compositional range $0.4 \leq x \leq 0.7$ of disintegrated powders were also studied at ambient and down to base (4 K) temperature, as well as a range of temperatures in between.

Using the composition $x = 0.6$ to disseminate the results seen for all the compositions, it is observed from the resultant traces in Figure 4-33 that the evolution of an antiferromagnetic peak is observed at ~4.6 Å, as the temperature decreases below room temperature. For 6040 this is around 170 K. The presence of the peak at this temperature is again commensurate with G-type antiferromagnetic order, with antiparallel moments aligning along the [111] direction, indexed as $(\frac{1}{2}\frac{1}{2}\frac{1}{2})_T$.

Antiferromagnetism in tetragonal materials is observed in several other systems, including $BiCoO_3$ (Belik, 2006) and $PbVO_3$ (Oka, 2008). In all these materials, the antiferromagnetism is observed to show antiparallel order along the [111] body diagonal, and electric polarisation along the [001] tetragonal $c$ axis.

Using the same technique to model the magnetic dependence on temperature as the sintered ceramics, the values of $T_N$ were calculated for the 5 disintegrated compositions. The results of which are shown with the agreement factor in Table 4-6 and illustrated graphically in Figure 4-32. The magnetic transition temperature is observed to follow a linear relationship with composition. With negligible internal stress present within the disintegrated materials, the Néel temperature increases as a direct effect of the increased concentration of magnetic iron ions within the lattice.

.
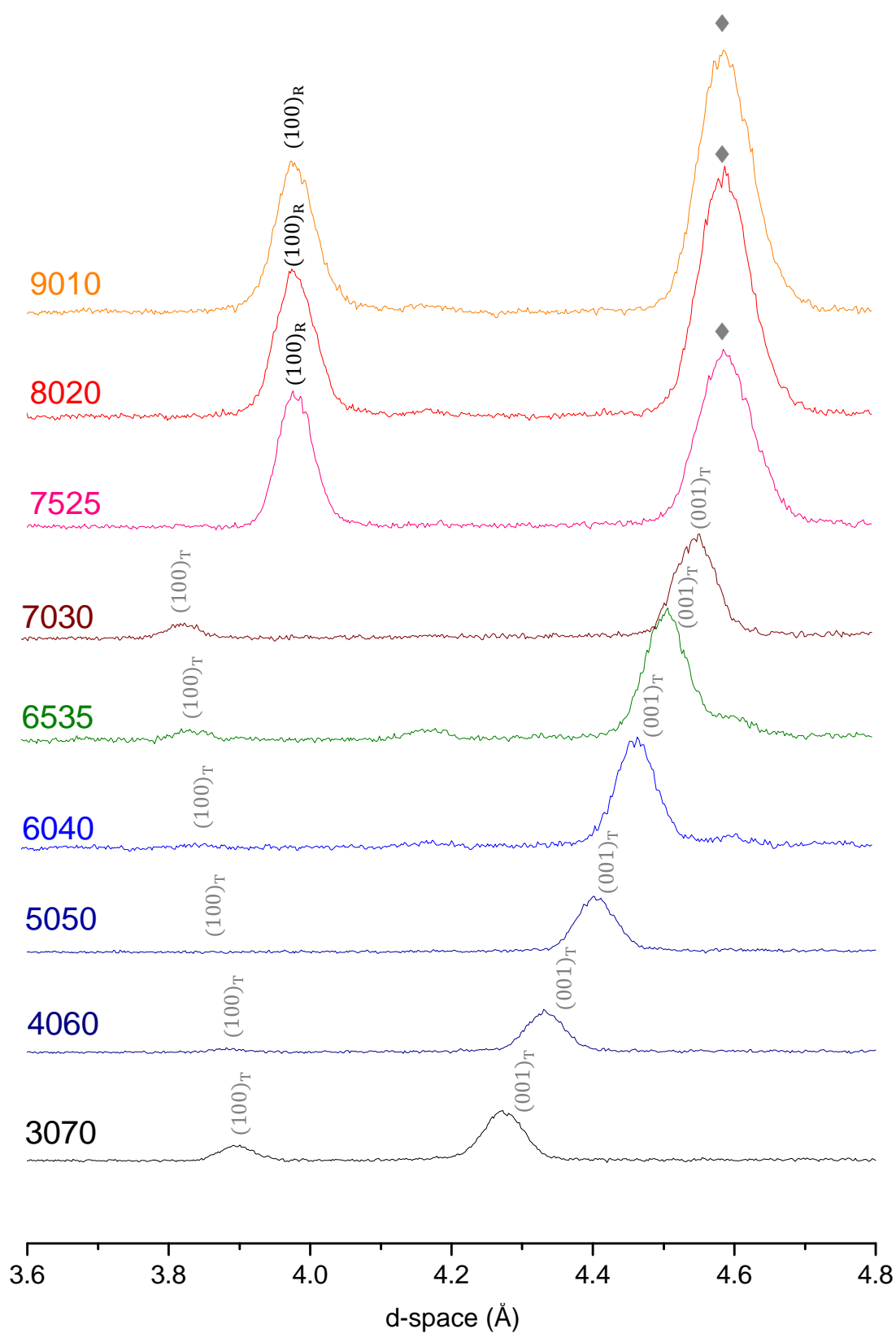
**Figure 4-32 Normalised neutron diffraction patterns collected from the A-bank on Polaris for fast cooled ceramics of xBiFeO$_3$ – (1-x)PbTiO$_3$ where 0.3 ≤ x ≤ 0.9 at ambient temperature. ♦ represents magnetic contributions.**
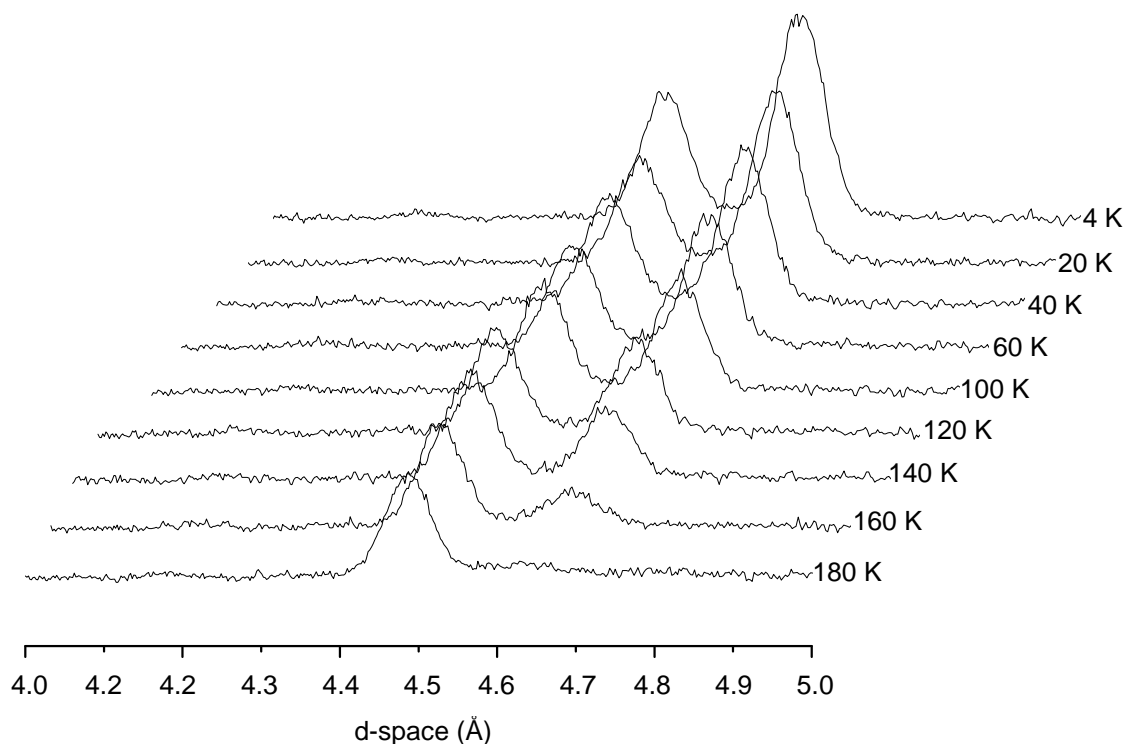
**Figure 4-33 Plot of the antiferromagnetic peak with decreasing temperature for the 6040 BFPT spontaneously disintegrated powder.**

**Table 4-6 Calculated Néel temperatures and their agreement factors from refinement to the (5/2) Brillouin function for disintegrated powders tetragonal phase.**

| Composition (x) | Calculated $T_N$ (K) | Agreement factor ($a$) |
|---|---|---|
| 0.7 | 220 | 0.0325 |
| 0.65 | 195 | 0.0664 |
| 0.6 | 170 | 0.0452 |
| 0.5 | 130 | 0.1253 |
| 0.4 | 80 | 0.3215 |
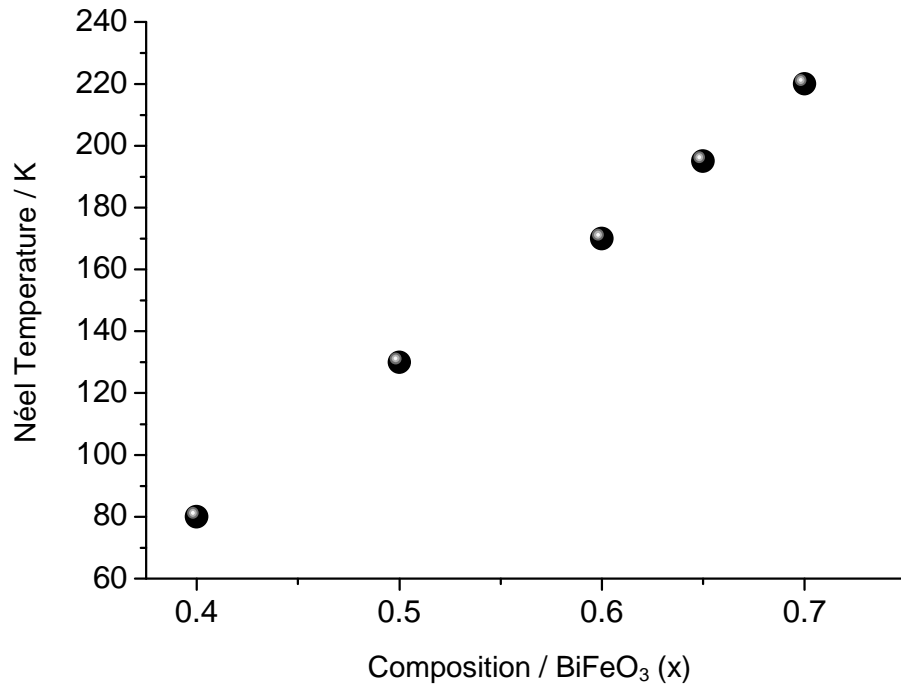
**Figure 4-34 Néel temperature as a function of composition for fast cooled spontaneously disintegrated powders of BFPT.**

Collating the magnetic transition temperature for both the sintered ceramics and spontaneously disintegrated powders allows a complete magnetic phase diagram, based solely on neutron diffraction, to be constructed. This is shown in Figure 4-33. It is apparent that both phases exhibit antiferromagnetism, with $T_N$ at temperatures above and below room temperature for the rhombohedral and tetragonal phases respectively.

### 4.6.4 Magnetic Phase Diagram
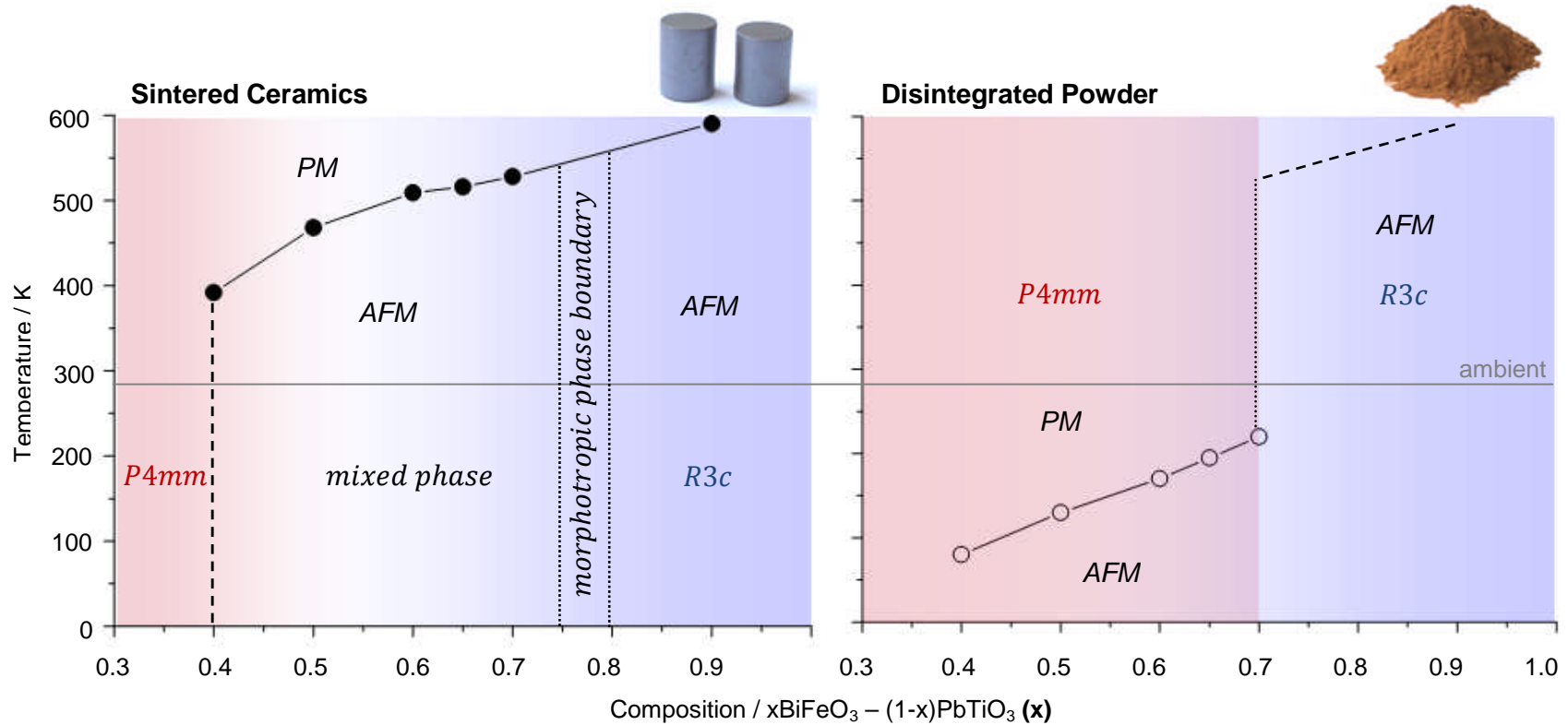


Figure 4-35 Magnetic and structural phase diagram summarising the Néel temperatures ($T_N$) of sintered ceramics and disintegrated powders as a function of temperature and composition. Rhombohedral ($R3c$) phase is identified by blue shading, tetragonal ($P4mm$) by red and mixed phase in between. The diagram labels areas below $T_N$ that are antiferromagnetic (AFM) and above that are paramagnetic (PM).

### 4.6.5 Conclusions

Through neutron diffraction, bulk polycrystalline ceramics of bismuth ferrite lead titanate are shown to observe G-type antiferromagnetism throughout the compositional range $0.4 \leq x \leq 0.9$, which are all attributed to containing rhombohedral phase contributions. Increasing the lead titanate concentration dilutes the iron ions by substitution, reducing the magnetic volume that interacts with the neutrons. This results in a reduction in peak intensity observed in the respective neutron traces until a purely tetragonal phase is reached which cannot sustain antiferromagnetic order. Analysis of the peak intensities as a function of temperature yields $T_N$ values which are in excellent agreement with those seen in the literature based on neutron diffraction structure refinement (Comyn, 2009). The trend of magnetic transition temperature is seen to increase proportionate to iron content, following the dilution mechanism, except for a perturbation corresponding with the onset of oxygen octahedral tilt at x = ~0.6.

Values of $T_N$ based on SQUID magnetometry in the literature (Zhu, 2008) are much lower than observed through neutron diffraction. This is confirmed by vibrating sample magnetometry, as the sensing coil method is sensitive to short range over long range order, the nature of which is reversed to typical powder neutron diffraction techniques.

Spontaneously disintegrated powders that exhibit wholly tetragonally phase $(0.3 < x \leq 0.7)$ (Figure 4-16 (c)) characterised by neutron diffraction at room temperature are shown to be absent of any antiferromagnetic order. However cooling these materials reveal a $T_N$ distribution dependent again on iron content, but at temperatures below room temperature. It is also indicated that in the tetragonal phase, the G-type AFM order is no longer in the same [111] vector as the poling direction, which for the P4mm distortion, $\vec{P}$ lies in the $c$ axis direction [001].

Antiferromagnetic order is never seen in purely tetragonal phase 3070 ceramics of either sintered or powdered state, suggesting the percolation threshold (Baker, 2002) has been reached, at which the iron content is too low to satisfy the spatial requirements for magnetic order (1.7.2).

## 4.7   INCOMMENSURATE MAGNETIC ORDER

### 4.7.1   Motivation

A study of the G-type magnetic order within the BFPT system was conducted as per the experimental procedure in 3.5.1-3 using the high resolution neutron powder diffractometer (HRPD) at ISIS.

As $BiFeO_3$ has been shown to exhibit G-type AFM structure with an incommensurate modulation discussed in section 1.11.4-6, the motivation for the experiment was to observe a similar IC order within the BFPT system, and whether any phase dependence on the magnetic structure was evident based on the presence of a tetragonal phase magnetic structure in 4.6.4.

### 4.7.2   Neutron Diffraction

The data collected using the highest resolution back scattered detectors are presented. When observing the purely AFM peak at ~4.6 Å, a shorter pulse of 40 ms was employed to cover a time of flight range of 200-240 ms. These shorter wavelengths require longer counting times as they are low in flux, falling outside of the Maxwellian flux distribution peak, as illustrated in Figure 2-10.

In previous chapters the pseudocubic setting has been used to index the rhombohedral phase. In this section, there is a need to use the hexagonal setting. This hexagonal setting is denoted by a subscript H at the end of the indices, for the pseudocubic rhombohedral an R, and for tetragonal phases, T, as discussed in 1.2.5.
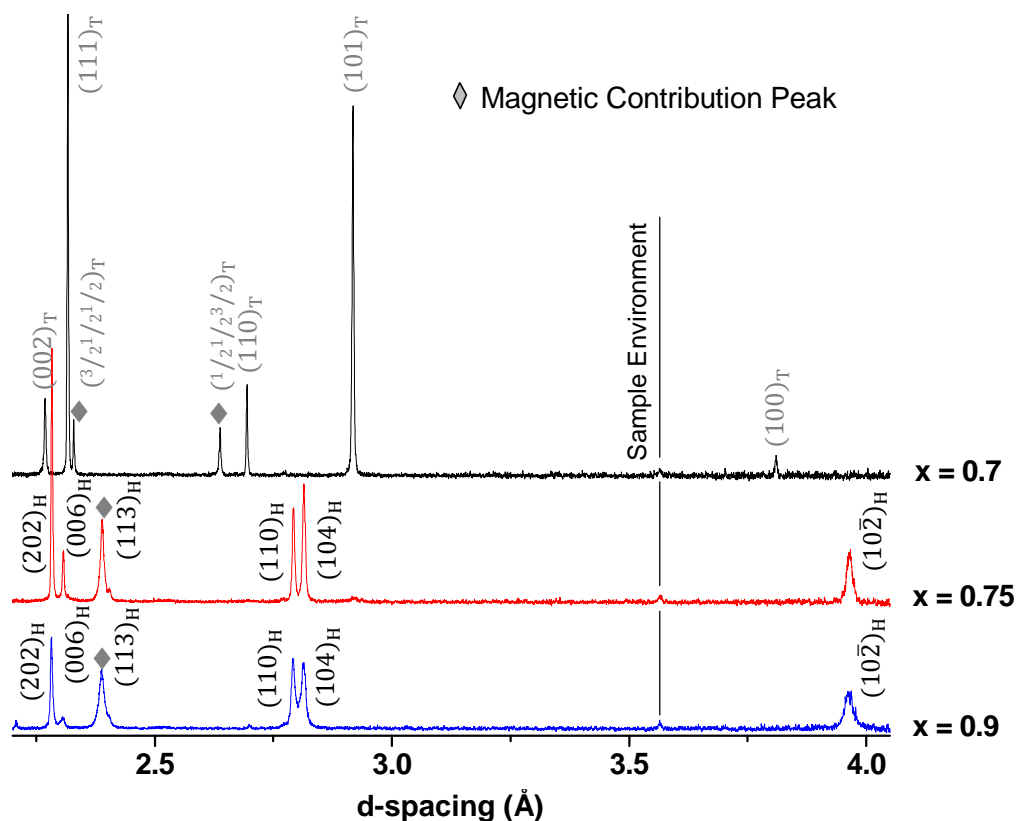
**Figure 4-36 Back scattered detector data from HRPD of xBiFeO₃-(1-x)PbTiO₃ for x = 0.7, 0.75, 0.9 below 4 Å (100 ms pulse). The patterns are indexed according to the P4mm tetragonal (T) and R3c hexagonal (H) settings.**
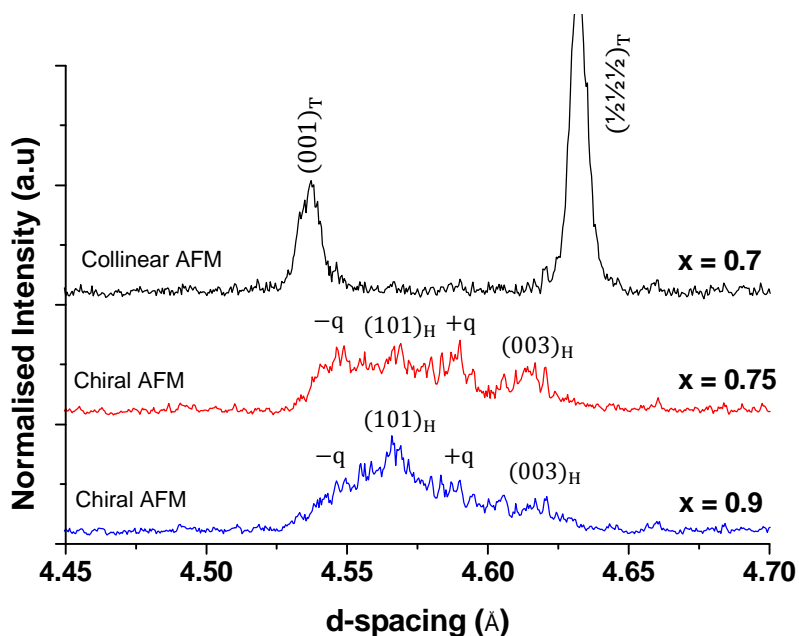


**Figure 4-37 Back scattered detector data from HRPD of xBiFeO₃-(1-x)PbTiO₃ for x = 0.7, 0.75, 0.9 around 4.6 Å (40 ms pulse). The patterns are indexed according to the P4mm tetragonal (T) (x =0.7) and R3c hexagonal (H) (x =0.75, 0.9) settings.**
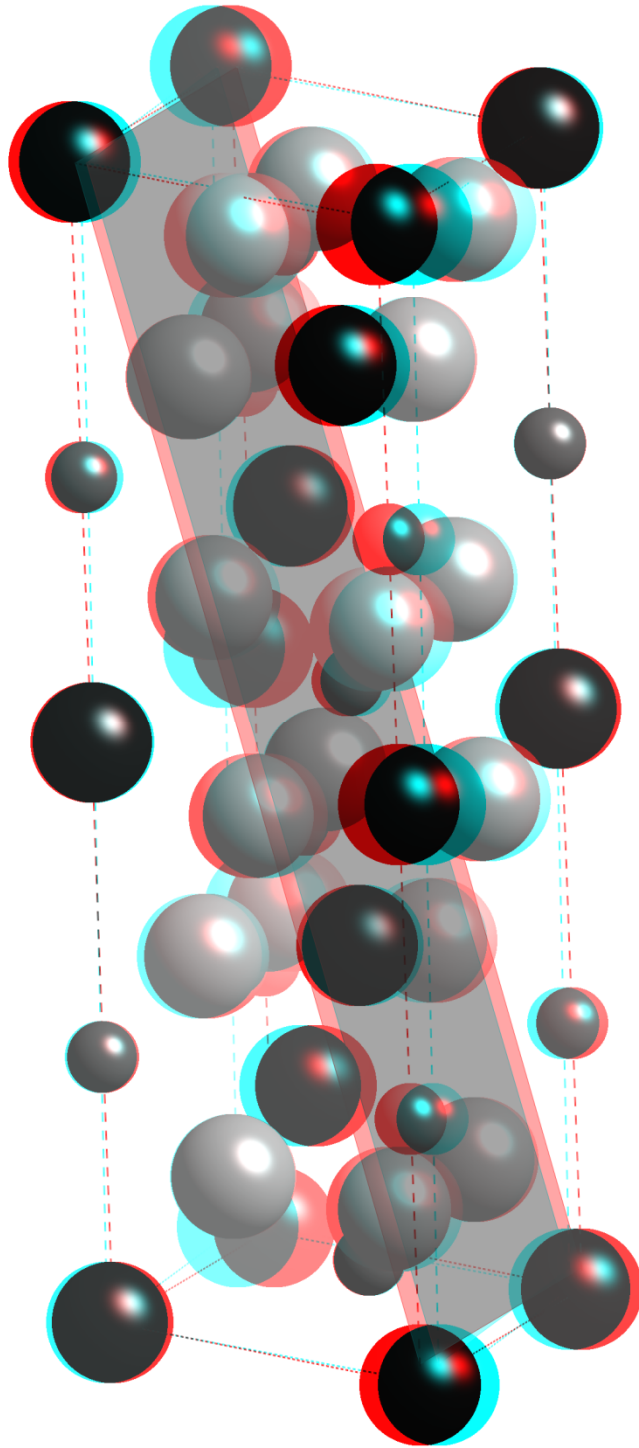
**Figure 4-38  Anaglyph of the BFPT rhombohedral R3c (hexagonal axis) unit cell with the (101)$_H$ plane highlighted.**
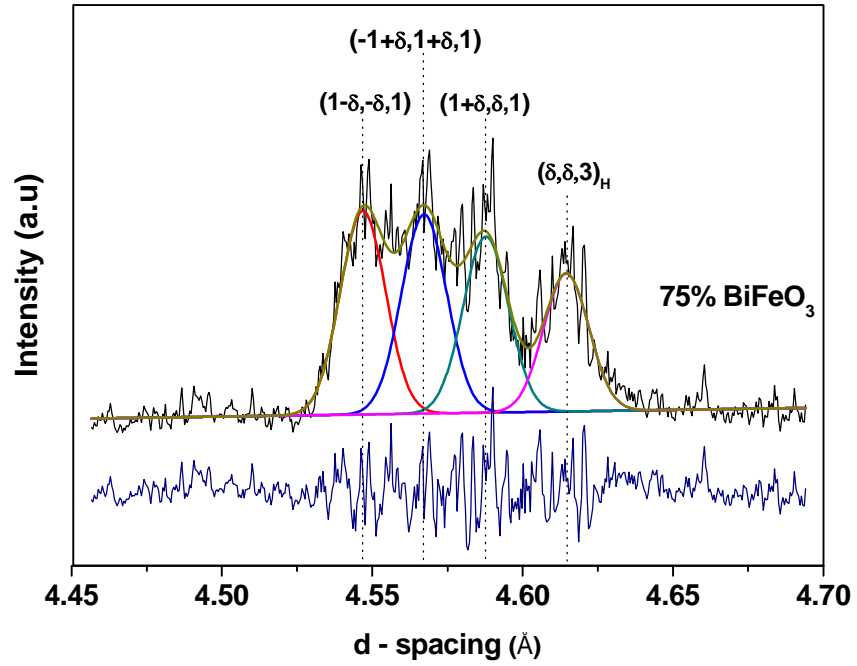
**Figure 4-39 Multiple peak fit of 0.75 BiFeO₃ – 0.25 PbTiO₃ over 40 ms pulse range.**

**(chi² = 1.55)**
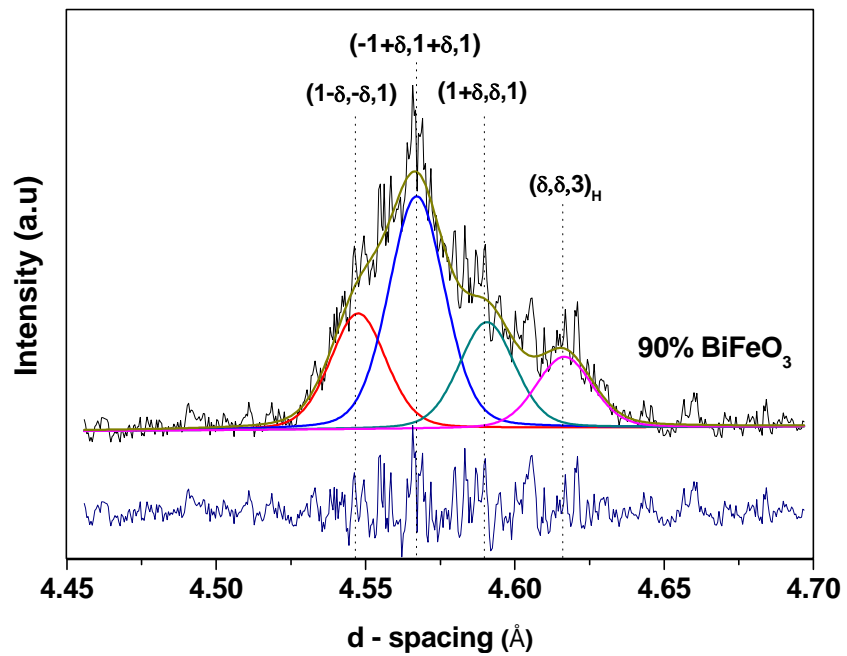


**Figure 4-40 Multiple peak fit of 0.9 BiFeO₃ – 0.1 PbTiO₃ over 40 ms pulse range.**

**(chi² = 1.58)**

Initial comparison of the 100 ms pulse for all three compositions (Figure 4-36), indicates a clear difference in structure for the x = 0.7 powder. Sharp, relatively stress-free peaks that correspond to tetragonal (P4mm) phase are observed with 2 extra peaks pertaining to magnetic reflections at 2.33 and 2.64 Å. Compositions with greater $BiFeO_3$ concentrations are predominantly rhombohedral (R3c), with x = 0.75 exhibiting a trace of tetragonality and x = 0.9 indicating the presence of an impurity phase (denoted by ■ ) (Comyn, 2009). Both  x = 0.75 and 0.9 compositions show increased peak broadening compared to 0.7, in keeping with the internal stress that is present in the materials that have not undergone spontaneous disintegration on cooling. These x= 0.9 and 0.75 compositions also show extra peaks relating to magnetic reflections, but are combined with the oxygen octahedral tilt peak $(113)_H$ (in hexagonal space) inherent in these materials (Comyn 2009).

The effects of phase dependence on the AFM peaks are shown in Figure 4-37, where the 3 compositions are again compared directly but using the 40 ms pulse. In the x = 0.7 material, there is a single, sharp peak at 4.63 Å (½½½) with equal breadth to the nuclear $(001)_T$ due to the collinear alignment of the G-type antiferromagnetic moments. However in x = 0.75 and 0.9 we observe magnetic scattering characteristic of the incommensurate (IC) structure, which is manifested by the splitting of the single antiferromagnetic peak into multiple peaks (Figure 4-39 & Figure 4-40). The relative intensities of the fitted peaks for x = 0.9 is in good agreement with the neutron diffraction data of bismuth ferrite previously run on HRPD (Sosnowska, 1997) even if presented here,  the diffraction profile does not show clearly resolved multiple peaks because of the internal stress presence causing sufficient broadening to blur the data.

For x = 0.75 and 0.9 the rhombohedral distortion and the modulation of the G-type antiferromagnetism modifies the indexation of the magnetic reflections. The rhombohedral distortion splits the originally equivalent $(½½½)_R$ and $(½½ -½)_R$ in pseudocubic space, or $(101)_H$ and $(003)_H$ in hexagonal (Figure 4-38).

In the case of collinear AFM, neutron diffraction contributes to magnetic Bragg peaks at commensurate positions, given by the reciprocal lattice vector;

$$\boldsymbol{G}_{hkl} = h\boldsymbol{a}^* + k\boldsymbol{b}^* + l\boldsymbol{c}^*$$

Equation 4-4 (Przenioslo, 2006 (b))

where $h, k, l$ are integer Miller indices and $\boldsymbol{a}^*$, $\boldsymbol{b}^*$ and $\boldsymbol{c}^*$ are the reciprocal lattice points, which in terms of the hexagonal lattice parameters $\boldsymbol{a}$ and $\boldsymbol{c}$ , correspond to the Cartesian coordinate vectors illustrated in Figure 4-41.
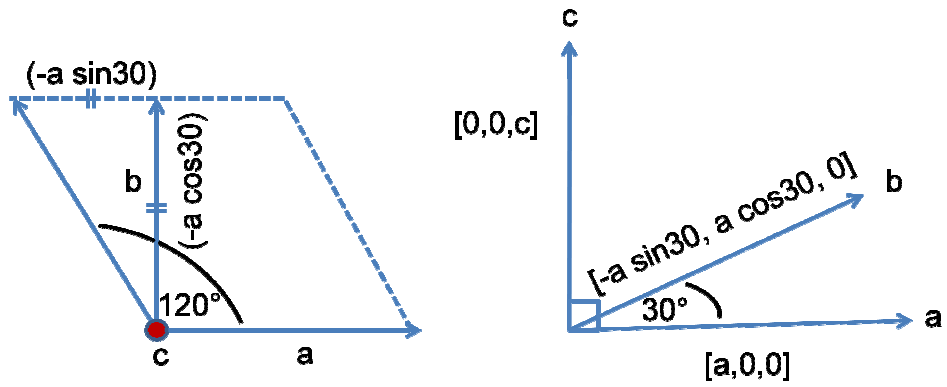
**Figure 4-41 Illustration of the a, b and c lattice vectors in hexagonal space**

The real space vectors from Figure 4-41 can be described as;

$$a = [a, 0, 0] \quad b = [-a \, sin30, a \, cos30, 0] \quad c = [0, 0, c]$$

The relationship to reciprocal space vectors are defined in Equation 4-5 as;

$$a^* = \frac{2\pi(b \times c)}{a \cdot (b \times c)} \quad b^* = \frac{2\pi(c \times a)}{b \cdot (c \times a)} \quad c^* = \frac{2\pi(a \times b)}{c \cdot (a \times b)}$$

Equation 4-5

Which consequently equates the reciprocal lattice points to;

$$a^* = \left[\frac{2\pi}{a}, \frac{2\pi}{\sqrt{3}a}, 0\right] \quad b^* = \left[0, \frac{4\pi}{\sqrt{3}a}, 0\right] \quad c^* = \left[0, 0, \frac{2\pi}{c}\right]$$

In the case of $BiFeO_3$, and as seen in the BFPT system, there is the case of periodic modulations of the magnetic moments, evident by the splitting of the $(101)_H$ into 3 peaks. This can be described with one propagation vector $q$, where the neutron diffraction contributes to magnetic satellite peaks at;

$$G_{hkl} \pm q$$

Equation 4-6

As there is no splitting of the $(003)_H$, then the propagation vector (Figure 1-42) of the incommensurate order ($q$) must lie perpendicular to the hexagonal $c^*$ axis (Sosnowska, 1982) (and electric polarization vector (Lebeugle, 2008)) along reciprocal lattice vectors $a^*$ and $b^*$ in the $ab$ direction.

The relationship between the interplanar spacing and the reciprocal lattice vector is given by;

$$d_{hkl} = \frac{2\pi}{\boldsymbol{G}_{hkl}}$$

<div align="right">Equation 4-7</div>

The reciprocal space diagram in Figure 4-42 shows satellites around the $(101)_H$ born by a magnetic helix (Sosnowska, 1982). These are indexed in Table 4-4 and can be grouped as equivalent d-space pairs, related by 3 fold symmetry. This reduces the list to 3 observed satellites at ~4.54 Å, ~4.59 Å and a third (by Equation 4-5), hidden by the dominant central $(101)_H$ peak.

**Table 4-7 Magnetic satellites of $BiFeO_3$ – $PbTiO_3$ and observed d-space.**

| ($hkl$) | Satellite Index | d-space obs (Å) x =0.9 | d-space obs (Å) x =0.75 |
|---|---|---|---|
| | 1 - 2δ, δ, 1 | 4.54757 | 4.54690 |
| | 1 − δ, - δ, 1 | | |
| $(101)_H$ | 1 − δ, 2δ, 1 | within $(101)_H$ | within $(101)_H$ |
| | 1 + δ, - 2δ, 1 | | |
| | 1 + 2δ, - δ, 1 | 4.59072 | 4.58777 |
| | 1 + δ, δ, 1 | | |

The length and direction of the $\boldsymbol{q}$ vector can be found by analysis of the satellite pairs around the $(101)_H$ and their orientation (ψ) relative to the $a^*$ axis. This can be expressed as in Equation 4-8.

$$\boldsymbol{q} = \delta.a^* + \delta.b^*$$

<div align="right">Equation 4-8 (Sosnowska, 1982)</div>

Where $\delta$ is the component of $\boldsymbol{q}$ along reciprocal lattice vectors $a^*$ and $b^*$. For all *(h0l)* reflections there are observed only 3 peaks, in excellent agreement with that of pure $BiFeO_3$, alluding to ψ = 30 °. According to other publications (Sosnowska, 1982) (Lebeugle, 2008) this then implies that *(hhl)* and *(hkl)* reflections should

observe four and six peaks respectively. Indeed reflections for the (113) can be seen on the broad shoulders of the nuclear peaks, but cannot be resolved for strain.

The $q$ vector then corresponds to the period of the IC order by Equation 4-9.

$$L = a \,/(2\delta)$$

Equation 4-9 (Stevenson, 2010)

where $a$ is the hexagonal lattice parameter. For the two outer peaks we can express the relationship to the central (101) peak as in Equation 4-10.

$$\frac{1}{d_+^2} - \frac{1}{d_-^2} = \frac{|G + q|^2}{4\pi^2} - \frac{|G - q|^2}{4\pi^2} = \frac{8\delta}{a^2}$$

Equation 4-10 (Stevenson, 2010)

where $d_-$ and $d_+$ represent the d-spacings of the $(1-\delta,-\delta,1)$, and $(1+\delta,\delta,1)$ reflections respectively and $G$ is the lattice vector of the (101) peak, providing a trivial method for the calculation of both $\delta$ and $L$:

$$L = \frac{4}{a} \Big/ \left( \frac{1}{d_+^2} - \frac{1}{d_-^2} \right)$$

Equation 4-11 (Stevenson, 2010)

Multiple peak fitting using WinPlotR software and subsequent refinement to attain the lowest chi$^2$ value (Figure 4-39 & Figure 4-40) provided accurate values for $d_+$ and $d_-$. Accordingly, $a$ was taken from refinements in section 4.4 and the values of $\delta$ and $L$ were calculated from the measured d-spacings and are shown in Table 4-8.
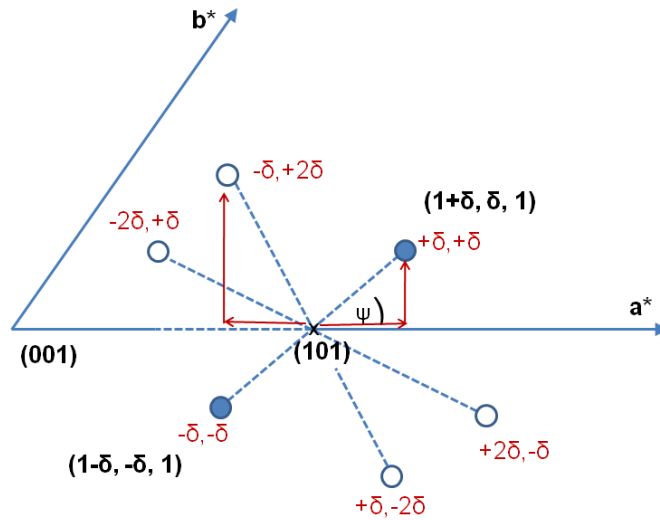
**Figure 4-42 Possible satellite configurations around the (101) reciprocal lattice point in BiFeO$_3$. (Sosnowska, 1982).**

**Table 4-8 Period of the IC order per composition in BFPT.**

| Composition (x) | delta (δ) | Period of IC Order (L) |
|---|---|---|
| x = 0.75 | 0.0033 | 840 (±20) Å |
| x = 0.9 | 0.0035 | 790 (±19) Å |
| BiFeO$_3$* | 0.0045 | 620 (±20) Å |

* (Sosnowska, 1982)

### 4.7.3 Conclusions

The IC nature of magnetic ordering in BiFeO$_3$-PbTiO$_3$ is observed to be phase dependant, only forming in compositions exhibiting rhombohedral symmetry and the period of the modulation is of the same order as in keeping with that of pure bismuth ferrite.

Increasing the percentage of lead titanate increases the period seen in Table 4-8, from 620 (±20) Å for bismuth ferrite (Sosnowska, 1982) to 790 (±19) Å  and 840 (±20) Å for 10 % and 25 % PbTiO$_3$ additions respectively, similarly to previous publications that studied doping of BiFeO$_3$ with other elements (Sosnowska, 2002). For x = 0.7, the tetragonal structure restores the collinear and commensurate antiferromagnetic order.

## 4.8   PRESSURE INDUCED PHASE TRANSFORMATION

### 4.8.1   Motivation

Previous work has been published on the effect hydrostatic pressure has on the $BiFeO_3$ (Haumont, 2006), (Pashkin, 2007) and $PbTiO_3$ (Janolin, 2008), (Ahart, 2008), end members. They are seen to exhibit multiple structural phase transitions at pressures from 2.5 GPa and 13 GPa respectively, as well as a magnetic transition (Gavriliuk, 2005) observed in BFO at 47 GPa. Literature by Wu (2005) presents an MPB in $PbTiO_3$ as a function of pressure, transitioning from tetragonal to rhombohedral with increasing pressure, through an intermediate monoclinic phase.

The motivation for the work reported here was to determine the effect of pressure on the disintegrated tetragonal form of $xBiFeO_3$-$(1-x)PbTiO_3$. An experiment was envisaged to ascertain whether pressure could be used, coupled with the phase volume difference reported by Smith (1968), to affect a phase transition to the AFM rhombohedral distortion at room temperature. This is described next.

### 4.8.2   Structural Neutron Diffraction

The previous sections have shown that at room temperature the R3c phase displays antiferromagnetic ordering, whereas P4mm is paramagnetic. Figure 4-43 and Table 4-9 show the results from a structural refinement of $0.7BiFeO_3 - 0.3PbTiO_3$ powder within the P-E cell at the initial sealing load of 7 tonnes, corresponding to a hydrostatic pressure $\approx 0$. The parameters are in excellent agreement with that of the powder without the P-E cell contributions in the previous experiments (Table 4-4).

The refinement contains contributions from four phases, the most dominant being the P4mm tetragonal phase of the 7030 BFPT powder, as well as peaks associated with the lead pressure marker, and no observed presence of AFM ordering. Weaker contributions are present due to WC and Ni which originate from the anvils of the P-E cell. The refined structural parameters for the ferroelectric phase are shown in Table 4-9. The lattice parameters ($a$ = 3.813 Å and $c$ = 4.534 Å) are similar to those reported previously from neutron diffraction on the Polaris instrument.

The structural refinement in this case was completed using the General Structure Analysis Software (GSAS). As discussed in section 2.6 this package again facilitates structure refinement by the Rietveld method but in the case of the PEARL experiment, the author acknowledges Dr. Comyn for his contribution to the experiment by conducting the refinements using GSAS (Comyn, 2008) (Comyn, 2000), a package unfamiliar to the author. Details of the refinement constraints and parameters used can be found in Appendix A.
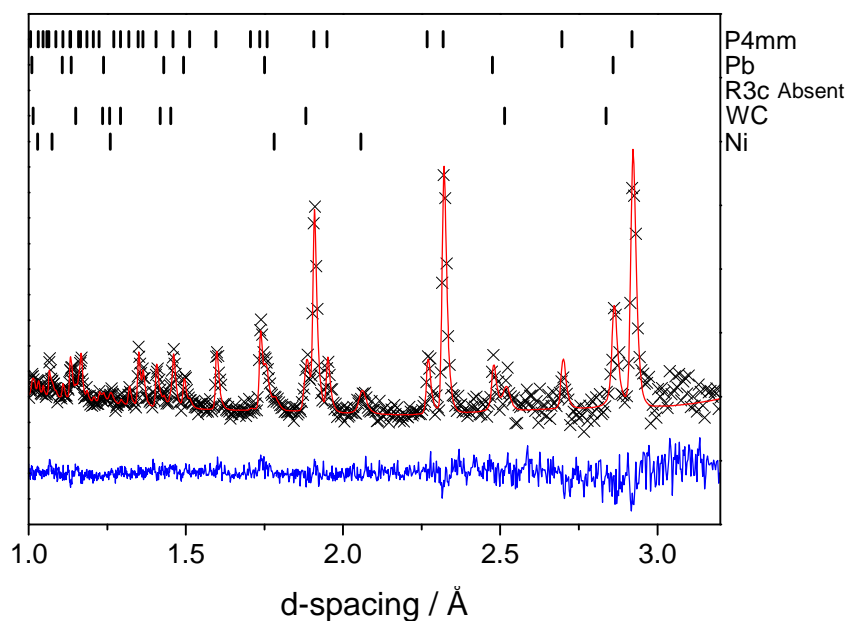
**Figure 4-43 Structural refinement for the 7030 BFPT disintegrated powder at 0 GPa within the P-E pressure cell. A number of data points have been removed to improve clarity. (Black) Observed data is shown by crosses, and the (red) line the refined model. The lower (blue) line shows the difference plot between the observed and calculated plots.**

**Table 4-9 Data from structural refinement for $0.7BiFeO_3 - 0.3PbTiO_3$ disintegrated powder at zero pressure. The atomic displacements shown are relative, reflecting a shift from the centrosymmetric position.**

| Parameter | $0.7BiFeO_3 - 0.3PbTiO_3$, P4mm |
|---|---|
| a | 3.813(1) Å |
| c | 4.534(6) Å |
| $z_{Bi,Pb}$ | 0 |
| $z_{Fe,Ti}$ | +0.05(2) |
| $z_{O1,O2}$ | +0.17(7) |
| $U_{ISO\,(all)}$ / Å$^2$ | 0.0179(2) |
| $R_p$ | 0.057 |
| $R_{wp}$ | 0.069 |

Figure 4-44 shows the effect of increasing hydrostatic pressure on the ferroelectric phase from refinements of the lead and R3c phase contributions. At a pressure of > 0.40 GPa, gradual transformation from P4mm to R3c occurs, with complete transformation at 0.77 GPa.

The transformation is not instantaneous, and a mixed phase region persists over a significant pressure range of 0.23 GPa. In addition, the P4mm and R3c phases coexist over a large time period (>18 hours) due to the long collection times required for neutron diffraction studies. Note that the transformation proceeds through a mixed phase region and not via an intermediate phase, such as monoclinic or orthorhombic as observed in other systems, such as reported in $PbTiO_3$ (Wu, 2005).
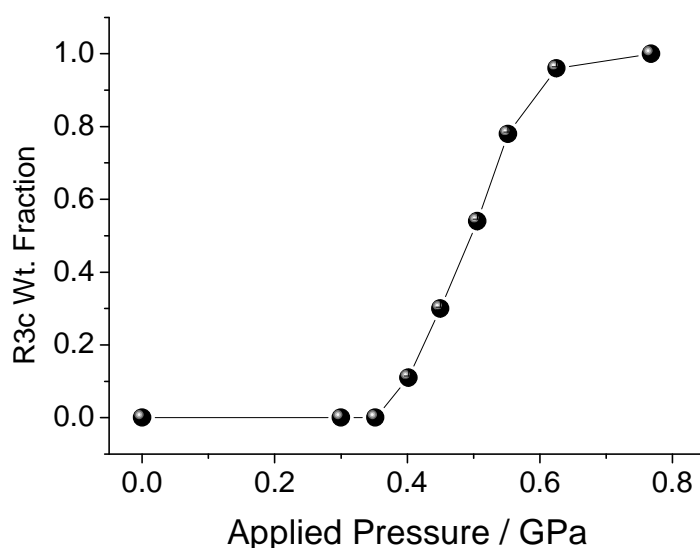


**Figure 4-44 Variation in weight fraction of R3c phase with increasing hydrostatic pressure for 7030 BFPT. Error bars (sigma, from refinement) are smaller than the symbols.**

The effect of pressure on the primitive unit cell volumes are plotted in Figure 4-45. As would be expected, the volume of each phase decreases as the pressure increases. Where the concentrations of the minority phases are low, such as at the onset of transformation (0.4 GPa), where the R3c phase is first apparent and where the transformation in near completion (0.65 GPa), the error bars in the calculation of volume from the structural refinements are high.

The P4mm phase is always a far higher volume (slightly less than 5%), and therefore a lower density than the R3c phase. It is this difference in volume discussed earlier that is proposed to be the driving force for the pressure induced phase transition.
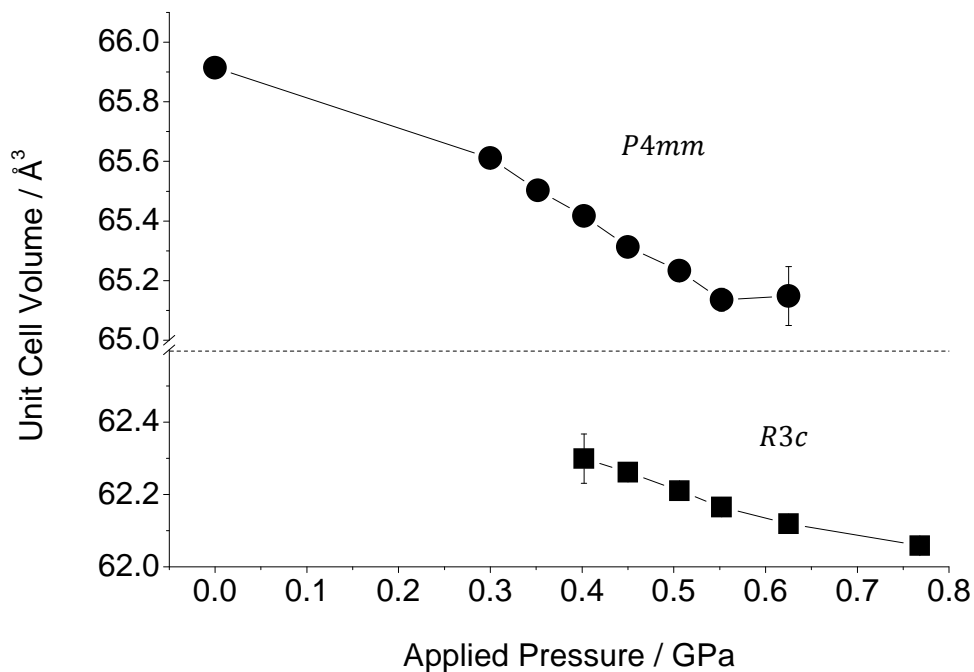
**Figure 4-45 Variation in unit cell volume for 7030 BFPT as a function of applied hydrostatic pressure. The primitive, pseudo-cubic unit cell volume is used for the R3c phase.**
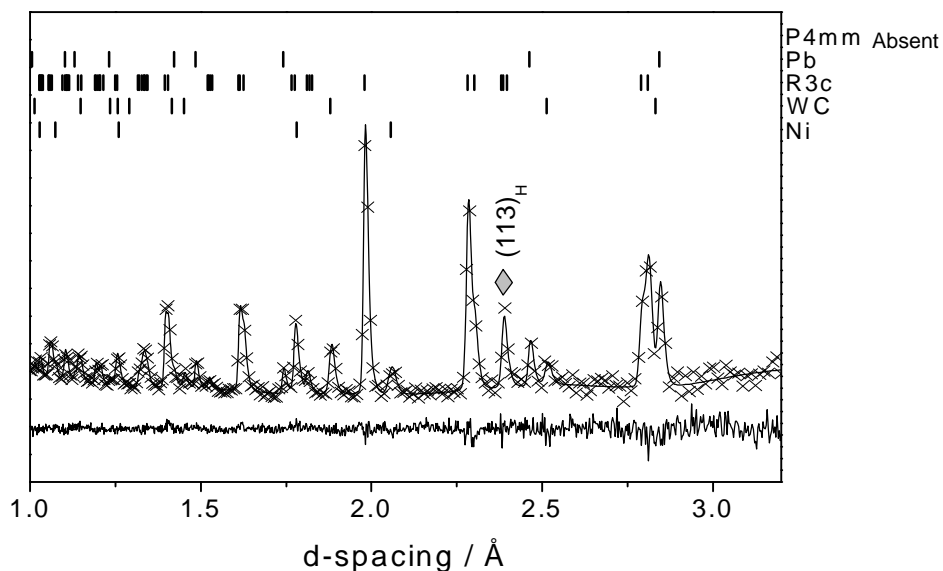


**Figure 4-46 Structural refinement for the 0.7BiFeO$_3$ – 0.3PbTiO$_3$ disintegrated powder after transformation to R3c phase at a pressure of 0.77 GPa, cf. Figure 1. A number of data points have been removed to improve clarity.◆ at 2.4 Å denotes both nuclear and magnetic contributions.**

Structural refinement of the disintegrated powder at a pressure of 0.77 GPa in Figure 4-46, is in excellent agreement with a fit for a transformation to 100% R3c phase. The $(113)_H$ reflection, which results from both oxygen octahedral tilting and antiferromagnetic ordering is marked.

Upon unloading the pressure cell, after completion of the experiment, it was observed that the transformed R3c phase persisted, and did not revert back to its original P4mm structure.

### 4.8.3  Magnetic Neutron Diffraction

As mentioned previously, the high resolution detector configuration used in PEARL has a limited d-spacing range < 4.15 Å. Determining the presence of magnetic ordering in the transformed R3c phase in BFPT is therefore difficult, as the purely AFM peak at ~4.6 Å is not visible, so magnetic refinement is heavily reliant on the $(113)_H$ reflection of the R3c phase at ca. 2.4 Å. The intensity of which is comprised of both nuclear and magnetic contributions in similar proportions at room temperature for the composition x = 0.7.

In order to improve the confidence in the magnetic refinement, the pressure cell was rotated to use the low angle, low resolution detector, which can detect up to 8.5 Å in order to observe diffraction from the AFM $(101)_H$ peak. The diffraction data collected is presented in Figure 4-29.

It is evident the peaks are extremely broad compared to the previous figures, due to the lower resolution, and below 3 Å is dominated by reflections from the pressure cell gaskets as in this mode they generate a far higher contribution to the signal than observed using the conventional, optimised 90° detector banks.

However, Figure 4-29 clearly shows a transformation from P4mm at zero pressure to R3c at 0.77 GPa, and with it a transformation from para- to antiferromagnetic ordering. The position of the P4mm $(001)_T$ and the R3c magnetic $(101)_H$ peaks are in similar but significantly different positions of 4.535 and 4.587 Å respectively at zero pressure, in keeping with that observed from HRPD in Figure 4-37. A large broad peak can be observed at 0.51 GPa at these positions, where both the P4mm structural and R3c magnetic peaks coexist in similar proportions. To recap, the peak at 4.535 Å in the lower trace is nuclear, whereby in top two at ca 4.6 Å (the position clearly changes as a function of pressure) it is entirely magnetic, with no nuclear contributions.
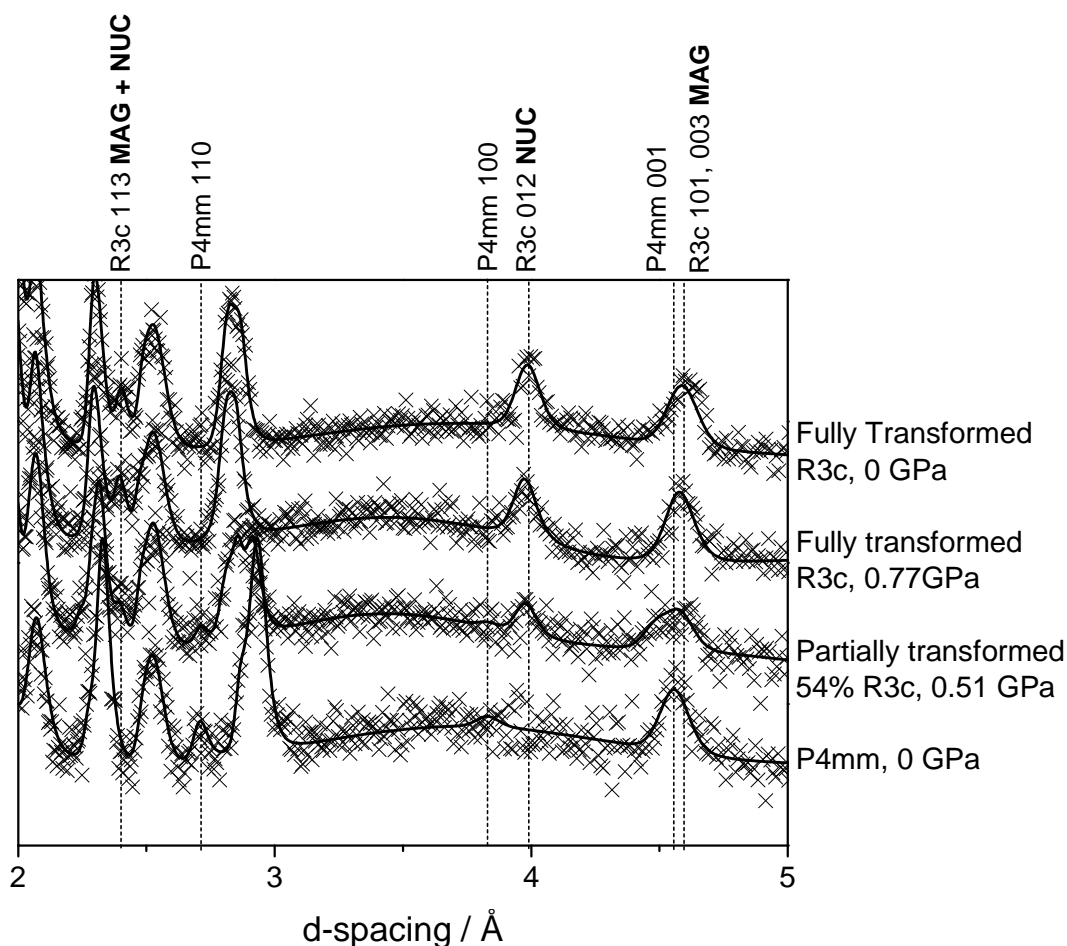
**Figure 4-47 Diffraction data of 0.7BiFeO$_3$ – 0.3PbTiO$_3$ collected using low-angle bank on Pearl at selected loads. The dashed lines show the position of various peaks of interest.**

### 4.8.4  Conclusions

At ambient temperature and pressure, the disintegrated powder composition x= 0.7 possess tetragonal symmetry, P4mm, with paramagnetic ordering. With the application of moderate hydrostatic pressures (0.77 GPa), the P4mm phase readily transforms to R3c rhombohedral symmetry, proposed to be driven by the same mechanism of original spontaneous disintegration, by attempting to relieve the stress within the material. A transformation from para- to antiferromagnetic ordering accompanies this structural transition.

## 4.9  MAGNETOELECTRIC EFFECTS

### 4.9.1  Motivation

So far it has been shown that the stress state within the BFPT system is pivotal to its synthesis and phase fractions, which in turn is seen to affect the materials magnetic order and, as stated in the literature, its electrical properties. The coupling of all these material properties has been proved by modifying the stress conditions within the lattice with the application of pressure; in turn transforming the ferroelectric structure to allow ordering of antiferromagnetism to be permitted.

The motivation for the following work was to determine if an electric field could influence the magnetic order. Could applying an external electric field induce strain within the paramagnetic tetragonal phase to generate sufficient stress (Figure 4-16 (b)) to drive phase transformation as a relief mechanism (Figure 4-16 (d)); in turn inducing a phase transformation to the antiferromagnetic rhombohedral structure at room temperature. Thus presenting strain mediated magnetoelectric effects in bulk polycrystalline $xBiFeO_3$-$(1-x)PbTiO_3$.

The composition $x = 0.7$ was selected as it represents a composition within the MPR, close to the MPB where the piezoelectric properties, coupling of electric field with mechanical strain is at a maximum, and most likely to affect a large enough stress.

Although bulk materials have not previously shown any ME effect, the existence of an MPB in this system was thought to generate the structural transformations required.

### 4.9.2  Neutron Diffraction

Diffraction data collected using the constant wavelength source of neutrons on the E2 instrument, of a 7030 BFPT sintered polycrystalline ceramic disc, electroded with silver and attached to an aluminium paddle is shown in Figure 4-48.

Indexing of the pattern observes predominantly rhombohedral R3c phase with additional peaks attributed to the aluminium and silver metal. The positions of the metals were calculated from crystallographic data through ICSD (CDS, 1996) using the $FM\bar{3}M$ (ISS # 225) space group for both Al and Ag.

The purely AFM peak $(½½½)_R$ / $(101)_H$ is observed at ~4.6 Å, but the oxygen tilt and magnetic contributions seen in the $(^1/_2{}^1/_2{}^3/_2)_R$ / $(113)_H$ peak are hidden by the overwhelming intensity and peak overlap of the $\{111\}_R$ and metals.

Electric field was applied to the sample and diffraction data was collected. Figure 4-49 illustrates the difference between the sample above with no field, and applying electric field parallel to the incident radiation direction of 10 MV m$^{-1}$. It is evident from the difference plot that an increase in intensity occurs for the structural $(100)_R$, $(110)_R$ and magnetic $(½½½)_R$ (Figure 4-50).
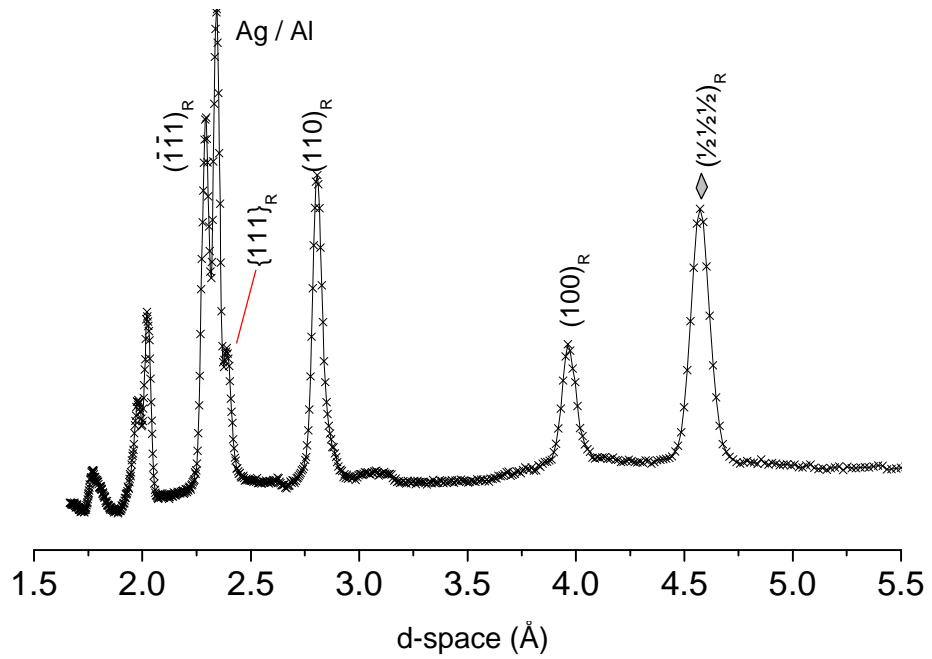
**Figure 4-48 Neutron diffraction pattern collected from the E2 instrument for a 7030 BFPT sintered silver electroded ceramic, attached to an aluminium paddle. E = 0 MV / m T = 250 K**
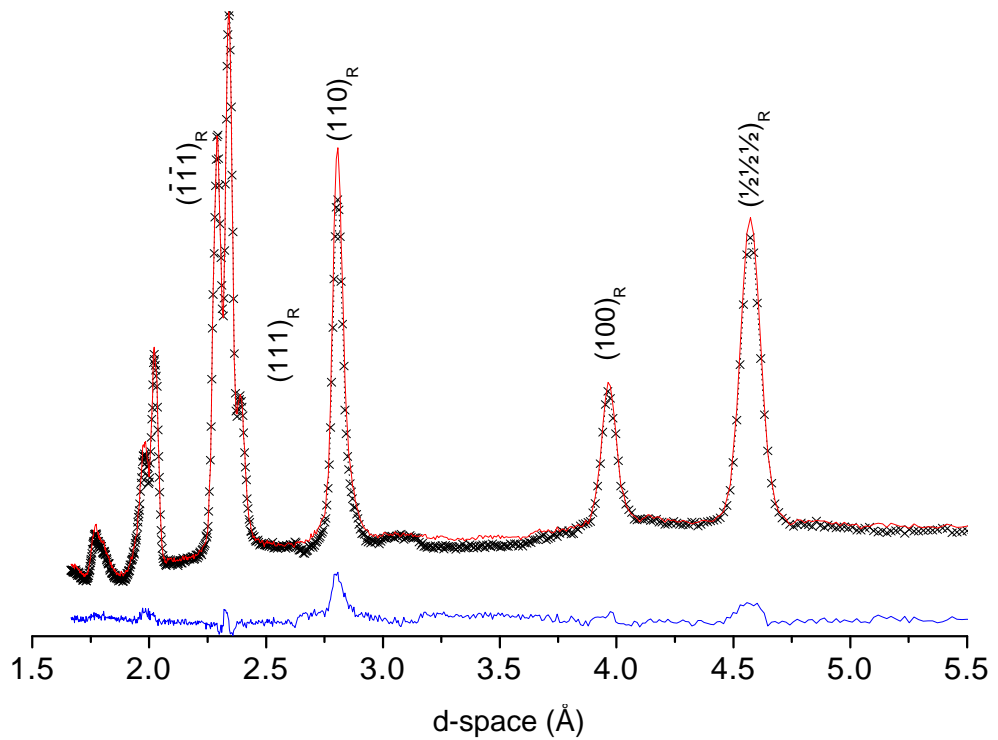


**Figure 4-49 (black) As Figure 4-25, 0 MV / m (red) Application of 10 MV / m (blue) Difference plot between 0 and 10 MV / m**
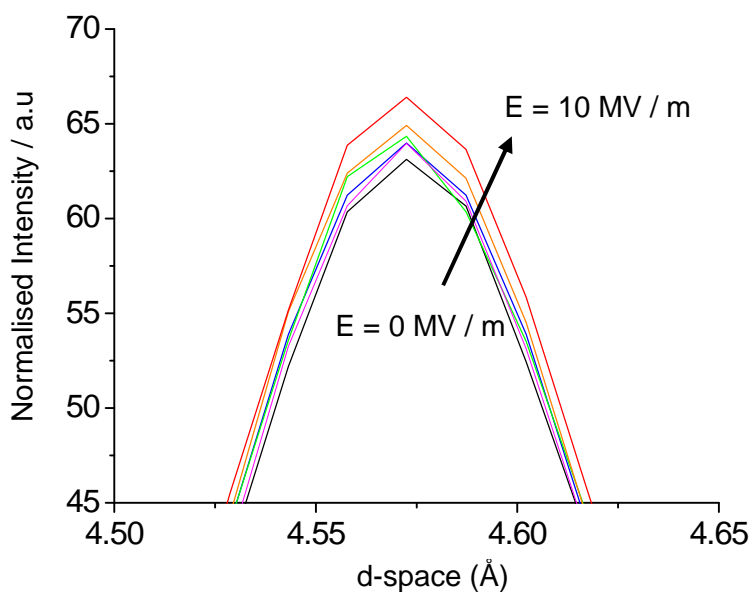
**Figure 4-50 Neutron diffraction of 7030 BFPT over a range of applied electric fields from 0 to 10 MV / m. The plot focuses on the (½½½)$_R$ antiferromagnetic peak.**
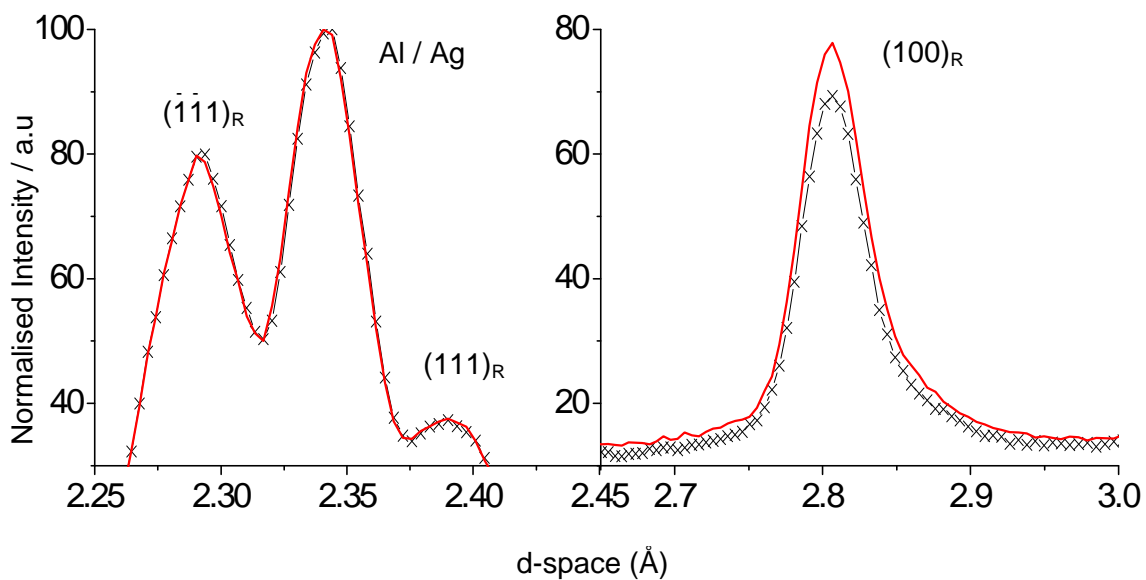


**Figure 4-51 Neutron diffraction of 7030 BFPT with (black) 0 MV / m and (red) 10 MV / m applied electric field. Bragg peaks are indexed respectively.**

The difference plot also shows a perturbation ca. 2.3 Å, but closer inspection observes this to represent a shift in d-space for the metals peak from 2.344(4) to 2.340(1) Å, a consequence of the piezoelectric nature of the material imparting a strain on the Al paddle and Ag electrode.

There is no significant or detectable change, beyond appropriate errors for the $\{111\}_R$ peak (consisting of 3 equivalent planes $(\bar{1}11),(\overline{111})$ and $(11\bar{1})$) with the application of electric field (Figure 4-51).

It is interesting to note that with the removal of the electric field back to 0 MV m$^{-1}$, the peak intensities return to within ± 1.4 % of the original values, an indication that the process is reversible.

Due to the inclusion of the metal peaks, it is impossible to derive an accurate measure of the contributions from the individual reflections, and thus does not allow a comparison between the magnetic $(½½½)_R$ and structural $(111)_R$ peaks, which occupy the same planes.

The geometry of the E2 instrument also needs careful consideration. The electric field needs to be applied across as thin a thickness of ceramic as possible, to reduce the likelihood of breakdown from material defects and reduce the voltage required to achieve the high fields needed. The incident neutron beam needs to intersect with as much sample as possible for realistic counting times and to maximise the statistics, so is directed parallel to the polarisation direction perpendicular to the discs diameter. Because of this, the diffraction cone that emanates and is detected by the position sensitive detectors, shows the whole ~5 Å range across a 32° angular range of detectors (Figure 3-7). This results in the $(½½½)_R$ planes being almost parallel to the polarisation direction, and the $(111)_R$ being produced from diffraction of planes over 20° from the same polarisation direction. This does not allow a direct correlation between the peaks as it cannot be distinguished from effects of texture.

Another disc, from the same batch as the sample used in E2, was subsequently irradiated with synchrotron radiation at ID11, ESRF, as per 3.5.2-1 electroded with gold and with the same d-space range over a much smaller, almost negligible, detector angle of 2.4° (Figure 3-8).

### 4.9.3  Synchrotron Diffraction

Diffraction collected using synchrotron radiation offers much faster collection times due to the intensity of the beam compared to neutron sources and the increased strength of interaction. The resolution of ID11 is also markedly increased compared to the E2 instrument, allowing dissolution of the peaks by profile fitting, yielding much lower error values than for the patterns in Figure 4-48.

This is illustrated in Figure 4-52, presenting synchrotron diffraction of the 7030 disc with much flatter background contributions, and definitions in the profile of the $\{111\}_R$ and $\{110\}_R$ overlapping peaks to be seen. Figure 4-53 shows how profile fitting in WinPlotR, part of the FullProf suite, can be used to attribute 4 peaks to the broad reflection at ~2.8 Å. Because of the high level of overlapping between multiple peaks, Gaussian profiles were fitted, as long peak 'tails' characteristic of Lorentzian functions produce unrealistic fits and large errors due to the proximity of neighbouring peaks interfering with background contributions. For example, a calculated Lorentzian peak can exceed 15-20 FWHMs to remove the truncation effect (McCusker, 1999).

Metal peaks associated with 40 nm gold electrodes are negligible as the sample diffraction dominates, being some 4 orders of magnitude thicker.

As with the neutron sample, electric field was applied and diffraction data collected. Figure 4-54 illustrates the difference between the sample with no field, and applying electric field, again parallel to the incident radiation direction of 10 MV m$^{-1}$.

The difference plot demonstrates an increase in intensity for all the peaks, which in this case are only nuclear, but particular increments are seen for the $(100)_R$ and $(110)_R$, in keeping with the neutron diffraction data. However in this instance the peaks are now comparable due to the reduced detector angle range.
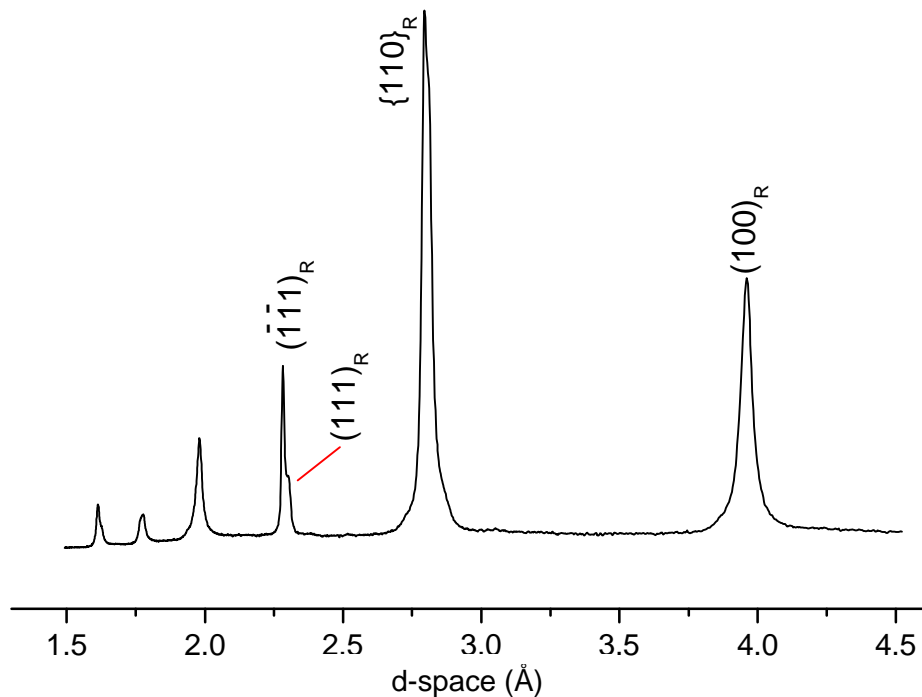


**Figure 4-52 Synchrotron diffraction collected from ID11 at the ESRF of 7030 BFPT sintered ceramic disc. E = 0 MV / m, T = ambient.**
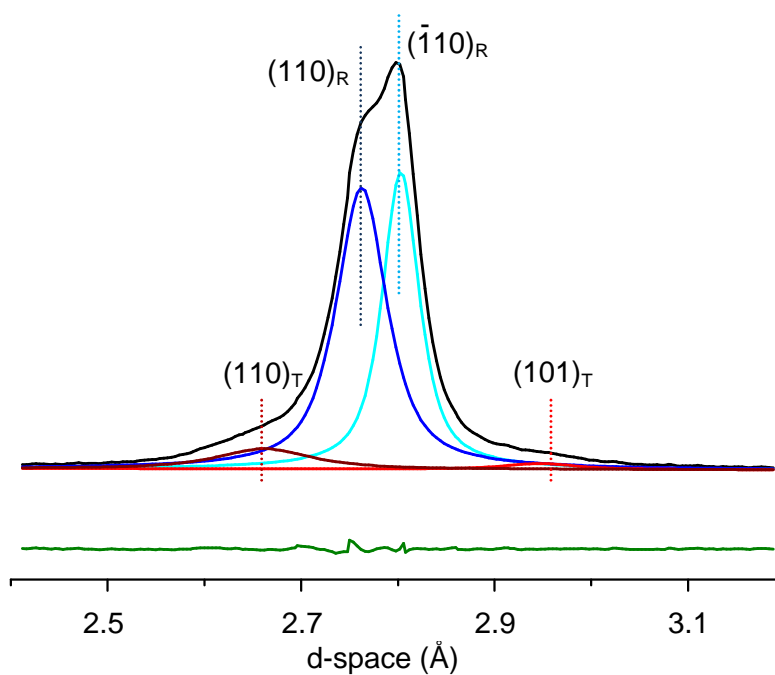
Figure 4-53 As Figure 4-29 focussed over the d-space range 2.5 – 3.1 Å. A profile fit has been employed with (black) the observed intensity, (blue) rhombohedral peaks and (red) tetragonal peaks identified. (Green) Difference plot between observed and calculated intensities ($chi^2$ = 0.00480).
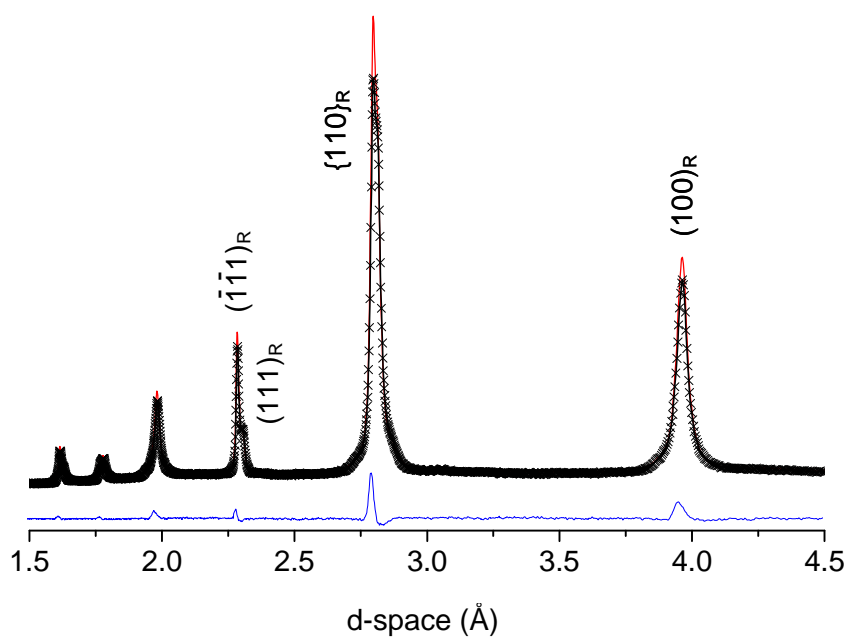


Figure 4-54 (black) As Figure 4-29, 0 MV / m (red) Application of 10 MV / m (blue) Difference plot between 0 and 10 MV / m

### 4.9.4 Magnetoelectric effects

Structure refinement is inappropriate for these electric field measurements due to the influence of texture or preferred orientation induced by the field on the polarisation direction. Instead least squares profile fitting the $(\frac{1}{2}\frac{1}{2}\frac{1}{2})_R$ AFM and structural $(100)_R$ reflections from neutron diffraction, and the $\{111\}_R$ family from the synchrotron experiment are shown in Figure 4-37 per step in applied electric field using WinPlotR. Further fits to represent the peaks found within the $\{110\}_R$ reflection, following the same method as for Figure 4-35, to model phase contributions from the R3c and P4mm phase are summarised and presented in Figure 4-38.
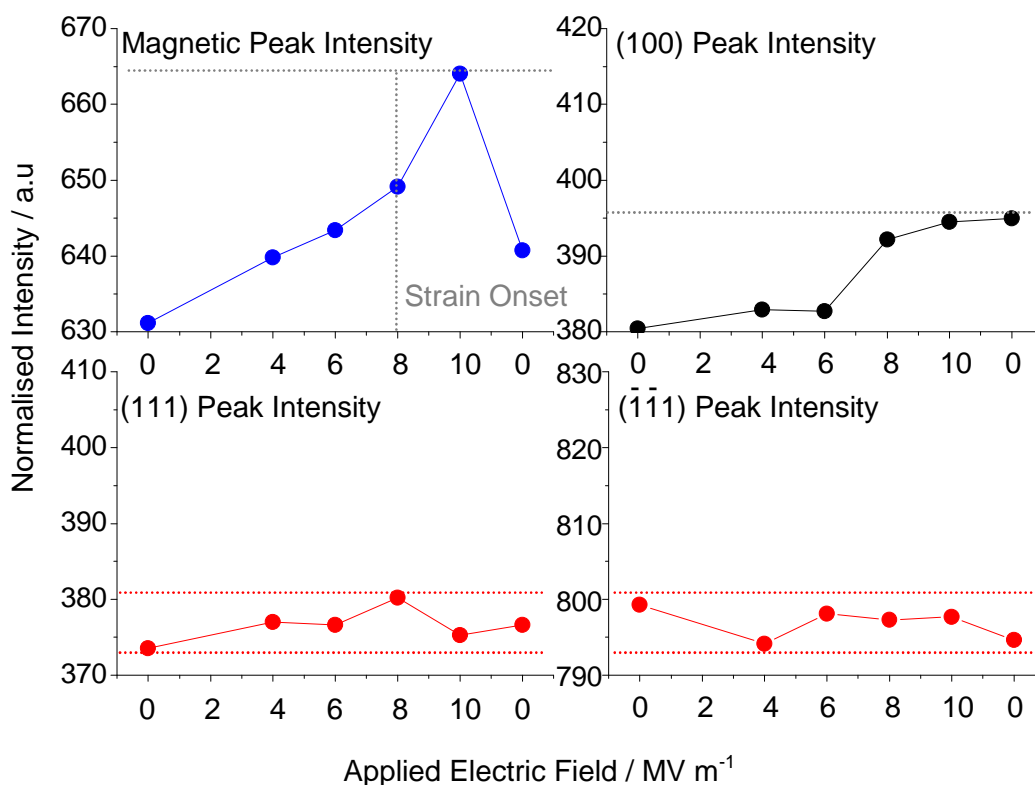


**Figure 4-55 Results of Gaussian peak profile fitting completed in WinPlotR for the peaks identified from neutron diffraction data collected on E2 (top row) and synchrotron data on ID11 (bottom row, red).**
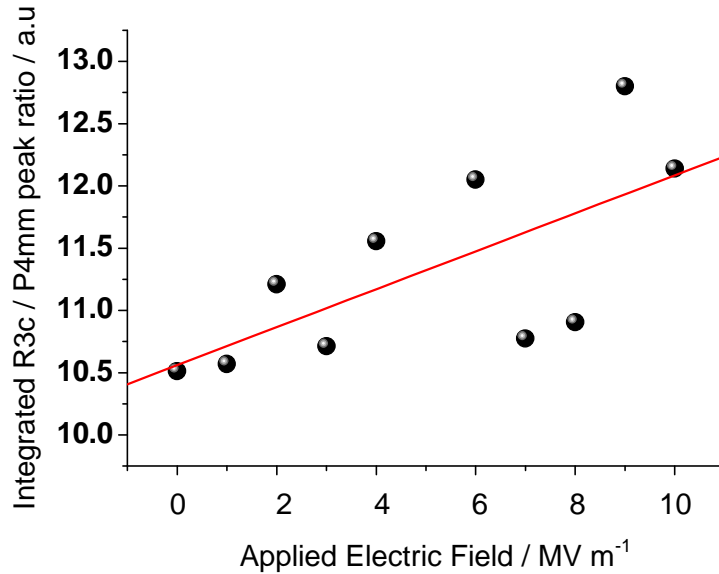
**Figure 4-56 Integrated intensity ratio of R3c : P4mm phase contributions from the synchrotron {110}$_R$ peak as a function of electric field with a linear trend (red).**

To propose a mechanism for the intensity differences in the peaks observed from the experiments, reasons for intensity changes in diffraction need to be explored, however elements that contribute to reflection intensity are many and in some cases complex, so the 3 most probable for a ferroelectric system are proposed.

*Domain Switching*

With the application of an electric field, it can be easily conceived that this would align more domains in the field direction, aligning more (½½½)$_R$ magnetic planes to satisfy Bragg's law, and therefore cause an increase in intensity.

This postulation also explains the intensity increase for the majority of the structural peaks, however Figure 4-37 clearly shows that the {111}$_R$ reflections do not follow the same relative increase in intensity, instead showing a change of ~1 % compared to over 5 % for the (100)$_R$ and (½½½)$_R$ making this an unlikely description, or at least not the principal reason for the results shown. However it is worthy to note the step change in intensity increase in the (100)$_R$ and (½½½)$_R$ at the field equivalent to the onset of strain seen in the electrical measurements section Table 1-10 for the 7030 BFPT composition.

*Phase Transformation*

Analysis of the $(110)_R$ peak provides a model which describes the presence of two tetragonal P4mm and principally two rhombohedral R3c peaks. Integration of the peaks and plotting the ratio of the areas associated with the R3c and P4mm phases provides a good approximation to the phase contributions as the applied field is increased. This is shown in Figure 4-38 and clearly shows a trend toward an increase in rhombohedral phase being present within the sample, suggesting that the electric field is inducing an increase in polarisation along the <111> polarisation direction. A strain associated with this is perhaps driving a transformation of tetragonal unit cells to take on a rhombohedral distortion, which at temperatures above 220 K (Table 4-6) is known to be the only phase capable of supporting an AFM order. This transformation is similar to the effect seen in the PEARL experiment, in that by increasing the rhombohedral phase, an increase in the regions which exhibit AFM are present; therefore observing an increase in magnetic peak intensity.

The increase of R3c phase (16.7 %) and AFM reflection intensity (~5 %) however is not proportional, suggesting that this mechanism may not fully explain the observed behaviour; however electric field driven phase transformations in piezoelectric and ferroelectric systems are well reported in the literature (Daniels, 2010) (Hall, 2008) (Noheda, 2002).

Caution must be taken with the hypotheses put forward thus far as they stem from comparison of peaks that occur from differing diffraction volumes to that of the purely AFM reflection.

A comparison can only be made realistically with the $(½½½)_R$ with the $(111)_R$ as they are representative of the same grains contributing to the diffraction. This is shown graphically in Figure 4-57.
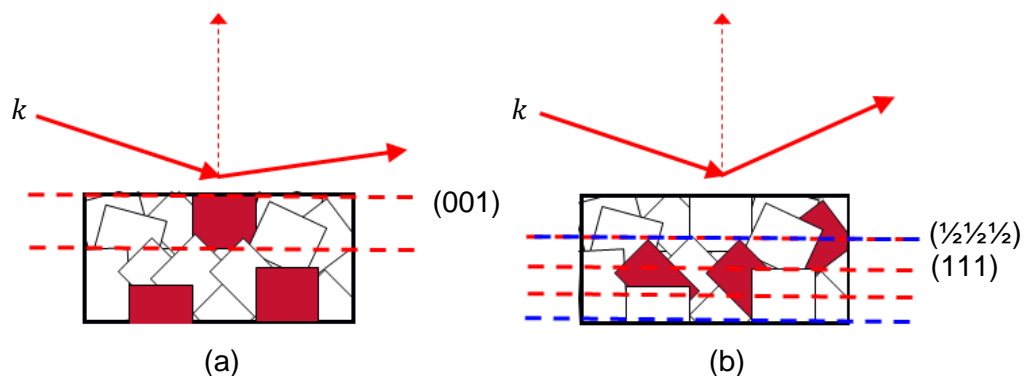


**Figure 4-57 Illustration of how diffraction volumes differ for (a) the (001) and (b) the (111) (red) and (½½½) (blue) when applicable grains satisfy Bragg's law. *k* represents the incident radiation wavevector.**

*Linear Magnetoelectric Effect*

In $BiFeO_3$ the linear ME is forbidden by symmetry (Catalan, 2009) and the presence of the IC order as previously discussed. However, high resolution neutron diffraction on HRPD has shown that we can readily alter the range of the IC modulation by changing the concentration of $PbTiO_3$ as well as observed its phase dependence, existing only as part of the rhombohedral structure.

It is not inconceivable, but difficult to convolute from the data presented, that a breakdown of the IC order could occur with application of electric field resulting in collinear AFM, breaking the symmetry requirements for linear magnetoelectric effects. The increase in AFM peak intensity without a subsequent change in the $(111)_R$ is not inconsistent with this theory, but comprehensive high resolution neutron diffraction would be required to determine any breaking of the IC order.

## 4.9.5  Conclusions

An increase in the purely AFM peak intensity from neutron diffraction is observed with proportionate intensity increases in the $\{110\}_R$ and $(100)_R$ also.

The $\{110\}_R$ can be treated with a profile model that is in excellent agreement with the presence of 4 peaks, 2 of which are related to the minority P4mm tetragonal phase and 2 to the rhombohedral R3c phase which is the only phase that can sustain AFM ordering at 250 K. Integration of these peaks give an approximation to phase contributions, which suggest an increase in rhombohedral phase is occurring with increasing electric field. This postulation consequently increases the proportion of AFM ordering and subsequently magnetic planes that can diffract, increasing the $(½½½)_R$ peak intensity.

However a comparison can only be made with the $(½½½)_R$ from the $(111)_R$ as the grains orientated to produce diffraction of these planes are the same.

# 5   OVERALL CONCLUSIONS

This work has two important outcomes:

(i) There is a strong form dependence of the bismuth ferrite lead titanate sub-solidus phase diagram which influences both ferroelectric and magnetic properties.

(ii) Polycrystalline ceramics of $xBiFeO_3 - (1-x)PbTiO_3$ with x = 0.7  have been shown, by neutron diffraction, to exhibit strain mediated magnetoelectric effects.

Scanning electron microscopy and a range of X-ray, synchrotron and neutron diffraction experiments, suggest that the properties of the BFPT ceramics are heavily dependent on internal stress. For compositions 0.4 ≤ x ≤ 0.7, cooling from the sintering temperature results in a structural transition from a cubic perovskite paraelectric, to a tetragonally (P4mm) distorted ferroelectric phase at the ferroelectric Curie point (638 °C for x = 0.7). At the onset of the tetragonal distortion characterised by an increase in the $c/a$ lattice parameter ratio, the constraints imposed on each grain by its neighbours result in the development of internal stress.

It has been observed for the lead titanate end member, that this stress can often overcome the energy required to separate the grain boundaries for grain sizes above a critical facet length. For BFPT the critical grain size is proposed to be approximately 7 microns. Elevated sintering temperatures (1100 °C) result in this dimension being exceeded, and together with fast cooling (>900 °C/hr) results in fracture, between neighbouring grains as a stress relief mechanism, resulting in unclamped, free, grain size particulates that exhibit wholly tetragonal phase and assume a large $c/a$ ratio = 1.17.

Conversely, sintering at temperatures 100 °C lower, and slow cooling (20 °C/hr) produces a distribution of grain sizes that fail to satisfy the critical grain size, prohibiting intergranular fracture. Instead a fractional phase transformation, from tetragonal to the (4 %) smaller primitive volume rhombohedral (R3c) phase, occurs to partially relieve the stress. This occurs for all compositions x ≥ 0.4. The stress relief is only partial, confirmed by diffraction peak broadening and a reduced $c/a$ ratio in the tetragonal phase. This explains the broad compositional range of phase coexistence in sintered ceramics.

At ambient temperature in polycrystalline ceramics, the rhombohedral phase is observed to exhibit G-type antiferromagnetic order along the [111] direction in all compositions x ≥ 0.4. For x = 0.75 this order is modulated by an 840 Å incommensurate periodicity, determined from high resolution powder diffraction, which decreases with increasing $BiFeO_3$ content.

The tetragonal phase is also observed to sustain G-type antiferromagnetism at temperatures below -53 °C (220 K) for x= 0.7 to -193 °C (80 K) for x = 0.8. The composition x = 0.3 is never observed to support antiferromagnetic order, as the dilution of magnetic iron ions exceeds the percolation threshold via substitution with titanium ions.

It has been shown by in situ neutron diffraction that the application of moderate (0.77 GPa) hydrostatic pressure to stress free tetragonal particulates (x = 0.7) results in a structural phase transformation from tetragonal to rhombohedral, accompanied by a transition from paramagnetic to antiferromagnetic order.

At room temperature, increasing the external stress on the system drives the lattice to compensate by transformation to the lower volume R3c phase. This is analogous to the effects of internal stress observed after sintering, which results in the mixed phase ceramics. In effect this equates to 'switching' magnetism on and off, with applied stress.

A similar principal has been explored in a subsequent neutron experiment. Applying an external electric field, up to 10 MV m$^{-1}$, to a polycrystalline ceramic has resulted in a modulation of the intensity (5 %) of the $(½½½)_R$ magnetic reflection. An increase in lattice strain through the piezoelectric effect, is suggested to drive a phase transformation in a small number of grains, which results in an increase in the concentration of antiferromagnetic rhombohedral phase, at room temperature.


Characterisation of magnetoelectric, multiferroic materials is of increasing importance in electronics and energy applications, as they have the potential to make greener, more efficient devices. This work has built on existing studies that have used qualitative laboratory techniques to fully characterise the ferroelastic, ferroelectric and antiferromagnetic contributions, and their coupling to one another to create a strain mediated material.

The bismuth ferrite lead titanate system has impact in engineering devices such as high temperature piezoelectric transducers and magnetoelectrics, but also expands out to the fundamental science of magnetic and electric systems by harnessing the ferroelastic strains and stresses inherent in this mixed phase ceramic. This thesis serves to advance potential understanding and cross disciplinary interaction, by presenting the first use of neutron diffraction on polycrystalline samples.

## 6   FURTHER WORK

As the work here represents aspects of both magnetic and ferroelectric characterization, as well as nuclear structure analysis, on a material that has not been as widely researched as its end members there is unsurprisingly an enormous amount of potential further work.

In depth investigation of the magnetoelectric coupling is perhaps the most novel aspect to pursue as a result of this thesis, principally due to the engineering applications that could ensue from modelling and manipulating the material to optimise the BFPT composition, internal stress and strain. It is also inherently interesting to understand the physics behind the magnetoelectric effect, especially as this represents some of the first measurements on bulk sintered ceramics.

In order to do this, high resolution diffraction is a pertinent starting point, implementing in situ electric field measurements whilst probing the incommensurate magnetic order at the $BiFeO_3$ rich end of the MPR. Instruments such as HRPD however are not built appropriately for this type of experiment, the low flux requires increased counting times, for which exposing ceramic samples to electric fields over extended periods is not practical; often resulting in catastrophic breakdown of the sample. Instead, Polaris at ISIS is currently being refurbished to house new more sensitive detectors, which will increase the resolution enough to theoretically resolve the reflections pertaining to the incommensurate order.

As previously concluded, bulk polycrystalline ceramics are not the ideal samples from which to determine anisotropic effects of strain or magnetization. The averaging effects of the many grains dilute the properties making it difficult to deconvolute appropriate information.

Work on flux grown single crystals of BFPT has previously not been successful in producing rhombohedrally distorted perovskite phase materials, which would be a key advancement in magnetoelectric characterisation for this system. Research into other synthesis techniques could produce crystals that would allow the phase transformations observed within the polycrystalline materials to be better characterized and controlled.

Internal stress and tetragonal strain is seen to be a major factor in controlling all aspects of the material, from electrical and magnetic properties, to synthesis. Further characterising the effects of this uniquely large stress from examination of hardness and fracture toughness might also yield interesting results, based on the relatively

large effect from applying moderate hydrostatic pressures. It can be envisaged that crack propagation in this materials could be prohibited via phase transformation to relieve local stress, or absorb the crack energy. Indications of the mechanical hardness of this material has already been observed by grinding and polishing of samples, where the x = 0.7 composition is often found to require substantially more silicon carbide paper contact and work than other samples to achieve the same material removal.

# 7 REFERENCES

Ahart, M., M. Somayazulu, R. E. Cohen, P. Ganesh, P. Dera, H. –K. Mao, R. J. Hemley, Y. Ren, P. Liermann and Z. Wu (2008) Nature. **451**, 545.

Aizu, K. (1970) "Possible species of Ferromagnetic, Ferroelectric, and Ferroelastic Crystals." Physical Review B. **2**. 3. 754-772.

Al Jawad, M (2004) "Time resolved neutron studies of metallic phase formation." Thesis (PhD). University of Leeds

André, G. (2003) "Cold Neutron Two-Axis Diffractometer" G4-1. LLB edition p. 21 – 22. Accessible online from <http:// *www-llb.cea.fr/spectros/pdf/g41-llb.pdf*>

Arfken, G. B. and H. J. Weber. (2001) "Mathematical methods for physicists." Academic Press. 5th International Ed. London.

Arnold, D. C., K. S. Knight, F. D. Morrison and P. Lightfoot (2009) Phys. Rev. Lett. **102**, 027602.

Ascher, E., H. Rieder, H. Schmid and H. Stossel. (1966) "Some of the properties of ferromagnetoelectric Nickel-Iodine Boracite." J. Appl. Phys. **37**. 3. 1404-5.

Astrov, D. N. (1960) Zh. Eksp. Teor. Fiz. **11**. 708. (In Russian)

Atou, T., H. Chiba, K. Ohoyama, Y. Yamaguchi and Y. Syono (1999) J. Solid State Chem. **145**. 639-42.

Baker, D. R., G. Paul, S. Sreenivasan, and H. E. Stanley. (2002) Phys. Rev. E, **66**, 046136.

Bacon, G. E. and K. Lonsdale. (1953) "Neutron diffraction." Rep. Prog. Phys. **16**, 1.

Belik, A. A., et al. (2006) Chem. Mater., **18**, 3. 798-803.

Bell, A. J. (2006) "Factors influencing the piezoelectric behaviour of PZT and other "morphtotropic phase boundary" ferroelectrics." Journal of Materials Science. **41**. 13-25.

Bell, A. J., A. Levander, S. Turner and T. P. Comyn (2007) "Internal Stress and Phase Coexistence in…" Proceedings of the 16th IEEE International Symposium on the Application of Ferroelectrics (ISAF), Nara, Japan. p. 406-409

Bell, A. J. (2008) "Ferroelectrics: The role of ceramic science and engineering." J. European Ceramic Society. **28**. 1307-17.

Bennington, S., A. C. Hannon and S. Langridge. (2006) "Neutron Training Course" Book and Presentations from the ISIS Neutron Training Course held at Rutherford Appleton Laboratories, Oxford. December 2006.

Besson, J. M., R. J. Nelmes, G. Hamel, J. S. Loveday, G. Weill and S. Hull. (1992) Physica B. **180**, 907-10.

Bhattacharjee, S., S. Tripathi and D. Pandey (2007) Appl. Phys. Lett. **91**, 042903.

Blundell, S. (2001) "Magnetism in condensed matter." Oxford, UK. Oxford University Press.

Bogardus, E. H. and R. Roy (1965) "Effects of strain induced by pressing and grinding $BaTiO_3$ and $SiO_2$." J. Am. Ceram. Soc. **48**, 4, 205-207.

Bohr, N. (1913) "On the Constitution of Atoms and Molecules." Philosophical Mag. **26.** 1.

Boomgaard, J. V. D et al (1974) J. Mater Sci. **9**, 1705

Boomgaard, J. V. D et al (1978) J. Mater Sci. **13**, 1538

Breit, G. and E. Wigner. (1936) "Capture of slow neutrons." Phys. Rev. **49**, 519.

Brillouin, L (1927) "Les moments de rotation et le magnétisme dans la mécanique ondulatoire (translated; the rotary moment and magnetism in wave mechanics)" Journal de Physique et le Radium. **8**. 74-84.

Brown, W. F., R. M. Hornreich and S. Shtrikman (1968) "Upper Bound on the Magnetic Susceptibility." Phys. Rev. **168**. 2. 574-577.

Burnett, T. L., T. P. Comyn and A. J. Bell (2005) J. Crystal Growth. **285**, 1-2, 156-61.

Burnett, T. L., T. P. Comyn and A. J. Bell (2006) J. Physics: Conference Series. **26**, 239-242.

Burnett, T. L. (2008) "Growth and characterisation of bismuth ferrite lead titanate single crystals." Thesis. Conducted in the Institute for Materials Research at the University of Leeds.

Caglioti, G., A. Paoletti and F. P. Ricci (1958). "Choice of collimators for a crystal spectrometer for neutron diffraction." Nuclear Instr. **3**. 223-228.

Callister, W (2000) "Materials Science and Engineering An Introduction." Fifth Edition. John Wiley & Sons.

Catalan, G. (2006) "Magnetocapacitance without magnetoelectric coupling." Appl. Phys. Lett. **88**. 102902.

Catalan, G. and J. F. Scott. (2009) "Physics and applications of Bismuth Ferrite." Adv. Mater. **21**. 2463-2485.

CDS – Fletcher, D.A., R. F. McMeeking and D. Parkin. (1996) "The United Kingdom Chemical Database Service." J. Chem. Inf. Comput. Sci. **36**, 746-749.

Chaix & Morel (2008) "Schéma de principe du synchrotron." [online] [accessed  26th July, 2010] Available at:

http://commons.wikimedia.org/wiki/File:Sch%C3%A9ma_de_principe_du_synchrotron.jpg

Cheng, J., N. Li and L. E. Cross (2003)(a) J. Appl. Phys. **94**. 8. 5153

Cheng, J. and L. E. Cross (2003)(b) J. Appl. Phys. **94**. 8. 5188.

Cheng, J., R. Eitel, N. Li and L. E. Cross (2003)(c) J. Appl. Phys. **94**. 1. 605.

Comyn, T. P., S. McBride and A. J. Bell (2004) Materials Letters. **58**, 30. 3844-3846.

Comyn, T. P., T. Stevenson and A. J. Bell. (2005) J. Phys. IV. **128**. 13-17.

Comyn, T. P., T. Stevenson et al. (2008) Appl. Phys. Lett. **93**, 23. 232901

Comyn, T. P., T. Stevenson et al. (2009) J. Appl. Phys. **105**. 9, 094108.

Crangle, J. (1977) "The structures and properties of solids" 6th Ed. Sheffield, UK. Edward Arnold Publishing.

Cullity, B. D. (1972) "Introduction to magnetic materials." Addison-Wesley Publishing

Cullity, B. D and S. R. Stock (2001) "Elements of X-Ray Diffraction" Third Edition. Prentice Hall, NJ, USA.

Curie, P. (1894) "Sur la symétrie des phénomènes physiques: symétrie d'un champ électrique et d'un champ magnétique." J. Physique. **3**. 393.

Daniels, J., W. Jo, J. Rödel, V. Honkimäki, J. L. Jones (2010) Acta Materialia, **58**, 6. 2103-2111.

Darby, M. I. (1967) "Tables of the Brillouin function and of the related function for the spontaneous magnetization." Brit. J. Appl. Phys., **18**, 1415.

Debye, P. (1926)  Phys. Zeits. **36** 300.

Dayanidhi, K. K. (1973) "A note on the derivation of Heesch groups." Acta Cryst. A29, 305.

Diamond Light Source Ltd. (2009) "About Us" and "Technology". [online] [Accessed: 26th July 2010] Available from: <http://www.diamond.ac.uk>

Dzyaloshinskii, I. E. (1959) Zh. Eksp. Teor. Fiziks. **10.** 628 (in Russian)

Ederer, C. and Spaldin, N. A., (2005)"Influence of strain and oxygen vacancies on the magnetoelectric properties of multiferroic bismuth ferrite." Phys. Rev. B. **71** 224103.

Ederer, C. and Spaldin, N. A.,(2005) "Weak ferromagnetism and magnetoelectric coupling in bismuth ferrite." Phys. Rev. B. **71** 060401

Eerenstein, W., F. D. Morrison, J. Dho, M. G. Blamire, J. F. Scott and N. D. Mathur (2005) Science. **307**. 1203a.

Eerenstein, W., N. D. Mathur and J. F. Scott (2006) "Multiferroic and magnetoelectric materials." Nature Review. **442**. 17. 759-765.

Eitel, R, C. A. Randall, T. R. Shrout and P. W. Rehrig. (2001) Jpn. J. Appl. Phys. **40**, 5999-6002.

Eitel, R. and C. A. Randall (2007). Phys. Rev. B. **71**, 094106.

Enzo, S., G. Fagherazzi, A. Benedetti and S. Polizzi (1988) J. Appl. Cryst. **21**, 536-542.

Etrema Products Inc. (2003) "Core Technology." [online]  [Accessed 15th July, 2010] Available from: http://www.etrema-usa.com/core/terfenold/

Fedulov, S. A. (1961) "Determination of Curie Temperature in Ferroelectric $BiFeO_3$." Dokl. Akad. Nauk SSSR. **6** 139.

Fiebig, M, T. Lottermoser et al. "Observation of coupled magnetic and electric domains." Nature. **419**. 6909. 818-20.

Fiebig, M. (2005) "Revival of the magnetoelectric effect." J. Phys. D: Appl. Phys. **38**. 123-5

Fiebig, M. (2007) "Magnetoelectric Correlations in Multiferroics." Presentation given in proceedings of the European School on Multiferroics, 2-6 July, 2007. Grenoble Institute of Technology, Grenoble, France. pp.27-38.

Finger, L. W, D. E. Cox and A. P. Jephcoat. (1994) "A correction for powder diffraction peak asymmetry due to axial divergence." J. Appl. Cryst. **27**, 892.

Fiorillo, F. (2004) "Measurement and characterisation of magnetic materials." Italy. Elsevier Inc.

Fischer, P., et al.(1980) "Temperature dependence of the crystal and magnetic structures of $BiFeO_3$." Journal of Physics. **13.** 1931.

Folen, V. J., G. T. Rado and E. W. Stalder (1961) Phys. Rev. Lett. **6**. 607.

Fortes, A. D. (2004) University College, University of London, Ph.D. Thesis.

Freeman, A. J., and Schmid, H., (1975) "Magnetoelectric Interaction Phenomena in Crystals." Proc. MEIPIC-1. (Seattle, USA. 21-24 May 1973.)

Gavriliuk, A. G. et al (2005). JETP Lett. **82**(4), 224.

Gilbert, W. (1600) " De Magnete" Volume 1893. Part 1. Dover Publications. Translated 1958.

Glazer, A. M. (1972) "The Classification of Tilted Octahedra in Perovskites." Acta. Cryst. B**28**, 3384.

Glazer, A. M. (2007) "Ferroelastics." Presentation given in proceedings of the European School on Multiferroics, 2-6 July, 2007. Grenoble Institute of Technology, Grenoble, France. pp.13-19.

Godec, Y. L., T. Strassle, G. Hamel, R. J. Nelmes, J. S. Loveday, W. G. Marshall and S. Klotz (2004) High Pressure Research. **24**, 1. 205-217.

Goldschmidt, V. M. (1926) "Die gesetze der krystallochemie" Naturwissenschafen. **14**, 477.

Goldstein, J. (2003) "Scanning electron microscopy and X-ray microanalysis." 3$^{rd}$ ed. Kluwer Academic, Plenum Pub., New York; London.

Goodhew, P. J., F. J. Humphreys and R. Beamland (2001). "Electron microscopy and analysis." Taylor and Francis. London.

Hall, D. A., T. Mori, P. Withers, et al. (2008) Mats. Sci. and Tech. **24**, 8. 927-933.

Hammond, C. (1992) "Introduction to Crystallography" Revised Edition. Oxford University Press.

Hammond, C. (1997) "The basics of crystallography and diffraction." International Union of Crystallography. Oxford University Press.

Hannon, A. C., S. Bennington and S. Langridge. (2006) "Neutron Training Course" Book and Presentations from the ISIS Neutron Training Course held at Rutherford Appleton Laboratories, Oxford. December 2006.

Hanumaiah, A., T. Bhimasankaram, S. V. Suryanarayana and G. S. Kumar. (1994) "Dielectric behaviour and magnetoelectric effect in cobalt ferrite-barium titanate composites." Bull. Mater. Sci. **17**, 405-09.

Harwood, M.G., P, Popper and D. F. Rushman (1947) 'Curie Point Of Barium Titanate', Nature, **160**(4054), 58-59

Haumont, R., J. Kreisel, P. Bouvier.(2006) Phase Transition, **79**(12), 1043.

Heath, J. (2005). "Dictionary of microscopy." Wiley. Chichester, UK.

Hill, N. A. (2000)(a) "Why are there so few magnetic ferroelectrics?" J. Phys. Chem. B **104** 6694-6709.

Hill, N. A. (2000)(b) "First principles study of multiferroic magnetoelectric manganites." AIP Conference Proceedings. 372-382.

Hill, N. A. (2002) "Density functional studies of multiferroic magnetoelectrics." Annu. Rev. Mater. Res **32** 1-37.

Hölzer, G., M. Fritsch, M. Deutsch, J. Hartwig and E. Forster (1997) "$K\alpha_{1,2}$ and $K\beta_{1,3}$ x-ray emission lines of the 3d transition metals." Phys. Rev. A. **56.** 6. 4554.

Huang, Z., Y. Cao, Y. Sun et al (1997) Phys .Rev. B. **56**. 5. 2623-26.

Hull, S., R. I. Smith, W. I. F. David, A. C. Hannon, J. Mayers and R. Cywinski,(1992) "The POLARIS Powder Diffractometer at ISIS." Physica B **180** & **181**, 1000-1002

Hund, F. (1925) "The configuration of polyatomic polar molecules I." Zeitschrift Fur Physik. **31. 81.**

Ibberson, R. M, W. I. F. David, K. S. Knight. (1992) CLRC Report RAL-92-031.

Jaffe, B., R. S. Roth and S. Marzullo. (1954) "Piezoelectric properties of Lead Zirconate-Lead Titanate Solid-Solution Ceramics." J. Appl. Phys. **25**. 809.

Jaffe, B., W. R. Cook and H. Jaffe. (1971) "Piezoelectric Ceramics." Academic Press, London.

Janolin, P. –E., et al. (2008) Phys. Rev. Lett. **101**, 237601.

Jiles, D. C. (2003) "Recent advances and future directions in magnetic materials." Acta Materialia **51**. 5907-39.

Jona, F. and G. Shirane. (1993) "Ferroelectric crystals." Dover Publications, Inc. New York.

Känzig, W. (1957) "Ferroelectrics & Antiferroelectrics." New York. Academic Press.

Khan, M. A. (2008) "Preparation and properties of bismuth ferrite-lead titanate thin films prepared by pulsed laser deposition." Thesis (Ph.D). Institute for Materials Research, University of Leeds.

Kim, D. H. et al (2008) Appl. Phys. Lett. **92**. 012911.

Kimura, T., S. Kawamoto, I. Yamada, M. Azuma, M. Takano and Y. Tokura (2003) "Magnetocapcitance effect in multiferroic $BiMnO_3$." Phys. Rev. B. **67**. 180401.

Kinane, C. (2008) "The interplay of magnetism and structure in patterned multilayer thin films." Thesis (Ph.D). Physics and Astronomy, University of Leeds

Kiselev, S. V., et al. (1964) "Neutron Diffraction study of the magnetic ordering and atomic…" Soviet Physics Solid State. **5** 11.

Klotz, S., J. M. Besson, G. Hamel, R. J. Nelmes, J. S. Loveday, W. G. Marshall and R. M. Wilson (1995) Appl. Phys. Lett. **66**, (14), 1735.

Kluwer, A. J. C. (1995) "International tables for crystallography." Mathematical, Physical and Chemical Tables, **C**. London.

Komarneni, S., V. C. Menon, Q. H. Li, R. Roy and F. Ainger. (1996) J. Am. Ceram. Soc. **79**, 1409.

Kubel, F. and H. Schmid, (1990) "Structure of a ferroelectric and ferroelastic monodomain crystal…" Acta Crystal **B 46** 698

Kumar, M. and V. R. Palkar (2000) Appl. Phys. Lett. **76**, 19. 2764.

Kumar, P. A. and K. Mandal (2007) J. Appl. Phys. **101**. 113906.

Landau, L. D. and E. Lifshitz (1960) "Electrodynamics of continuous media." Reading. Addison-Wesley (translation of Russian ed. 1958)

Larson, A. C. and R. B. Von Dreele (2004) "General Structure Analysis System (GSAS)," Los Alamos National Lab Report No. LAUR 86-748.

Lawson, A. C., A. C. Larson, M. C. Aronson, S. Johnson, Z. Fisk, P. C. Canfield, J. D. Thompson and R. B. Von Dreele. (1994) "Magnetic and crystallographic order in α-manganese." J. Applied Physics. **76.** 10. 7049-51.

Lebeugle, D., D. Coulson, A. Forget, M. Viret, A. M. Bataille and A. Guskasov (2008) "Electric-field induced spin flop in $BiFeO_3$ single crystals at room temperature." Phys. Rev. Lett. **100**. 227602.

Li, J., J. Wang, M. Wuttig, R. Ramesh, N. Wang, B. Ruette, A. P. Pyatakov, A. K.; Zvezdin and D. Vielhand (2004) Appl. Phys. Lett. **84**. 12. 5261-63.

Lightfoot, P. (2010) "High Temperature Phase Transitions in $BiFeO_3$." Presentation IL4 at the 19th International Symposium on the Application of Ferroelectrics (ISAF)  8-12 th August, Edinburgh, Scotland. 2010.

Lines, M. E and A. M. Glass. (1977) "Principles and Applications of Ferroelectrics and Related Materials." Clarendon Press, Oxford.

Lonkai, Th., D. G. Tomuta, U. Amann, J. Ihringer, R. W. A. Hendrix, D. M. Tobbens and J. A. Mydosh (2004) "Development of the high-temperature phase of hexagonal manganites." Phys. Rev. B. **69**. 134108. (DOI: 10.1103/PhysRevB.69.134108)

Lutterotti, L. and P. Scardi. (1990) J. Appl. Cryst. **23**, 246-252.

Lujan, M., J. P. Rivera, H. Schmid et al. (1994) Ferroelectrics. **161**. 77.

Martin, L. W., S. P. Crane, Y-H. Chu, M. B. Holcomb, M. Gajek, M. Huijben, C-H. Yang, N. Balke and R Ramesh (2008) "Mulitferroics and magnetoelectrics: thin films and nanostructures." J. Phys: Condens. Matter. **20**. 43. 434220.

Matsuo, Y. and H. Sasaki (1966) "Effect of grain size on microcracking in lead titanate ceramics." J. Am. Cer. Soc. **49**, 4. 229-230.

Maxwell, J. C. (1865) "A Dynamical Theory of the Electromagnetic Field." Philosophical Transactions of the Royal Society of London. **155**. 459-512.

McCusker, L. B., R. B. Von Dreele, D. E. Cox, D. Louër and P. Scardi (1999) "Rietveld refinement guidelines." J. Appl. Cryst. **32**, 36-50.

Megaw , H. D. (1945) 'Crystal Structure Of Barium Titanate', Nature, **155**(3938)  484-485

Megaw, H.D. (1946) 'Changes in polycrystalline barium-strontium titanate at its transition temperature', Nature, **157**(3975)  20-21.

Michel, C. et al. (1969) "The atomic structure of $BiFeO_2$."  Solid State Communications **7** 701 -704

Mitchell, R. H (2002) "Perovskites: modern and ancient" Almaz Press, Thunder Bay, Canada.

Moreira dos Santos, A., S. Parashar, A. R. Raju, Y. S. Zhao, A. K. Cheetham and C. N. R. Rao (2002) Solid State Comms. **122**. 49-52.

Moriya, T. (1960) "Anisotropic superexchange interaction and weak ferromagnetism." Phys Rev. **120**. 1.91-98.

Morrish, A. H. (1965) "The physical principles of magnetism." John Wiley & Sons. New York.

Moulson, A. J. and J. M. Herbert (2003) "Electroceramics: Materials, Properties, Applications." 2$^{nd}$ Edition. John Wiley & Sons Ltd.

Muhtar, A., M. Somayazulu, R. E. Cohen, P. Ganesh, P. Dera, H. Mao, R. J. Hemley, Y. Ren, P. Liermann and Z. Wu. (2008) "Origin of morphotropic phase boundaries in ferroelectrics." Nature. **451**. 545-9.

Néel, L. (1932) Ann. Phys., Paris. **17**, 5.

Néel, L. and R. Pauthenet. (1952) C. R. Acad. Sci., Paris. **234**. 1991.

Noheda, B., D. E. Cox, G. Shirane, J. A. Gonzalo, L. E. Cross and S-E. Park. (1999) "A monoclinic ferroelectric phase in the $Pb(Zr_{1-x}Ti_x)O_3$ solid solution." Appl. Phys. Lett. **74.** 14. 2059.

Noheda, B., Z. Zhong, D. Cox G. Shirane, S.-E. Park and P. Rehrig (2002) Phys. Rev. B. 65, 22.

Nye, J. F. (1979) "Physical properties of Crystals: Their representation by Tensors and Matrices" Clarendon Press, Oxford.

O'Dell, T. H. (1970) "The electrodynamics of magneto-electric media." American Elsevier Pub. Co. Amsterdam, Holland.

Oka, K., et al (2008) Inorg. Chem.,**47**, 16. 7355-7359.

Ørsted, H.C. (1820), "Experimenta Circa Effectum Conflictus Electrici in Acum Magneticam", Hafniae, Schultz, 1820.

Pashkin, A., K. Rabia, S. Frank, C. A. Kuntscher, R. Haumont, R. Saint-Martin & J. Kreisel (2007) Condensed Matter, 0712.0736.

Pearl (2010) "ISIS – Pearl high pressure powder diffractometer." [online] [Accessed 15th July, 2010] Available from: <http://www.isis.stfc.ac.uk/instruments/pearl/>

Prellier, W., M. P. Singh and P. Murugavel (2005) "The single-phase multiferroic oxides: from bulk to thin film." J. Phys: Condens. Matter. **17**. R803-832.

Prinz, G. A. (1999) "Magnetoelectronics applications." J. Mag & Mag. Materials. **200** 57.

Przenioslo, R., M. Regulski and I. Sosnowska (2006(a)) J. Phys. Soc. Jpn. **75**. 8. 084718.

Przenioslo, R., A. Palewicz, M. Regulski, I. Sosnowska, R. M. Ibbotson and K. S. Knight (2006(b)) J. Phys: Condens. Matter. **18.** 2069-2075.

Ponomarev, B. K., S. A. Ivanov, Y. F. Popov, V. D. Negrii and B. S. Red'kin (1994) "Magnetoelectric properties of some rare earth molybdates." Ferroelectrics. **161.** 43-48

Qi, X., M. Wei, Y. Lin, Q. Jia, D. Zhi, J. Dho, M. G. Blamire and J. L. MacManus-Driscoll (2005). Appl. Phys. Lett. **86**. 071913.

Rameika, J. P. and A. M. Glass. (1970) Materials Research Bulletin. **5**. 37-45

Ramesh, R. and N. Spaldin (2007) "Multiferroics: progress and prospects in thin films." Nature Materials. **6**. 21.

Ranjan, R. (2007) "Electronic structure and magnetism of EuTiO3: a first-principles study" J. Phys: Condensed Matter. **19**. 406217

Rietveld, H. M. (1966) Acta. Cryst. **20**, 508.

Rietveld, H. M. (1967) Acta. Cryst. **22**, 151.

Rietveld, H. M. (1969) J. Appl. Cryst. **2**, 65.

Rodríguez-Carvajal, J. (1993) "Recent advances in magnetic structure determination by neutron powder diffraction." Physica B. **192**, 55-69.

Roginskaya, Yu., E., et al. (1966) "The nature of the dielectric and magnetic properties of $BiFeO_3$." Soviet physics JETP **23** 1 47

Röntgen, W. C. (1888) Ann. Phys. **35**. 264.

Ryu, J., S. Priya, A. V. Carazo and K. Uchino. (2001) J. Am. Ceram. Soc. **84**. 12. 2905-908

Ryu, J., S. Priya, K. Uchino and H-E. Kim (2002) "Magnetoelectric effect in composites of magnetorestrictive and piezoelectric materials." J. Electroceramics. **8**. 107-119.

Sai Sunder, V. V. S. S., A. Halliyal and A. M. Umarji. (1995) "Investigation of tetragonal distortion in the $PbTiO_3$-$BiFeO_3$ system by high-temperature x-ray diffraction." J. Mater. Res. **10**. 5. 1301-06.

Sani, A. and M. Hanfland. (2002) "Pressure and Temperature Dependence of the Ferroelectric-Paraelectric Phase Transition in $PbTiO_3$." J. Solid State Chemistry. **167.** 446-452.

Sawaguchi, E. (1953) "Ferroelectricity versus Antiferroelectricity in the solid solutions of $PbZrO_3$ and $PbTiO_3$." J. Phys. Soc. Jpn. **8.** 615-629

Schmid, H., H. Rieder and E. Ascher (1965) "Magnetic susceptibilities of some 3d transition metal boracites." Solid State Comms. **3**. 327-330.

Schmid, H, (1994)(a) "Multi-ferroic Magnetoelectrics." Ferroelectrics. **162**. 317-38.

Schmid, H. (1994)(b) "Magnetic ferroelectric materials." Bull. Materials Science. **17**. 1411-14.

Schmid, H., et al (1994)(c) Proc. MEIPIC –2. (Ascona, Switzerland. 13-18 September 1993.) Ferroelectrics **161** Conf Vol.

Schmid, H. (2003) Chapter in "Introduction to complex mediums for optics and electromagnets." SPIE Publishing, WA, USA. Edited by W. S. Weiglhofer & A. Lakhtakia.

Scott, J. F and C. A. Araujo (1989) Science. **246**. 1400.

Scott, J. F. (2007)(a) "Applications of Modern Ferroelectrics." Science. **315**. 954-959

Scott, J. F. (2007)(b) "Electrical characterization of magnetoelectrical materials." J. Mater. Res. **22**. 8. 2053-62.

Sears, V. F. (1992) "Neutron scattering lengths and cross sections." Neutron News. **3**. 3. 26-36.

Sekher, M. C. and N. V. Prasad (2006) Ferroelectrics. **345**. 1. 45-47.

Selbach, S. M., M-A, Einarsrud and T. Grande. (2009) "On the Thermodynamic Stability of $BiFeO_3$." Chem. Mater. **21**, 169-173.

Shirane, G., S. Hoshino and K. Suzuki (1950) "X-ray study of the phase transition in lead titanate." Physical Review. **80**. 6. 1105-06.

Shirane, G., R. Pepinsky, and B. C. Frazer (1956) Acta Crystallography. **9**.131–140 .

Shull, C. G., (1995) "Early development of neutron scattering." Rev. Mod. Phys. **67**, 4. 753 – 757.

Shvartsman, V. V., W. Kleeman, R. Haumont and  J. Kreisel (2007) Applied Phys. Lett. **90**. 172115.

Smith, R. I. and S. Hull (1997) "User guide for the Polaris powder diffractometer at ISIS." RAL Technical Reports, RAL-TR-97-038. CCLRC (now STFC).

Smith, R. I. (2006) "Neutron Training Course" Book and Presentations Edited by S. Bennington,  A. C. Hannon and S. Langridge. from the ISIS Neutron Training Course held at Rutherford Appleton Laboratories, Oxford. December 2006.

Smith, R. T., G. D. Achenbach, R. Gerson and W. J. James (1968) J. Appl. Phys. **39**, 1.

Smolenskii, G. A. and V. A. Joffe (1958) Communications de Colloque International.

Smolenskii, G. A., et al. (1963)  "Antiferromagnetic properties of some perovskites."  Soviet Physics JETP **16** 3, 622-624

Sommerfield, (1948)

Sosnowska, I., (1982) "Spiral magnetic ordering in bismuth ferrite." J. Phys. C: Solid State Phys. **15**. 4835-46.

Sosnowska, I., (1997) "Very High Resolution Diffractometry at Pulsed Neutron Sources." J. Neutron Res. **6**. 149-60.

Sosnowska, I., (2002) "Crystal structure and spiral magnetic ordering of $BiFeO_3$ doped with manganese." Appl. Phys. A. **74**. 1040-1042

Spaldin, N. A. and M. Fiebig (2005) "The renaissance of Magnetoelectric Multiferroics." Science. **309**. 391.

Stevenson, T., T. P. Comyn, A. J. Bell and R. Cywinski. (2007) 16th IEEE ISAF 27-31 May 2007, Nara, Japan. 1&2. 421-3.

Stevenson, T., T. P. Comyn, A. D-Aladine and A. J. Bell (2010) "Change in periodicity of the incommensurate magnetic order towards commensurate order in bismuth ferrite lead titanate." J. Magnetism and Magnetic Materials. **322**, 64-67.

Stoner, E. C. (1933) **"**Atomic moments in ferromagnetic metals and alloys with nonferromagnetic elements**."** Philos. Mag. **15**. 1080.

Squires, G. L (1978) "Introduction to the Theory of Thermal Neutron Scattering" Dover Publications, Mineola, NY, USA.

Sugie, H., N. Iwata and K. Kohn (2002) "Magnetic Ordering of Rare Earth Ions and Magnetic-Electric Interaction of Hexagonal $RMnO_3$ (R=Ho, Er, Yb or Lu)." J. Phys. Soc. Jpn. **71**. 1558-1564.

Suryanarayana, S. V. (1994) "Magnetoelectric interaction phenomena in materials." Bull. Mater. Sci. **17**. 7. 1259-1270.

Tabares-Munõz, C., J. Rivera, J. –P. Bezinge, A. Monnier and H. Schmid (1985) Jpn. J. Appl. Phys. **24**. 1051-3.

Thomas, H. L. (1985) "Léon Nicolas Brillouin – A biographical memoir." National Academy of Sciences. Washington D.C., USA.

Tipler, P. A. and R.A. Llewellyn (2003) "Modern Physics" 4th ed .W. H. Freeman Pub.

Tolédano, P. H. Schmid, M. Clin and J. P. Rivera (1985) Phys. Rev. B. **32**. 9. 32.

Tomashpol'skii, Y. Y., Venevtsev, Y. N., Zhdanov, G. S., Soviet Physics- Doklady **8** 12. 1144-45 (1964)

Trollier-McKinstry, S., L. E. Cross and Y. Yamashita. (2004) "Piezoelectric Single Crystals and their Applications." p.21 An introduction to Piezoelectric single crystals

Tutov, A., G., (1970) "The space group and some electric and magnetic properties of bismuth ferrite." Soviet physics- solid state **11** 9 2170-2171

van Aken, B. B., A. Meetsma and T. T. M. Palstra (2001) "Hexagonal $YMnO_3$." Acta Cryst. C. **57**. 230-2

van Suchtelen, (1972) J. Philips Res. Rep. **27**, 28

Valasek, J. (1920) "Piezo-electric and allied phenomena in Rochelle Salt." Rochelle Salt **17-4** 475.

Venevstev, Y. N. (1960) Sov. Phys. Crystallogr. **5**, 594.

Vickery, R. C. and A. Klann (1957) J. Chem. Phys. **27.** 5. 1161.

Von Dreele, R (2009) Private communication. 11th August 2009.

Wadhawan, V. K. (2000) "Introduction to ferroic materials." Indore, India. Gordon and Breach Publishing.

Wang, J., J. B. Neaton, H. Zheng, V. Nagarajan, S. B. Ogale, B. Liu, D. Vielhand, V. Vaithyanathan, D. G. Schlom, U. V. Waghmare, N. A. Spaldin, K. M. Rabe, M. Wuttig and R. Ramesh. (2003) "Epitaxial $BiFeO_3$ Multiferroic Thin Film Heterostructures." Science. **299**. 5613. 1719-22

Wang, J., J. B. Neaton, H. Zheng, V. Nagarajan, S. B. Ogale, B. Liu, D. Vielhand, V. Vaithyanathan, D. G. Schlom, U. V. Waghmare, N. A. Spaldin, K. M. Rabe, M. Wuttig and R. Ramesh. (2005) "Response to comment on Epitaxial $BiFeO_3$ Multiferroic Thin Film Heterostructures." Science. **307**. 1203b.

Williamson, G. K. and W. H. Hall (1953) "X-ray line broadening from filed aluminium and wolfram." Acta Metallurgica. **1**. 22-31.

Wollan, E. O. and W. C. Koehler. (1955) Neutron diffraction study of the magnetic properties of the series of perovskite-type compounds $[(1-x)La, xCa]MnO_3$" Physical Review. **100**. 2. 545.

Woodward, D. I., I. M. Reaney, R. E. Eitel and C. A. Randall (2003) J. Appl. Phys. **94**, 5. 3313-18.

Woodward, D. I., J. Knudsen and I. M. Reaney. (2005) "Review of crystal and domain structures in the $PbZr_xTi_{1-x}O_3$ solid solution. Phys. Rev. B. **72**. 104110.

Wu, Z and R. E. Cohen (2005) Phys. Rev. Lett. **95**, 037601.

Wul, B. (1945) "Dielectric constants of some titanates." Nature. **156**. 480.

Wul, B (1946) 'Barium Titanate - a new ferro-electric', Nature, **157**(3998), 808-808.

Yagnik, C. M. (1971) J. Appl. Phys. **42,** 1.

Yakel, H. L., W. C. Koehler, E. F. Bertaut and E. F. Forrat (1963) Acta. Cryst. **16**. 957.

Zaslavskii, A. I. and A. G. Tutov (1960) "Structure of the new antiferromagnetic $BiFeO_3$." Sov. Phys.- Doklady. **135**. 4. 1257.

Zavaliche, F., H. Zheng, L. Mohaddes-Ardabili, S. Y. Yang, Q. Zhan et al (2005) "Electric field-induced magnetization switching in epitaxial columnar nanostructures." Nano Letters. **5**. 9. 1793-1796.

Zheng, H., J. Wang, S. E. Lofland, Z. Ma et al (2004) Science. **303**. 661.

Zhu, W-M., and Z. -G. Ye, (2007) Appl. Phys. Lett. **89.** 232904.

Zhu, W-M., H. –Y. Guo and Z. -G. Ye, (2008) Phys. Rev. B. **78.** 014401

Zuo, R., W. Yang, J. Fu, S. Su and L. Li (2009) Materials Chemistry and Physics. **113**, 361-4.

Zvezdin, A. K., A. M. Kadomtseva, S. S. Krotov, A. P. Pyatakov, Yu. F. Popov and G. P. Vorob'ev (2006) "Magnetoelectric interaction and magnetic field control of electric polarization in multiferroics." J. Magnetism and Magnetic Materials. **300**. 224-228.

# 8 APPENDICES

## 8.1 APPENDIX A – RIETVELD REFINEMENT PARAMETERS

For the purposes of the structural refinement, a number of constraints were imposed. It was found necessary to employ one isotropic temperature factor ($B_{iso}$ in FullProf, $U_{iso}$ in GSAS) universally across both R3c and P4mm ferroelectric models, that is $B_{iso}$ (P4mm) = $B_{iso}$ (R3c). Separate temperature factors were trialled for each of the sites, i.e., one temperature factor for each of the A (Pb,Bi), B (Fe,Ti) and O (O1 and O2 in the case of the tetragonal P4mm phase), but negative temperature factors on the B-site are resultant; for low concentrations of a phase, this effect was most pronounced. Additionally to temperature factor constrains, the large A-site atoms were fixed at the origin and not refined. The atomic displacements of the B-site atoms were constrained to each other, within the same phase, and likewise the oxygen atoms in the tetragonal phase. The occupancy of each of the atoms was set at the intended stoichiometry, and not refined; such a strategy was considered valid as a result of the weight loss measurements reported in chapter 3.

## 8.1.1 APPENDIX A (i) – REFINEMENT AGREEMENT FACTORS

In the FullProf suite software, two sets of indices are calculated, according to the number of points recorded, '$n$'.

These indices are defined below where;

$y_c$ – calculated counts  $\qquad\qquad$ $\sigma^2$ - variance of the observed $y$

$y$ - observed counts  $\qquad\qquad\qquad$ $w = \dfrac{1}{\sigma^2}$

$n$ – number of points

---

Profile Factor, $R_p$;

$$R_P = 100 \frac{\sum_{i=1,n} |y_i - y_{c,i}|}{\sum_{i=1,n} y_i}$$

Weighted Profile Factor, $R_{wp}$;

$$R_{wp} = 100 \left[ \frac{\sum_{i=1,n} w_i |y_i - y_{c,i}|^2}{\sum_{i=1,n} w_i {y_i}^2} \right]^{1/2}$$

Expected Weighted Profile Factor, $R_{exp}$;

$$R_{exp} = 100 \left[ \frac{n - p}{\sum_i w_i {y_i}^2} \right]^{1/2}$$

Goodness of fit indicator, $S$;

$$S = \frac{R_{wp}}{R_{exp}}$$

Reduced chi-square, $\chi^2$;

$$\chi^2 = \left[\frac{R_{wp}}{R_{exp}}\right]^2 = S^2$$

## 8.2  APPENDIX B – IMAGES

All of the images that appear as 3D anaglyphs throughout the text can be found here for the 1 dimensional original.
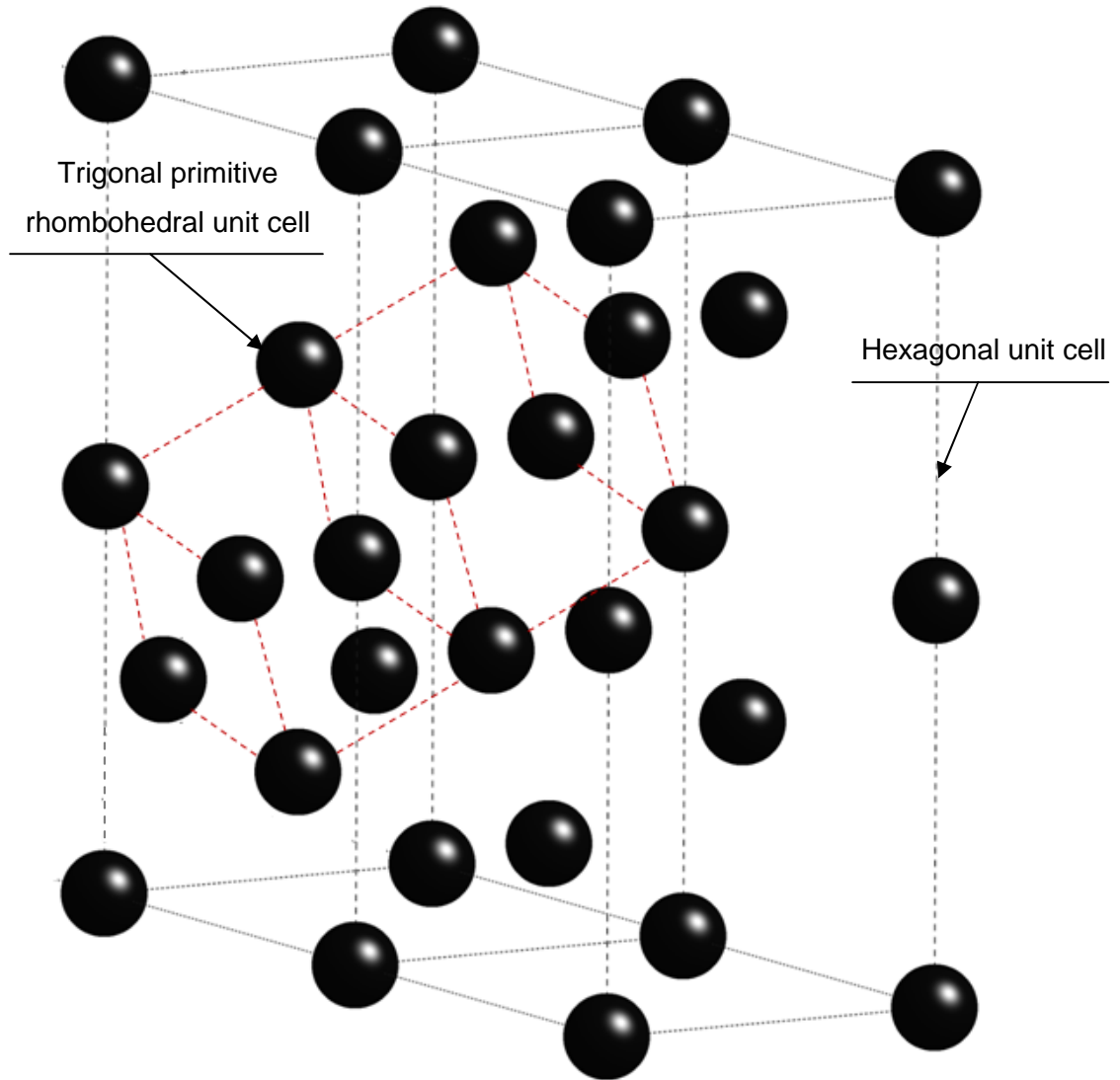


**Figure 1-9 An example of the rhombohedral lattice system whereby the atoms can arrange to be grouped in the hexagonal or trigonal (within) crystal system.**
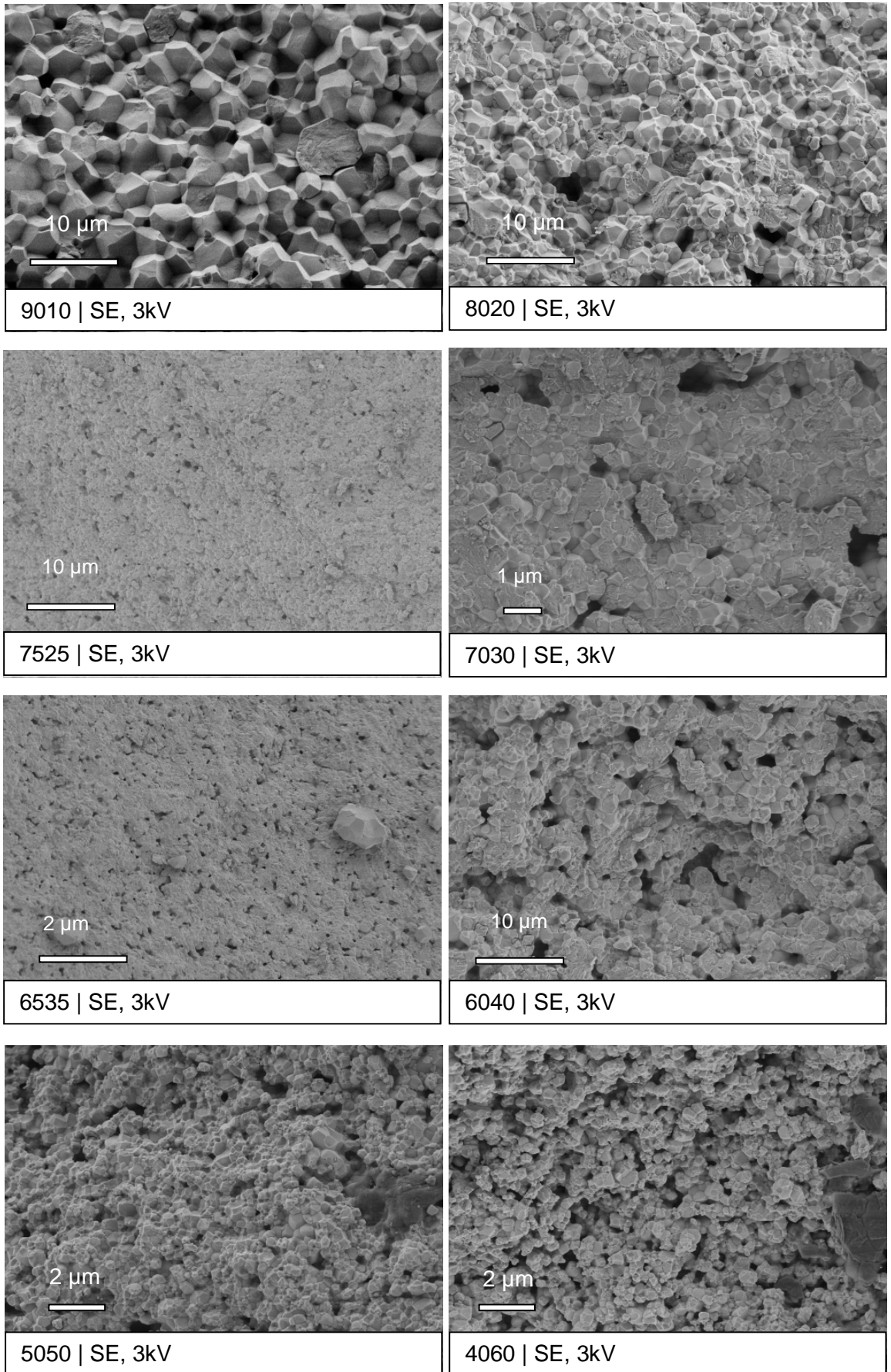
**Figure 4-11 Scanning electron micrographs of fractured BFPT sintered ceramics using secondary electron (SE) imaging.**

# 9   PUBLICATIONS

1. Stevenson, T., T. P. Comyn, A. D-Aladine and A. J. Bell. (2010) "Change in incommensurate magnetic order towards commensurate order in bismuth ferrite lead titanate." Journal of Magnetism and Magnetic Materials. **322**, 22. pp.64-67. DOI: 10.1016/j.jmmm.2010.07.043

2. Levin, I., S. Karimi, V. Provenzano, C. L. Dennis, H. Wu, T. P. Comyn, T. J. Stevenson, R. I. Smith and I. M. Reaney. (2010) "Reorientation of magnetic dipoles at the antiferroelectric-paraelectric phase transition of $Bi_{1-x}Nd_xFeO_3$." Physical Review B. 81, 020103(R). DOI: 10.1103/PhysRevB.81.020103

3. Comyn, T. P., T. Stevenson, M. Al-Jawad, S. Turner, R. I. Smith, A. J. Bell and R. Cywinski (2009) "High temperature neutron diffraction studies of $0.9BiFeO_3$-$0.1PbTiO_3$." Journal of Applied Physics. **105**. 9, 094108. DOI: 10.1063/1.3116735

4. Skidmore, T. A., T. Stevenson, T. P. Comyn and S. J. Milne (2008) "Phase development during mixed oxide processing of a NKN-LTO powder." Key Engineering Materials. **368**. pp. 1886-1889. DOI:10.4028/www.scientific.net/KEM.368-372.1886.

5. Comyn, T. P., T. Stevenson, M. Al-Jawad, S. L. Turner, R. I. Smith, W. G. Marshall, A. J. Bell and R. Cywinski (2008) "Phase-specific magnetic ordering in $BiFeO_3$ – $PbTiO_3$." Applied Physics Letters. **93**, 23, 232901. DOI: 10.1063/1.3042209

6. Stevenson, T., T. P. Comyn, A. J. Bell and R. Cywinski (2007) "Multiferroic (ferroelectro-magnetic) properties of bismuth ferrite lead titanate." 16th IEEE International Symposium on Applications of Ferroelectrics. Nara, Japan. pp. 421-423.

7. Comyn, T. P., T. Stevenson and A. J. Bell (2005) "Piezoelectric properties of $BiFeO_3$ – $PbTiO_3$ ceramics." Journal de Physique IV. **128**, 128. pp. 13-17. DOI: 10.1051/jp4:2005128003.

# 10  ATTENDED CONFERENCES & MEETINGS

1. 15$^{th}$ International Symposium on the Applications of Ferroelectrics (2006) Sunset Beach, North Carolina, USA.

2. European School of Multiferroics (2007) Grenoble, France. (Oral Presentation).

3. 16$^{th}$ International Symposium on the Applications of Ferroelectrics (2007) Nara, Japan. (Presentation).

4. Ferroelectrics (2007) Dundee, United Kingdom (Oral Presentation)

5. U.S. Navy Workshop on Acoustic Transduction Materials and Devices (2008) Penn State, Pennsylvania, USA. (Oral Presentation)

6. Electroceramics XI Meeting (2008) Manchester, United Kingdom (Oral Presentation)

7. Piezo Conference (2009) Zakopane, Poland. (Oral Presentation)

8. International Conference on Neutron Scattering (2009) Knoxville, Tennessee. USA. (Oral Presentation)

9. Transition Metal Oxides Meeting (2009) Liverpool, United Kingdom (Presentation)

10. 18$^{th}$ International Symposium on the Applications of Ferroelectrics (2009) Xi'an, China. (Oral Presentation).

11. 19$^{th}$ International Symposium on the Applications of Ferroelectrics (2010) Edinburgh, United Kingdom.

## 10.1  RESEARCH MOBILITY

- World Universities Network (WUN) Research Mobility Program (2008) University of Illinois at Urbana – Champaign. (http://www.Illinois.edu). Hosted by Professor David Payne.

Made on a Mac